



HAL
open science

Geodynamo simulations in the Earth's core dynamical regime: a systematic study

Tobias Schwaiger

► **To cite this version:**

Tobias Schwaiger. Geodynamo simulations in the Earth's core dynamical regime: a systematic study. Earth Sciences. Université Paris Cité, 2020. English. NNT: 2020UNIP7203 . tel-03344030

HAL Id: tel-03344030

<https://theses.hal.science/tel-03344030v1>

Submitted on 14 Sep 2021

HAL is a multi-disciplinary open access archive for the deposit and dissemination of scientific research documents, whether they are published or not. The documents may come from teaching and research institutions in France or abroad, or from public or private research centers.

L'archive ouverte pluridisciplinaire **HAL**, est destinée au dépôt et à la diffusion de documents scientifiques de niveau recherche, publiés ou non, émanant des établissements d'enseignement et de recherche français ou étrangers, des laboratoires publics ou privés.

Université de Paris
Institut de Physique du Globe de Paris
École doctorale Sciences de la Terre et de l'environnement et
physique de l'Univers STEP'UP n°560
Équipe de Dynamique des Fluides Géologiques

Geodynamo simulations in the Earth's core dynamical regime: a systematic study

par

Tobias Schwaiger

Thèse de doctorat de Sciences de la Terre et de l'environnement

dirigée par **Julien Aubert**
& **Thomas Gastine**

soutenue le 23 novembre 2020 devant un jury composé de :

	Johannes Wicht	Rapporteur
Senior Scientist (Max Planck Institute for Solar System Research)		
	Henri-Claude Nataf	Rapporteur
Directeur de Recherche (ISTerre - CNRS)		
	Céline Guervilly	Examinatrice
NERC Researcher (University of Newcastle)		
	Krista Soderlund	Examinatrice
Research Scientist (University of Texas at Austin)		
	Alexandre Fournier	Président du jury
Professeur (IPGP - Université de Paris)		
	Thomas Gastine	Co-Directeur de thèse
Chargé de Recherche (IPGP - CNRS)		
	Julien Aubert	Directeur de thèse
Directeur de Recherche (IPGP - CNRS)		



PhD Thesis

Geodynamo simulations in the Earth's core
dynamical regime: a systematic study

by

Tobias Schwaiger

Advisors: Julien Aubert, Thomas Gastine

Institut de Physique du Globe de Paris
École Doctorale STEP'UP
Université de Paris

Contents

Summary	5
Résumé	7
1 Introduction	9
1.1 Structure of the Earth's deep interior	9
1.2 Geomagnetic field	11
1.2.1 Sources	11
1.2.2 Observations	11
1.2.3 Geomagnetic field models	13
1.2.4 Power spectrum	15
1.2.5 Time variations	17
1.3 Core dynamics	18
1.3.1 Geodynamo hypothesis	18
1.3.2 Core flow inversions	19
1.3.3 Magnetic field strength in the core	23
1.3.4 Dynamically-relevant time scales	24
1.3.5 Force balance governing flow dynamics	25
1.4 Objectives of this work	30
2 A magneto-hydrodynamic model for the geodynamo	32
2.1 Magneto-hydrodynamic equations	32
2.1.1 Continuity equation	32
2.1.2 Momentum equation	33
2.1.3 Induction equation	36
2.1.4 Heat transport equation	38
2.2 Reference state	40
2.3 Equations for the convective perturbations	42
2.4 Boussinesq approximation	46
2.5 Non-dimensionalisation	47
2.6 Boundary conditions	50

3	Theoretical scaling laws for the flow length scale	52
3.1	Leading-order geostrophy	52
3.1.1	VAC balance	53
3.1.2	CIA balance	54
3.1.3	MAC balance	54
3.2	Leading-order magnetostrophy	56
4	Numerical methods	59
4.1	Poloidal-toroidal decomposition	59
4.2	Evolution equations of scalar fields	60
4.2.1	Poloidal and toroidal flow potentials	61
4.2.2	Poloidal and toroidal magnetic potentials	62
4.2.3	Temperature perturbation	63
4.2.4	Pressure	63
4.3	Spherical harmonic expansion	65
4.4	Spectral evolution equations	67
4.5	Radial representation	69
4.5.1	Finite difference method	69
4.5.2	Chebyshev collocation method	71
4.6	Boundary conditions	75
4.7	Time integration	75
4.8	Simulations computed for this work	77
5	Force balance in numerical geodynamo simulations: a systematic study	79
5.1	Introduction	80
5.2	Numerical model	83
5.3	Results	86
5.3.1	Force balance spectra	86
5.3.2	Convective pattern	90
5.3.3	2D force spectra	92
5.4	Discussion	97
6	Relating force balances and flow length scales in geodynamo simulations	101
6.1	Introduction	102
6.2	Methods	106
6.2.1	Numerical models	106
6.2.2	Energetically relevant length scales	108
6.2.3	Dynamically relevant length scales	109
6.3	Results	111
6.3.1	Convective length scales in dynamo simulations	111
6.3.2	Convective length scales in rotating convection simulations	118
6.4	Discussion	119
6.5	Conclusions	121

7	Conclusions and perspectives	123
7.1	Summary of the results	124
7.1.1	Force balance regimes	124
7.1.2	Relating force balances to flow length scales	126
7.2	Some preliminary findings and open questions	128
7.3	Implications for the geodynamo	131
A	Derivation of terms for the evolution equations of the scalar potentials	132
B	Results of simulations	135
B.1	Dynamo models	135
B.2	Rotating convection models	139
	Acknowledgements	158

Summary

The Earth's magnetic field is generated by dynamo action in the liquid outer core. Based on theoretical considerations and estimates of the physical properties of the core, it is expected that the flow dynamics driving this process are controlled by a balance between pressure, Coriolis, buoyancy and Lorentz forces, while contributions from inertia and viscous forces are negligible. The hierarchy of the remaining forces has been the subject of a long-standing controversy. It has been suggested that the prevailing force equilibrium could be either geostrophic or magnetostrophic. In the former case, the dominant force balance is only between Coriolis and pressure forces, whereas in the latter case it additionally includes the Lorentz force. If geostrophy is prevailing, the Lorentz force enters the force balance at the next order, where it is compensated by buoyancy and non-geostrophic Coriolis forces. This type of force equilibrium is therefore sometimes referred to as quasi-geostrophic Magneto-Archimedean-Coriolis (QG-MAC) balance.

In addition to observations and theoretical considerations, numerical simulations are an important tool for our understanding of the Earth's dynamo mechanism. Since the first successful geodynamo models were calculated 25 years ago, computing resources have increased considerably. Nevertheless, current models still operate at parameters that are far from the expected conditions of the Earth's core. Despite this limitation, numerical dynamos have proven to be capable of reproducing numerous features of the geomagnetic field. However, it remains uncertain whether these results are obtained for the correct physical reasons. Studies that attempted to determine the numerically achieved physical regime led to contradictory interpretations. Some argued for geophysically-relevant force balances, i.e. QG-MAC or magnetostrophic balances, while others have suggested that the dynamics could be viscously controlled and thus not applicable to the Earth's core.

In this work, we performed a systematic survey of the force balance in the numerically accessible parameter space to identify whether these diverging results are due either to misinterpretations or to the fact that the respective models operate in different dynamical regimes. By analysing in detail the variations of the force balances, including their length-scale dependence, we found that the majority of dynamos that generate a predominantly dipolar magnetic field are governed by a QG-MAC balance. In such models the prevailing force equilibrium is either geostrophic at all length scales or split into large-scale geostrophy and small-scale magnetostrophy. At the next order, the non-geostrophic part of the Coriolis force is mainly compensated by buoyancy at large scales and by the Lorentz force towards smaller scales. Inertia and viscous forces represent second-order contributions. This QG-

MAC balance seems to be structurally very robust throughout the investigated parameter space. Dynamos with a different sequence of the forces, where inertia and/or viscosity replace the Lorentz force in the first-order force balance, can only be found close to the onset of dynamo action and in models that produce a multipolar magnetic field. At the same time, none of our dynamos is governed by system-scale magnetostrophy. Thus our study illustrates that most numerical dynamos are controlled by a QG-MAC balance, while cases where viscosity and inertia play a dominant role are the exception rather than the norm.

We further show that it is possible to relate the computed force balances to flow length scale measures, a task that has proven to be challenging so far. Our study suggests that this can be achieved by using the length scales associated with cross-over points in a spectral representation of the force balance. We found that in most of our analysed numerical dynamos, the scale at which buoyancy and Lorentz forces equilibrate can be associated with the dominant scale of convection. Thus, the QG-MAC balance prevailing in these models is indeed reflected in the convective pattern. Additionally, in models with a strong magnetic field, the so-called magnetostrophic cross-over length scale, at which the dominant force equilibrium changes from large-scale geostrophy to small-scale magnetostrophy, can be related to the loss of the axial invariance of the flow beyond this scale. Furthermore, we show that both these length scales obtained in our simulations are compatible with the predictions provided by theoretical scaling laws based on the assumption of a QG-MAC balance or a length-scale-dependent combination of geostrophy and magnetostrophy.

Our results therefore indicate that the Earth's core is most likely controlled by a QG-MAC balance, in which the dominant force equilibrium transitions into a magnetostrophic balance towards small scales. Extrapolation of the theoretical scalings which assume this type of force balance to the conditions of the Earth's core suggests that the dominant flow length scale of the geodynamo is about 200 km, while magnetostrophic effects are deferred to scales below 50 km.

Résumé

Le champ magnétique de la Terre est généré par un effet de dynamo dans le noyau externe liquide. Sur la base de considérations théoriques et d'estimations des propriétés physiques du noyau, on estime que la dynamique de l'écoulement à l'origine de ce processus est contrôlée par un équilibre entre la pression, la force de Coriolis, la flottabilité et les forces de Lorentz, tandis que les contributions de l'inertie et des forces visqueuses sont négligeables. La hiérarchie des forces restantes a fait l'objet d'une controverse. Il a été suggéré que l'équilibre des forces dominantes pourrait être soit géostrophique, soit magnétostrophique. Dans le premier cas, l'équilibre des forces dominantes se situe uniquement entre les forces de Coriolis et les forces de pression, alors que dans le second cas, il inclut en plus la force de Lorentz. Si la géostrophie est dominante, la force de Lorentz entre dans l'équilibre des forces au premier ordre, où elle est compensée par la flottabilité et les forces de Coriolis non géostrophiques. Ce type d'équilibre des forces est donc parfois appelé équilibre quasi-géostrophique Magnéto-Archimédienne-Coriolis (QG-MAC).

Au-delà des observations et des considérations théoriques, les simulations numériques sont un outil important pour notre compréhension du mécanisme de la dynamo terrestre. Depuis que les premiers modèles de la géodynamo ont été calculés il y a 25 ans, les ressources informatiques ont considérablement augmenté. Néanmoins, les modèles actuels fonctionnent toujours avec des paramètres qui sont loin des conditions attendues du noyau de la Terre. Malgré cette limitation, les dynamos numériques se sont révélées capables de reproduire de nombreuses caractéristiques du champ géomagnétique. Cependant, il n'est pas certain que ces résultats soient obtenus pour des raisons physiques correctes. Les études qui ont tenté de déterminer le régime physique obtenu numériquement ont donné lieu à des interprétations contradictoires. Certains ont plaidé en faveur d'équilibres de forces géophysiquement pertinents, c'est-à-dire de QG-MAC ou d'équilibres magnétostrophiques, tandis que d'autres ont suggéré que la dynamique pourrait être contrôlée visqueusement et serait donc inapplicable au noyau de la Terre.

Dans ce travail, nous avons effectué une étude systématique de l'équilibre des forces dans l'espace paramétrique accessible numériquement, afin de déterminer si ces résultats divergents sont le résultat de mauvaises interprétations, ou du fait que les modèles respectifs fonctionnent dans des régimes dynamiques différents. En analysant en détail les variations des balances de force, y compris leur dépendance à l'échelle de la longueur, nous avons constaté que la majorité des dynamos qui génèrent un champ magnétique principalement dipolaire sont régies par une balance QG-MAC. Dans ces modèles, l'équilibre de

force prédominant est soit géostrophique sur toutes les échelles de longueur, soit divisé en géostrophie à grande échelle et magnétostrophie à petite échelle. Dans l'ordre suivant, la partie non géostrophique de la force de Coriolis est principalement compensée par la flottabilité à grande échelle et par la force de Lorentz vers des échelles plus petites. L'inertie et les forces visqueuses représentent des contributions du second ordre. Cet équilibre QG-MAC semble être structurellement très robuste dans tout l'espace des paramètres étudiés. Les dynamos avec une séquence différente des forces, où l'inertie et/ou la viscosité remplacent la force de Lorentz dans la balance des forces du premier ordre, ne peuvent être trouvées que près du lancement de l'action de la dynamo et dans les modèles qui produisent un champ magnétique multipolaire. En même temps, aucune de nos dynamos n'est régie par la magnétostrophie à l'échelle du système. Notre étude montre donc que la plupart des dynamos numériques sont contrôlées par un équilibre QG-MAC, tandis que les cas où la viscosité et l'inertie jouent un rôle dominant sont l'exception plutôt que la norme.

Nous montrons par ailleurs qu'il est possible de relier les balances de force calculées à des mesures d'échelle de longueur d'écoulement, une tâche qui s'est avérée difficile à accomplir jusqu'à présent. Notre étude suggère que cela peut être réalisé en utilisant les échelles de longueur associées aux points de croisement dans une représentation spectrale de la balance des forces. Nous avons constaté que dans la plupart des dynamos numériques que nous avons analysées, l'échelle à laquelle la flottabilité et les forces de Lorentz s'équilibrent peut être associée à l'échelle dominante de la convection. Ainsi, l'équilibre QG-MAC qui prévaut dans ces modèles se reflète effectivement dans le modèle de convection. De plus, dans les modèles à fort champ magnétique, l'équilibre des forces dominantes passe de la géostrophie à grande échelle à la magnétostrophie à petite échelle, peut être liée à la perte de l'invariance axiale de l'écoulement au-delà de cette échelle. De plus, nous montrons que ces deux échelles de longueur obtenues dans nos simulations sont compatibles avec les prédictions fournies par les lois d'échelle théoriques basées sur l'hypothèse d'un équilibre QG-MAC ou d'une combinaison de géostrophie et de magnétostrophie dépendant de l'échelle de longueur.

Nos résultats indiquent donc que le noyau de la Terre est probablement contrôlé par un équilibre QG-MAC, dans laquelle l'équilibre des forces dominantes passe à un équilibre magnétostrophique vers les petites échelles. L'extrapolation des échelles théoriques qui supposent ce type d'équilibre des forces aux conditions du noyau terrestre suggère que l'échelle de longueur dominante d'écoulement de la géodynamo est d'environ 200 km, tandis que les effets magnétostrophiques se trouvent à des échelles inférieures à 50 km.

Chapter 1

Introduction

1.1 Structure of the Earth's deep interior

The principal structure of the our planet's deep interior was derived mainly from the study of seismic waves during the first half of the 20th century. The Earth's core was detected by [Oldham \(1906\)](#) who observed delayed arrival times of secondary shear waves at large epicentral distances, which he attributed to a central core in which the seismic velocities are smaller than in its surrounding volume, known as the mantle. Only a few years later, the location of the core-mantle boundary (CMB) was determined by [Gutenberg \(1912\)](#) who suggested a depth of 2900 km. This is very close to the currently-adopted value of 2890 km, which corresponds to a core radius of 3480 km. At this time, the core was still believed to be entirely solid, despite there being no observations of shear waves traveling through the core. The liquid nature of the Earth's core was deduced by [Jeffreys \(1926\)](#) by combining seismic observations with the analysis of solid Earth tides. [Lehmann \(1936\)](#) discovered that the core is divided into an inner and outer part. Today, the accepted value for the depth of the inner-core boundary (ICB) is 5150 km, which corresponds to an inner core radius of 1220 km. [Jacobs \(1953\)](#) finally confirmed that the inner core is solid. The combination of seismic wave travel times, normal modes and the moment of inertia of the Earth later led to the construction of the Preliminary Reference Earth Model (PREM) by [Dziewonski and Anderson \(1981\)](#), which today is still widely used as a reference model for the radial structure of the Earth.

The chemical composition of the different layers of the Earth is not directly accessible, with the exception of volcanic lavas in the case of the mantle. Our principal source of information is therefore the abundance of elements found in chondritic meteorites, which are believed to be representative of the material from which the Earth was formed. By combining this with the density profiles obtained from seismological observations, it can be deduced that the Earth's core has to be predominantly made of iron, while the mantle consists mainly of silicates ([Birch, 1952, 1964](#)).

The precise composition of the Earth's core is not known with certainty. Cosmochemical abundances suggest that it consists predominantly of iron alloyed with 5 – 15% nickel

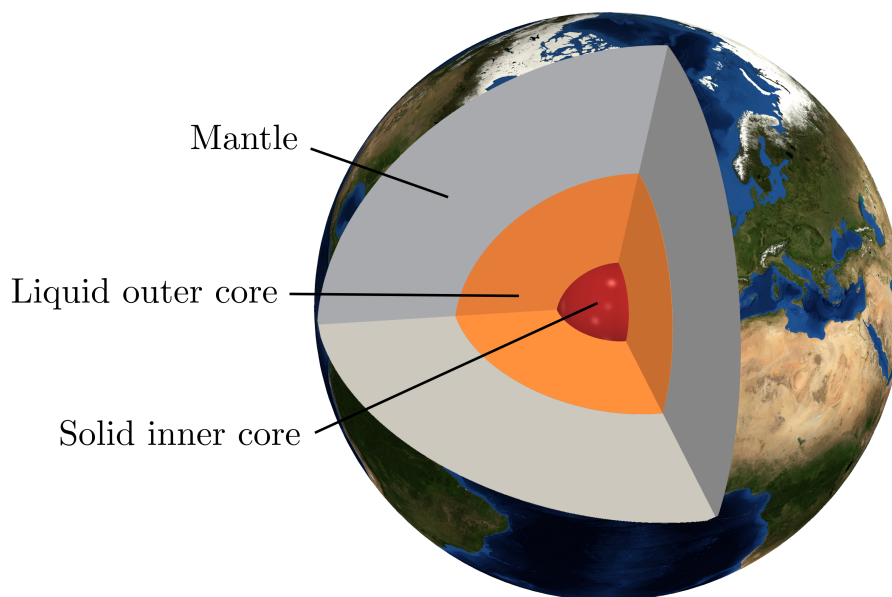


Figure 1.1: Structure of the Earth’s deep interior. This figure was created in `paraview` using a satellite image by NASA (<https://visibleearth.nasa.gov>) for the Earth’s surface.

(e.g. Vočadlo, 2015). The presence of nickel can, however, not be unambiguously proven since it has a similar density as iron, which makes the two elements indistinguishable for seismological methods. It has been argued that small amounts of nickel do not significantly affect the physical properties of iron under core conditions (Martorell et al., 2013). Its existence in the Earth’s core is therefore often ignored.

The liquid outer core is up to 10% lighter than pure iron at the expected pressure and temperature conditions (e.g. Alfè et al., 2002a; Poirier, 1994). The density of the solid inner core is believed to be closer to that of pure iron, although still somewhat lower (Jephcoat and Olson, 1987). It is therefore clear that some lighter constituents must be present in both the inner and outer cores, with a larger fraction in the latter. The identity of the lighter elements is, however, debated (for reviews see e.g. Poirier, 1994; Hirose et al., 2013). The most widely assumed candidates are sulfur, silicon and oxygen. Using *ab initio* computations, Alfè et al. (2002a) demonstrated that sulfur and silicon are equally likely to be incorporated into the crystal structure of iron or partitioned into the liquid phase, whereas oxygen partitions almost entirely into the liquid phase. This suggests that the density contrast across the ICB, excluding the phase change, is primarily the result of the difference in oxygen concentrations between the inner and outer cores. However, there are also several studies that argued for other light elements to be predominantly partitioned into the fluid core (see Vočadlo, 2015). Independent of the type of element, the release of light constituents as well as latent heat during the crystallisation of the inner core represent buoyancy sources that help drive convection in the outer core, and are thus crucial for maintaining the geodynamo and consequently also Earth’s magnetic field.

1.2 Geomagnetic field

1.2.1 Sources

The geomagnetic field is generated by various sources both within and outside the Earth (see e.g. [Hulot et al., 2015](#)). Its spatial extent is controlled by the solar wind. Sources of internal origin include the self-sustained dynamo process (the geodynamo), which is the result of convective motions of liquid metal in the core, and magnetised rocks that are mainly found in the crust. Together these two sources create the internal field. The external field is generated by coupled electric current systems in the ionosphere and the magnetosphere resulting from the interaction between the geomagnetic field and the interplanetary magnetic field produced by the Sun.

Of these different sources, the largest contribution by far to the Earth’s magnetic field is generated by the geodynamo. Consequently, this field is commonly referred to as the core or main field. It is predominantly dipolar, with a tilt of about 10 degrees with respect to the rotation axis. At the Earth’s surface, its intensity is about $30 \mu\text{T}$ around the equator and $60 \mu\text{T}$ near the poles. The magnetic field generated by magnetised rocks is known as the crustal field. It is on average significantly weaker than the core field. Depending on its location, it can vary in magnitude between less than one and thousands of nanotesla. The intensities of the magnetic field produced by the ionospheric and magnetospheric currents are highly variable in space and time and can range from less than 100 to thousands of nanotesla.

1.2.2 Observations

Documented, geographically-dispersed observations of the geomagnetic field date back about 500 years (e.g. [Jackson et al., 2000](#); [Jonkers et al., 2003](#); [Jackson and Finlay, 2015](#)). During the time period from the 16th to the end of the 18th century, magnetic field measurements were mostly performed by mariners. These observations were exclusively directional and primarily served the purpose of navigation. Extensive land surveying did not begin until the 19th century. The first measurement of the absolute field intensity was carried out by Carl Friedrich Gauss in Göttingen in 1832. Only a few years later, Gauss founded together with Wilhelm Weber and Alexander von Humboldt the Göttingen Magnetic Union (Göttinger Magnetischer Verein) with the goal of carrying out standardised measurements of variations in the Earth’s magnetic field at locations all over the world. This association thus represented the first geomagnetic observatory network. The number of observatories gradually increased over time to about 150 at present. Today, most of these observatories are members of INTERMAGNET (<https://www.intermagnet.org/>). This global geomagnetic observatory network was created in 1987 to establish cooperation between different sites, to ensure high measurement standards and to make the data widely available. The geographical locations of the (currently 131) INTERMAGNET observatories (IMOs) are illustrated in Fig. 1.2. It is evident that the majority of the observatories are located in the Northern hemisphere, with a particularly high density in Europe. How-

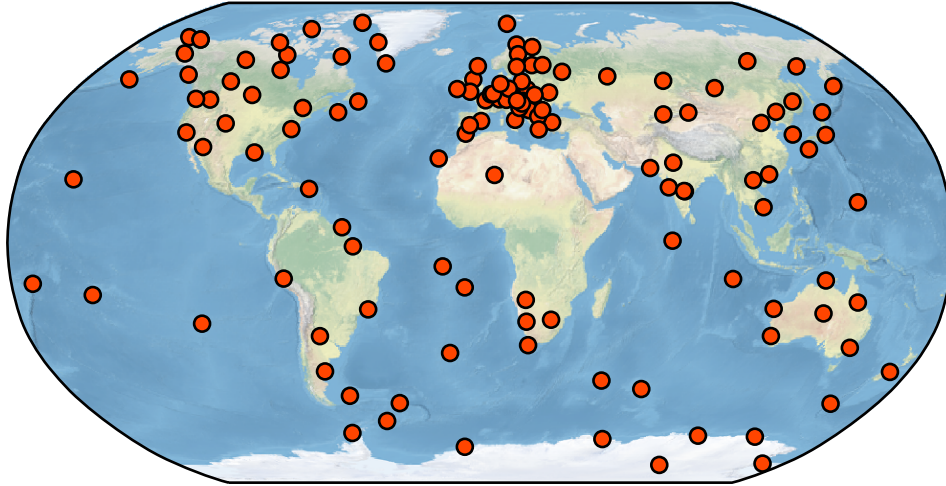


Figure 1.2: Geographical locations of the 131 geomagnetic observatories that are currently part of the observatory network INTERMAGNET. An up-to-date list of the members can be found at <https://www.intermagnet.org/>.

ever, even if the sites were more evenly distributed across the continents, global coverage would still be difficult to achieve with ground data alone, as two-thirds of the Earth's surface are covered by oceans.

With the advent of satellite missions in the second half of the 20th century, obtaining a worldwide homogeneous data distribution became possible. The first satellite to carry out magnetic field observations in space was Sputnik 3 (Dolginov et al., 1962). Global magnetic field measurements were later performed by NASA's OGO series of satellites, which were operational between 1965 and 1971. However, these early missions provided only field intensity data. The first globally-distributed vector measurements of the Earth's magnetic field were recorded by NASA's Magsat satellite, which was launched in 1979 and stayed in orbit for about half a year (Langel et al., 1980). During the following two decades there was no satellite mission that provided high-quality data. Only after the launch of the Danish Ørsted satellite in 1999 did the global coverage of the magnetic field continue. Ørsted recorded high-precision field intensity and vector data for 14 years. The satellite is still in operation today, but at this point in time only provides scalar measurements. Shortly after Ørsted two other satellite missions were launched into orbit, namely the SAC-C (2000-2004) and CHAMP (2000-2010) satellites. The former experienced technical difficulties which caused it to only record scalar field intensity measurements, while the latter provided high-precision scalar and vector data. The most recent satellite mission, Swarm, was launched in 2013. It consists of a constellation of three identical satellites: two satellites fly side by side at lower altitude (about 450 km) to make gradient measurements

of the field, and a third satellite at higher altitude (510 km) on a different polar orbit than the other two (Friis-Christensen et al., 2006). This configuration was designed to provide high quality data for the intensity, vector components and variations of the geomagnetic field, which enables better differentiation between its various sources compared to previous missions.

Satellite missions have been the key to achieving true global coverage of the Earth’s magnetic field. An added benefit is that each satellite samples the field with a single set of instruments. A disadvantage, however, is that due to the movement of the satellite it is difficult to distinguish between spatial and temporal variations. Observatory recordings, on the other hand, provide a high resolution of the temporal variations of the field at stationary locations. For models of the Earth’s magnetic field, therefore, frequently a combined analysis of satellite and observatory data is adopted (see e.g. Hulot et al., 2015).

1.2.3 Geomagnetic field models

The Earth’s magnetic field is commonly described using spherical harmonic analysis. This mathematical concept was introduced to geomagnetism by Gauss in 1839, when he published his fundamental work on terrestrial magnetism called (in German) *Allgemeine Theorie des Erdmagnetismus*. An English translation has been authored by Glassmeier and Tsurutani (2014). The basis for the use of spherical harmonic analysis is the poor electric conductivity of the lower atmosphere, which allows us to assume that electric currents are negligible at the Earth’s surface. From Ampère’s law it then follows that the magnetic field is curl-free ($\nabla \times \mathbf{B} = 0$). It can therefore be expressed as the gradient of a scalar potential V , i.e.

$$\mathbf{B} = -\nabla V, \quad (1.2.1)$$

where the negative sign appears due to convention. Since Gauss’ law of magnetism dictates that magnetic fields are divergence-free ($\nabla \cdot \mathbf{B} = 0$), the scalar potential is required to satisfy the Laplace equation

$$\nabla^2 V = 0. \quad (1.2.2)$$

For the Earth, the geomagnetic potential can be decomposed into two potentials, V_{int} and V_{ext} , describing the sources of internal and external origin, respectively:

$$V = V_{\text{int}} + V_{\text{ext}}. \quad (1.2.3)$$

Spherical harmonics are the natural solutions to Eq. (1.2.2). The potentials on the right-hand side of the above relation can thus be expressed by

$$V_{\text{int}}(r, \theta, \varphi) = a \sum_{\ell=1}^{\infty} \left(\frac{a}{r}\right)^{\ell+1} \sum_{m=0}^{\ell} [g_{\ell m} \cos(m\varphi) + h_{\ell m} \sin(m\varphi)] P_{\ell m}(\cos \theta) \quad (1.2.4)$$

and

$$V_{\text{ext}}(r, \theta, \varphi) = a \sum_{\ell=1}^{\infty} \left(\frac{r}{a}\right)^{\ell} \sum_{m=0}^{\ell} [q_{\ell m} \cos(m\varphi) + s_{\ell m} \sin(m\varphi)] P_{\ell m}(\cos \theta). \quad (1.2.5)$$

In the two above equations, r is the radius (i.e. the distance to the center of the Earth), θ the co-latitude and φ the longitude. $P_{\ell m}$ are the Schmidt quasi-normalised associated Legendre polynomials of degree ℓ and order m (e.g. [Abramowitz and Stegun, 1970](#)). The quantities $(g_{\ell m}, h_{\ell m})$ and $(q_{\ell m}, s_{\ell m})$ are the Gauss coefficients of the internal and external fields, respectively. The parameter a represents the mean radius of the Earth (6371.2 km).

The vector components of the internal magnetic field can then be obtained by substituting the geomagnetic potential V in Eq. (1.2.1) by expression (1.2.4). This yields in spherical coordinates

$$B_r(r, \theta, \varphi) = \sum_{\ell=1}^{\ell_{\text{max}}} (\ell + 1) \left(\frac{a}{r}\right)^{\ell+2} \sum_{m=0}^{\ell} [g_{\ell m} \cos(m\varphi) + h_{\ell m} \sin(m\varphi)] P_{\ell m}(\cos \theta), \quad (1.2.6)$$

$$B_{\theta}(r, \theta, \varphi) = - \sum_{\ell=1}^{\ell_{\text{max}}} \left(\frac{a}{r}\right)^{\ell+2} \sum_{m=0}^{\ell} [g_{\ell m} \cos(m\varphi) + h_{\ell m} \sin(m\varphi)] \frac{\partial P_{\ell m}(\cos \theta)}{\partial \theta}, \quad (1.2.7)$$

$$B_{\varphi}(r, \theta, \varphi) = \sum_{\ell=1}^{\ell_{\text{max}}} \left(\frac{a}{r}\right)^{\ell+2} \sum_{m=0}^{\ell} [g_{\ell m} \sin(m\varphi) - h_{\ell m} \cos(m\varphi)] \frac{m P_{\ell m}(\cos \theta)}{\sin \theta} \quad (1.2.8)$$

In his publication from 1839, Gauss computed the geomagnetic field components for the year 1835 under the assumption that $V_{\text{ext}} = 0$ by inverting for the coefficients $g_{\ell m}$ and $h_{\ell m}$ up to degree $\ell_{\text{max}} = 4$ using 84 data points. He went on to compare his results to the observed data. The excellent agreement between the two led him to conclude that the geomagnetic field is predominantly dipolar and must be generated mainly by sources in the Earth's interior.

For comparison, Fig. 1.3a-b show the radial components of the internal magnetic field at the Earth's surface of the model calculated by Gauss for the year 1835 and the most recent model of the International Geomagnetic Reference Field (IGRF), IGRF-13, for the year 2020 ([Alken et al., 2020](#)). IGRF models include all available ground and satellite data and are published every five years by the International Association of Geomagnetism and Aeronomy (IAGA). Their goal is to provide a standard mathematical description of the large-scale part of the internal magnetic field for the given epoch, and to give predictions for the temporal evolution of the main field over the next five years. For this purpose, a weighted average of different models by various research groups all around the world is determined. The agreement between Gauss' model and IGRF-13 is remarkable, especially considering that the IGRF model has a significantly higher spatial resolution with a maximum spherical harmonic degree of $\ell_{\text{max}} = 13$. Assuming the field up to $\ell = 13$, i.e. the large-scale field, to be entirely generated by the geodynamo in the Earth's core (a reasonable assumption, as we will see later), allows us to downward continue the radial

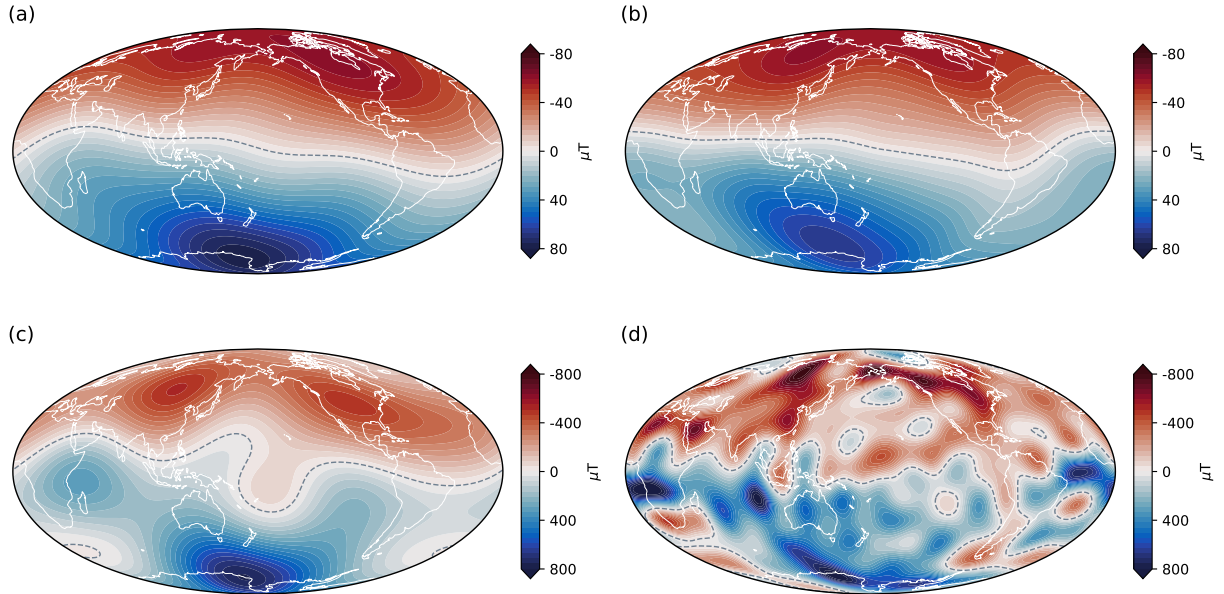


Figure 1.3: Comparison of Gauss' model for the year 1835 (a,c) and the most recent IGRF model, IGRF-13, for the year 2020 (b,d). (a,b): radial components of the respective magnetic fields at the Earth's surface; (c,d): radial components of the respective magnetic fields at the CMB. Gauss' model has a maximum spherical harmonic degree $\ell = 4$, while the IGRF-13 model is truncated at $\ell = 13$. A Mollweide projection is used in all representations.

component of the magnetic field to the CMB by setting $r = 3480$ km in Eq. (1.2.6). The resulting radial field strengths are illustrated in Fig. 1.3c-d. The difference in resolution between the two models is much clearer at the CMB compared to at the Earth's surface, where the smaller scales are strongly attenuated.

Since IGRF models only aim at describing the Earth's main magnetic field, they do not necessarily give precise field values at a given location at the Earth's surface because of local variations due to magnetised rocks in the crust not being taken into account.

1.2.4 Power spectrum

The reason why models like IGRF-13, which are intended specifically to describe the magnetic field generated by the geodynamo process in the Earth's core, are truncated at degree $\ell = 13$ becomes obvious when the power spectrum of the geomagnetic field is considered. For the field of internal origin it is defined by

$$R_\ell(r) = (\ell + 1) \left(\frac{a}{r}\right)^{2\ell+4} \sum_{m=0}^{\ell} (g_{\ell m}^2 + h_{\ell m}^2). \quad (1.2.9)$$

This definition was introduced by [Mauersberger \(1956\)](#) and [Lowes \(1974\)](#), which is why the above expression is commonly referred to as Mauersberger-Lowes spectrum. Figure 1.4

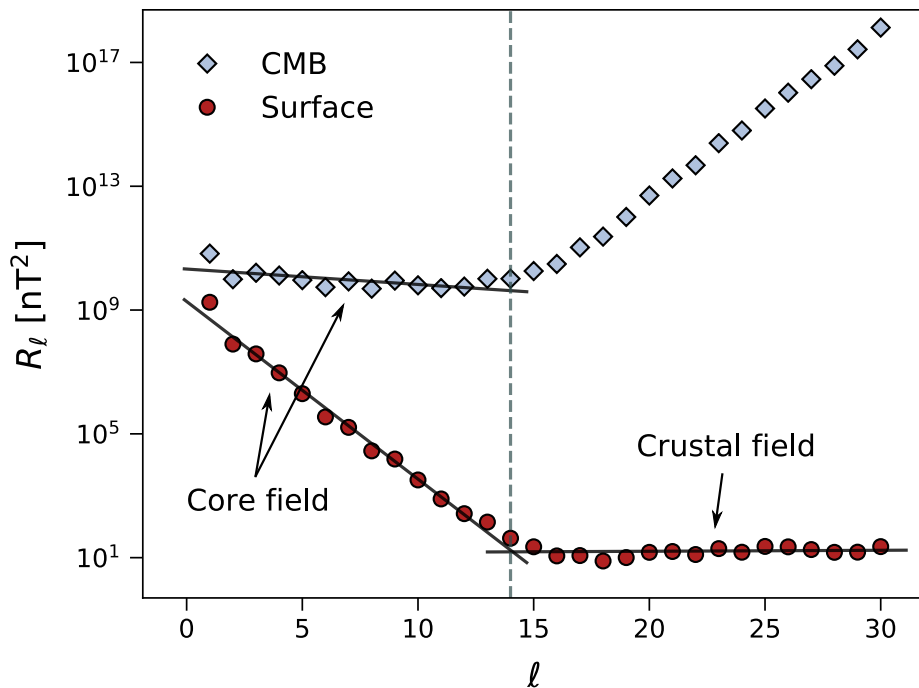


Figure 1.4: Spatial power spectrum of the geomagnetic field of internal origin at the Earth’s surface (circles) and at the CMB (squares). The Gauss coefficients that were used to compute the spectrum given by Eq. (1.4) are taken from the SIFM model based on Swarm satellite data for the year 2014 (Olsen et al., 2015). The spectral power of the CMB field beyond degree $\ell = 13$ is non-physical (see text).

depicts the power spectrum of the internal magnetic field at the Earth’s surface and at the CMB for the Swarm Initial Field Model (SIFM) model for the year 2014 (Olsen et al., 2015). For the Earth’s surface field (denoted by circles), we observe the expected dominance of the dipole ($\ell = 1$). For larger degrees, the spectral power decreases approximately linearly until about $\ell = 14$. Beyond $\ell = 14$, the slope of the spectrum becomes essentially flat. This dichotomy of the power spectrum is considered to be the result of different sources dominating on the respective length scales (see e.g. Kono, 2015). The steadily decaying slope at the large-scales ($\ell \leq 13$) is attributed to the field generated by the geodynamo in the core, while the flat portion of the spectrum towards smaller scales ($\ell \geq 15$) is due to the crustal field. At $\ell = 14$ the contributions of the two sources are expected to be approximately equal. The core field obviously still provides contributions at larger degrees, but these are relatively small at the Earth’s surface due to the strong geometric attenuation of short wavelengths far away from the source and as a consequence they are hidden by the crustal field. Conversely some larger scale content of the crustal field is likely masked by the core field. However, the crustal field alone would not be able to explain the largest wavelengths since the Curie temperature limits the depth down to which rocks can carry a remanent magnetisation to only a few tens of kilometers.

Similar to the magnetic field components discussed in the previous section, the surface spectrum can be projected onto the CMB (denoted by squares) by using $r = 3480$ km in Eq. (1.4) instead of $r = 6371.2$ km. At the CMB the dipole is still the strongest field contribution. However, because of the greatly reduced distance to the source of the large-scale field, the smaller scales are now much more enhanced due to the $(a/r)^{2\ell+4}$ factor in Eq. (1.4). As a consequence, the CMB spectrum is much flatter than at the Earth's surface for degrees $\ell \leq 13$. Since this downward projection involves the assumption that there are no sources between the Earth's surface and the core, this obviously means that all degrees $\ell \geq 14$ are rendered non-physical since they are produced by the crustal field.

1.2.5 Time variations

The Earth's magnetic field varies on a wide range of time scales. The fastest fluctuations, with periods on the order of seconds to tens of years, are caused by the external field due to changes in the activity of the solar wind. The longest variations of the external field partially overlap with the so-called geomagnetic secular variation, which comprises changes of the core field on time scales from years to centuries. This can make it challenging to separate the two (e.g. [Constable and Constable, 2013](#)). One characteristic of the secular variation is the slow westward drift of magnetic field features at the Earth's surface, which was first recognised by [Halley \(1683, 1692\)](#). This westward movement is, however, not present uniformly across the globe. It can be observed primarily in the Atlantic hemisphere, while the secular variation in the Pacific hemisphere is much weaker and less systematic ([Fisk, 1931](#)). Time-dependent models of the Earth's magnetic field using historical observations ([Bloxham and Jackson, 1992](#); [Jackson et al., 2000](#)) show that this feature has persisted for at least the last four centuries. Another important aspect of the geomagnetic secular variation is the rapid decay of the axial dipole moment at a rate of about 5% per century since the first geomagnetic observatories began operating in the 1830s (e.g. [Olson and Amit, 2006](#)). It has been speculated that this dipole decay could be the onset of an imminent polarity reversal of the Earth's magnetic field (e.g. [Constable and Korte, 2006](#)). Such reversals are arguably the most striking feature of the temporal evolution of the field. The duration between two such events varies between hundred thousand years up to tens of millions of years (e.g. [Lowrie and Alvarez, 1981](#)). The time required for the polarity transition itself ranges from one to ten thousand years (e.g. [Valet and Fournier, 2016](#)).

In the following sections it will become apparent that the temporal variations of the Earth's magnetic field represent an important source of information about the Earth's core and its dynamics.

1.3 Core dynamics

1.3.1 Geodynamo hypothesis

The oldest permanently magnetised minerals found at the Earth’s surface indicate that the geomagnetic field must have persisted for at least 3.5 Gyr or possibly even 4.2 Gyr (Tarduno et al., 2010, 2015). In the absence of a regeneration mechanism, using characteristic values for the Earth’s core (see Table 1.1) results in a decay time for the dipole magnetic field of

$$\tau_{\text{dip}} = \frac{r_o^2}{\pi^2 \lambda} \approx 56 \text{ kyr}, \quad (1.3.1)$$

where r_o is the outer core radius and λ the magnetic diffusivity. This measure indicates how long it would take for the dipole field to decay by the factor e (see e.g. Roberts and King, 2013). As a consequence, the geomagnetic field would fade away in a comparatively short period of time. Thus, there must be a mechanism operating in the Earth’s interior that continuously regenerates the field. Today, it is generally accepted that this mechanism is dynamo action resulting from turbulent convective motions of liquid metal in the Earth’s outer core. This idea of a self-sustaining fluid dynamo was first proposed by Larmor (1919), mainly in the context of the Sun’s magnetic field. He argued that motions of an electrically conducting fluid under the influence of an initially small magnetic field would be able to induce an electric field which in turn regenerates the magnetic field. Larmor contemplated that such a mechanism could also be responsible for the geomagnetic field, although noting that it would require fluidity in the Earth’s deep interior. At this point in time, the Earth was however still assumed to be solid throughout (see Section 1.1). Even after the fluid nature of the outer core was established, it took some time for the geodynamo hypothesis to gain traction. A first theoretical basis for the concept suggested by Larmor was eventually provided by Elsasser (1946), Bullard (1949) and Parker (1955), who laid the foundation for the modern magneto-hydrodynamic (MHD) theory of convection-driven dynamos.

The dynamo mechanism proposed by Larmor requires a continuous energy source capable of driving the fluid flows in the Earth’s core necessary to sustain the geomagnetic field. In today’s Earth, it is assumed that convective motions in the core are caused by thermal and compositional buoyancy forces, which are ultimately the result of the cooling of the core since its formation. The accretion and subsequent differentiation of the Earth about 4.5 billion years ago led to the release of large amounts of kinetic and gravitational energy, which caused the core temperature to rise dramatically, leading to the complete melting of the core (e.g. Nimmo, 2015b). Since this initial state, the core loses heat to the surrounding mantle, making it thermally buoyant. The cooling resulting from the outward transport of heat by conduction and convection eventually led to the formation of the solid inner core due to the freezing of liquid iron at the center of the Earth. The latent heat released during this crystallisation process provides an additional source of thermal buoyancy. More importantly, the solidification also leads to compositional buoyancy since the core fluid contains a significant amount of light elements. These are not readily incorporated into the crystal structure of iron and therefore released into the liquid outer core,

thereby providing a source of gravitational power. Considerations of the Earth’s energy budget in combination with recent estimates of the thermal conductivity of the Earth’s core (Pozzo et al., 2012; de Koker et al., 2012) suggest that the solidification of the inner core began less than 0.6 Gyr ago (Davies et al., 2015). With the growth of the inner core over time, the role of compositional convection in driving the geodynamo increased to such an extent that it is probably more important than thermal driving in the present core (Nimmo, 2015a). This idea of vigorous convection in the Earth’s core is supported by the fact that the density profile determined from seismological observations closely follows the adiabatic gradient (Dziewonski and Anderson, 1981). The convective flow is expected to be organised into columnar vortices that are aligned with the rotation axis, since the Earth represents a rapidly-rotating system (e.g. Chandrasekhar, 1961). The term rapid is hereby understood in the sense that the rotation rate Ω times a relevant length scale, e.g. the thickness of the Earth’s core L , is much larger than the typical fluid velocity, i.e. $\Omega L \gg U$. Using the characteristic values given in Table 1.1 shows that this situation is (at least on large scales) easily met in the Earth’s core. The columnarity of the flow is a consequence of the Proudman-Taylor theorem, which states that fluid motions tend to be independent of the direction of the rotation axis if the force balance of the system is dominated by an equilibrium between pressure and Coriolis forces, i.e. by the so-called geostrophic balance. While there is much support for such a leading-order geostrophy, both from recent theoretical considerations (e.g. Davidson, 2013; Calkins, 2018) and from geodynamo simulations (e.g. Yadav et al., 2016; Aubert et al., 2017; Schaeffer et al., 2017), there is some debate whether the Lorentz force could also play a dominant role, as we will see in Section 1.3.5. Before discussing the force balance in detail, we will first review in the next two sections how the flow velocity and the magnetic field strength in the outer core can be estimated. The knowledge of these two quantities is crucial to our understanding of the dynamical regime of the Earth’s core.

1.3.2 Core flow inversions

The movement of geomagnetic field features observed at the Earth’s surface is interpreted as the result of advection of the magnetic field near the core surface. Therefore, secular variation data can be used to reconstruct the underlying flow. To this end, the radial component of the core-generated field and its secular variation, which is given by its time derivative, are considered. These observations can be projected from the Earth’s surface onto the top of the core by using the downward continuation outlined in Section 1.2.3. The temporal evolution of the magnetic field within the Earth’s core, which is described by the induction equation (see Section 2.1.3), is governed by the competition between advection of the field and its diffusion. In case of negligible diffusion, i.e. in a perfectly electrically conducting fluid, the magnetic field moves along with the motion of the fluid as if frozen to it (see e.g. Jackson and Finlay, 2015). Under this condition, the magnetic field can thus be used to trace the flow. The use of this so-called frozen flux approximation when inverting for the core flow was first proposed by Roberts and Scott (1965).

Table 1.1: Parameter estimates for the Earth’s outer core. Note that there is some controversy surrounding the physical properties of liquid metal under the expected core conditions. References: 1 = [Dziewonski and Anderson \(1981\)](#), 2 = [Pozzo et al. \(2013\)](#), 3 = [Gomi et al. \(2013\)](#), 4 = [Alfè et al. \(2002b\)](#), 5 = [Jones \(2015\)](#), 6 = [Stacey \(1993\)](#), 7 = [Pozzo et al. \(2012\)](#), 8 = [Loper and Roberts \(1981\)](#) 9 = [Finlay and Amit \(2011\)](#), 10 = [Gillet et al. \(2010\)](#).

Symbol	Definition	Estimate	Reference
Ω	Rotation rate	$7.29 \times 10^{-5} \text{ s}^{-1}$	
r_i	Inner core radius	$1.22 \times 10^6 \text{ m}$	1
r_o	Outer core radius	$3.48 \times 10^6 \text{ m}$	1
L	Thickness of outer core	$2.26 \times 10^6 \text{ m}$	1
ρ_i	Density at the inner-core boundary	$1.2 \times 10^4 \text{ kg m}^{-3}$	1
ρ_o	Density at the core-mantle boundary	$9.9 \times 10^3 \text{ kg m}^{-3}$	1
ρ	Mean core density	$1.1 \times 10^4 \text{ kg m}^{-3}$	1
g_o	Gravity at core-mantle boundary	10.68 m s^{-2}	1
μ	Magnetic permeability	$4\pi \times 10^{-7} \text{ H m}^{-1}$	
ν	Viscous diffusivity	$10^{-6} \text{ m}^2 \text{ s}^{-1}$	2
α	Thermal expansion coefficient	10^{-5} K^{-1}	3
γ	Grüneisen parameter	1.5	4
T'	Typical superadiabatic temperature perturbation	10^{-4} K	5
c_p	Specific heat capacity at constant pressure	$850 \text{ J kg}^{-1} \text{ K}^{-1}$	6
k	Thermal conductivity	$100 \text{ W m}^{-1} \text{ K}^{-1}$	7
κ	Thermal diffusivity	$10^{-5} \text{ m}^2 \text{ s}^{-1}$	$\kappa = k/\rho c_p$
κ_ξ	Chemical diffusivity	$3 \times 10^{-9} \text{ m}^2 \text{ s}^{-1}$	8
λ	Magnetic diffusivity	$0.7 \text{ m}^2 \text{ s}^{-1}$	7
U	Typical flow velocity	$4 \times 10^{-4} \text{ m s}^{-1}$	9
B	Typical magnetic field strength	$4 \times 10^{-3} \text{ T}$	10

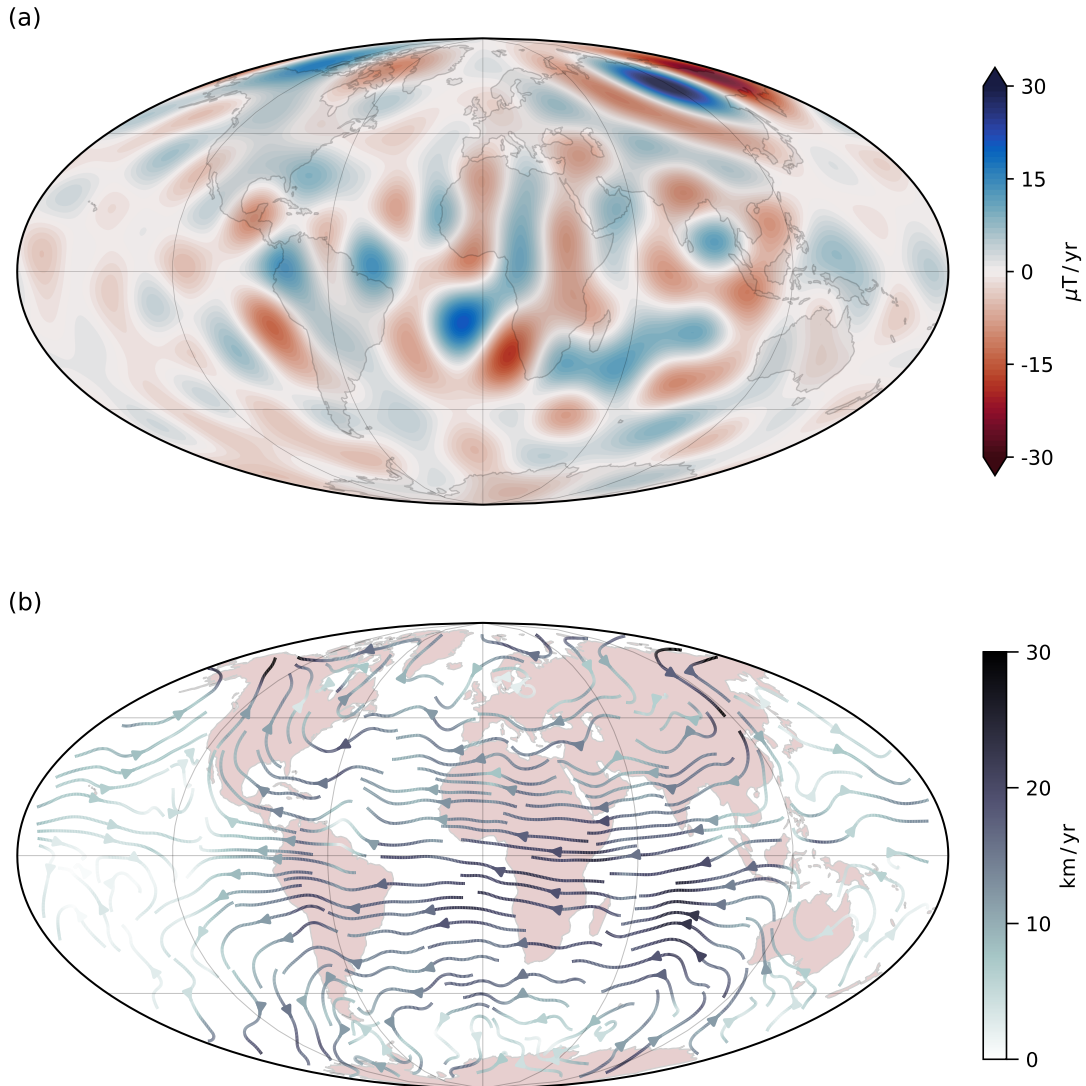


Figure 1.5: (a) Mollweide projection of the radial secular variation at the CMB up to spherical harmonic degree $\ell = 13$ for the year 2015 from the CHAOS-6x8 model. (b) Core surface flow obtained by [Aubert \(2020\)](#) by using the radial magnetic field and secular variation data for the year 2015 from the CHAOS-6x8 model ([Finlay et al., 2016](#)).

The CMB is an impenetrable boundary for the core fluid due to the difference in composition and phase between the outer core and the mantle. This means that the radial component of the velocity field must be zero. Because the CMB represents a rigid boundary, hydrodynamic arguments further demand that the horizontal velocities there also disappear. Consequently, core flow inversions seek the flow just beneath the hydromagnetic boundary layers, for which it is still reasonable to assume a vanishing radial velocity. Due

to the boundary layers being very thin compared to the horizontal length scale of the core, changes in the radial magnetic field at this depth with respect to the core surface can be considered to be negligible (e.g. [Finlay et al., 2010](#); [Holme, 2015](#)). The radial magnetic field and its secular variation are coupled to the velocity field via the aforementioned induction equation. Even after making the assumptions discussed above, there remain two major issues that occur when trying to invert this equation for the flow. It is obvious that one equation for two unknowns, i.e. the horizontal velocity components, is not sufficient to determine a unique solution. Furthermore, any arbitrarily small scale flow could theoretically be responsible for the observable large-scale secular variation.

Various strategies have been employed in an attempt to alleviate these difficulties. To provide additional constraints on the flow, a second equation involving the velocity can be obtained by making assumptions about the expected core dynamics. One of the most frequently made approximations is that the flow just below the CMB is considered to be tangentially geostrophic (e.g. [Jackson, 1997](#); [Hulot et al., 2002](#); [Pais et al., 2004](#)). Thus, it is assumed that the flow there is controlled by an equilibrium between the horizontal components of the Coriolis and the pressure forces ([Hills, 1979](#); [Le Mouél, 1984](#)). Another dynamical constraint that has been adopted at times is the quasi-geostrophic approximation (e.g. [Pais and Jault, 2008](#); [Gillet et al., 2009, 2015](#); [Kloss and Finlay, 2019](#)). In this case it is assumed that the rapid rotation of the Earth leads to convection being predominantly controlled by a balance between Coriolis and pressure forces throughout the core (not only just below the surface, as in the tangential geostrophy assumption), while buoyancy and Lorentz forces are regarded as only minor disturbances. Such a force equilibrium results in the core flow largely being organised into columnar vortices that are aligned with the rotation axis. One consequence of this approximation is that the flow length scales in the equatorial plane can be considered to be much smaller than those associated to the convection columns. Furthermore, the columnarity of the flow allows us to exploit the implied equatorial mirror symmetry of the flow outside the inner core tangent cylinder, which is coaxial with the axis of rotation, thus greatly reducing the number of possible solutions to the inverse problem. Other dynamic considerations used in the past to mitigate the non-uniqueness of the velocity field include the assumption that the flow is either steady (e.g. [Gubbins, 1982](#)) or purely toroidal (e.g. [Whaler, 1986](#)). Yet, the application of these additional constraints does not lead to a unique solution, since, as already mentioned, any arbitrarily small-scale flow could be responsible for the observable geomagnetic secular variation. However, it is impossible to derive potential small scales with certainty from the observations, because large-scale flow alone is sufficient to explain them. Thus, typically the assumption is made that the observable secular variation is the result of large-scale flow, which is referred to as the “large-scale approximation” (see e.g. [Holme, 2015](#)). In practice, this is achieved by applying a regularisation or damping to the velocity field to ensure that the energy contained in the small scales decays rapidly.

As an alternative strategy, several recent studies have relied on statistical information derived from Earth-like numerical geodynamo models to reduce the non-uniqueness of the inverse problem (e.g. [Fournier et al., 2011](#); [Barrois et al., 2017](#); [Gillet et al., 2019](#)). With

this method it is possible to image the flow not only at the CMB, but also in the entire core (Aubert, 2013, 2014, 2015). Aubert (2020) extended this statistical approach by additionally constraining the core surface flow to be controlled by a quasi-geostrophic Magneto-Archimedean-Coriolis (QG-MAC) balance. This assumption is closely related to the tangential geostrophic and quasi-geostrophic approximations mentioned above, since the leading-order force equilibrium is again between Coriolis and pressure forces, i.e. a geostrophic balance. However, unlike in the case of the aforementioned constraints, buoyancy and Lorentz forces are no longer subdominant when a QG-MAC balance is assumed. The geophysical relevance of this dynamical consideration is well-supported by both theoretical arguments (e.g. Davidson, 2013; Calkins, 2018) and numerical geodynamo simulations (e.g. Yadav et al., 2016; Aubert et al., 2017; Aubert, 2019) (see Section 1.3.5).

As an example, one of the solutions for the core surface flow obtained by Aubert (2020) is illustrated in Fig. 1.5b. The velocities shown were inverted from radial magnetic field and secular variation data up to degree $\ell = 13$ for the year 2015, as provided by the CHAOS-6x8 model of Finlay et al. (2016). A feature that is clearly observable is the strong westward drift in the Atlantic hemisphere. Velocities in the Pacific hemisphere, on the other hand, are much slower and less systematic, as could be expected given the weaker secular variation there (see Fig 1.5a). However, the detailed pattern of the surface flows may vary between models due to different underlying assumptions. Regardless of their precise results, core flow inversions provide an observation-based estimate of the typical flow magnitude near the surface of the Earth’s core, which is crucial for our understanding of its dynamical regime. The solution obtained by Aubert (2020), which is shown in Fig. 1.5b yields a root-mean-square (r.m.s.) velocity $U_{\text{rms}} \approx 13 \text{ km yr}^{-1} \approx 4 \times 10^{-4} \text{ m s}^{-1}$. This is consistent with the values obtained by other authors, which typically range from $4 - 22 \text{ km yr}^{-1}$ (see Finlay and Amit, 2011). In the following, we will consider the characteristic flow velocity in the Earth’s core to be $U = 4 \times 10^{-4} \text{ m s}^{-1}$.

1.3.3 Magnetic field strength in the core

The assessment of the dynamical state of the Earth’s core in addition to the flow magnitude also requires knowledge of the magnetic field strength in its interior. Downward continuation of the large-scale radial magnetic field to the CMB yields a r.m.s. magnitude of about 0.3 mT at the core surface. However, extrapolation of this value into the liquid core is not possible. The flow at the core surface inverted from geomagnetic observations can indirectly be used to infer the magnetic field strength in its interior. It has been argued that the axi- and equatorially symmetric zonal part of the flow is the result of standing torsional waves (Jault et al., 1988), i.e. oscillatory motions of fluid on cylindrical surfaces coaxial to the Earth’s rotation axis. These geostrophic motions, which are typically termed torsional oscillations, generate Alfvén waves that propagate in the cylindrical radial direction (e.g. Wicht and Christensen, 2010). If the propagation speed of these torsional Alfvén waves is known, it is possible to estimate the magnitude of the cylindrical magnetic field.

To obtain a model of the magnetic field in the cylindrical radial direction, Zatman

and Bloxham (1997) fitted a steady flow and two harmonic waves, representing torsional oscillations about a basic state, to the axi- and equatorially symmetric zonal part of a time-dependent core flow model. They found periods of about 50 and 80 years for the fitted waves, consistent with a 60 year signal observed in changes of the length of day, i.e. in variations of the rotation period of the Earth (see e.g. Roberts et al., 2007), which has been argued to be the result of angular momentum changes produced by torsional oscillations in the core (Braginsky, 1970). By subsequently inverting the fitted harmonic waves for a model of the cylindrical radial magnetic field, they found a r.m.s. intensity of 0.4 mT. The estimated field strength inside the liquid core would therefore be essentially of the same order of magnitude as at the CMB. This rather unexpected result has been shown to be inconsistent with numerical geodynamo simulations, which suggest that the field within the Earth’s core should be about ten times stronger than at its surface (e.g. Aubert et al., 2009), i.e. of the order of a few millitesla.

A more recent study by Gillet et al. (2010) argued for torsional waves in their core surface flow models that propagate much faster. These waves occur at a periodicity of six years and take only about four years to travel from the ICB to the equator. By calculating the corresponding changes in the core angular momentum, they showed that these oscillations are strongly correlated with a six-year signal in variations of the Earth’s rotation period (Abarca del Rio et al., 2000). The much faster propagation speed of torsional waves than previously speculated requires a significantly stronger ambient magnetic field. Gillet et al. (2010) estimated a r.m.s. magnitude of the magnetic field in the cylindrical radial direction of about 2 mT, resulting in a total r.m.s. field strength of 4 mT in the core, if isotropy is assumed. Additional support for these higher-frequency torsional oscillations is given by the detection of a six-year signal in several geomagnetic field models (Silva et al., 2012). A similar magnitude of about 3 mT was inferred by Buffett (2010) from signatures of anomalous dissipation in Earth’s nutation (e.g. Mathews et al., 2002). Hereafter, we will adopt $B = 4$ mT as a typical value for the field intensity in the outer core.

1.3.4 Dynamically-relevant time scales

The convective dynamics in the Earth’s core take place over a wide range of time scales. In Section 1.3.1, we have already mentioned some of them with the decay time of the dipole magnetic field and the geological time scale, notably the age of the Earth and the formation of the inner core. Furthermore, we have addressed the influence of the Earth’s rapid rotation on core convection, which represents the shortest dynamically relevant time scale with a period of

$$\tau_{\Omega} = \frac{2\pi}{\Omega} = 1 \text{ d.} \tag{1.3.2}$$

Inertial waves occurring on this daily time scale are expected to be responsible for the organisation of the flow into the columnar vortices (Davidson et al., 2006). An estimate for the typical time scale of the motion of these fluid columns is given by the eddy overturn

time

$$\tau_U = \frac{L}{U} \approx 200 \text{ yr}, \quad (1.3.3)$$

based on the velocity obtained from core flow inversions and considering the thickness of the Earth's core as characteristic flow length scale, as we will continue to do in the developments that follow. The time scale of convection is therefore very slow compared to the Earth's rotation period. In between the two is the Alfvén time scale, which controls the period of hydromagnetic waves. Using characteristic values it is given by

$$\tau_A = \frac{\sqrt{\rho\mu} L}{B} \approx 2 \text{ yr}, \quad (1.3.4)$$

where ρ is the mean core density and μ the magnetic permeability. When the strength of the magnetic field in the cylindrical radial direction is considered ($B_{\text{cyl}} = 2 \text{ mT}$, see Section 1.3.3) rather than the magnitude of the total field, this yields exactly the four years it takes for torsional Alfvén waves to propagate through the core as found by Gillet et al. (2010).

Other time scales of interest are related to the different diffusion processes. The most dynamically-relevant one is the magnetic diffusion time defined by

$$\tau_\lambda = \frac{D^2}{\lambda} \approx 270 \text{ kyr}, \quad (1.3.5)$$

which gives essentially the same information as the dipole decay time (Eq. 1.3.1). The thermal, compositional and viscous diffusion times on the other hand are

$$\tau_\kappa = \frac{L^2}{\kappa} \approx 16 \text{ Gyr}, \quad (1.3.6)$$

$$\tau_\xi = \frac{L^2}{\kappa_\xi} \approx 54 \text{ Tyr}, \quad (1.3.7)$$

$$\tau_\nu = \frac{L^2}{\nu} \approx 160 \text{ Gyr}, \quad (1.3.8)$$

where κ , κ_ξ and ν are the thermal, chemical and viscous diffusivities, respectively. Thus, all three time scales are not only much larger than the magnetic diffusion time but also larger than the age of the Earth, which implies that dissipation of energy in the outer core occurs primarily in the form of Ohmic heating.

1.3.5 Force balance governing flow dynamics

1.3.5.1 Dimensionless numbers

Based on the MHD theory of convection-driven dynamos (see Chapter 2) it is known that convection in the Earth's core is influenced by six different forces, namely Coriolis,

pressure, buoyancy, Lorentz, inertial and viscous forces. Our main tool to study their relative importance and thus to know which dynamical regime the Earth's core is in, are dimensionless numbers, which can be computed from the core's physical properties. These can be interpreted as order of magnitude estimates of the ratio between two forces. Due to the Earth being a rapidly rotating system, typically the relative strengths of the individual forces with respect to the Coriolis force are considered. Since we adopt the thickness of the outer core as a characteristic flow length scale, the dimensionless numbers only provide an estimate of the global-scale force balance.

The ratio between viscous and Coriolis forces can be estimated with the help of the so-called Ekman number

$$E = \frac{\nu}{\Omega L^2} \sim \mathcal{O}(10^{-15}), \quad (1.3.9)$$

while the relative amplitudes of inertia and Coriolis forces are given by the Rossby number

$$Ro = \frac{U}{\Omega L} \sim \mathcal{O}(10^{-6}). \quad (1.3.10)$$

The smallness of E and Ro allows us to conclude that inertial and in particular viscous contributions are insignificant compared to rotational effects. The strength of buoyancy relative to Coriolis forces can be estimated by defining the following buoyancy number

$$Bu = \frac{\alpha T' g_o}{\Omega U} \sim \mathcal{O}(10^{-1}), \quad (1.3.11)$$

where α represents the thermal expansion coefficient, T' a superadiabatic temperature perturbation and g_o the gravity at the CMB. The ratio between Lorentz and Coriolis forces in planetary dynamos is often assessed by evaluating the traditional form of the Elsasser number, which is defined by

$$\Lambda_t = \frac{B^2}{\rho \mu \lambda \Omega} \sim \mathcal{O}(10). \quad (1.3.12)$$

This suggests a dominant role of the Lorentz force in governing the flow dynamics. The traditional Elsasser number, however, does not contain any length or velocity scales, and hence may provide an inaccurate measure of the force ratio (e.g. [Soderlund et al., 2012, 2015](#); [Dormy, 2016](#)). For a more exact estimate, [Soderlund et al. \(2012, 2015\)](#) therefore introduced the dynamic Elsasser number

$$\Lambda_d = \frac{B^2}{\rho \mu \Omega U L} \sim \mathcal{O}(10^{-2}). \quad (1.3.13)$$

In contrast to Λ_t , the dynamic Elsasser number indicates that the Lorentz force is two orders of magnitude smaller than the Coriolis force, suggesting that convection dynamics are rotationally-dominated. The final force that has not been considered so far is the one due to pressure. In the case of negligible inertia and viscosity, the pressure force

Table 1.2: Theoretical scaling laws and thereby estimated values for convective flow length scales in the Earth’s outer core using the characteristic values given in Table 1.1.

Force balance	Scaling law	Earth’s core value
MS	$\mathcal{L} \sim L$	~ 2000 km
QG-MAC	$\mathcal{L} \sim Ro^{1/4}L$	~ 100 km
QG+MS	$\mathcal{L}_X \sim \Lambda_t^2 L / Rm$	~ 1000 km
QG-VAC	$\mathcal{L} \sim E^{1/3}L$	~ 30 m

compensates the part of the Coriolis force that is not balanced by buoyancy and Lorentz forces.

The hierarchy of the forces indicated by dimensionless numbers is different, depending on which Elsasser number is used to estimate the Lorentz force. It is clear, however, that in any event viscosity and inertia represent the least important contributions, since they are far smaller than the other four forces. When considering the dynamic Elsasser number, buoyancy and Lorentz forces come about one or two orders of magnitude below the prevailing force equilibrium between pressure and Coriolis forces. The leading-order force balance in this case is therefore geostrophic (e.g. [Busse, 1970](#)). The traditional Elsasser number, on the other hand, suggests a much stronger Lorentz force, so that the dominant force balance would be between pressure, Coriolis and Lorentz forces, which is termed magnetostrophic (MS) balance (e.g. [Roberts, 1978](#)). As already pointed out above, the non-dimensional numbers only provide information about the force balance on the system scale. The true force balance in the Earth’s core is likely more complicated due to the length-scale dependence of the forces (e.g. [Aurnou and King, 2017](#); [Aubert et al., 2017](#)). Based on scaling analysis of Λ_d (Eq. [1.3.13](#)), which is described in detail in Section [3.2](#), [Aurnou and King \(2017\)](#) for instance argued that only the large-scale flow is predominantly geostrophic, while magnetostrophy occurs on smaller scales.

1.3.5.2 Effect of the force balance on the convective pattern

The nature of the leading-order force balance has a significant effect on the convective pattern. A dominant geostrophic balance would result in convection being primarily organised into columnar eddies that are aligned with the rotation axis as a result of the Proudman-Taylor theorem. In the case of magnetostrophy, on the other hand, the Lorentz force would be able to relax this rotational constraint, and thus break up the columnarity of the flow, resulting in larger scale flow.

In an attempt to obtain estimates of characteristic length scales of the convective flow in the Earth’s outer core, several scaling laws have been proposed, based on the different hypotheses about the dominant force balance. Here, we recall the possible scalings that are also listed in Table [1.2](#). Their derivation involves assumptions about the underlying equations. However, this goes beyond the scope of the introduction, but will be discussed

in detail later on in Chapter 3. In case of leading-order geostrophy, followed by a balance between buoyancy, Lorentz and ageostrophic (non-geostrophic) Coriolis forces at the next order, i.e. in case of a QG-MAC balance, the following scaling for the typical flow length scale has been suggested (Davidson, 2013)

$$\mathcal{L} \sim Ro^{1/4}L \approx 100 \text{ km.} \quad (1.3.14)$$

The alternative assumption of the outer core being in a magnetostrophic regime suggests that the strong Lorentz force should be able to relax the rotational constraint imposed by the Coriolis force to such an extent that convection occurs on the system scale (e.g. Roberts, 1978; Hollerbach, 1996), so that

$$\mathcal{L} \sim L \approx 2000 \text{ km.} \quad (1.3.15)$$

Aurnou and King (2017) introduced a scaling to account for the length-scale dependence of geostrophy and magnetostrophy. In this case the Lorentz force is hypothesised to reach leading order only beyond a magnetostrophic cross-over length scale, which is defined by

$$\mathcal{L}_X \sim \frac{\Lambda_t^2}{Rm}L \approx 1000 \text{ km,} \quad (1.3.16)$$

where $Rm = UL/\lambda$ is the magnetic Reynolds number. The comparison of measured convective length scales with scaling laws such as those mentioned above is often used in fluid dynamics to draw conclusions about the underlying force balance. As we will see in the next section, this approach has also been applied to numerical simulations of the geodynamo.

1.3.5.3 Numerical dynamo simulations

In addition to observations and theoretical considerations, numerical simulations are an important tool for our understanding of the Earth's dynamo mechanism. The first successful geodynamo models were calculated 25 years ago by Glatzmaier and Roberts (1995) and Kageyama and Sato (1995). Since then computing resources have increased considerably. Nevertheless, current models still operate at parameters that are far from the expected conditions of the Earth's core (see Table 1.3). Despite this limitation, numerical dynamos have proven to be capable of reproducing numerous features of the geomagnetic field (e.g. Christensen et al., 2010). However, it remains uncertain whether these results are obtained for the correct physical reasons. Consequently, many studies have been conducted in an attempt to answer this question. Two different approaches can be used for this purpose. Firstly, the comparison of the scaling behaviour of measured flow length scales and velocities to scaling laws, which allows us to infer the underlying force balance. Secondly, the explicit calculation of the magnitude of the individual forces.

The analysis of the scaling behaviour of convective length scales in geodynamo simulations has not led to an agreement with any of the theoretically expected scaling laws given

Table 1.3: Dimensionless parameters in numerical geodynamo simulations and in the Earth’s outer core.

Parameter	Symbol	Definition	Meaning	Simulations	Earth
Ekman	E	$\frac{\nu}{\Omega L^2}$	$\frac{\text{viscous force}}{\text{Coriolis force}}$	$10^{-7} - 10^{-3}$	$\mathcal{O}(10^{-15})$
Rayleigh	Ra	$\frac{\alpha g_o L^3 \Delta T}{\nu \kappa}$	vigour of convection	$10^5 - 10^{11}$	$\mathcal{O}(10^{22})$
Magnetic Prandtl	Pm	$\frac{\nu}{\lambda}$	$\frac{\text{magnetic diffusion time}}{\text{viscous diffusion time}}$	$0.01 - 20$	$\mathcal{O}(10^{-6})$
Prandtl	Pr	$\frac{\nu}{\kappa}$	$\frac{\text{thermal diffusion time}}{\text{viscous diffusion time}}$	$0.1 - 10$	$\mathcal{O}(10^{-1})$
Nusselt	Nu	$\frac{Q}{Q_c}$	$\frac{\text{total core heat flow}}{\text{conductive core heat flow}}$	$1.5 - 60$	$\mathcal{O}(10^8)$
Rossby	Ro	$\frac{U}{\Omega L}$	$\frac{\text{inertia}}{\text{Coriolis force}}$	$10^{-4} - 10^{-1}$	$\mathcal{O}(10^{-6})$
Reynolds	Re	$\frac{UL}{\nu}$	$\frac{\text{viscous diffusion time}}{\text{eddy overturn time}}$	$10 - 10^4$	$\mathcal{O}(10^9)$
Magnetic Reynolds	Rm	$\frac{UL}{\lambda}$	$\frac{\text{magnetic diffusion time}}{\text{eddy overturn time}}$	$50 - 3000$	$\mathcal{O}(10^3)$
Traditional Elsasser	Λ_t	$\frac{B^2}{\rho \mu \lambda \Omega}$	$\frac{\text{Lorentz force}}{\text{Coriolis force}}$	$0.1 - 100$	$\mathcal{O}(10)$
Dynamic Elsasser	Λ_d	$\frac{B^2}{\rho \mu \Omega U L}$	$\frac{\text{Lorentz force}}{\text{Coriolis force}}$	$0.01 - 1$	$\mathcal{O}(10^{-2})$
Energy ratio	\mathcal{M}	$\frac{B^2}{\rho \mu U^2}$	$\frac{\text{magnetic energy}}{\text{kinetic energy}}$	$1 - 200$	$\mathcal{O}(10^4)$

in the previous section. Instead, it has been shown that typical flow length scale measures roughly follow the viscous scaling (e.g. [King and Buffett, 2013](#); [Oruba and Dormy, 2014](#))

$$\mathcal{L} \sim E^{1/3} L \approx 30 \text{ m.} \quad (1.3.17)$$

This has led to the suggestion that convection in numerical dynamos is viscously-controlled and therefore not applicable to the Earth’s core. The seemingly missing influence of the magnetic field is consistent with the results of [Soderlund et al. \(2012\)](#), who reported that in many dynamo simulations the flow occurs on a scale similar to that of rotating convection, which they attributed to a subdominant role of the Lorentz force. The difference between the convective pattern in dynamo solutions and non-magnetic models, however, has been shown to become clearer when the simulations are computed at more extreme parameters (e.g. [Sakuraba and Roberts, 2009](#); [Yadav et al., 2016](#)).

Explicit calculations of the r.m.s. strength of the forces (e.g. [Wicht and Christensen, 2010](#); [Soderlund et al., 2012, 2015](#); [Yadav et al., 2016](#); [Aubert et al., 2017](#); [Aubert, 2019](#)) did not confirm a dominant role of viscosity in the dynamo models. Instead, these studies showed that the force equilibrium in geodynamo simulations typically is composed of a zeroth-order balance between Coriolis and pressure forces, followed by a balance between buoyancy, Lorentz and ageostrophic Coriolis forces. The flow dynamics are thus mainly controlled by a QG-MAC balance. Inertia and viscosity were found to be second-order contributions, although the difference between them and the first-order forces proved to be rather small in models computed at moderate control parameters, in particular if viscous boundary layers are not excluded ([Soderlund et al., 2012](#)). Recent high-resolution simulations (e.g. [Yadav et al., 2016](#); [Aubert et al., 2017](#); [Schaeffer et al., 2017](#); [Aubert, 2019](#)) in advanced parameter regimes showed that the relative importance of viscosity and inertia decreases in more realistic setups, the leading-order structure of the force balance, however, remains essentially unchanged. This is particularly evident in the study by [Aubert et al. \(2017\)](#), who defined a path in parameter space to connect models with moderate parameters to the conditions of the Earth’s core. The observed invariance of the principal force equilibrium in simulations up to the middle of this path supports the idea that the QG-MAC balance could indeed be the relevant force balance for the Earth’s core. A novel approach introduced by [Aubert et al. \(2017\)](#) is the spectral analysis of forces. This has provided access to the length-scale dependence of the force balance. It revealed that in their models the leading-order force balance is subdivided into large-scale geostrophy and small-scale magnetostrophy. Similarly, in the first-order MAC equilibrium, the ageostrophic Coriolis force is predominantly balanced by buoyancy on large scales and by the Lorentz force towards smaller scales. Therefore, most dynamo models to date support a QG-MAC equilibrium, although there is the possibility that small scales are in a magnetostrophic state. Some studies have, however, also reported dynamos that could be controlled by system-scale magnetostrophy ([Dormy, 2016](#); [Dormy et al., 2018](#); [Raynaud et al., 2020](#)).

1.4 Objectives of this work

In the previous sections, we have seen that the presumed force balance in the Earth’s core as well as the force balance identified in numerical geodynamo simulations are highly-debated topics. On the one hand, it has been argued for dynamo models controlled by a QG-MAC balance as well as for dynamos governed by system-scale magnetostrophy. Both could possibly be relevant for the Earth’s core, since the theoretically expected dynamics are not definitively known. On the other hand, however, there are also a number of studies advocating for a subdominant role of the Lorentz force or even viscous control. Since the different studies typically include different control parameters for the simulations, the diverging results could be due either to misinterpretations or to the fact that the respective models operate in different dynamical regimes. Thus, the first goal of this thesis is to systematically investigate the force balance in the numerically accessible parameter space to see which different force balance regimes can be found and whether the transitions

between them are sharp or not. This would not only improve our understanding of force balances, but could also help with the choice of input parameters for geodynamo simulations to ensure that they operate in a geophysically-relevant regime.

Furthermore, it has proven to be challenging to relate the force balances derived from the analysis of the scaling behaviour of flow length scale measures to the results obtained by explicit calculation of the forces. The key to a successful approach is to measure length scales that are both representative of the energy contained in the solution and also indicative of the underlying physics. The second goal of this thesis therefore is to define length scale measures that fulfill these two criteria. Only if the considered length scale measures are in fact representative of a geophysically-relevant force balance, it is possible to extrapolate them in a meaningful way to the conditions of the Earth. This could provide important information about whether the flow in the Earth's core is in fact large scale as is generally assumed for core flow inversions.

This thesis is structured as follows. Chapter 2 describes the derivation of the used magneto-hydrodynamic model. In Chapter 3, different theoretical scaling laws for the flow length scale are outlined. Details about the numerical implementation of the MHD model are given in Chapter 4. Chapter 5 describes the systematic analysis of the force balance in numerical geodynamo simulations, which is identical to the published *Geophysical Journal International* (GJI) article [Schwaiger et al. \(2019\)](#), except for some notations that have been adapted within this manuscript for consistency. Chapter 6 deals with relating force balances and flow length scales in dynamo models. This chapter, together with Chapter 3, is published in the GJI article [Schwaiger et al. \(2020\)](#). Finally, conclusions and perspectives of this work are given in Chapter 7.

Chapter 2

A magneto-hydrodynamic model for the geodynamo

This chapter introduces the magneto-hydrodynamic model for the geodynamo under the Boussinesq approximation that we consider in our numerical simulations. More detailed derivations of the equations can be found for example in [Kay and Nedderman \(1985\)](#), [Batchelor \(2000\)](#), [Davidson \(2001\)](#), [Braginsky and Roberts \(1995\)](#) and [Anufriev et al. \(2005\)](#).

2.1 Magneto-hydrodynamic equations

2.1.1 Continuity equation

The continuity equation, which describes the conservation of mass in a moving fluid, can be derived by considering a macroscopic control volume V fixed in space which is enclosed by the surface ∂V . Assuming no internal sources, the principle of conservation of mass dictates that the rate of change of mass within the volume must equal the net rate of inflow of mass through the bounding surface. This balance is given by

$$\int_V \frac{\partial \rho}{\partial t} dV = - \oint_{\partial V} \rho \mathbf{u} \cdot \mathbf{n} dS, \quad (2.1.1)$$

where $\rho = \rho(\mathbf{x}, t)$ is the mass density and $\mathbf{u} = \mathbf{u}(\mathbf{x}, t)$ the fluid velocity at position \mathbf{x} and time t . The right-hand side (RHS) of Eq. (2.1.1) can be transformed into a volume integral by applying the divergence theorem, i.e.

$$\oint_{\partial V} \rho \mathbf{u} \cdot \mathbf{n} dS = \int_V \nabla \cdot (\rho \mathbf{u}) dV. \quad (2.1.2)$$

Equation (2.1.1) can then be rearranged such that it reads

$$\int_V \left[\frac{\partial \rho}{\partial t} + \nabla \cdot (\rho \mathbf{u}) \right] dV = 0. \quad (2.1.3)$$

Since this relation is required to hold for any volume, it follows that

$$\frac{\partial \rho}{\partial t} + \nabla \cdot (\rho \mathbf{u}) = 0. \quad (2.1.4)$$

This represents the differential form of the law of conservation of mass in a moving fluid, which is known as the continuity equation. Expanding the divergence term in (2.1.4) into

$$\nabla \cdot (\rho \mathbf{u}) = \mathbf{u} \cdot \nabla \rho + \rho \nabla \cdot \mathbf{u}, \quad (2.1.5)$$

and introducing the material derivative

$$\frac{D}{Dt} \equiv \frac{\partial}{\partial t} + \mathbf{u} \cdot \nabla, \quad (2.1.6)$$

allows to rewrite the continuity equation as

$$\frac{1}{\rho} \frac{D\rho}{Dt} + \nabla \cdot \mathbf{u} = 0. \quad (2.1.7)$$

2.1.2 Momentum equation

An element of fluid is subject to body forces (e.g. gravitational forces) that act on the mass of the element through a force field without direct contact and surface forces which arise from physical contact of the surface area of the element with its surroundings. The body force per unit volume is given by $\rho \mathbf{f}$, with \mathbf{f} representing the body force per unit mass. The surface forces are given by

$$\oint_{\partial V} \bar{\sigma} \cdot \mathbf{n} \, dS = \int_V \nabla \cdot \bar{\sigma} \, dV, \quad (2.1.8)$$

where $\bar{\sigma}$ is the stress tensor. Newton's second law states that the total force acting on an element of volume, i.e. the sum of body and surface forces, must be equal to its mass times its acceleration. This yields the following equation of motion for an element of fluid

$$\rho \frac{D\mathbf{u}}{Dt} = \rho \mathbf{f} + \nabla \cdot \bar{\sigma}. \quad (2.1.9)$$

It is convenient to decompose the stress tensor $\bar{\sigma}$ into isotropic and non-isotropic parts, which yields the following expression.

$$\bar{\sigma} = -p \bar{\delta} + \bar{\tau}, \quad (2.1.10)$$

where p is the isotropic fluid pressure, $\bar{\delta}$ the identity tensor and $\bar{\tau}$ the deviatoric stress tensor, which describes the non-isotropic viscous stress components. It can be shown that $\bar{\tau}$ is symmetric, i.e. $\tau_{ij} = \tau_{ji}$ (e.g. [Kay and Nedderman, 1985](#)). Substituting $\bar{\sigma}$ in Eq. (2.1.9) by relation (2.1.10) yields

$$\rho \frac{D\mathbf{u}}{Dt} = \rho \mathbf{f} - \nabla p + \nabla \cdot \bar{\tau}. \quad (2.1.11)$$

To develop this basic equation of motion further, we make an assumption about the relationship between stress and deformation. Viscous fluids are generally considered to be Newtonian, i.e. stress is expected to relate linearly to the rate of strain. Combining this assumption with the symmetry of $\bar{\tau}$, and considering the medium to be isotropic results in the following expression for the deviatoric stress tensor (e.g. [Kay and Nedderman, 1985](#))

$$\tau_{ij} = 2\eta e_{ij} + \lambda e_{kk} \delta_{ij}. \quad (2.1.12)$$

In this equation e_{ij} is the strain rate tensor, which specifies the changes of volume and shearing that the fluid element experiences due to the viscous stresses. It is defined by

$$e_{ij} = \frac{1}{2} \left(\frac{\partial u_i}{\partial x_j} + \frac{\partial u_j}{\partial x_i} \right), \quad (2.1.13)$$

with $e_{kk} = \nabla \cdot \mathbf{u}$ describing the volumetric rate of strain. The two material variables λ and η are related through Stokes' hypothesis

$$\lambda = -\frac{2}{3}\eta. \quad (2.1.14)$$

Inserting this into (2.1.12) results in

$$\tau_{ij} = 2\eta \left[e_{ij} - \frac{1}{3} (\nabla \cdot \mathbf{u}) \delta_{ij} \right]. \quad (2.1.15)$$

Replacing the deviatoric stress tensor in Eq. (2.1.11) with relation (2.1.15) and assuming the dynamic viscosity η to be constant yields the Navier-Stokes equation

$$\rho \frac{D\mathbf{u}}{Dt} = -\nabla p + \rho \mathbf{f} + \eta \nabla^2 \mathbf{u} + \frac{1}{3} \eta \nabla (\nabla \cdot \mathbf{u}). \quad (2.1.16)$$

Equation (2.1.16) is valid in an inertial reference frame. In the case of the Earth typically a reference frame fixed on the surface is considered for measurements of positions and velocities. Any such frame is, however, subject to the Earth's rotation, i.e. rotating with respect to an inertial frame. To modify the Navier-Stokes equation accordingly, suppose a frame of reference that rotates at a constant angular velocity $\boldsymbol{\Omega}$ relative to an inertial frame. The common origin of coordinates of both frames is defined by the point \mathbf{O} . To an observer in the fixed frame, the rate of change of a vector \mathbf{P} is then given by (e.g. [Batchelor, 2000](#))

$$\left(\frac{d\mathbf{P}}{dt} \right)_F = \left(\frac{d\mathbf{P}}{dt} \right)_R + \boldsymbol{\Omega} \times \mathbf{P}, \quad (2.1.17)$$

where $(d\mathbf{P}/dt)_R$ represents the rate of change of \mathbf{P} to a rotating observer. The relation of the velocities between the two frames of reference can thus be obtained by applying rule (2.1.17) to the position vector \mathbf{r} , which yields

$$\mathbf{u}_F = \mathbf{u}_R + \boldsymbol{\Omega} \times \mathbf{r}. \quad (2.1.18)$$

Applying the transformation (2.1.17) to \mathbf{u}_F neglecting precession and nutation gives

$$\left(\frac{d\mathbf{u}_F}{dt}\right)_F = \left(\frac{d\mathbf{u}_F}{dt}\right)_R + \boldsymbol{\Omega} \times \mathbf{u}_F. \quad (2.1.19)$$

Inserting Eq. (2.1.18) into this relation results in

$$\frac{d\mathbf{u}_F}{dt} = \left(\frac{d\mathbf{u}_R}{dt}\right)_R + \boldsymbol{\Omega} \times \left(\frac{d\mathbf{r}}{dt}\right)_R + \boldsymbol{\Omega} \times \mathbf{u}_R + \boldsymbol{\Omega} \times (\boldsymbol{\Omega} \times \mathbf{r}). \quad (2.1.20)$$

This describes the transformation of the accelerations between the two frames, which can be rewritten in condensed form as

$$\mathbf{a}_F = \mathbf{a}_R + 2\boldsymbol{\Omega} \times \mathbf{u}_R + \boldsymbol{\Omega} \times (\boldsymbol{\Omega} \times \mathbf{r}). \quad (2.1.21)$$

The absolute acceleration observed in the fixed frame therefore equals the sum of the apparent acceleration measured in the rotating frame, the Coriolis acceleration $2\boldsymbol{\Omega} \times \mathbf{u}$ and the centripetal acceleration $\boldsymbol{\Omega} \times (\boldsymbol{\Omega} \times \mathbf{r})$.

Application of this transformation to Eq. (2.1.16) yields the Navier-Stokes equation for a viscous fluid in a rotating frame of reference

$$\rho \frac{D\mathbf{u}}{Dt} = -\nabla p + \rho \mathbf{f} - 2\rho \boldsymbol{\Omega} \times \mathbf{u} - \rho \boldsymbol{\Omega} \times (\boldsymbol{\Omega} \times \mathbf{r}) + \eta \nabla^2 \mathbf{u} + \frac{1}{3} \eta \nabla (\nabla \cdot \mathbf{u}), \quad (2.1.22)$$

where $-2\rho \boldsymbol{\Omega} \times \mathbf{u}$ and $-\rho \boldsymbol{\Omega} \times (\boldsymbol{\Omega} \times \mathbf{r})$ represent the Coriolis and centrifugal forces respectively. These two terms are commonly referred to as fictitious or inertial forces since they vanish when $\boldsymbol{\Omega} = 0$, i.e. in the absence of rotation of the frame. The above equation can be shortened by expressing the centripetal acceleration as the gradient of a potential function, i.e.

$$\boldsymbol{\Omega} \times (\boldsymbol{\Omega} \times \mathbf{r}) = -\nabla \left[\frac{(\boldsymbol{\Omega} \times \mathbf{r})^2}{2} \right]. \quad (2.1.23)$$

By introducing the modified pressure $p^* = p - \rho (\boldsymbol{\Omega} \times \mathbf{r})^2 / 2$, the Navier-Stokes equation can then be rewritten as

$$\rho \frac{D\mathbf{u}}{Dt} = -\nabla p^* + \rho \mathbf{f} - 2\rho \boldsymbol{\Omega} \times \mathbf{u} + \eta \nabla^2 \mathbf{u} + \frac{1}{3} \eta \nabla (\nabla \cdot \mathbf{u}), \quad (2.1.24)$$

The body forces per unit volume $\rho \mathbf{f}$ in the above equation can be defined more precisely. For the Earth's core they obviously include the gravitational force per unit volume $\rho \mathbf{g}$. Additionally, it is necessary to consider electromagnetic forces experienced by the fluid, since the liquid metal in the outer core represents a moving conductor in the presence of a magnetic field. The Lorentz (or electromagnetic) force per unit volume is given by (e.g. Davidson, 2001)

$$\rho \mathbf{f}_L = \rho_e \mathbf{E} + \mathbf{j} \times \mathbf{B}, \quad (2.1.25)$$

where \mathbf{E} represents the electric field, \mathbf{j} the electric current density, \mathbf{B} the magnetic field and ρ_e the electric charge density. In the Earth's outer core, the electrostatic force $\rho_e \mathbf{E}$ is expected to be negligible compared to $\mathbf{j} \times \mathbf{B}$ since typical fluid velocities are of the order of millimeters per second and hence much smaller than the speed of light c , i.e. $|\mathbf{u}| \ll c$ (e.g. Davidson, 2001). This is known as the MHD approximation. Therefore, the Lorentz force can be reduced to

$$\rho \mathbf{f}_L \simeq \mathbf{j} \times \mathbf{B}. \quad (2.1.26)$$

The Navier-Stokes equation thus reads

$$\rho \frac{D\mathbf{u}}{Dt} = -\nabla p^* + \rho \mathbf{g} + \mathbf{j} \times \mathbf{B} - 2\rho \boldsymbol{\Omega} \times \mathbf{u} + \eta \nabla^2 \mathbf{u} + \frac{1}{3} \eta \nabla (\nabla \cdot \mathbf{u}). \quad (2.1.27)$$

2.1.3 Induction equation

The evolution of the Earth's magnetic field is governed by the induction equation. For its derivation, it is necessary to consider Maxwell's equations, which are

$$\nabla \cdot \mathbf{E} = \frac{\rho_e}{\epsilon} \quad (\text{Maxwell-Gauss}), \quad (2.1.28)$$

$$\nabla \times \mathbf{E} = -\frac{\partial \mathbf{B}}{\partial t} \quad (\text{Maxwell-Faraday}), \quad (2.1.29)$$

$$\nabla \cdot \mathbf{B} = 0 \quad (\text{Maxwell-Thompson}), \quad (2.1.30)$$

$$\nabla \times \mathbf{B} = \mu \left(\mathbf{j} + \epsilon \frac{\partial \mathbf{E}}{\partial t} \right) \quad (\text{Maxwell-Ampère}), \quad (2.1.31)$$

where \mathbf{B} is the magnetic induction, \mathbf{E} the electric field, \mathbf{j} the electric current density and ρ_e the electric charge density. The constants ϵ and μ represent the permittivity and the magnetic permeability of free space, respectively. The former can be expressed as $\epsilon = (\mu c^2)^{-1}$, where c is the speed of light. Equation (2.1.31) can then be rewritten as

$$\nabla \times \mathbf{B} = \mu \mathbf{j} + \frac{1}{c^2} \frac{\partial \mathbf{E}}{\partial t}. \quad (2.1.32)$$

The last term in this equation, which describes the displacement currents, can be discarded since $|\mathbf{u}| \ll c$ in the Earth's outer core. Equation (2.1.31) therefore reduces to Ampère's law

$$\nabla \times \mathbf{B} = \mu \mathbf{j}. \quad (2.1.33)$$

For the derivation of the magnetic induction equation from Maxwell's equations, suppose a fluid with electric conductivity σ . If the fluid is at rest, the electric current density is related to the electric field by Ohm's law

$$\mathbf{j} = \sigma \mathbf{E}. \quad (2.1.34)$$

The Earth's outer core is, however, expected to be convecting. Hence, the fluid core represents a moving conductor, and as a result Ohm's law has to be modified. To this end, consider a reference frame moving at velocity \mathbf{u} with respect to a fixed reference frame. The electric and magnetic fields in the moving frame (\mathbf{E}' and \mathbf{B}') can then be obtained from the corresponding fields in the fixed frame (\mathbf{E} and \mathbf{B}) through the following relations (e.g. [Dormy and Soward, 2007](#))

$$\mathbf{E}' = (1 - \gamma_u) \frac{\mathbf{u} \cdot \mathbf{E}}{|\mathbf{u}|^2} \mathbf{u} + \gamma_u (\mathbf{E} + \mathbf{u} \times \mathbf{B}), \quad (2.1.35)$$

$$\mathbf{B}' = (1 - \gamma_u) \frac{\mathbf{u} \cdot \mathbf{B}}{|\mathbf{u}|^2} \mathbf{u} + \gamma_u \left(\mathbf{B} - \frac{\mathbf{u} \times \mathbf{E}}{c^2} \right), \quad (2.1.36)$$

where $\gamma_u = (1 - |\mathbf{u}|^2/c^2)^{-1/2}$ represents the Lorentz factor. The aforementioned assumption $|\mathbf{u}| \ll c$ yields $\gamma_u \approx 1$. Scaling Eq. (2.1.29) with the typical length scale L and the typical time scale τ yields

$$|\mathbf{E}| \sim |\mathbf{u}| |\mathbf{B}|, \quad (2.1.37)$$

where $|\mathbf{u}| = L/\tau$. Combining this with Eq. (2.1.36) shows that \mathbf{B}' scales as

$$\mathbf{B}' \sim \mathbf{B} \left(1 - \frac{|\mathbf{u}|^2}{c^2} \right) \sim \mathbf{B}. \quad (2.1.38)$$

Hence, the transformations (2.1.35) and (2.1.36) can be reduced to

$$\mathbf{E}' = \mathbf{E} + \mathbf{u} \times \mathbf{B}, \quad (2.1.39)$$

$$\mathbf{B}' = \mathbf{B}. \quad (2.1.40)$$

Relative to the fixed frame, Ohm's law can then be expressed as

$$\mathbf{j} = \sigma (\mathbf{E} + \mathbf{u} \times \mathbf{B}). \quad (2.1.41)$$

Inserting this into Eq. (2.1.33) and subsequently taking the curl of both sides results in

$$\nabla \times (\nabla \times \mathbf{B}) = \nabla \times [\mu\sigma (\mathbf{E} + \mathbf{u} \times \mathbf{B})]. \quad (2.1.42)$$

By assuming the electric conductivity to be constant and using the vector identity

$$\nabla \times (\nabla \times \mathbf{B}) = \nabla (\nabla \cdot \mathbf{B}) - \nabla^2 \mathbf{B}, \quad (2.1.43)$$

relation (2.1.42) can be rewritten as

$$\nabla (\nabla \cdot \mathbf{B}) - \nabla^2 \mathbf{B} = \mu\sigma [\nabla \times \mathbf{E} + \nabla \times (\mathbf{u} \times \mathbf{B})]. \quad (2.1.44)$$

Inserting Eq. (2.1.30) and (2.1.29) yields

$$-\nabla^2 \mathbf{B} = \mu\sigma \left[-\frac{\partial \mathbf{B}}{\partial t} + \nabla \times (\mathbf{u} \times \mathbf{B}) \right]. \quad (2.1.45)$$

Introducing the magnetic diffusivity $\lambda = 1/(\mu\sigma)$ yields the following expression of the magnetic induction equation for a fluid with constant electric conductivity

$$\frac{\partial \mathbf{B}}{\partial t} = \nabla \times (\mathbf{u} \times \mathbf{B}) + \lambda \nabla^2 \mathbf{B}. \quad (2.1.46)$$

2.1.4 Heat transport equation

Convection in the outer core is driven by thermal and compositional buoyancy forces. Thermal driving results from temperature gradients due to the cooling down of the Earth since its formation combined with the release of latent heat during the crystallisation of iron and nickel at the inner-core boundary (ICB). This crystallisation process is also responsible for the compositional driving since it leads to the release of light elements at the ICB which cannot be incorporated into the solid inner core. In this section, we will for simplicity only consider thermal buoyancy sources. This type of driving mechanism is governed by the thermal energy equation, which can be derived from the principles of thermodynamics.

The first law of thermodynamics says that in a closed system any transition between two thermodynamic states leads to a change of the system's internal energy that equates the sum of heat supplied to the system and the work done on the system by its surroundings. In differential form, this principle can be expressed as

$$de = \delta Q + \delta W, \quad (2.1.47)$$

where de represents the change in internal energy per unit mass, δQ the supplied heat per unit mass and δW the work done per unit mass.

Consider a quasi-static infinitesimal compression of a fluid element. This transformation can be considered to be reversible. The work done on the fluid is then given by $-pdV$, where $V = \rho^{-1}$ is the volume per unit mass. In this case the first law of thermodynamics becomes

$$de = dQ + \frac{p}{\rho^2}d\rho. \quad (2.1.48)$$

The entropy change dS during a reversible process is related to the heat added to the system through the following relation

$$dQ = TdS. \quad (2.1.49)$$

Expressing the entropy as a function of pressure and temperature, i.e.

$$S = S(p, T), \quad (2.1.50)$$

yields the following equation for the changes in entropy

$$dS = \left(\frac{\partial S}{\partial T}\right)_p dT + \left(\frac{\partial S}{\partial p}\right)_T dp. \quad (2.1.51)$$

Maxwell's relations of thermodynamics state that

$$\left(\frac{\partial S}{\partial p}\right)_T = -\left(\frac{\partial V}{\partial T}\right)_p = \frac{1}{\rho^2} \left(\frac{\partial \rho}{\partial T}\right)_p. \quad (2.1.52)$$

Introducing the coefficient of thermal expansion

$$\alpha \doteq \frac{1}{V} \left(\frac{\partial V}{\partial T} \right)_p = -\frac{1}{\rho} \left(\frac{\partial \rho}{\partial T} \right)_p \quad (2.1.53)$$

allows to rewrite expression (2.1.52) as

$$\left(\frac{\partial S}{\partial p} \right)_T = -\frac{\alpha}{\rho}. \quad (2.1.54)$$

Substituting this relation together with the definition of the heat capacity at constant pressure c_p , which is given by

$$c_p \doteq T \left(\frac{\partial S}{\partial T} \right)_p, \quad (2.1.55)$$

into Eq. (2.1.51) yields

$$dS = \frac{c_p}{T} dT - \frac{\alpha}{\rho} dp. \quad (2.1.56)$$

The rate of change of the entropy is therefore given by

$$\frac{DS}{Dt} = \frac{c_p}{T} \frac{DT}{Dt} - \frac{\alpha}{\rho} \frac{Dp}{Dt}. \quad (2.1.57)$$

By introducing the heat flux \mathbf{q} and a term \mathcal{H} which denotes the internal heating, the rate of change of the supplied heat can be expressed as

$$\rho \frac{DQ}{Dt} = -\nabla \cdot \mathbf{q} + \mathcal{H} \quad (2.1.58)$$

For the Earth's outer core the heat source term encompasses several contributions

$$H = Q_v + Q_j + \mathcal{H}^R, \quad (2.1.59)$$

where Q_v and Q_j represent viscous and ohmic dissipation, respectively. The term \mathcal{H}^R denotes internal heating due to radiogenic elements. By assuming Fourier's law $\mathbf{q} = -k\nabla T$ to describe the heat flux, Eq. (2.1.58) can be written as

$$\rho \frac{DQ}{Dt} = \nabla \cdot (k\nabla T) + \mathcal{H} \quad (2.1.60)$$

Using relation (2.1.49) and assuming the thermal conductivity k to be constant results in

$$\rho T \frac{DS}{Dt} = k\nabla^2 T + \mathcal{H}. \quad (2.1.61)$$

Substituting Eq. (2.1.57) into the above relation finally yields the heat transport equation

$$\rho c_p \frac{DT}{Dt} - \alpha T \frac{Dp}{Dt} = k \nabla^2 T + \mathcal{H}. \quad (2.1.62)$$

In summary, the compressible equations that govern thermal convection in planetary dynamos for homogeneous λ , μ and k are then

$$\frac{1}{\rho} \frac{D\rho}{Dt} = -\nabla \cdot \mathbf{u}, \quad (2.1.63)$$

$$\rho \frac{D\mathbf{u}}{Dt} = -\nabla p + \rho \mathbf{g} + \frac{1}{\mu} (\nabla \times \mathbf{B}) \times \mathbf{B} - 2\rho \boldsymbol{\Omega} \times \mathbf{u} + \eta \nabla^2 \mathbf{u} + \frac{1}{3} \eta \nabla (\nabla \cdot \mathbf{u}), \quad (2.1.64)$$

$$\frac{\partial \mathbf{B}}{\partial t} = \nabla \times (\mathbf{u} \times \mathbf{B}) + \lambda \nabla^2 \mathbf{B}, \quad (2.1.65)$$

$$\nabla \cdot \mathbf{B} = 0, \quad (2.1.66)$$

$$\rho c_p \frac{DT}{Dt} - \alpha T \frac{Dp}{Dt} = k \nabla^2 T + \mathcal{H}, \quad (2.1.67)$$

where we denote the modified pressure p^* simply as p . In addition to this set of equations, an equation of state for the density is required to complete the system

$$\rho = \rho(p, T). \quad (2.1.68)$$

This closed system of equations complemented by boundary conditions could in theory be solved numerically. However, because of convection being driven by density perturbations that are tiny compared to the mean core density, even very small errors in the full density can lead to unreliable solutions. Therefore, in numerical schemes it is more useful to only study the small disturbances about a reference state that are caused by convective motions instead of solving for the full thermodynamic variables.

2.2 Reference state

The Earth's outer core is expected to be well-mixed and close to adiabatically-stratified. Thus, we adopt a reference state that is non-magnetic, hydrostatic, adiabatic and spherically-symmetric (Braginsky and Roberts, 1995; Anufriev et al., 2005; Jones, 2015). Hence, one can develop the convective fluctuations around this background state in the following way:

$$\rho(\mathbf{r}, t) = \rho_a(r) + \rho'(\mathbf{r}, t), \quad (2.2.1a)$$

$$p(\mathbf{r}, t) = p_a(r) + p'(\mathbf{r}, t), \quad (2.2.1b)$$

$$T(\mathbf{r}, t) = T_a(r) + T'(\mathbf{r}, t), \quad (2.2.1c)$$

$$S(\mathbf{r}, t) = S_a(r) + S'(\mathbf{r}, t). \quad (2.2.1d)$$

The values of the adiabatic reference state are denoted by the subscript a . The small perturbations about this reference state due to the convection are referred to with the superscript $'$. It should be noted that in the case of the Earth this background state is not truly stationary, but rather evolving slowly on geological time scales, i.e. on time scales of millions of years.

From Eq. (2.1.56), it follows that the spatial variations of the entropy are given by

$$\nabla S = \frac{c_p}{T} \nabla T - \frac{\alpha}{\rho} \nabla p. \quad (2.2.2)$$

For the reference state this expression reduces to

$$\frac{c_p}{T_a} \frac{dT_a}{dr} = \frac{\alpha}{\rho_a} \frac{dp_a}{dr} + \underbrace{\frac{dS_a}{dr}}_{=0}, \quad (2.2.3)$$

since it is assumed to be adiabatic.

The hydrostatic background state is given by the balance between the pressure gradient force and gravity

$$\frac{dp_a}{dr} = -g\rho_a. \quad (2.2.4)$$

Inserting this into (2.2.3) yields

$$\frac{c_p}{T_a} \frac{dT_a}{dr} = -\alpha g. \quad (2.2.5)$$

By introducing the Dissipation number (e.g. Schubert et al., 2001; Anufriev et al., 2005)

$$Di = \frac{g\alpha L}{c_p}, \quad (2.2.6)$$

the expression for the temperature gradient (Eq. 2.2.5) can be reformulated as

$$\frac{L}{T_a} \frac{dT_a}{dr} = -Di. \quad (2.2.7)$$

Finally, the radial variations of the density in the reference state can be derived from the Grüneisen parameter γ , which is defined by (e.g. Vočadlo et al., 2003)

$$\gamma = \frac{\rho}{T} \left(\frac{\partial T}{\partial \rho} \right)_S. \quad (2.2.8)$$

For the adiabatic reference state (which is isentropic) γ is given by

$$\gamma = \frac{\rho_a}{T_a} \left(\frac{\partial T_a}{\partial \rho_a} \right)_S = \frac{\rho_a}{T_a} \frac{dT_a}{d\rho_a} = \frac{\rho_a}{T_a} \frac{dT_a}{dr} \frac{dr}{d\rho_a}. \quad (2.2.9)$$

Inserting Eq. (2.2.7) into this relation then yields the following expression for the density gradient

$$\frac{L}{\rho_a} \frac{d\rho_a}{dr} = -\frac{Di}{\gamma}. \quad (2.2.10)$$

In summary, the adiabatic reference state is therefore governed by the following set of equations

$$\frac{dp_a}{dr} = -g\rho_a, \quad \frac{L}{T_a} \frac{dT_a}{dr} = -Di, \quad \frac{L}{\rho_a} \frac{d\rho_a}{dr} = -\frac{Di}{\gamma}, \quad S_a = \text{const}, \quad Di = \frac{g\alpha L}{c_p}. \quad (2.2.11)$$

2.3 Equations for the convective perturbations

It is convenient to introduce a parameter ε to quantify the ratio between the small fluctuations and the reference state:

$$\varepsilon \sim \frac{|\rho'|}{|\rho_a|} \sim \frac{|p'|}{|p_a|} \sim \frac{|T'|}{|T_a|} \sim \frac{|S'|}{|S_a|} \ll 1. \quad (2.3.1)$$

To derive the convective perturbation equations, we now solve the MHD equations in first order of ε .

Applying the decomposition (2.2.1a) to the continuity equation (2.1.4) yields

$$\frac{\partial}{\partial t} (\rho_a + \rho') + \nabla \cdot [(\rho_a + \rho') \mathbf{u}] = 0. \quad (2.3.2)$$

Since the reference state is time-independent this reduces to

$$\frac{\partial \rho'}{\partial t} + \nabla \cdot (\rho' \mathbf{u}) + \nabla \cdot (\rho_a \mathbf{u}) = 0. \quad (2.3.3)$$

The second term on the LHS is of second order. To estimate the order of the time derivative, we consider the magnitude ratio of the two remaining terms by scaling the divergence

operator as $1/L$ and using the convective turnover time $\tau = L/U$ as unit of time. This yields

$$\frac{|\partial\rho'/\partial t|}{|\nabla \cdot (\rho_a \mathbf{u})|} \sim \frac{\rho'}{\rho_a} \sim \varepsilon. \quad (2.3.4)$$

The time derivative is thus also of second order. Neglecting this term is equivalent to filtering out sound waves. As a first order approximation, the continuity equation can then be reduced to

$$\nabla \cdot (\rho_a \mathbf{u}) = 0. \quad (2.3.5)$$

Expanding the divergence operator and using the fact that the reference state only varies with radius yields

$$\rho_a \nabla \cdot \mathbf{u} + \mathbf{u} \cdot \nabla \rho_a = \rho_a \nabla \cdot \mathbf{u} + u_r \frac{d\rho_a}{dr} = 0. \quad (2.3.6)$$

Finally, substituting Eq. (2.2.10) into the above expression gives

$$\rho_a \nabla \cdot \mathbf{u} - \frac{u_r \rho_a D_i}{L\gamma} = 0. \quad (2.3.7)$$

The next step is to derive the momentum equation for the convective perturbations. Inserting the decompositions of the thermodynamic quantities into Eq. (2.1.27) results in

$$\begin{aligned} (\rho_a + \rho') \frac{D\mathbf{u}}{Dt} = & -\nabla(p_a + p') + (\rho_a + \rho') \mathbf{g} - 2(\rho_a + \rho') \boldsymbol{\Omega} \times \mathbf{u} + \\ & + \mathbf{j} \times \mathbf{B} + \eta \left[\nabla^2 \mathbf{u} + \frac{1}{3} \nabla (\nabla \cdot \mathbf{u}) \right] \end{aligned} \quad (2.3.8)$$

Removing the hydrostatic background state given by

$$-\nabla p_a + \rho_a \mathbf{g} = 0 \quad (2.3.9)$$

modifies Eq. (2.3.8) to

$$(\rho_a + \rho') \frac{D\mathbf{u}}{Dt} = -\nabla p' + \rho' \mathbf{g} - 2(\rho_a + \rho') \boldsymbol{\Omega} \times \mathbf{u} + \mathbf{j} \times \mathbf{B} + \eta \left[\nabla^2 \mathbf{u} + \frac{1}{3} \nabla (\nabla \cdot \mathbf{u}) \right] \quad (2.3.10)$$

By neglecting the second order terms $\rho' D\mathbf{u}/Dt$ and $2\rho' \boldsymbol{\Omega} \times \mathbf{u}$, the Navier-Stokes equation reduces to

$$\rho_a \frac{D\mathbf{u}}{Dt} = -\nabla p' + \rho' \mathbf{g} - 2\rho_a \boldsymbol{\Omega} \times \mathbf{u} + \mathbf{j} \times \mathbf{B} + \eta \left[\nabla^2 \mathbf{u} + \frac{1}{3} \nabla (\nabla \cdot \mathbf{u}) \right]. \quad (2.3.11)$$

We now want to express ρ' as a function of the pressure and temperature perturbations, i.e.

$$\rho' = \rho'(p', T'). \quad (2.3.12)$$

To this end, we apply the chain rule to the equation of state (Eq. 2.1.68). This results in the following relation for the density variations

$$d\rho = \left(\frac{\partial \rho}{\partial T} \right)_p dT + \left(\frac{\partial \rho}{\partial p} \right)_T dp. \quad (2.3.13)$$

Introducing the isothermal bulk modulus K_T , which is given by

$$K_T \doteq \rho \left(\frac{\partial p}{\partial \rho} \right)_T, \quad (2.3.14)$$

and using the definition of the thermal expansion coefficient α (Eq. 2.1.53) allows to rewrite Eq. (2.3.13) as

$$d\rho = -\rho\alpha dT + \frac{\rho}{K_T} dp. \quad (2.3.15)$$

This can be further modified by defining the heat capacity at constant volume c_V

$$c_V \doteq T \left(\frac{\partial S}{\partial T} \right)_V, \quad (2.3.16)$$

which then allows to express the isothermal bulk modulus as

$$K_T = \frac{\gamma c_V \rho}{\alpha}. \quad (2.3.17)$$

Inserting this relation into Eq. (2.3.13) yields

$$d\rho = -\rho\alpha dT + \frac{\alpha}{c_V \gamma} dp. \quad (2.3.18)$$

We will see later on that it is convenient to reformulate the last term using the dissipation number Di (Eq. 2.2.6). The above equation then reads

$$d\rho = -\rho\alpha dT + \frac{c_p Di}{c_V \gamma g L} dp. \quad (2.3.19)$$

Replacing $d\rho$, dT , dp by the convective perturbations ρ' , T' , p' , and considering the remaining thermodynamic quantities to be governed by the reference state, yields

$$\rho' = -\rho_a \alpha T' + \frac{c_p Di}{c_V \gamma g L} p'. \quad (2.3.20)$$

Substituting this into Eq. (2.3.11) yields the following formulation of the momentum equation for the convective perturbations

$$\begin{aligned} \rho_a \frac{D\mathbf{u}}{Dt} = & -\nabla p' - \rho_a \alpha T' \mathbf{g} + \frac{c_p D_i}{c_V \gamma g L} p' \mathbf{g} - 2\rho_a \boldsymbol{\Omega} \times \mathbf{u} + \mathbf{j} \times \mathbf{B} + \\ & + \eta \left[\nabla^2 \mathbf{u} + \frac{1}{3} \nabla (\nabla \cdot \mathbf{u}) \right]. \end{aligned} \quad (2.3.21)$$

Before inserting the decompositions (Eq. 2.2.1a-2.2.1d) into the heat transport equation (Eq. 2.1.62), we note that for fluids with $\alpha T \ll 1$ pressure variations can be neglected. Eq. (2.1.62) thus reduces to a temperature equation

$$\rho c_p \frac{DT}{Dt} = k \nabla^2 T + \mathcal{H}. \quad (2.3.22)$$

This approximation is known as the anelastic liquid approximation. Anufriev et al. (2005) noted that these conditions are reasonably fulfilled in the Earth's outer core where $\alpha T \sim 6 \times 10^{-2}$. Applying the decompositions (2.2.1a) and (2.2.1c) to the above equation then results in

$$(\rho_a + \rho') c_p \left[\frac{\partial}{\partial t} (T_a + T') + \mathbf{u} \cdot \nabla (T_a + T') \right] = k \nabla^2 (T_a + T') + \mathcal{H}. \quad (2.3.23)$$

The time derivative $\partial T_a / \partial t$ vanishes since the reference state is static. Neglecting all second-order terms then yields

$$\rho_a c_p \left(\frac{\partial T'}{\partial t} + \mathbf{u} \cdot \nabla T' + \mathbf{u} \cdot \nabla T_a \right) = k \nabla^2 (T_a + T') + \mathcal{H} \quad (2.3.24)$$

By introducing the thermal diffusivity $\kappa \doteq k / \rho_a c_p$ this can be rewritten as

$$\frac{\partial T'}{\partial t} + \mathbf{u} \cdot \nabla T' = \kappa \nabla^2 (T_a + T') - \mathbf{u} \cdot \nabla T_a + \tilde{\mathcal{H}}, \quad (2.3.25)$$

where the source term has been adjusted to $\tilde{\mathcal{H}} = \mathcal{H} / \rho_a c_p$.

In summary, the equations for the convective perturbations are then

$$\rho_a \nabla \cdot \mathbf{u} = \frac{u_r \rho_a D_i}{L \gamma}, \quad (2.3.26)$$

$$\begin{aligned} \rho_a \frac{D\mathbf{u}}{Dt} = & -\nabla p' - \rho_a \alpha T' \mathbf{g} + \frac{c_p D_i}{c_V \gamma g L} p' \mathbf{g} - 2\rho_a \boldsymbol{\Omega} \times \mathbf{u} + \mathbf{j} \times \mathbf{B} + \\ & + \eta \left[\nabla^2 \mathbf{u} + \frac{1}{3} \nabla (\nabla \cdot \mathbf{u}) \right], \end{aligned} \quad (2.3.27)$$

$$\frac{\partial T'}{\partial t} + \mathbf{u} \cdot \nabla T' = \kappa \nabla^2 (T_a + T') - \mathbf{u} \cdot \nabla T_a + \tilde{\mathcal{H}}. \quad (2.3.28)$$

2.4 Boussinesq approximation

Despite the approximations included in the anelastic liquid equations (Eq. 2.3.26-2.3.28), numerical studies of the geodynamo process are still computationally extremely demanding. Thus, to further reduce the complexity and therefore the required computational resources, core convection is usually studied under the Boussinesq approximation, which essentially states that the density variations in the fluid can be neglected except for when they are multiplied by the gravitational acceleration \mathbf{g} .

The Boussinesq equations can be obtained from the anelastic liquid equations (Eq. 2.3.26-2.3.28) by setting the dissipation number Di to zero, i.e. all terms that include Di will vanish. This corresponds to the so-called thin-layer approximation since $Di = g\alpha L/c_p \rightarrow 0$ implies that

$$L \ll \frac{c_p}{g\alpha}. \quad (2.4.1)$$

In the Earth's core, this assumption is not perfectly satisfied since $Di \approx 0.3$. This value is, however, argued to be sufficiently small to use the Boussinesq approximation, which has the advantage that the convection equations simplify significantly.

In the limit $Di \rightarrow 0$ the continuity equation (Eq. 2.3.26) reduces to

$$\nabla \cdot \mathbf{u} = 0. \quad (2.4.2)$$

The momentum equation (Eq. 2.3.27) also greatly simplifies. It is now given by

$$\rho_a \frac{D\mathbf{u}}{Dt} = -\nabla p' - \rho_a \alpha T' \mathbf{g} - 2\rho_a \boldsymbol{\Omega} \times \mathbf{u} + \mathbf{j} \times \mathbf{B} + \eta \nabla^2 \mathbf{u}, \quad (2.4.3)$$

where Eq. (2.4.2) has been inserted into the viscous term. In the above equation buoyancy forces due to pressure perturbations are now neglected.

In the Boussinesq limit, the temperature equation (Eq. 2.3.28) becomes

$$\frac{\partial T'}{\partial t} + \mathbf{u} \cdot \nabla T' = \kappa \nabla^2 T' + \tilde{H}, \quad (2.4.4)$$

since from Eq. (2.2.7) it follows that $\nabla T_a = 0$ when $Di \rightarrow 0$. Note that in the Boussinesq limit the viscous and ohmic dissipation terms contained in the last term (see Eq. 2.1.59) also vanish since they are proportional to Di (Anufriev et al., 2005).

The magneto-hydrodynamic equations under the Boussinesq approximation are therefore given by

$$\rho \left(\frac{\partial \mathbf{u}}{\partial t} + \mathbf{u} \cdot \nabla \mathbf{u} \right) = -\nabla p - \rho \alpha T \mathbf{g} - 2\rho \boldsymbol{\Omega} \times \mathbf{u} + \mathbf{j} \times \mathbf{B} + \eta \nabla^2 \mathbf{u}, \quad (2.4.5)$$

$$\frac{\partial T}{\partial t} + \mathbf{u} \cdot \nabla T = \kappa \nabla^2 T + \mathcal{H}, \quad (2.4.6)$$

$$\frac{\partial \mathbf{B}}{\partial t} = \nabla \times (\mathbf{u} \times \mathbf{B}) + \lambda \nabla^2 \mathbf{B}, \quad (2.4.7)$$

$$\nabla \cdot \mathbf{u} = 0, \quad (2.4.8)$$

$$\nabla \cdot \mathbf{B} = 0. \quad (2.4.9)$$

For simplicity, we neglected all super- and subscripts in the above equations (and will continue to do so from hereafter).

2.5 Non-dimensionalisation

It is convenient to non-dimensionalise the magneto-hydrodynamic equations. The thereby introduced dimensionless parameters provide information about the physical regime of the dynamo as they measure the relative importance of the individual forces. There are various ways in which the equations can be scaled. We non-dimensionalise the equations following [Christensen et al. \(2001\)](#). To this end, any quantity will be expressed as the product of a dimensionless part (denoted by a hat) and its unit, i.e. we write for vectors

$$\mathbf{x} = \hat{\mathbf{x}} \mathcal{X}, \quad (2.5.1)$$

and for scalars

$$x = \hat{x} \mathcal{X}. \quad (2.5.2)$$

To scale the equations, we adopt the thickness of the outer core $L = r_o - r_i$ as reference length scale, whereby r_i and r_o are the inner and outer core radii respectively. The viscous diffusion time $\tau_\nu = L^2/\nu$ serves as unit of time, where $\nu = \eta/\rho$ is the kinematic viscosity (or viscous diffusivity). The gradient and the time derivative operator can then be scaled as

$$\frac{\partial}{\partial t} = \frac{1}{\tau_\nu} \frac{\partial}{\partial \hat{t}} = \frac{\nu}{L^2} \frac{\partial}{\partial \hat{t}}, \quad (2.5.3)$$

$$\nabla = \frac{1}{L} \hat{\nabla}. \quad (2.5.4)$$

We begin by non-dimensionalising the magnetic induction equation. The magnetic field \mathbf{B} is scaled by $\sqrt{\rho\mu\lambda\Omega}$ and the velocity field by L/τ_ν , such that $\mathbf{B} = \sqrt{\rho\mu\lambda\Omega}\hat{\mathbf{B}}$ and $\mathbf{u} = L/\tau_\nu\hat{\mathbf{u}}$. This yields for Eq. (2.4.7):

$$\frac{\partial\hat{\mathbf{B}}}{\partial\hat{t}} = \hat{\nabla} \times (\hat{\mathbf{u}} \times \hat{\mathbf{B}}) + \frac{\lambda}{\nu}\hat{\nabla}^2\hat{\mathbf{B}}. \quad (2.5.5)$$

Introducing the magnetic Prandtl number Pm , which is the ratio of viscous and magnetic diffusivities, i.e.

$$Pm = \frac{\nu}{\lambda}, \quad (2.5.6)$$

allows us to rewrite the dimensionless magnetic induction equation as

$$\frac{\partial\hat{\mathbf{B}}}{\partial\hat{t}} = \hat{\nabla} \times (\hat{\mathbf{u}} \times \hat{\mathbf{B}}) + \frac{1}{Pm}\hat{\nabla}^2\hat{\mathbf{B}}. \quad (2.5.7)$$

The magnetic Prandtl number can also be understood as the time scale ratio τ_λ/τ_ν , where τ_λ is the magnetic diffusion time. The Earth's core is expected to be in a small Pm regime (see Table 1.3).

The next step is the non-dimensionalisation of the temperature equation (Eq. 2.4.6). To this end, the temperature perturbation T is scaled with the superadiabatic temperature difference ΔT between the ICB and the CMB. By neglecting any internal heating, the evolution equation of the temperature then becomes

$$\frac{\partial\hat{T}}{\partial\hat{t}} + \hat{\mathbf{u}} \cdot \hat{\nabla}\hat{T} = \frac{\kappa}{\nu}\hat{\nabla}^2\hat{T}. \quad (2.5.8)$$

The non-dimensional ratio κ/ν is the inverse of the hydrothermal Prandtl number Pr , which is defined by

$$Pr = \frac{\nu}{\kappa}. \quad (2.5.9)$$

In terms of time scales, Pr represents the ratio between the thermal diffusion time and the viscous diffusion time, i.e. τ_κ/τ_ν . By using the definition of Pr , the dimensionless temperature equation can be expressed as

$$\frac{\partial\hat{T}}{\partial\hat{t}} + \hat{\mathbf{u}} \cdot \hat{\nabla}\hat{T} = \frac{1}{Pr}\hat{\nabla}^2\hat{T}. \quad (2.5.10)$$

For the non-dimensionalisation of the momentum equation (Eq. 2.4.5), we assume that the outer core rotates uniformly with rotation rate Ω about the axis \mathbf{e}_z , i.e. $\boldsymbol{\Omega} = \Omega\mathbf{e}_z$. The gravitational acceleration \mathbf{g} is assumed to increase linearly with radius (Dziewonski and Anderson, 1981), such that the gravity profile follows $\mathbf{g} = -g_o\mathbf{r}/r_o$, where g_o represents the

gravitational acceleration at the CMB. The non-hydrostatic pressure p scales with $\rho L^2/\tau_\nu^2$, i.e. $p = \rho L^2/\tau_\nu^2 \hat{p}$. Applying these scalings to the momentum equation yields

$$\begin{aligned} \frac{\partial \hat{\mathbf{u}}}{\partial \hat{t}} + \hat{\mathbf{u}} \cdot \hat{\nabla} \hat{\mathbf{u}} = & -\hat{\nabla} \hat{p} - 2 \frac{\Omega L^2}{\nu} \mathbf{e}_z \times \hat{\mathbf{u}} + \frac{\alpha g_o L^3 \Delta T}{\nu^2} \frac{\mathbf{r}}{r_o} \hat{T} + \\ & + \frac{\Omega L^2 \lambda}{\nu^2} \left(\hat{\nabla} \times \hat{\mathbf{B}} \right) \times \hat{\mathbf{B}} + \hat{\nabla}^2 \hat{\mathbf{u}}. \end{aligned} \quad (2.5.11)$$

To rewrite this expression, we have to introduce two additional dimensionless parameters. The first parameter is the Ekman number E , which is defined by

$$E = \frac{\nu}{\Omega L^2}. \quad (2.5.12)$$

It represents the ratio of the planetary rotation period Ω^{-1} and the viscous diffusion time τ_ν . The Ekman number can also be interpreted as a proxy for the ratio between viscous and Coriolis forces. In the Earth's core, E is expected to be vanishing (see Table 1.3) meaning that viscous effects are marginal compared to rotational forces.

The second dimensionless parameter that we need to introduce is the Rayleigh number Ra , which is defined by

$$Ra = \frac{\alpha g_o L^3 \Delta T}{\nu \kappa}. \quad (2.5.13)$$

It represents the ratio between the buoyancy forces driving convection and diffusive effects which obstruct the flow. The Rayleigh number thus represents a measure for the vigour of convection. For convection to occur it has to surpass a critical value, below which heat is exclusively transferred by conduction. In the Earth's outer core, the Rayleigh number is believed to be much larger than its critical value for convection onset (e.g. Christensen, 2011).

After introducing the Ekman and Rayleigh numbers, Eq. (2.5.11) can be rewritten as

$$\frac{\partial \hat{\mathbf{u}}}{\partial \hat{t}} + \hat{\mathbf{u}} \cdot \hat{\nabla} \hat{\mathbf{u}} = -\hat{\nabla} \hat{p} - \frac{2}{E} \mathbf{e}_z \times \hat{\mathbf{u}} + \frac{Ra}{Pr} \frac{\mathbf{r}}{r_o} \hat{T} + \frac{1}{EPm} \left(\hat{\nabla} \times \hat{\mathbf{B}} \right) \times \hat{\mathbf{B}} + \hat{\nabla}^2 \hat{\mathbf{u}}. \quad (2.5.14)$$

Finally, the non-dimensional solenoidal conditions of the velocity field and the magnetic field are given by

$$\hat{\nabla} \cdot \hat{\mathbf{u}} = 0, \quad (2.5.15)$$

$$\hat{\nabla} \cdot \hat{\mathbf{B}} = 0. \quad (2.5.16)$$

To numerically integrate these dimensionless equations in time, it is required to specify boundary conditions for the velocity, magnetic and temperature fields. The set of mechanical, magnetic and thermal boundary conditions used within this thesis is outlined in the next section.

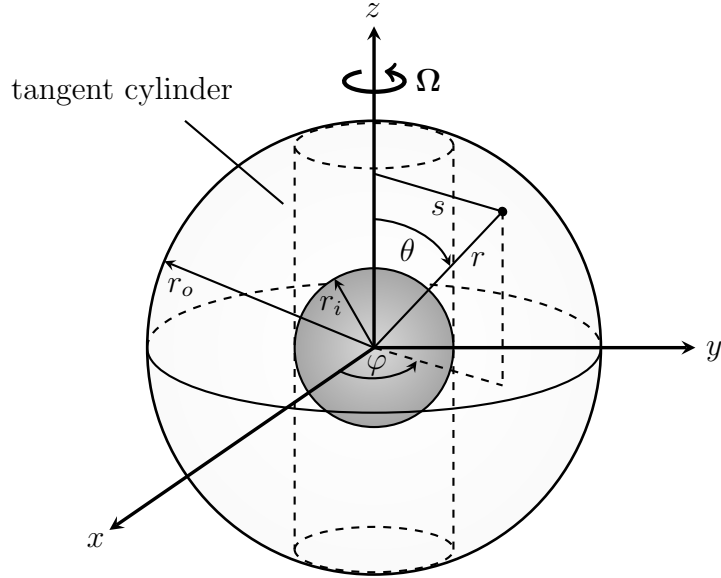


Figure 2.1: Sketch of the model geometry. The spherical shell, which is bounded by spheres with radii r_i and r_o , is rotating with the angular frequency Ω about the z -axis. The dashed cylinder aligned with the rotation axis illustrates the inner core tangent cylinder. The cartesian, cylindrical and spherical coordinate systems are given by (x, y, z) , (s, φ, z) and (r, θ, φ) .

2.6 Boundary conditions

In numerical geodynamo simulations, convection in the Earth’s outer core is modeled by considering a fluid domain that is bounded by two spheres with radii r_i and r_o , corresponding to the ICB and the CMB respectively. A radius ratio $r_i/r_o = 0.35$ as for the present-day Earth is adopted. This model geometry is illustrated in Fig. 2.1.

The set of boundary conditions assumed in this thesis is mainly chosen for comparison purpose with the largest possible number of published dynamo models, which typically rely on the simplest possible option, and not necessarily motivated by geophysical relevance. The most frequently used boundary condition for the velocity field is the constraint that \mathbf{u} vanishes entirely at r_i and r_o within the rotating reference frame, i.e.

$$\mathbf{u} = 0 \quad \text{at } r \in \{r_i, r_o\}, \quad (2.6.1)$$

which implies that the bounding spheres are rigid, impenetrable and co-rotating. This type of boundary condition is referred to as no-slip or rigid. This in fact represents a reasonable assumption for the Earth’s outer core, although it should be noted that there is no theoretical argument for the inner core and the mantle to be co-rotating.

Unlike the velocity field, the magnetic field is not confined to the fluid shell. Here, we assume that both the inner core and the mantle are electrically insulating, a condition that is obviously not realistic, since the inner core is made of solid metal. Nevertheless,

this assumption is widely used in geodynamo models for the sake of simplicity. As a consequence, no electric currents can flow outside the fluid shell and Ampère’s law (Eq. 2.1.33) reduces to

$$\nabla \times \mathbf{B} = 0 \quad \text{at } 0 \leq r \leq r_i \text{ and } r_o \leq r \leq \infty \quad (2.6.2)$$

In these insulating regions, the magnetic field can therefore be expressed as the gradient of a scalar potential Φ , i.e.

$$\mathbf{B} = -\nabla\Phi, \quad (2.6.3)$$

such that the solenoidal condition of \mathbf{B} yields

$$\nabla^2\Phi = 0. \quad (2.6.4)$$

The magnetic field inside the fluid shell matches the potential fields in the inner core and the mantle continuously.

Finally, for the thermal boundary condition, we assume that convection is driven by a fixed temperature difference $\Delta T = T_o - T_i$ between the two bounding spheres. The temperature of the inner boundary T_i is thereby considered to be larger than the temperature of the outer boundary T_o . In this scenario, there are no internal heat sources, which means that the heating term \mathcal{H} in the heat transport equation (Eq. 2.4.6) vanishes. This condition is a crude approximation of the thermodynamics in the Earth’s outer core. There, convective motions are driven by a combination of thermal and compositional buoyancy forces, with the latter likely being more relevant. Thermal convection is the result of the release of latent heat due to the crystallisation of liquid metal at the ICB and the secular cooling of the inner and outer cores. Internal heating due to radioactive decay could potentially be another heat source. However, it is typically ignored since its relevance in the Earth’s core is unknown. The amount of heat lost from the outer core is controlled by mantle convection. Compositional convection, on the other hand, is driven by the release of light elements during the solidification of the outer core. In principle, the nature of the thermal boundary conditions is not expected to play a critical role as the simulations approach the physical regime of the Earth’s core (Aubert et al., 2017).

Chapter 3

Theoretical scaling laws for the flow length scale

In this chapter, we introduce several theoretical scalings of relevant length scales that have been suggested for dynamos and non-magnetic rotating convection based on different assumptions regarding the governing force balance. The starting point for these scalings is the Navier-Stokes equation for thermally-driven Boussinesq convection in a rotating reference frame:

$$\underbrace{\rho \left(\frac{\partial \mathbf{u}}{\partial t} + \mathbf{u} \cdot \nabla \mathbf{u} \right)}_{\text{Inertia}} + \underbrace{2\rho \boldsymbol{\Omega} \times \mathbf{u}}_{\text{Coriolis}} = \underbrace{-\nabla p}_{\text{Pressure}} + \underbrace{\rho \alpha T \mathbf{g}}_{\text{Buoyancy}} + \underbrace{\mathbf{j} \times \mathbf{B}}_{\text{Lorentz}} + \underbrace{\rho \nu \nabla^2 \mathbf{u}}_{\text{Viscosity}}, \quad (3.0.1)$$

where \mathbf{u} is the velocity field, $\boldsymbol{\Omega}$ the rotation vector, p the pressure, T the temperature, \mathbf{g} the gravitational acceleration, \mathbf{B} the magnetic field and $\mathbf{j} = 1/\mu \nabla \times \mathbf{B}$ the electric current density. The labels denote the corresponding forces.

3.1 Leading-order geostrophy

Since the Earth's core is rapidly rotating, the leading-order force balance is often assumed to be geostrophic (e.g. [Busse, 1970](#); [Calkins, 2018](#)), that is a balance between the Coriolis force and the pressure gradient:

$$2\rho \boldsymbol{\Omega} \times \mathbf{u} = -\nabla p. \quad (3.1.1)$$

Taking the curl yields

$$\frac{\partial \mathbf{u}}{\partial z} = 0, \quad (3.1.2)$$

which is known as the Proudman-Taylor theorem. It constrains the fluid flow to the two dimensions perpendicular to the rotation axis. The only truly geostrophic flows in spherical

shells are however axisymmetric, and as such cannot drive the geodynamo according to Elsasser's anti-dynamo theorem (Elsasser, 1946). Therefore, poloidal flow, which can only arise from deviations to geostrophy, is required in the Earth's core. This non-geostrophic (ageostrophic) flow can be obtained from (3.0.1) by taking its curl to remove the pressure gradient, which yields the vorticity equation

$$\frac{\partial \boldsymbol{\omega}}{\partial t} + \mathbf{u} \cdot \nabla \boldsymbol{\omega} - \boldsymbol{\omega} \cdot \nabla \mathbf{u} + 2\Omega \frac{\partial \mathbf{u}}{\partial z} = \nabla \times (\alpha T \mathbf{g}) + \frac{1}{\rho} \nabla \times (\mathbf{j} \times \mathbf{B}) + \nu \nabla^2 \boldsymbol{\omega}, \quad (3.1.3)$$

where $\boldsymbol{\omega} = \nabla \times \mathbf{u}$ is the vorticity.

Based on the assumption of triple force balances in (3.1.3), three different scalings for the convective flow length scale have been suggested. All three triple balances have in common the thermal wind balance, that is the balance between ageostrophic Coriolis and buoyancy terms, termed AC in the following. It is supplemented by a third force term that is hypothesised to be responsible for breaking the Proudman-Taylor constraint. This third force could be viscosity, inertia or the Lorentz force forming the respective VAC, CIA and MAC force balance. By virtue of the small Ekman and Rossby numbers in the Earth's core, the Lorentz force is considered to be the geophysically most relevant candidate. Nevertheless, we will outline all three scalings below. Since the parameters in geodynamo simulations are far from Earth's conditions, the dynamics might be controlled by inertia or viscosity in numerical models. In addition, for the purpose of comparison our study includes a series of non-magnetic rotating convection simulations, for which obviously only scalings that do not involve the Lorentz force are relevant.

3.1.1 VAC balance

Assuming a balance between viscous, buoyancy and Coriolis terms, which is sometimes referred to as the VAC balance (VAC for Viscous-Archimedean-Coriolis), in (3.1.3) and using \mathcal{L}_\perp and \mathcal{L}_\parallel to describe the integral length scales perpendicular and parallel to the rotation axis, respectively, yields the following order of magnitude estimates

$$\frac{\nu \omega}{\mathcal{L}_\perp^2} \sim \frac{\alpha T' g_o}{\mathcal{L}_\perp} \sim \frac{\Omega U}{\mathcal{L}_\parallel}. \quad (3.1.4)$$

The zeroth-order geostrophic balance leads to convection predominantly occurring in columnar vortices aligned with the rotation axis. Therefore, it can be assumed that $\mathcal{L}_\parallel \sim L$. Combining this with the assumption $\omega \sim U/\mathcal{L}_\perp$, the balance between Coriolis and viscous terms yields

$$\frac{\mathcal{L}_\perp}{L} \sim \left(\frac{\nu}{\Omega L^2} \right)^{1/3} = E^{1/3}, \quad (3.1.5)$$

which corresponds to the flow length scale at the onset of convection (e.g. Busse, 1970; King and Buffett, 2013).

3.1.2 CIA balance

The combination of large Reynolds ($Re = UL/\nu \sim \mathcal{O}(10^9)$) and low Rossby numbers in the Earth's core has resulted in some studies considering a turbulent quasi-geostrophic balance between Coriolis, inertia and buoyancy terms in (3.1.3). The acronym CIA (CIA for Coriolis-Inertia-Archimedean) is commonly used to refer to this type of balance. The amplitudes of the individual terms are given by

$$\frac{\Omega U}{\mathcal{L}_{\parallel}} \sim \frac{U\omega}{\mathcal{L}_{\perp}} \sim \frac{\alpha T' g_o}{\mathcal{L}_{\perp}}. \quad (3.1.6)$$

Combining the assumption $\mathcal{L}_{\parallel} \sim L$ with the balance between curled Coriolis and inertial forces leads to

$$\frac{\mathcal{L}_{\perp}}{L} \sim \frac{\omega}{\Omega}. \quad (3.1.7)$$

Assuming again $\omega \sim U/\mathcal{L}_{\perp}$ yields the following prediction for the integral flow length scale \mathcal{L}_{\perp}

$$\frac{\mathcal{L}_{\perp}}{L} \sim \left(\frac{U}{\Omega L} \right)^{1/2} \sim Ro^{1/2}, \quad (3.1.8)$$

which is commonly referred to as the Rhines scaling (e.g. Rhines, 1975; Cardin and Olson, 1994; Aubert et al., 2001; Cabanes et al., 2017; Guervilly et al., 2019).

3.1.3 MAC balance

The last option consists of assuming a triple balance between Lorentz, buoyancy and Coriolis terms in (3.1.3), the so-called MAC balance (MAC for Magneto-Archimedean-Coriolis) (e.g. Starchenko and Jones, 2002; Davidson, 2013; Calkins, 2018). In addition to the aforementioned integral length scales \mathcal{L}_{\parallel} and \mathcal{L}_{\perp} , the MAC balance theory put forward by Davidson (2013) (see also Wicht and Sanchez (2019) for a detailed derivation) introduces the magnetic dissipation length scale

$$\mathcal{L}_{\text{ohm}} = \sqrt{\frac{\int_V \mathbf{B}^2 dV}{\int_V (\nabla \times \mathbf{B})^2 dV}}, \quad (3.1.9)$$

where V is the outer core volume. Ohmic dissipation is expected to carry most of the energy loss in the limit of magnetic energy much larger than kinetic energy ($E_{\text{mag}} \gg E_{\text{kin}}$) and small magnetic Prandtl number ($Pm = \nu/\lambda \ll 1$). Both requirements are fulfilled in the Earth's core.

Assuming the ageostrophic flow dynamics described by (3.1.3) to be controlled by a MAC balance, and using $\mathbf{j} \times \mathbf{B} \sim B^2/\mu\mathcal{L}_{\perp}$, yields the following order of magnitude estimates

$$\frac{B^2}{\rho\mu\mathcal{L}_{\perp}^2} \sim \frac{\alpha T' g_o}{\mathcal{L}_{\perp}} \sim \frac{\Omega U}{\mathcal{L}_{\parallel}}. \quad (3.1.10)$$

Combining the balance between the Lorentz and buoyancy terms with the estimate for the input power per unit mass

$$\mathcal{P} = \frac{\alpha g_o}{V r_o} \int_V r u_r T dV \sim \alpha g_o U T', \quad (3.1.11)$$

yields the following relation for the magnetic energy density

$$\frac{B^2}{\rho\mu} \sim \frac{\mathcal{P}\mathcal{L}_\perp}{U}. \quad (3.1.12)$$

In the Earth's core, the energy input is expected to be almost entirely balanced by ohmic dissipation

$$\mathcal{D}_{\text{ohm}} = \frac{1}{\rho V} \int_V \frac{\lambda}{\mu} (\nabla \times \mathbf{B})^2 dV. \quad (3.1.13)$$

However, in numerical dynamos this may not necessarily be the case due to viscosity still being sizeable. To account for remaining viscous effects, the factor f_{ohm} , which quantifies the relative fraction of heat dissipated via Ohmic losses, is introduced. As a result, the total energy loss per unit mass can be expressed by

$$\mathcal{D} = \frac{1}{f_{\text{ohm}}} \mathcal{D}_{\text{ohm}} \sim \frac{1}{f_{\text{ohm}}} \frac{\lambda B^2}{\mu \rho \mathcal{L}_{\text{ohm}}^2}. \quad (3.1.14)$$

Hence, considering that for a saturated dynamo the energy input should be balanced by dissipation, $\mathcal{P} \sim \mathcal{D}$, yields

$$\frac{B^2}{\rho\mu} \sim \frac{\mathcal{L}_{\text{ohm}}^2}{\lambda} f_{\text{ohm}} \mathcal{P}. \quad (3.1.15)$$

By combining equations (3.1.12) and (3.1.15), we therefore obtain

$$f_{\text{ohm}} \frac{U}{\mathcal{L}_\perp} \sim \frac{\lambda}{\mathcal{L}_{\text{ohm}}^2}. \quad (3.1.16)$$

In the above expression, U/\mathcal{L}_\perp denotes the typical large-scale vorticity related to the convective columns, while $\lambda/\mathcal{L}_{\text{ohm}}^2$ can be interpreted as a characteristic small-scale vorticity (see Davidson, 2013). Thus, when $f_{\text{ohm}} = 1$, Eq. (3.1.16) indicates that large- and small-scale vorticities are proportional to each other. This proportionality is an inherent feature of quasi-2D turbulence such as rapidly-rotating convection (e.g. Davidson, 2004). The non-dimensional form of Eq. (3.1.16) provides a way to estimate the integral length scale \mathcal{L}_\perp

$$\frac{\mathcal{L}_\perp}{L} \sim f_{\text{ohm}} \left(\frac{\mathcal{L}_{\text{ohm}}}{L} \right)^2 Rm, \quad (3.1.17)$$

where $Rm = UL/\lambda$ is the magnetic Reynolds number. Making the additional assumption that large- and small-scale vorticities are independent of the rotation rate implies that the

magnetic energy density itself is also independent of Ω . Based on a dimensional analysis, [Davidson \(2013\)](#) argues that $B^2/\rho\mu$ can hence be expressed as a function of the power per mass generated by buoyancy forces and the flow length scale alone, which yields

$$\frac{B^2}{\rho\mu} \sim \mathcal{L}_{\parallel}^{2/3} (f_{\text{ohm}}\mathcal{P})^{2/3}. \quad (3.1.18)$$

The balance between the buoyancy and Coriolis terms in (3.1.10) together with Eq. (3.1.11) results in the following relation

$$\frac{\mathcal{L}_{\perp}}{\mathcal{L}_{\parallel}} \sim \frac{\mathcal{P}}{\Omega U^2}. \quad (3.1.19)$$

Combining Eqs. (3.1.12), (3.1.18) and (3.1.19), and assuming $\mathcal{L}_{\parallel} \sim L$, leads to the following scaling for the flow length scale

$$\frac{\mathcal{L}_{\perp}}{L} \sim f_{\text{ohm}}^{1/2} Ro^{1/4}. \quad (3.1.20)$$

Therefore, we finally end up with an expression that only depends on a system-scale dimensionless number.

3.2 Leading-order magnetostrophy

As an alternative to a prevalent geostrophic balance, it has been suggested that the flow dynamics in the Earth's core could be in a magnetostrophic regime (e.g. [Roberts, 1978](#); [Hollerbach, 1996](#)). This would imply that the leading-order force balance consists of Coriolis, pressure and Lorentz forces

$$2\rho\boldsymbol{\Omega} \times \mathbf{u} = -\nabla p + \mathbf{j} \times \mathbf{B}. \quad (3.2.1)$$

In this scenario, the Lorentz force is expected to be strong enough to relax the rotational constraint imposed by the Coriolis force. It has been commonly assumed that the convective length scale can then reach the system scale

$$\mathcal{L}_{\parallel} \sim \mathcal{L}_{\perp} \sim L. \quad (3.2.2)$$

So far, system-scale magnetostrophy has not been attained in numerical geodynamo simulations, although it has been approached in some models with strong magnetic control (e.g. [Dormy, 2016](#); [Raynaud et al., 2020](#)). Numerical dynamos in the currently accessible parameter space, however, frequently exhibit a magnetostrophic balance at smaller length scales (e.g. [Aurnou and King, 2017](#); [Aubert, 2019](#)).

The assessment of whether a dynamo is in a magnetostrophic balance is generally based on the evaluation of the Elsasser number Λ , which is a measure of the relative strengths of the Lorentz and Coriolis forces:

$$\Lambda = \frac{|\mathbf{F}_{\text{Lorentz}}|}{|\mathbf{F}_{\text{Coriolis}}|} = \frac{|\mathbf{j} \times \mathbf{B}|}{|2\rho\boldsymbol{\Omega} \times \mathbf{u}|} \sim \frac{JB}{\rho\Omega U}. \quad (3.2.3)$$

Using Ohm's law to scale the current density as $J \sim \sigma UB$, where $\sigma = 1/(\mu\lambda)$, results in the traditional form of the Elsasser number

$$\Lambda_t = \frac{B^2}{\rho\mu\lambda\Omega} \quad (3.2.4)$$

This definition allows one to obtain estimates of the force ratio for planetary dynamos based on magnetic field observations, yielding $\Lambda_t \sim \mathcal{O}(10)$ for the Earth. This has been used to argue for a dominant role of Lorentz forces, and therefore the geodynamo being in the magnetostrophic regime. [Soderlund et al. \(2012\)](#) note that this might not be the correct interpretation of Λ_t since the estimate $J \sim \sigma UB$ is only expected to hold when $Rm \ll 1$. This is, however, not the case for global-scale dynamics in the Earth's core for which $Rm \sim \mathcal{O}(10^3)$. Hence, Λ_t is only relevant on small length scales where $Rm \ll 1$ and is likely not an appropriate measure to assess global-scale magnetostrophy. [Soderlund et al. \(2012, 2015\)](#) suggested that a more meaningful estimate of the relative strengths of Lorentz and Coriolis forces in the Earth's core can be obtained by scaling the electric current density using Ampère's law under the magneto-hydrodynamic approximation

$$\mathbf{J} = \frac{\nabla \times \mathbf{B}}{\mu} \sim \frac{B}{\mu\mathcal{L}_B}, \quad (3.2.5)$$

where \mathcal{L}_B is the length scale of magnetic field structures. Inserting this into (3.2.3) results in the dynamic Elsasser number (e.g. [Christensen et al., 1999](#); [Cardin et al., 2002](#); [Soderlund et al., 2012](#))

$$\Lambda_d = \frac{B^2}{\rho\mu\Omega U \mathcal{L}_B} \sim \frac{\Lambda_t}{Rm} \frac{L}{\mathcal{L}_B}. \quad (3.2.6)$$

The dependence of Λ_d on \mathcal{L}_B^{-1} implies that the relative strength of the Lorentz force increases with decreasing length scale. Building on these developments, [Aurnou and King \(2017\)](#) attempted to estimate the flow scale at which the zeroth-order force balance changes from geostrophy to magnetostrophy, that is the flow scale at which $\Lambda_d = 1$. To this end, they assumed quasi-steady induction ($\partial\mathbf{B}/\partial t = 0$) which results in the following balance:

$$\frac{BU}{\mathcal{L}_U} \sim \frac{\lambda B}{\mathcal{L}_B^2}, \quad (3.2.7)$$

where \mathcal{L}_U is the length scale of the flow. This yields the following relation for the magnetic length scale:

$$\frac{\mathcal{L}_B}{L} \sim \left(\frac{\mathcal{L}_U}{RmL} \right)^{1/2}. \quad (3.2.8)$$

Replacing \mathcal{L}_B/L in (3.2.6) with relation (3.2.8) results in

$$\Lambda_d \sim \left(\frac{\Lambda_t^2}{Rm} \frac{L}{\mathcal{L}_U} \right)^{1/2}. \quad (3.2.9)$$

3. THEORETICAL SCALING LAWS FOR THE FLOW LENGTH SCALE

Based on this expression [Aurnou and King \(2017\)](#) interpret Λ_t^2/Rm as a dimensionless length scale

$$\frac{\mathcal{L}_X}{L} = \frac{\Lambda_t^2}{Rm}. \quad (3.2.10)$$

The dynamic Elsasser number can therefore be rewritten as

$$\Lambda_d \sim \left(\frac{\mathcal{L}_X}{\mathcal{L}_U} \right)^{1/2}, \quad (3.2.11)$$

indicating that the flow is in geostrophic balance on length scales larger than \mathcal{L}_X due to the Lorentz force being subdominant to the Coriolis force ($\Lambda_d < 1$). On scales smaller than \mathcal{L}_X , the Lorentz force is expected to be dominant ($\Lambda_d > 1$), suggesting that the flow is in magnetostrophic balance. Hence, [Aurnou and King \(2017\)](#) refer to \mathcal{L}_X as the magnetostrophic cross-over length scale.

Chapter 4

Numerical methods

This chapter outlines the numerical methods that were used to solve the geodynamo equations described in Chapter 2. More detailed descriptions can be found in [Glatzmaier \(1984\)](#), [Glatzmaier \(2013\)](#), [Christensen and Wicht \(2015\)](#) and in the documentation of the open-source numerical code MagIC ([Wicht, 2002](#); [Gastine et al., 2016](#), freely available at <https://github.com/magic-sph/magic>), which has been used to simulate all considered models.

In MagIC, the MHD equations are solved by employing a pseudo-spectral method, in which spherical harmonic functions are used to expand the unknowns in the angular directions. The radial dependencies can either be represented using a Chebyshev collocation method or a finite difference scheme. The Coriolis force and the non-linear terms are computed in physical space, since this reduces computational costs. Hence, this approach is termed pseudo-spectral. For the spherical harmonic transforms between grid and spectral space, MagIC resorts to the open-source library SHTns ([Schaeffer, 2013](#), freely available at <https://bitbucket.org/nschaeff/shtns>).

4.1 Poloidal-toroidal decomposition

For solenoidal vector fields, it is convenient to apply the poloidal-toroidal decomposition ([Chandrasekhar, 1961](#)) since it reduces three unknown vector components to two unknown scalar fields. It states that any vector \mathbf{v} that fulfills $\nabla \cdot \mathbf{v} = 0$ can be represented as the sum of a poloidal and a toroidal field. This decomposition is given by

$$\mathbf{v} = \underbrace{\nabla \times \nabla \times (\mathbf{e}_r V_p)}_{\text{poloidal field}} + \underbrace{\nabla \times (\mathbf{e}_r V_t)}_{\text{toroidal field}}, \quad (4.1.1)$$

where \mathbf{e}_r represents the radial unit vector. The poloidal and toroidal scalar potentials V_p and V_t are unique, with the exception that they can be multiplied by a purely radial function $f(r)$ without resulting in a change of \mathbf{v} due to a gauge freedom on the radial dependence.

In spherical polar coordinates, the poloidal-toroidal decomposition of the vector \mathbf{v} can be written as

$$v_r = -\nabla_H^2 V_p, \quad (4.1.2)$$

$$v_\theta = \frac{1}{r} \frac{\partial^2 V_p}{\partial r \partial \theta} + \frac{1}{r \sin \theta} \frac{\partial V_t}{\partial \varphi}, \quad (4.1.3)$$

$$v_\varphi = \frac{1}{r \sin \theta} \frac{\partial^2 V_p}{\partial r \partial \varphi} - \frac{1}{r} \frac{\partial V_t}{\partial \theta}, \quad (4.1.4)$$

where ∇_H^2 represents the horizontal part of the Laplace operator:

$$\nabla_H^2 = \frac{1}{r^2 \sin \theta} \frac{\partial}{\partial \theta} \left(\sin \theta \frac{\partial}{\partial \theta} \right) + \frac{1}{r^2 \sin^2 \theta} \frac{\partial^2}{\partial \varphi^2}. \quad (4.1.5)$$

The curl of \mathbf{v} is then given by

$$(\nabla \times \mathbf{v})_r = -\nabla_H^2 V_t \quad (4.1.6)$$

$$(\nabla \times \mathbf{v})_\theta = -\frac{1}{r \sin \theta} \frac{\partial}{\partial \varphi} \left(\frac{\partial^2}{\partial r^2} + \nabla_H^2 \right) V_p + \frac{1}{r} \left(\frac{\partial^2 V_t}{\partial r \partial \theta} \right) \quad (4.1.7)$$

$$(\nabla \times \mathbf{v})_\varphi = \frac{1}{r} \frac{\partial}{\partial \theta} \left(\frac{\partial^2}{\partial r^2} + \nabla_H^2 \right) V_p + \frac{1}{r \sin \theta} \frac{\partial^2 V_t}{\partial r \partial \varphi}. \quad (4.1.8)$$

The poloidal and toroidal scalar potentials are related to the radial components of \mathbf{v} and $\nabla \times \mathbf{v}$, respectively:

$$\mathbf{e}_r \cdot \mathbf{v} = -\nabla_H^2 V_p, \quad (4.1.9)$$

$$\mathbf{e}_r \cdot (\nabla \times \mathbf{v}) = -\nabla_H^2 V_t. \quad (4.1.10)$$

Under the Boussinesq approximation, Eq. (4.1.1) can be applied to the velocity and magnetic fields, i.e.

$$\mathbf{u} = \nabla \times \nabla \times (\mathbf{e}_r W) + \nabla \times (\mathbf{e}_r Z), \quad (4.1.11)$$

$$\mathbf{B} = \nabla \times \nabla \times (\mathbf{e}_r G) + \nabla \times (\mathbf{e}_r H). \quad (4.1.12)$$

Hence, instead of six vector field components now only four scalar potentials have to be solved for. In the next section, we will derive the temporal evolution equations for the poloidal and toroidal scalar potentials for the velocity (W, Z) and the magnetic field (G, H), the non-hydrostatic pressure p and the temperature perturbation T .

4.2 Evolution equations of scalar fields

Before deriving the evolution equations, we recall the dimensionless MHD equations describing Boussinesq convection in a rotating spherical shell in the presence of a magnetic

field, which were derived in Chapter 2. This set of equations is given by

$$\frac{\partial \mathbf{u}}{\partial t} + \mathbf{u} \cdot \nabla \mathbf{u} = -\nabla p - \frac{2}{E} \mathbf{e}_z \times \mathbf{u} + \frac{Ra}{Pr r_o} T + \frac{1}{EPm} (\nabla \times \mathbf{B}) \times \mathbf{B} + \nabla^2 \mathbf{u}, \quad (4.2.1)$$

$$\frac{\partial T}{\partial t} + \mathbf{u} \cdot \nabla T = \frac{1}{Pr} \nabla^2 T, \quad (4.2.2)$$

$$\frac{\partial \mathbf{B}}{\partial t} = \nabla \times (\mathbf{u} \times \mathbf{B}) + \frac{1}{Pm} \nabla^2 \mathbf{B}, \quad (4.2.3)$$

$$\nabla \cdot \mathbf{B} = 0, \quad (4.2.4)$$

$$\nabla \cdot \mathbf{u} = 0. \quad (4.2.5)$$

For simplicity, we removed all superscripts indicating dimensionless quantities.

4.2.1 Poloidal and toroidal flow potentials

We will start by deriving the temporal evolution equation of the poloidal flow potential $W(r, \theta, \varphi, t)$. To this end, it is convenient to group the non-linear terms and the Coriolis force in Eq. (4.2.1) into one force term

$$\mathbf{F} = -\frac{2}{E} \mathbf{e}_z \times \mathbf{u} - \mathbf{u} \cdot \nabla \mathbf{u} + \frac{1}{EPm} (\nabla \times \mathbf{B}) \times \mathbf{B}. \quad (4.2.6)$$

These forces are calculated in physical space in contrast to the remaining terms. For the following developments we will therefore take them as given. The Navier-Stokes equation then reads

$$\frac{\partial \mathbf{u}}{\partial t} + \nabla p - \frac{Ra}{Pr r_o} T - \nabla^2 \mathbf{u} = \mathbf{F}. \quad (4.2.7)$$

The evolution equation of the poloidal flow potential $W(r, \theta, \varphi, t)$ can be obtained by taking the radial component of the above equation. Using relation (4.1.9), this yields for the time derivative

$$\mathbf{e}_r \cdot \frac{\partial \mathbf{u}}{\partial t} = \frac{\partial}{\partial t} (\mathbf{e}_r \cdot \mathbf{u}) = -\nabla_H^2 \frac{\partial W}{\partial t}, \quad (4.2.8)$$

and for the viscosity term (see Appendix A for the derivation)

$$\mathbf{e}_r \cdot \nabla^2 \mathbf{u} = -\nabla_H^2 \left(\frac{\partial^2 W}{\partial r^2} + \nabla_H^2 W \right). \quad (4.2.9)$$

The dot product of Eq. (4.2.7) with \mathbf{e}_r therefore gives

$$-\nabla_H^2 \frac{\partial W}{\partial t} + \frac{\partial p}{\partial r} - \frac{Ra}{Pr r_o} T + \nabla_H^2 \frac{\partial^2 W}{\partial r^2} + \nabla_H^2 \nabla_H^2 W = \mathbf{e}_r \cdot \mathbf{F}. \quad (4.2.10)$$

The temporal evolution equation for the toroidal flow potential $Z(r, \theta, \varphi, t)$ can be derived by curling the Navier-Stokes equation and subsequently taking the scalar product with \mathbf{e}_r . Applying the curl operator to Eq. (4.2.7) leads to

$$\frac{\partial}{\partial t} (\nabla \times \mathbf{u}) - \frac{Ra}{Pr} \nabla \times \left(\frac{\mathbf{r}}{r_o} T \right) - \nabla^2 (\nabla \times \mathbf{u}) = \nabla \times \mathbf{F}. \quad (4.2.11)$$

When taking the scalar product of both sides of the above expression with \mathbf{e}_r , the buoyancy term vanishes. Applying relation (4.1.10), yields for the time derivative term

$$\mathbf{e}_r \cdot \frac{\partial}{\partial t} (\nabla \times \mathbf{u}) = \frac{\partial}{\partial t} (\mathbf{e}_r \cdot \nabla \times \mathbf{u}) = -\nabla_H^2 \frac{\partial Z}{\partial t}, \quad (4.2.12)$$

and for the viscous term

$$\mathbf{e}_r \cdot \nabla \times (\nabla^2 \mathbf{u}) = -\nabla_H^2 \left(\frac{\partial^2 Z}{\partial r^2} + \nabla_H^2 Z \right). \quad (4.2.13)$$

The evolution equation of the toroidal flow potential is therefore given by

$$-\nabla_H^2 \frac{\partial Z}{\partial t} + \nabla_H^2 \frac{\partial^2 Z}{\partial r^2} + \nabla_H^2 \nabla_H^2 Z = \mathbf{e}_r \cdot (\nabla \times \mathbf{F}). \quad (4.2.14)$$

4.2.2 Poloidal and toroidal magnetic potentials

The evolution equations for the poloidal and toroidal magnetic potentials $G(r, \theta, \varphi, t)$ and $H(r, \theta, \varphi, t)$ can be obtained by applying the same procedure to the magnetic induction equation (Eq. 4.2.3). The non-linear induction term is not expressed in terms of potential functions. Therefore, we simply denote it by

$$\mathbf{D} = \nabla \times (\mathbf{u} \times \mathbf{B}), \quad (4.2.15)$$

and rewrite Eq. (4.2.3) as

$$\frac{\partial \mathbf{B}}{\partial t} - \frac{1}{Pm} \nabla^2 \mathbf{B} = \mathbf{D}. \quad (4.2.16)$$

Taking the dot product of this equation with \mathbf{e}_r and applying relations (4.2.8) and (4.2.9) to the magnetic field yields the following temporal evolution for the poloidal magnetic potential

$$-\nabla_H^2 \frac{\partial G}{\partial t} + \frac{1}{Pm} \left(\nabla_H^2 \frac{\partial^2 G}{\partial r^2} + \nabla_H^2 \nabla_H^2 G \right) = \mathbf{e}_r \cdot \mathbf{D}, \quad (4.2.17)$$

while applying the operator $\mathbf{e}_r \cdot (\nabla \times)$ and using relations (4.2.12) and (4.2.13) gives for the toroidal magnetic potential

$$-\nabla_H^2 \frac{\partial H}{\partial t} + \frac{1}{Pm} \left(\nabla_H^2 \frac{\partial^2 H}{\partial r^2} + \nabla_H^2 \nabla_H^2 H \right) = \mathbf{e}_r \cdot (\nabla \times \mathbf{D}). \quad (4.2.18)$$

4.2.3 Temperature perturbation

The temperature equation is already a scalar equation. However, we will see later on that it is convenient to decompose the total Laplacian of T into its radial and horizontal components

$$\nabla^2 T = \frac{1}{r^2} \frac{\partial}{\partial r} \left(r^2 \frac{\partial T}{\partial r} \right) + \nabla_H^2 T = \frac{\partial^2 T}{\partial r^2} + \frac{2}{r} \frac{\partial T}{\partial r} + \nabla_H^2 T. \quad (4.2.19)$$

After inserting this into (4.2.2), the evolution equation of the temperature perturbation reads

$$\frac{\partial T}{\partial t} - \frac{1}{Pr} \left(\frac{\partial^2 T}{\partial r^2} + \frac{2}{r} \frac{\partial T}{\partial r} + \nabla_H^2 T \right) = -\mathbf{u} \cdot \nabla T. \quad (4.2.20)$$

4.2.4 Pressure

So far we have derived the temporal evolution equations for the flow potentials, the magnetic field potentials and the temperature perturbations. However, the pressure still remains an unknown. There are two different approaches to resolve this problem. One option is to apply the operator ($\mathbf{e}_r \cdot \nabla \times \nabla \times$) to the Navier-Stokes equation, which yields an evolution equation for the poloidal flow potential without the pressure that can be used to replace Eq. (4.2.10). Alternatively, an additional evolution equation involving the pressure and the poloidal flow potential can be derived by taking the horizontal divergence of the Navier-Stokes equation (Eq. 4.2.7). In MagIC, the former approach is employed when a finite difference method is used for the radial representation, while the latter is used in the case of a Chebyshev collocation method.

We start with deriving an additional evolution equation for the pressure. Applying the horizontal divergence to the Navier-Stokes equation yields

$$\nabla_H \cdot \frac{\partial \mathbf{u}}{\partial t} + \nabla_H \cdot \nabla p - \nabla_H \cdot \nabla^2 \mathbf{u} = \nabla_H \cdot \mathbf{F}, \quad (4.2.21)$$

whereby the buoyancy term vanishes because $\nabla_H \cdot (T\mathbf{r}/r_o) = 0$. The horizontal divergence operator is defined by

$$\nabla_H \cdot \mathbf{v} = \frac{1}{r \sin \theta} \frac{\partial}{\partial \theta} (\sin \theta v_\theta) + \frac{1}{r \sin \theta} \frac{\partial v_\varphi}{\partial \varphi}. \quad (4.2.22)$$

To express the velocity in Eq. (4.2.21) in terms of the poloidal flow potential, it is convenient to write the total divergence of a vector \mathbf{v} as

$$\nabla \cdot \mathbf{v} = \frac{1}{r^2} \frac{\partial}{\partial r} (r^2 v_r) + \nabla_H \cdot \mathbf{v}, \quad (4.2.23)$$

Hence, the time-derivative term can be rewritten as

$$\nabla_H \cdot \frac{\partial \mathbf{u}}{\partial t} = \frac{\partial}{\partial t} (\nabla_H \cdot \mathbf{u}) = \frac{\partial}{\partial t} \left[\nabla \cdot \mathbf{u} - \frac{1}{r^2} \frac{\partial}{\partial r} (r^2 u_r) \right]. \quad (4.2.24)$$

Since in the Boussinesq approximation $\nabla \cdot \mathbf{u} = 0$, this expression can be simplified to

$$\nabla_H \cdot \frac{\partial \mathbf{u}}{\partial t} = -\frac{\partial}{\partial t} \left(\frac{2u_r}{r} + \frac{\partial u_r}{\partial r} \right). \quad (4.2.25)$$

Using relation (4.1.9), the horizontal divergence of the time derivative is then given by

$$\nabla \cdot \frac{\partial \mathbf{u}}{\partial t} = \frac{\partial}{\partial t} \left[\frac{2}{r} \nabla_H^2 W + \frac{\partial}{\partial r} (\nabla_H^2 W) \right] = \nabla_H^2 \frac{\partial}{\partial t} \left(\frac{\partial W}{\partial r} \right). \quad (4.2.26)$$

By taking advantage of the decompositions (4.2.19) and (4.2.23), the pressure gradient term can be rewritten as

$$\nabla_H \cdot \nabla p = \nabla \cdot \nabla p - \frac{1}{r^2} \frac{\partial}{\partial r} \left(r^2 \frac{\partial p}{\partial r} \right) = \nabla_{HP}^2. \quad (4.2.27)$$

The viscous term (see Appendix A) is given by

$$\nabla_H \cdot (\nabla^2 \mathbf{u}) = \nabla_H^2 \left(\frac{\partial^3 W}{\partial r^3} + \nabla_H^2 \frac{\partial W}{\partial r} - \frac{2}{r} \nabla_H^2 W \right). \quad (4.2.28)$$

Equation (4.2.21) can thus be rewritten as

$$\nabla_H^2 \frac{\partial}{\partial t} \left(\frac{\partial W}{\partial r} \right) + \nabla_{HP}^2 - \nabla_H^2 \left(\frac{\partial^3 W}{\partial r^3} + \nabla_H^2 \frac{\partial W}{\partial r} - \frac{2}{r} \nabla_H^2 W \right) = \nabla_H \cdot \mathbf{F}. \quad (4.2.29)$$

Alternatively, the pressure can be eliminated by applying the double-curl operator to Eq. (4.2.7), which yields

$$\nabla \times \nabla \times \frac{\partial \mathbf{u}}{\partial t} + \frac{Ra}{Pr} \nabla \times \nabla \times \left(\frac{\mathbf{r}}{r_o} T \right) - \nabla \times \nabla \times \nabla^2 \mathbf{u} = \nabla \times \nabla \times \mathbf{F}. \quad (4.2.30)$$

The radial component of the above expression can then be used to derive a substitute evolution equation for the poloidal flow potential. For the time derivative this leads to

$$\mathbf{e}_r \cdot \nabla \times \nabla \times \frac{\partial \mathbf{u}}{\partial t} = \frac{\partial}{\partial t} [\mathbf{e}_r \cdot (\nabla (\nabla \cdot \mathbf{u}) - \nabla^2 \mathbf{u})]. \quad (4.2.31)$$

Since $\nabla \cdot \mathbf{u} = 0$, this reduces to

$$\mathbf{e}_r \cdot \nabla \times \nabla \times \frac{\partial \mathbf{u}}{\partial t} = -\frac{\partial}{\partial t} \mathbf{e}_r \cdot (\nabla^2 \mathbf{u}). \quad (4.2.32)$$

Using relation (4.2.9) then yields

$$\mathbf{e}_r \cdot \nabla \times \nabla \times \frac{\partial \mathbf{u}}{\partial t} = \nabla_H^2 \frac{\partial}{\partial t} \left(\frac{\partial^2 W}{\partial r^2} + \nabla_H^2 W \right). \quad (4.2.33)$$

For the buoyancy term, we obtain

$$\begin{aligned}
 \mathbf{e}_r \cdot \frac{Ra}{Pr} \nabla \times \nabla \times \left(\frac{\mathbf{r}}{r_o} T \right) &= \frac{Ra}{Pr} \left[\mathbf{e}_r \cdot \nabla \left(\nabla \cdot \left(\frac{\mathbf{r}}{r_o} T \right) \right) - \mathbf{e}_r \cdot \nabla^2 \left(\frac{\mathbf{r}}{r_o} T \right) \right] \\
 &= \frac{Ra}{Pr} \left[\frac{\partial}{\partial r} \left[\frac{1}{r^2} \frac{\partial}{\partial r} \left(r^2 \left(\frac{r}{r_o} T \right) \right) \right] - \nabla^2 \left(\frac{r}{r_o} T \right) + \frac{2}{r^2} \left(\frac{r}{r_o} T \right) \right] \\
 &= -\frac{Ra}{Pr} \frac{r}{r_o} \nabla_H^2 T
 \end{aligned} \tag{4.2.34}$$

The viscous term (see Appendix A) is given by

$$\mathbf{e}_r \cdot \nabla \times \nabla \times \nabla^2 \mathbf{u} = \nabla_H^2 \left[\frac{\partial^4 W}{\partial r^4} + 2 \nabla_H^2 \frac{\partial^2 W}{\partial r^2} - \frac{4}{r} \nabla_H^2 \frac{\partial W}{\partial r} + \nabla_H^2 \left(\nabla_H^2 + \frac{6}{r^2} \right) W \right]. \tag{4.2.35}$$

Thus, the following evolution equation is obtained for the poloidal flow potential

$$\begin{aligned}
 & - \nabla_H^2 \left[\frac{\partial^4 W}{\partial r^4} + 2 \nabla_H^2 \frac{\partial^2 W}{\partial r^2} - \frac{4}{r} \nabla_H^2 \frac{\partial W}{\partial r} + \nabla_H^2 \left(\nabla_H^2 + \frac{6}{r^2} \right) W \right] + \\
 & + \nabla_H^2 \frac{\partial}{\partial t} \left(\frac{\partial^2 W}{\partial r^2} + \nabla_H^2 W \right) - \frac{Ra}{Pr} \frac{r}{r_o} \nabla_H^2 T = \mathbf{e}_r \cdot \nabla \times \nabla \times \mathbf{F}.
 \end{aligned} \tag{4.2.36}$$

This expression can be used to replace Eqs. (4.2.10) and (4.2.29). In this case, there are only five unknowns that have to be solved for: the flow potentials (W, Z), the magnetic potentials (G, H) and the temperature perturbation T .

4.3 Spherical harmonic expansion

The spherical harmonic functions $Y_{\ell m}$ at colatitude θ and longitude φ are defined by

$$Y_{\ell m}(\theta, \varphi) = P_{\ell m}(\cos \theta) e^{im\varphi}, \tag{4.3.1}$$

where ℓ and m represent the spherical harmonic degree and order. $P_{\ell m}$ denotes the associated Legendre polynomials. The spherical harmonic functions up to degree and order four are illustrated in Fig. (4.1).

Various normalisations can be chosen for $Y_{\ell m}$. In the case of a complete normalisation, Eq. (4.3.1) is replaced by

$$Y_{\ell m}(\theta, \varphi) = \sqrt{\frac{(2\ell+1)(\ell-|m|)!}{4\pi(\ell+|m|)!}} P_{\ell m}(\cos \theta) e^{im\varphi}, \tag{4.3.2}$$

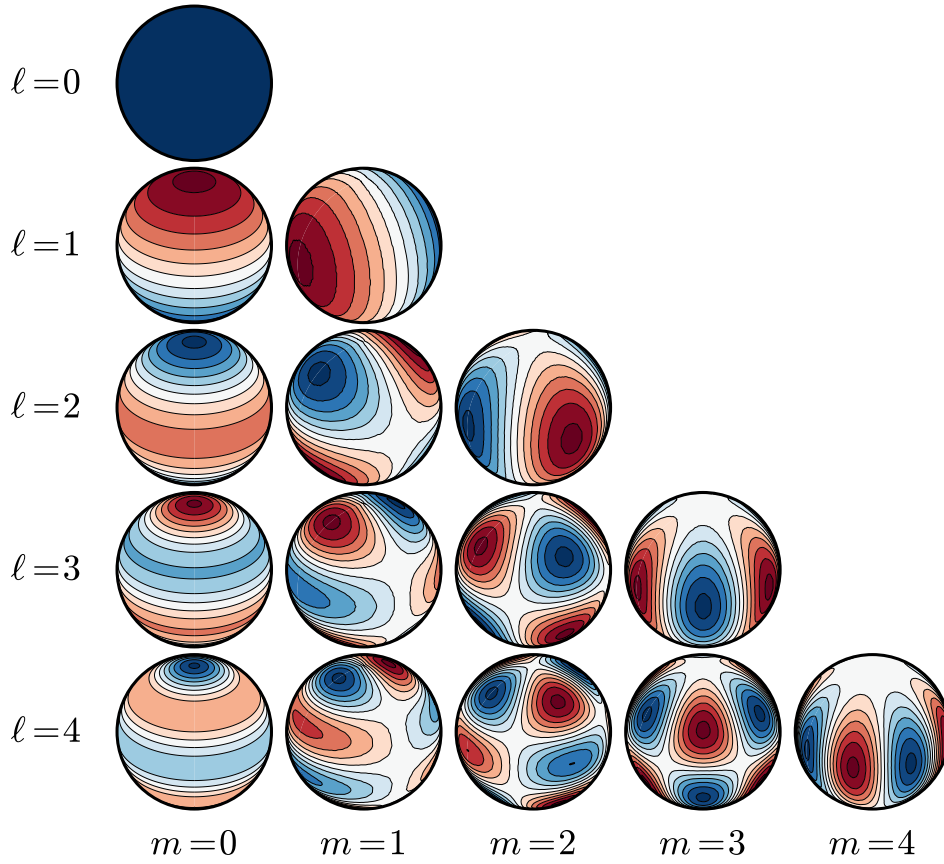


Figure 4.1: Spherical harmonic functions $Y_{\ell m}$ up to degree and order four.

for which the following orthogonality relation holds

$$\int_{\varphi=0}^{2\pi} \int_{\theta=0}^{\pi} Y_{\ell m}(\theta, \varphi) Y_{\ell' m'}^*(\theta, \varphi) \sin \theta \, d\theta d\varphi = \delta_{\ell\ell'} \delta_{mm'}, \quad (4.3.3)$$

where δ_{ij} is the Kronecker delta. The asterisk denotes the complex conjugate.

As an example, the spherical harmonic expansion of the poloidal magnetic field potential G can then be written as

$$G(r, \theta, \varphi, t) \simeq \sum_{\ell=0}^{\ell_{\max}} \sum_{m=-\ell}^{\ell} G_{\ell m}(r, t) Y_{\ell m}(\theta, \varphi), \quad (4.3.4)$$

where ℓ_{\max} denotes the truncation in spherical harmonic degree and order. The spherical harmonic coefficients $G_{\ell m}(r, t)$ of the poloidal magnetic potential are given by

$$G_{\ell m}(r, t) = \frac{1}{\pi} \int_0^{\pi} G_m(r, \theta, t) P_{\ell m}(\cos \theta) \sin \theta \, d\theta, \quad (4.3.5)$$

with

$$G_m(r, \theta, t) = \frac{1}{2\pi} \int_0^{2\pi} G(r, \theta, \varphi, t) e^{-im\varphi} d\varphi. \quad (4.3.6)$$

Only coefficients with $m \geq 0$ have to be dealt with in the above relations, because the potential $G(r, \theta, \varphi, t)$ is a real-valued function for which $G_{\ell m}^*(r, t) = G_{\ell, -m}(r, t)$. Equations (4.3.5) and (4.3.6) correspond to a two-step transform from physical (or grid) space (r, θ, φ) to spectral space (r, ℓ, m) , with the former representing a Legendre transform and the latter a Fourier transform. The inverse transform is defined by Eq. (4.3.4). In practice, these transforms are handled numerically by truncated sums. The Legendre transform (Eq. 4.3.5) is approximated by

$$G_{\ell m}(r, t) \simeq \frac{1}{N_\theta} \sum_{k=0}^{N_\theta-1} w_k G_m(r, \theta_k, t) P_{\ell m}(\cos \theta_k), \quad (4.3.7)$$

where θ_k denotes the Gaussian quadrature points and w_k the respective Gauss-Legendre weights (Abramowitz and Stegun, 1970; Glatzmaier, 2013). The Fourier transform (Eq. 4.3.6) is discretised using

$$G_m(r, \theta_k, t) \simeq \frac{1}{N_\varphi} \sum_{j=0}^{N_\varphi-1} G(r, \theta_k, \varphi_j, t) e^{-im\varphi_j} \quad \text{with } \varphi_j = \frac{2j\pi}{N_\varphi} \quad \forall j \in [0, N_\varphi - 1], \quad (4.3.8)$$

where φ_j are the N_φ evenly-spaced longitudinal points. This allows the use of fast Fourier transforms (FFTs) for the evaluation of (4.3.8). In MagIC, the computation of (4.3.7) and (4.3.8) is handled by the spherical harmonic transform library SHTns (Schaeffer, 2013).

4.4 Spectral evolution equations

The spectral evolution equations can be obtained by expanding the flow potentials (W, Z) , the magnetic potentials (G, H) , the pressure p (if needed) and the temperature perturbation T into spherical harmonics like in Eq. (4.3.4).

$Y_{\ell m}$ form complete and orthogonal eigenfunctions of the horizontal Laplacian, such that

$$\nabla_H^2 Y_{\ell m} = -\frac{\ell(\ell+1)}{r^2} Y_{\ell m} \quad \forall (\ell, m). \quad (4.4.1)$$

Using this expression, we start with the derivation of the spectral evolution equation of the poloidal flow potential W . Expanding all potentials as in Eq. (4.3.4) yields for the terms

on the LHS of Eq. (4.2.10):

$$-\nabla_H^2 \frac{\partial W}{\partial t} = \sum_{\ell=0}^{\ell_{\max}} \sum_{m=0}^{\ell} \frac{\partial W_{\ell m}}{\partial t} \frac{\ell(\ell+1)}{r^2} Y_{\ell m}, \quad (4.4.2)$$

$$\frac{\partial p}{\partial r} = \sum_{\ell=0}^{\ell_{\max}} \sum_{m=0}^{\ell} \frac{\partial p_{\ell m}}{\partial r} Y_{\ell m}, \quad (4.4.3)$$

$$-\frac{Ra}{Pr} \frac{r}{r_o} T = -\frac{Ra}{Pr} \frac{r}{r_o} \sum_{\ell=0}^{\ell_{\max}} \sum_{m=0}^{\ell} T_{\ell m} Y_{\ell m}, \quad (4.4.4)$$

$$\nabla_H^2 \frac{\partial^2 W}{\partial r^2} = -\sum_{\ell=0}^{\ell_{\max}} \sum_{m=0}^{\ell} \frac{\partial^2 W_{\ell m}}{\partial r^2} \frac{\ell(\ell+1)}{r^2} Y_{\ell m}, \quad (4.4.5)$$

$$\nabla_H^2 \Delta_H W = \sum_{\ell=0}^{\ell_{\max}} \sum_{m=0}^{\ell} W_{\ell m} \left[\frac{\ell(\ell+1)}{r^2} \right]^2 Y_{\ell m}. \quad (4.4.6)$$

Inserting these expressions into Eq. (4.2.10), multiplying with the complex conjugate $Y_{\ell m}^*$ and subsequently integrating over spherical surfaces (using relation (4.3.3) for the product $Y_{\ell m} Y_{\ell m}^*$) yields the spectral evolution equation for the poloidal flow potential at the degree ℓ and order m

$$\begin{aligned} \frac{\ell(\ell+1)}{r^2} \left[\frac{\partial}{\partial t} + \frac{\ell(\ell+1)}{r^2} - \frac{\partial^2}{\partial r^2} \right] W_{\ell m} + \frac{\partial p_{\ell m}}{\partial r} - \frac{Ra}{Pr} \frac{r}{r_o} T_{\ell m} = \\ = \int_{\varphi=0}^{2\pi} \int_{\theta=0}^{\pi} \mathbf{e}_r \cdot \mathbf{F} Y_{\ell m}^* \sin \theta \, d\theta d\varphi. \end{aligned} \quad (4.4.7)$$

Applying the same procedure as for the poloidal flow potential W to the evolution equations of the toroidal flow potential Z (Eq. 4.2.14), the magnetic potentials G and H (Eq. 4.2.17 and 4.2.18), the temperature perturbation T (Eq. 4.2.20) and the pressure p (Eq. 4.2.29) yields the spectral equations for the expansion coefficients $Z_{\ell m}$, $G_{\ell m}$, $H_{\ell m}$, $T_{\ell m}$ and $p_{\ell m}$. In case of the use of the double-curl formalism to eliminate the pressure this obviously also applies to the alternative evolution equation for the poloidal flow potential (Eq. 4.2.36). Thus, the spectral equation for the toroidal flow potential reads

$$\frac{\ell(\ell+1)}{r^2} \left[\frac{\partial}{\partial t} + \frac{\ell(\ell+1)}{r^2} - \frac{\partial^2}{\partial r^2} \right] Z_{\ell m} = \int_{\varphi=0}^{2\pi} \int_{\theta=0}^{\pi} \mathbf{e}_r \cdot (\nabla \times \mathbf{F}) Y_{\ell m}^* \sin \theta \, d\theta d\varphi. \quad (4.4.8)$$

Analogously, the spectral evolution equations for the poloidal and toroidal magnetic field coefficients $G_{\ell m}$ and $H_{\ell m}$ are given by

$$\frac{\ell(\ell+1)}{r^2} \left[\frac{\partial}{\partial t} + \frac{1}{Pm} \frac{\ell(\ell+1)}{r^2} + \frac{1}{Pm} \frac{\partial^2}{\partial r^2} \right] G_{\ell m} = \int_{\varphi=0}^{2\pi} \int_{\theta=0}^{\pi} \mathbf{e}_r \cdot \mathbf{D} Y_{\ell m}^* \sin \theta \, d\theta d\varphi \quad (4.4.9)$$

and

$$\frac{\ell(\ell+1)}{r^2} \left[\frac{\partial}{\partial t} + \frac{1}{Pm} \frac{\ell(\ell+1)}{r^2} + \frac{1}{Pm} \frac{\partial^2}{\partial r^2} \right] H_{\ell m} = \int_{\varphi=0}^{2\pi} \int_{\theta=0}^{\pi} \mathbf{e}_r \cdot (\nabla \times \mathbf{D}) Y_{\ell m}^* \sin \theta \, d\theta d\varphi. \quad (4.4.10)$$

For the temporal evolution of the temperature perturbation, we obtain

$$\left[\frac{\partial}{\partial t} + \frac{1}{Pr} \frac{\ell(\ell+1)}{r^2} - \frac{1}{Pr} \left(\frac{2}{r} \frac{\partial}{\partial r} + \frac{\partial^2}{\partial r^2} \right) \right] T_{\ell m} = \int_{\varphi=0}^{2\pi} \int_{\theta=0}^{\pi} \mathbf{u} \cdot \nabla T Y_{\ell m}^* \sin \theta \, d\theta d\varphi. \quad (4.4.11)$$

The spectral equation for the pressure reads

$$\begin{aligned} \frac{\ell(\ell+1)}{r^2} \left[\frac{2\ell(\ell+1)}{r} \frac{\partial}{\partial r} - \left(\frac{\partial}{\partial t} + \frac{\ell(\ell+1)}{r^2} \right) \frac{\partial}{\partial r} + \frac{\partial^3}{\partial r^3} \right] W_{\ell m} \\ - \frac{\ell(\ell+1)}{r^2} p_{\ell m} = \int_{\varphi=0}^{2\pi} \int_{\theta=0}^{\pi} \nabla_H \cdot \mathbf{F} Y_{\ell m}^* \sin \theta \, d\theta d\varphi. \end{aligned} \quad (4.4.12)$$

Finally, the substitute spectral evolution equation of the poloidal flow potential (where pressure has been eliminated) is given by

$$\begin{aligned} \frac{\ell(\ell+1)}{r^2} \left[\frac{\partial^4}{\partial r^4} - \left(2 \frac{\ell(\ell+1)}{r^2} + \frac{\partial}{\partial t} \right) \frac{\partial^2}{\partial r^2} + \frac{4\ell(\ell+1)}{r} \frac{\partial}{\partial r} \right] W_{\ell m} + \\ + \left[\frac{\ell(\ell+1)}{r^2} \right]^2 \left[\frac{\ell(\ell+1)}{r^2} - \frac{6}{r^2} + \frac{\partial}{\partial t} \right] W_{\ell m} + \frac{Ra}{Pr} \frac{r}{r_o} \frac{\ell(\ell+1)}{r^2} T_{\ell m} \\ = \int_{\varphi=0}^{2\pi} \int_{\theta=0}^{\pi} \mathbf{e}_r \cdot (\nabla \times \nabla \times \mathbf{F}) Y_{\ell m}^* \sin \theta \, d\theta d\varphi. \end{aligned} \quad (4.4.13)$$

4.5 Radial representation

At this stage the angular discretisation has been fully specified, and we now turn to the description of the radial discretisation. In MagIC, a finite difference method and a Chebyshev collocation method is supported.

4.5.1 Finite difference method

In case a finite difference method is used to represent the radial dependencies, the set of spectral evolution equations that have to be solved consists of Eqs. (4.4.8-4.4.11) and (4.4.13). The radial derivatives contained in these equations are thereby approximated with finite differences. This method is based on the definition of the derivative of a function f at a point $x \in \mathbb{R}$, which is given by

$$\frac{\partial f}{\partial x} = \lim_{h \rightarrow 0} \frac{f(x+h) - f(x)}{h}. \quad (4.5.1)$$

Hence, for sufficiently small h the finite difference $(f(x+h) - f(x))/h$ can be used to replace the derivative $\partial f/\partial x$.

In MagIC, a centered finite difference scheme is employed on an irregular grid. To this end, the radial domain $r_i < r < r_o$ is discretised into $N + 1$ grid points with a variable sampling step h_i such that $r_i = r_{i-1} + h_i$. This is schematically illustrated in Fig. (4.2). The sampling step h_i is decreased towards the inner and outer boundaries to be able to resolve potential strong gradients due to boundary layers.

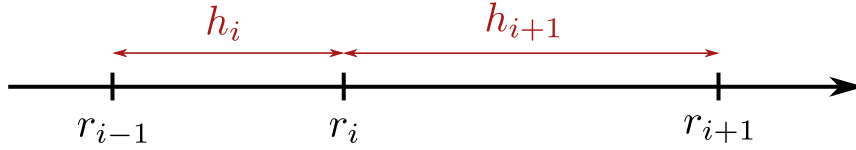


Figure 4.2: Sketch of the discretisation of a 1-D domain with a variable discretisation step.

To derive the expressions for the first and second radial derivatives of a function f , we need to consider the Taylor expansions at the points r_{i-1} and r_{i+1} :

$$f_{i+1} = f_i + h_{i+1} \left. \frac{\partial f}{\partial r} \right|_{r_i} + \frac{h_{i+1}^2}{2} \left. \frac{\partial^2 f}{\partial r^2} \right|_{r_i} + \frac{h_{i+1}^3}{6} \left. \frac{\partial^3 f}{\partial r^3} \right|_{r_i} + \frac{h_{i+1}^4}{24} \left. \frac{\partial^4 f}{\partial r^4} \right|_{r_i} + \mathcal{O}(h_{i+1}^5), \quad (4.5.2)$$

$$f_{i-1} = f_i - h_i \left. \frac{\partial f}{\partial r} \right|_{r_i} + \frac{h_i^2}{2} \left. \frac{\partial^2 f}{\partial r^2} \right|_{r_i} - \frac{h_i^3}{6} \left. \frac{\partial^3 f}{\partial r^3} \right|_{r_i} + \frac{h_i^4}{24} \left. \frac{\partial^4 f}{\partial r^4} \right|_{r_i} + \mathcal{O}(h_i^5), \quad (4.5.3)$$

where we used the notation $f(r_i) = f_i$. Multiplying the first equation by h_i^2 and the second by h_{i+1}^2 , and subsequently subtracting them, results in

$$\begin{aligned} h_i^2 f_{i+1} - h_{i+1}^2 f_{i-1} - h_i^2 f_i + h_{i+1}^2 f_i &= (h_i^2 h_{i+1} + h_{i+1}^2 h_i) \left. \frac{\partial f}{\partial r} \right|_{r_i} + \\ &+ \frac{1}{6} (h_i^2 h_{i+1}^3 + h_{i+1}^2 h_i^3) \left. \frac{\partial^3 f}{\partial r^3} \right|_{r_i} + \dots \end{aligned} \quad (4.5.4)$$

Rearranging this expression then yields for the first derivative

$$\left. \frac{\partial f}{\partial r} \right|_{r_i} = \frac{1}{h_{i+1} + h_i} \left[\frac{h_i}{h_{i+1}} (f_{i+1} - f_i) + \frac{h_{i+1}}{h_i} (f_i - f_{i-1}) \right] - \frac{h_i h_{i+1}}{6} \left. \frac{\partial^3 f}{\partial r^3} \right|_{r_i} + \dots \quad (4.5.5)$$

Since the dominant error term is of order $\mathcal{O}(h_i h_{i+1})$, this can be written as

$$\left. \frac{\partial f}{\partial r} \right|_{r_i} = \frac{1}{h_{i+1} + h_i} \left[\frac{h_i}{h_{i+1}} (f_{i+1} - f_i) + \frac{h_{i+1}}{h_i} (f_i - f_{i-1}) \right] + \mathcal{O}(h_i h_{i+1}), \quad (4.5.6)$$

It should be noted that in the limit $h = h_i = h_{i+1}$ this simplifies to the usual second-order central difference scheme

$$\left. \frac{\partial f}{\partial r} \right|_{r_i} = \frac{f_{i+1} - f_{i-1}}{2h} + \mathcal{O}(h^2). \quad (4.5.7)$$

To obtain the second derivative, we multiply Eq. (4.5.2) by h_i and Eq. (4.5.3) by h_{i+1} , and subsequently sum the two expressions. This yields

$$\begin{aligned} h_i f_{i+1} + h_{i+1} f_{i-1} - (h_{i+1} + h_i) f_i &= \frac{1}{2} (h_i h_{i+1}^2 + h_{i+1} h_i^2) \frac{\partial^2 f}{\partial r^2} \Big|_{r_i} + \\ &+ \frac{1}{6} (h_i h_{i+1}^3 - h_{i+1} h_i^3) \frac{\partial^3 f}{\partial r^3} \Big|_{r_i} + \\ &+ \frac{1}{24} (h_i h_{i+1}^4 + h_{i+1} h_i^4) \frac{\partial^4 f}{\partial r^4} \Big|_{r_i} + \dots \end{aligned} \quad (4.5.8)$$

Rearranging this equation then yields for the second derivative

$$\frac{\partial^2 f}{\partial r^2} = \frac{2}{h_i + h_{i+1}} \left(\frac{f_{i+1} - f_i}{h_{i+1}} - \frac{f_i - f_{i-1}}{h_i} \right) - \underbrace{\frac{1}{3} (h_{i+1} - h_i) \frac{\partial^3 f}{\partial r^3} \Big|_{r_i}}_{*} - \frac{1}{12} \frac{h_{i+1}^3 + h_i^3}{h_i + h_{i+1}} \frac{\partial^4 f}{\partial r^4} \Big|_{r_i} + \dots \quad (4.5.9)$$

The order of the truncation error in this expression is difficult to estimate, since the error is dominated by the term denoted by an asterisk which is specific to irregular grids (see e.g. Dormy, 1997). This term vanishes in the limit $h = h_i = h_{i+1}$, for which the above equation reduces to the second derivative of the second-order central difference scheme

$$\frac{\partial^2 f}{\partial r^2} \Big|_{r_i} = \frac{f_{i+1} - 2f_i + 2f_{i-1}}{h^2} + \mathcal{O}(h^2). \quad (4.5.10)$$

Therefore, to minimise the error, the difference $(h_{i+1} - h_i)$ has to be minimised, which means that it is not possible to rapidly change the sampling step without significantly decreasing the order of convergence of the scheme. One possible option that allows to contain the truncation error is to consider a geometric progression such that $h_{i+1} = qh_i$, with a factor q close to 1. Hence, the sampling step can only change very gradually, which means that the geometric progression has to be started well before the boundaries to achieve a dense grid spacing in the boundary layers.

In MagIC, a radial grid that is comprised of several parts is adopted, with a geometric progression towards the boundaries and a regular grid spacing in the bulk. The segmentation between the two can be tuned by input parameters (Dormy, 1997).

4.5.2 Chebyshev collocation method

Alternatively, a Chebyshev collocation method can be used for the radial representation. The set of spectral evolution equations that has to be solved is then given by Eq. (4.4.7-4.4.12). Chebyshev polynomials allow to expand the radial variations of the unknowns into complete sets of functions. The Chebyshev polynomial of degree $n \geq 0$ is defined by

$$C_n(x) = \cos[n \arccos(x)], \quad (4.5.11)$$

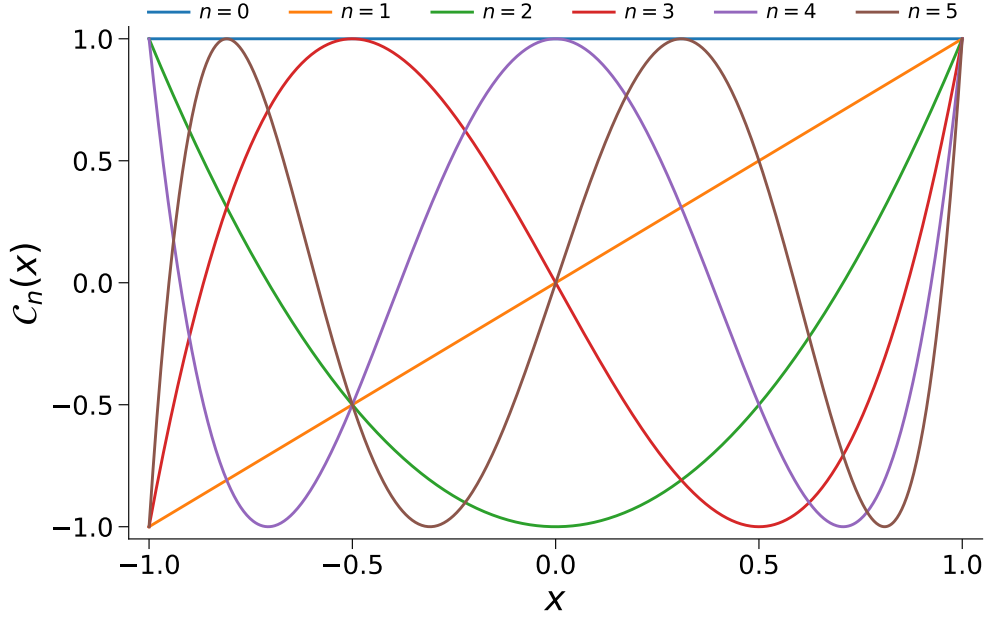


Figure 4.3: Chebyshev polynomials up to degree $n = 5$.

where $-1 \leq x \leq 1$. Figure 4.3 illustrates the Chebyshev polynomials up to degree $n = 5$.

To evaluate the Chebyshev polynomials, it is advantageous to choose the Gauss-Lobatto collocation points x_k which are defined by

$$x_k = \cos\left(\frac{\pi k}{N}\right), \quad k = 0, 1, \dots, N. \quad (4.5.12)$$

At these points the Chebyshev polynomials are then given by

$$C_n(x_k) = \cos\left(\frac{n\pi k}{N}\right). \quad (4.5.13)$$

Due to the spherical shell geometry, it is useful to map the domain of the Chebyshev polynomials ($-1 \leq x \leq 1$) onto the radius range ($r_i \leq r \leq r_o$). In MagIC, this is done by employing an affine mapping defined by

$$r(x) = \frac{1}{2} [r_o(1+x) + r_i(1-x)]. \quad (4.5.14)$$

Using the Chebyshev representation, the poloidal magnetic field potential $G_{\ell m}(r, t)$ can then be expanded in radius as follows

$$G_{\ell m}(r, t) \simeq \sum_{n=0}^N G_{\ell mn}(t) C_n(x), \quad (4.5.15)$$

where N denotes the degree of truncation. The coefficients $G_{\ell mn}(t)$ in the above expression are defined by

$$G_{\ell mn}(t) = \frac{2 - \delta_{n0} - \delta_{nN}}{\pi} \int_{-1}^1 \frac{G_{\ell m}(r(x), t) C_n(x)}{\sqrt{1-x^2}} dx. \quad (4.5.16)$$

Numerically, this integral can be handled by using the Gaussian quadrature rule

$$\int_{-1}^1 f(x) w(x) dx \simeq \sum_{n=0}^N w_n f(x_n). \quad (4.5.17)$$

For the collocation points $x_k = \cos(\pi k/N)$, the weights w_n are given by ([Abramowitz and Stegun, 1970](#))

$$w_n = \begin{cases} \frac{\pi}{N} & n = 1, 2, \dots, N-1 \\ \frac{\pi}{2N} & n = 0, N. \end{cases} \quad (4.5.18)$$

Equation (4.5.16) can thus be approximated by

$$G_{\ell mn}(t) \simeq \frac{1}{2N} \left[G_{\ell m}(r_0, t) + G_{\ell m}(r_N, t) + 2 \sum_{n=1}^{N-1} G_{\ell m}(r_n, t) \cos\left(\frac{nk\pi}{N}\right) \right]. \quad (4.5.19)$$

This expression represents a fast discrete cosine transform (DCT) ([Press et al., 1992](#), Chapter 12). Being able to use fast DCTs to change from physical space to Chebyshev representations and vice versa is one major benefit of the Gauss-Lobatto nodal points. An additional advantage is the increased density of the radial grid points towards the inner and outer boundaries, which improves the resolution of potential boundary layers.

However, the dense spacing of the radial grid points near the boundaries can also cause severe time step limitations in models with a sizeable Lorentz force due to the propagation of Alfvén waves ([Christensen et al., 1999](#)). In MagIC, this restriction can be mitigated by adopting a mapping of the Gauss-Lobatto collocation points as suggested by [Kosloff and Tal-Ezer \(1993\)](#), which is defined by

$$y_k = \frac{\arcsin(\alpha_{\text{map}} x_k)}{\arcsin(\alpha_{\text{map}})}, \quad (4.5.20)$$

where α_{map} denotes the mapping coefficient. By replacing x_k in relation (4.5.14) by y_k a more uniform spacing of the radial grid points, and hence larger time steps, can be achieved ([Boyd, 2001](#), § 16.9). To ensure spectral convergence, the mapping coefficient α_{map} has to fulfill the following condition ([Gastine et al., 2020](#)):

$$\alpha_{\text{map}} \leq \left[\cosh\left(\frac{|\ln \epsilon|}{N_r - 1}\right) \right]^{-1}, \quad (4.5.21)$$

where ϵ is the machine precision.

Finally, by combining the Chebyshev representation in radius (Eq. 4.5.15) with the spherical harmonic expansion in the angular directions (Eq. 4.3.4) the full spectral representation of the poloidal magnetic potential reads

$$G(r_k, \theta, \varphi, t) \simeq \sum_{\ell=0}^{\ell_{\max}} \sum_{m=0}^{\ell} \sum_{n=0}^N G_{\ell mn}(t) C_n(r_k) Y_{\ell}^m(\theta, \varphi). \quad (4.5.22)$$

The same expansion is applied to the toroidal magnetic potential $H_{\ell m}$, the velocity potentials $W_{\ell m}$ and $Z_{\ell m}$, the temperature perturbation $T_{\ell m}$ and the non-hydrostatic pressure $p_{\ell m}$. The set of equations (4.4.7-4.4.12) then modifies to

$$\begin{aligned} \frac{\ell(\ell+1)}{r^2} \left[\left(\frac{d}{dt} + \frac{\ell(\ell+1)}{r^2} \right) C_n - C_n'' \right] W_{\ell mn} + C_n' p_{\ell mn} - \frac{Ra}{Pr} \frac{r}{r_o} C_n T_{\ell mn} = \\ = \int_{\varphi=0}^{2\pi} \int_{\theta=0}^{\pi} \mathbf{e}_r \cdot \mathbf{F} Y_{\ell m}^* \sin \theta \, d\theta d\varphi, \end{aligned} \quad (4.5.23)$$

$$\frac{\ell(\ell+1)}{r^2} \left[\left(\frac{d}{dt} + \frac{\ell(\ell+1)}{r^2} \right) C_n - C_n'' \right] Z_{\ell mn} = \int_{\varphi=0}^{2\pi} \int_{\theta=0}^{\pi} \mathbf{e}_r \cdot (\nabla \times \mathbf{F}) Y_{\ell m}^* \sin \theta \, d\theta d\varphi, \quad (4.5.24)$$

$$\frac{\ell(\ell+1)}{r^2} \left[\left(\frac{d}{dt} + \frac{1}{Pm} \frac{\ell(\ell+1)}{r^2} \right) C_n + \frac{1}{Pm} C_n'' \right] G_{\ell mn} = \int_{\varphi=0}^{2\pi} \int_{\theta=0}^{\pi} \mathbf{e}_r \cdot \mathbf{D} Y_{\ell m}^* \sin \theta \, d\theta d\varphi, \quad (4.5.25)$$

$$\frac{\ell(\ell+1)}{r^2} \left[\left(\frac{d}{dt} + \frac{1}{Pm} \frac{\ell(\ell+1)}{r^2} \right) C_n + \frac{1}{Pm} C_n'' \right] H_{\ell mn} = \int_{\varphi=0}^{2\pi} \int_{\theta=0}^{\pi} \mathbf{e}_r \cdot (\nabla \times \mathbf{D}) Y_{\ell m}^* \sin \theta \, d\theta d\varphi \quad (4.5.26)$$

and

$$\begin{aligned} -\frac{\ell(\ell+1)}{r^2} \left[\frac{\ell(\ell+1)}{r^2} \frac{2}{r} C_n + \left(\frac{d}{dt} - \frac{\ell(\ell+1)}{r^2} \right) C_n' + C_n''' \right] W_{\ell mn} \\ - \frac{\ell(\ell+1)}{r^2} C_n p_{\ell mn} = \int_{\varphi=0}^{2\pi} \int_{\theta=0}^{\pi} \nabla_H \cdot \mathbf{F} Y_{\ell m}^* \sin \theta \, d\theta d\varphi. \end{aligned} \quad (4.5.27)$$

In the above equations Einstein's summation convention is used for the sum over the Chebyshev polynomials. The operators C_n' , C_n'' and C_n''' denote the first, second and third radial derivatives of the Chebyshev polynomials, respectively. They can be easily obtained using recurrence relations (Glatzmaier, 2013, §9.4). It should be noted that C_n , C_n' , C_n'' and C_n''' are dense matrices.

4.6 Boundary conditions

In our models, we consider impenetrable, no-slip boundaries. These conditions require that radial and horizontal velocities vanish, i.e.

$$W_{\ell m}(r, t) = 0, \quad (4.6.1)$$

$$\frac{\partial}{\partial r} W_{\ell m}(r, t) = 0, \quad (4.6.2)$$

$$Z_{\ell m}(r, t) = 0, \quad (4.6.3)$$

at $r = r_i$ and $r = r_o$.

For the magnetic boundary conditions, we assume that both boundaries are electrically insulating. Since the toroidal magnetic field cannot penetrate the insulating regions, it has to vanish at the boundaries, i.e.

$$H_{\ell m}(r, t) = 0 \quad \text{at } r \in \{r_i, r_o\}. \quad (4.6.4)$$

For the poloidal magnetic field matching conditions to a potential field have to be formulated. These are given by

$$\frac{\partial}{\partial r} G_{\ell m}(r, t) - \frac{\ell + 1}{r} G_{\ell m}(r, t) \quad \text{at } r = r_i, \quad (4.6.5)$$

and

$$\frac{\partial}{\partial r} G_{\ell m}(r, t) + \frac{\ell}{r} G_{\ell m}(r, t) \quad \text{at } r = r_o. \quad (4.6.6)$$

Finally, convection in our models is driven by a fixed superadiabatic temperature difference between the two boundaries. Thus, we impose

$$T_{\ell m}(r, t) = \text{const.} \quad \text{at } r \in \{r_i, r_o\}, \quad (4.6.7)$$

with $T_{\ell m}(r_i, t) > T_{\ell m}(r_o, t)$.

4.7 Time integration

Equations (4.5.23-4.5.27) form a semi-discrete set of equations, where the full spatial discretisation has been specified. In this section, we will now turn to the time discretisation. The spectral evolution equations represent ODEs in which the coefficients only depend on time. For their time integration MagIC employs a mixed implicit/explicit (IMEX) algorithm, since the simulated convection dynamics exhibit a large range of time scales (see Section 1.3.4). In general form the equations can therefore be expressed as

$$\frac{dy}{dt} = \mathcal{I}(y, t) + \mathcal{E}(y, t), \quad y(t_0) = y_0, \quad (4.7.1)$$

where $\mathcal{I}(y, t)$ indicates the terms that are treated implicitly, and $\mathcal{E}(y, t)$ the ones that are advanced in time explicitly. The latter correspond to the contributions that were summarised on the RHS of the evolution equations, i.e. the non-linear and Coriolis terms. In theory, a fully implicit treatment should yield better numerical stability as well as the possibility to use larger time step sizes. This would, however, lead to the coupling of all spherical harmonic modes due to the non-linear terms. Similarly, the Coriolis term couples the modes (ℓ, m, n) with $(\ell + 1, m, n)$ and $(\ell - 1, m, n)$ in addition to the coupling of the poloidal and toroidal flow potentials (Marti et al., 2016). The numerical costs become prohibitive when using a dense matrix formulation because of the required memory storage. A purely, explicit treatment on the other hand has the disadvantage that the linear terms impose much stricter temporal stability constraints compared to the non-linear ones (e.g. Gastine, 2019), which would lead to extremely small time steps being required. Hence, in MagIC a mixed implicit/explicit approach is used to mitigate the difficulties associated with each method.

In MagIC, IMEX multistep (e.g. Ascher et al., 1995) and IMEX multistage (e.g. Ascher et al., 1997) algorithms are supported. Here we will only outline some of the basics of IMEX multistep methods, which use the information of several previous steps to generate the next solution point. In its general form such a scheme is given by

$$y_{n+1} = \sum_{j=0}^k a_j y_{n+1-j} + \delta t \left(\sum_{j=1}^k b_j^{\mathcal{E}} \mathcal{E}_{n+1-j} + \sum_{j=0}^k b_j^{\mathcal{I}} \mathcal{I}_{n+1-j} \right), \quad (4.7.2)$$

where k denotes the number of steps that are used and δt the time step size. We used the notation $\mathcal{E}_{n+1-j} = \mathcal{E}(y_{n+1-j}, t_{n+1-j})$ and $\mathcal{I}_{n+1-j} = \mathcal{I}(y_{n+1-j}, t_{n+1-j})$. The vectors \mathbf{a} , $\mathbf{b}^{\mathcal{E}}$ and $\mathbf{b}^{\mathcal{I}}$ represent the weighting factors of the algorithm. The above equation can be rearranged as follows:

$$(I - b_0^{\mathcal{I}} \delta t \mathcal{I}) y_{n+1} = \sum_{j=1}^k a_j y_{n+1-j} + \delta t \sum_{j=1}^k (b_j^{\mathcal{E}} \mathcal{E}_{n+1-j} + b_j^{\mathcal{I}} \mathcal{I}_{n+1-j}), \quad (4.7.3)$$

where I denotes the identity matrix. One widely used IMEX multi-step algorithm in geodynamo simulations, which was introduced by Glatzmaier (1984), is a second-order scheme in which the implicit terms are integrated in time using a Crank-Nicolson method (Crank and Nicolson, 1947) and the explicit terms using a second-order Adams-Bashforth scheme (hereafter CNAB2). For a constant time step δt , it is given by the weights $\mathbf{a} = (1, 0)$, $\mathbf{b}^{\mathcal{E}} = (3/2, -1/2)$ and $\mathbf{b}^{\mathcal{I}} = (1/2, 1/2)$.

Using relation (4.7.1), time-stepping equations are formulated for all spectral coefficients of spherical harmonic degree ℓ and order m for each radial grid point r_k , with the exception of pressure. As an example, the equation to advance the poloidal magnetic potential $G_{\ell mn}(t)$ in time with a CNAB2 scheme is given by

$$\left(\mathcal{A}_{kn} - \frac{1}{2} \delta t \mathcal{I}_{kn} \right) G_{\ell mn}(t + \delta t) = \left(\mathcal{A}_{kn} + \frac{1}{2} \delta t \mathcal{I}_{kn} \right) G_{\ell mn}(t) + \frac{3}{2} \delta t \mathcal{E}_{k\ell m}(t) - \frac{1}{2} \delta t \mathcal{E}_{k\ell m}(t - \delta t). \quad (4.7.4)$$

In case Chebyshev polynomials are chosen for the radial representation, the matrices \mathcal{A}_{kn} and \mathcal{I}_{kn} in the above expression are defined by

$$\mathcal{A}_{kn} = \frac{\ell(\ell+1)}{r_k^2} C_{nk} \quad (4.7.5)$$

and

$$\mathcal{I}_{kn} = \frac{\ell(\ell+1)}{r_k^2} \frac{1}{Pm} \left(C_{nk}'' - \frac{\ell(\ell+1)}{r_k^2} C_{nk} \right), \quad (4.7.6)$$

where $C_{nk} = C_n(r_k)$. It should be noted that again Einstein's summation convention is used for the Chebyshev polynomials. Both \mathcal{A}_{kn} and \mathcal{I}_{kn} are independent of time. \mathcal{A}_{kn} must be updated though if the time step δt is modified. The explicit contribution in (4.7.4) represents the non-linear induction term

$$\mathcal{E}_{k\ell m}(t) = \int_{\varphi=0}^{2\pi} \int_{\theta=0}^{\pi} \mathbf{e}_r \cdot \mathbf{D} Y_{\ell m}^* \sin \theta \, d\theta d\varphi. \quad (4.7.7)$$

Numerical stability requirements limit the maximum allowable time step size. A guideline for the choice of δt is given by the Courant condition, which states that δt must be smaller than the advection time between two grid points. This criterion alone, however, would not be sufficient in models with a strong Lorentz force due to the propagation of Alfvén waves near the boundaries. Therefore, a modified Courant condition is additionally adopted in which the fluid velocity is replaced by the Alfvén velocity, which depends on the magnetic field strength (Christensen et al., 1999).

4.8 Simulations computed for this work

In this work, we attempt to systematically study the force balance that governs the flow dynamics in numerical dynamo models. To this end, we computed a series of 110 simulations, most of which cover a similar parameter space as previous large studies, as shown in Fig. 4.4. At $E = 10^{-6}$, we significantly increased the number of models though. The range of control parameters covered in this thesis extends over $10^{-6} \leq E \leq 10^{-4}$, $0.03 \leq Pm \leq 15$, $1.5 \times 10^6 \leq Ra \leq 2.66 \times 10^{10}$ with $Pr = 1$. The majority of dynamo models published to date use a simple set of boundary conditions, in which both boundaries are assumed to be rigid (no-slip), electrically insulating and have a fixed temperature. Therefore, to be able to directly compare our results with these studies, we have decided to adopt the same boundary conditions in this work. Furthermore, to investigate how the presence of a magnetic field changes our results, we performed 24 non-magnetic rotating convection simulations in the same range of parameters as used for the dynamo models. The control parameters and relevant results of the dynamo and non-magnetic rotating convection simulations are listed in the Tables B.1 and B.2, respectively.

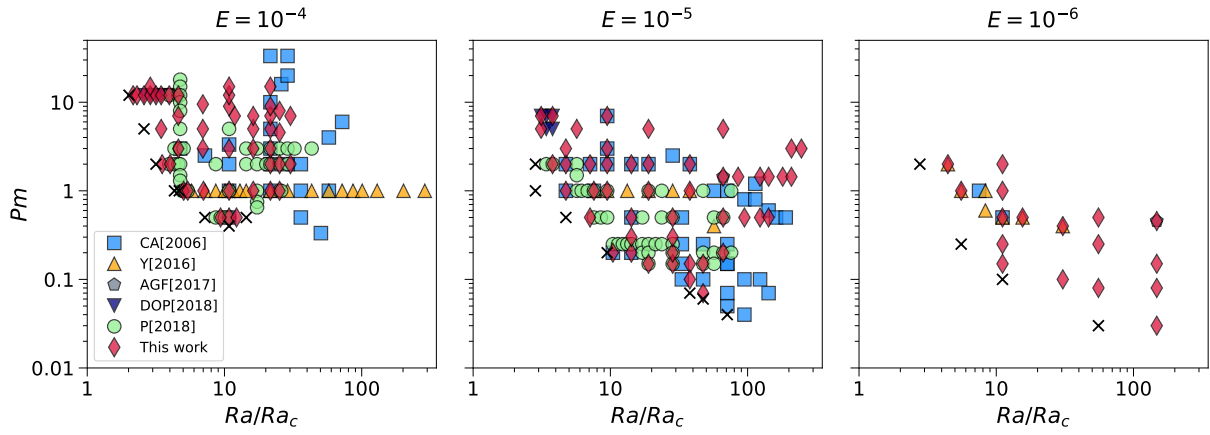


Figure 4.4: Parameter space covered by the simulations computed for this work in comparison to previous studies that used the same set of boundary conditions. CA[2006] denotes [Christensen and Aubert \(2006\)](#), Y[2016] [Yadav et al. \(2016\)](#), AGF[2017] [Aubert et al. \(2017\)](#), DOP[2018] [Dorny et al. \(2018\)](#) and P[2018] [Petitdemange \(2018\)](#). The crosses indicate so-called failed dynamos, i.e. simulations in which convection was not able to sustain a magnetic field. All shown models operate with $Pr = 1$ and use the same set of boundary conditions.

Chapter 5

Force balance in numerical geodynamo simulations: a systematic study

This chapter is a reproduction of the Geophysical Journal International (GJI) article [Schwaiger et al. \(2019\)](#). In this paper, we systematically analysed the force balance in numerical geodynamo models by explicitly computing the forces and assessing their length-scale dependence. Thereby, we show that most dynamo models within the investigated parameter space are governed by a QG-MAC balance and thus can be considered relevant for studying the Earth's core dynamics.

Abstract

Dynamo action in the Earth's outer core is expected to be controlled by a balance between pressure, Coriolis, buoyancy and Lorentz forces, with marginal contributions from inertia and viscous forces. Current numerical simulations of the geodynamo, however, operate at much larger inertia and viscosity because of computational limitations. This casts some doubt on the physical relevance of these models.

Our work aims at finding dynamo models in a moderate computational regime which reproduce the leading-order force balance of the Earth. By performing a systematic parameter space survey with Ekman numbers in the range $10^{-6} \leq E \leq 10^{-4}$, we study the variations of the force balance when changing the forcing (Rayleigh number, Ra) and the ratio between viscous and magnetic diffusivities (magnetic Prandtl number, Pm). For dipole-dominated dynamos, we observe that the force balance is structurally robust throughout the investigated parameter space, exhibiting a quasi-geostrophic (QG) balance (balance between Coriolis and pressure forces) at zeroth order, followed by a first-order MAC balance between the ageostrophic Coriolis, buoyancy and Lorentz forces. At second order this balance is disturbed by contributions from inertia and viscous forces. Dynamos with a different sequence of the forces, where inertia and/or viscosity replace the Lorentz force in

the first-order force balance, can only be found close to the onset of dynamo action and in the multipolar regime. To assess the agreement of the model force balance with that expected in the Earth’s core, we introduce a parameter quantifying the distance between the first- and second-order forces. Analysis of this parameter shows that the strongest-field dynamos can be obtained close to the onset of convection (Ra close to critical) and in situations of reduced magnetic diffusivity (high Pm). Decreasing the Ekman number gradually expands this regime towards higher supercriticalities and lower values of Pm .

Our study illustrates that most classical numerical dynamos are controlled by a QG-MAC balance, while cases where viscosity and inertia play a dominant role are the exception rather than the norm.

5.1 Introduction

The Earth’s magnetic field is believed to be generated by dynamo action in the liquid outer core. The flow dynamics driving this process are expected to be controlled by a balance between pressure, Coriolis, buoyancy and Lorentz forces, with marginal contributions from inertia and viscous forces (e.g., [Roberts and King, 2013](#)). However, the exact structure of the leading-order force balance is still debated (e.g., [Dormy, 2016](#); [Aubert et al., 2017](#); [Aurnou and King, 2017](#)).

Historically, theoretical considerations largely based on asymptotic studies of magnetoconvection resulted in the distinction between weak- and strong-field regimes of dynamo action (e.g., [Hollerbach, 1996](#)). In a system dominated by rapid rotation, as is the case for the Earth’s core, fluid motions tend to be invariant in the direction of the rotation axis, and fulfill the so-called Proudman-Taylor constraint. In the weak-field regime, this rotational constraint is broken by the viscous force or inertia, while the Lorentz force is substantially weaker, leading to small-scale convection. Increasing the vigour of convection increases the magnetic field strength and as a result, the Lorentz force could eventually break the rotational constraint, leading to larger convective scales. This induces a catastrophic runaway growth of the magnetic field until convection occurs on the scale of the system size. At this point the magnetic field equilibrates at Elsasser number $\Lambda \sim \mathcal{O}(1)$, where Λ measures the relative amplitudes of the Lorentz and Coriolis forces:

$$\Lambda = \frac{|\mathbf{F}_{\text{Lorentz}}|}{|\mathbf{F}_{\text{Coriolis}}|} = \frac{|\mathbf{J} \times \mathbf{B}|}{|2\rho\boldsymbol{\Omega} \times \mathbf{u}|} \sim \frac{JB}{\rho\Omega U}, \quad (5.1.1)$$

with J representing the current density, B the magnetic field strength, ρ the fluid density, Ω the rotation rate and U the flow velocity. The resulting regime is referred to as strong-field regime due to the Lorentz force now being much stronger than the viscous forces and inertia. Since a magnetic field with $\Lambda \sim \mathcal{O}(1)$ facilitates convection ([Malkus, 1959](#)), it has been suggested that the core flow dynamics are in a magnetostrophic (MS) state, where pressure, Coriolis and Lorentz forces balance each other at zeroth order ([Wu and Roberts, 2013](#)). To assess based on geomagnetic observations whether the geodynamo operates in

a magnetostrophic regime, the Elsasser number has traditionally been estimated using the following definition:

$$\Lambda_t = \frac{B^2}{\rho\mu\lambda\Omega}, \quad (5.1.2)$$

where μ represents the magnetic permeability and λ the magnetic diffusivity. Inserting characteristic values of the Earth (e.g., [Christensen and Aubert, 2006](#)) yields $\Lambda_t \sim \mathcal{O}(1)$, which has often been used to argue for Lorentz and Coriolis forces being of the same order of magnitude in the outer core. The definition of Λ_t , however, does not include length and velocity scales and therefore may provide an inaccurate measure of the relative amplitudes of the forces ([Soderlund et al., 2012, 2015](#); [Calkins, 2018](#)). A more rigorous estimate of this force ratio can be obtained using a dynamic Elsasser number, defined as ([Soderlund et al., 2012](#)):

$$\Lambda_d = \frac{B^2}{\rho\mu\Omega UL}, \quad (5.1.3)$$

where L represents the thickness of the outer core. Employing characteristic values to this definition yields $\Lambda_d \sim \mathcal{O}(10^{-2})$ for the Earth, indicating that the Lorentz force is two orders of magnitude smaller than the Coriolis force. This suggests that core flow dynamics could be controlled by a geostrophic balance between pressure and the Coriolis force at leading order, which would result in quasi-geostrophic (QG) instead of magnetostrophic convection dynamics ([Soderlund et al., 2012](#); [Calkins, 2018](#)). This is in agreement with recent studies of the core flow based on the inversion of geomagnetic secular variation data, which suggest that on global scales QG flows appear to describe the observations best (e.g., [Gillet et al., 2012](#)). Theoretical grounding for how such large-scale quasi-geostrophy could be possible has recently been provided by [Aurnou and King \(2017\)](#), who suggested based on scaling analysis of the Elsasser number, that magnetostrophic flow dynamics may be deferred to smaller scales, inaccessible to geomagnetic observations. [Aurnou and King \(2017\)](#) therefore argue for a length scale dependent combination of zeroth-order quasi-geostrophy and magnetostrophy.

In addition to observations and theoretical considerations, global numerical dynamo simulations represent an important tool for our understanding of the dynamo mechanism. Although computational resources have increased significantly since the first successful dynamo simulations computed more than 20 years ago ([Glatzmaier and Roberts, 1995](#)), current numerical models still operate at parameters far from the expected conditions of the Earth's core. Despite this limitation, numerical dynamos have proven to be very successful in reproducing numerous features of the geomagnetic field (e.g., [Christensen et al., 2010](#)). However, it remains uncertain whether these results are obtained for the right physical reasons. As a consequence many studies have been performed, trying to answer this question. [Soderlund et al. \(2012\)](#) found that convection in many dynamo simulations does not occur on the system scale, but rather on a scale similar to that of rotating convection. As a result, they argued for a subdominant role of the magnetic field

in those numerical models, which was attributed to a sizeable contribution of viscosity (e.g., King and Buffett, 2013; Oruba and Dormy, 2014). Some authors even suggested that the majority of dynamos found to date belong to the viscous weak-field regime (e.g., Dormy, 2016; Dormy et al., 2018). However, the discrepancy between dynamo solutions and non-magnetic convection was shown to become more obvious when the viscosity in the models is lowered (e.g., Sakuraba and Roberts, 2009; Yadav et al., 2016). By explicitly computing the magnitude of all forces (e.g., Wicht and Christensen, 2010; Soderlund et al., 2012, 2015) and their level of cancellation (e.g., Yadav et al., 2016), numerical dynamos were found to be quasi-geostrophic at zeroth order, with buoyancy and Lorentz forces balancing the ageostrophic Coriolis force, i.e. the part of the Coriolis force which is not balanced by pressure. More recently, Aubert et al. (2017) introduced a length scale dependent approach for a more refined analysis of the force balance. High resolution dynamos (e.g., Yadav et al., 2016; Schaeffer et al., 2017; Sheyko et al., 2018) at advanced parameter regimes support this QG-MAC (Quasi-Geostrophic Magneto-Archimedean-Coriolis) balance, which suggests that it could go all the way to the core (Aubert et al., 2017).

While the majority of dynamo models to date therefore seem to support a QG-MAC balance, some studies also report dynamos that could be controlled by a magnetostrophic balance at zeroth order (e.g., Dormy, 2016; Dormy et al., 2018). Dormy (2016) and Dormy et al. (2018) were further able to observe close to the onset of dynamo action a catastrophic runaway growth of the magnetic field from viscously dominated weak-field dynamos to strong-field dynamos in their models, similar to that predicted by asymptotic studies of rotating magneto-convection. These conflicting interpretations illustrate that not only the presumed force balance in the Earth’s core but also the force balance obtained in current numerical models are still highly-debated topics.

By performing a systematic survey of the numerically accessible parameter space, we attempt to enable a better understanding of force balances. To this end, we will make use of the scale dependent force balance representations introduced in Aubert et al. (2017). Additionally, we will introduce new tools to directly relate the physical scale at which the dynamo is organised locally to the governing force balance. Throughout this work, we adopt the following naming conventions. Some authors use the term ‘magnetostrophic’ (strictly) to describe a zeroth-order MS balance (e.g., Roberts, 1978; Dormy, 2016; Dormy et al., 2018). Other authors consider ‘magnetostrophic’ as the QG-MAC balance (e.g., Yadav et al., 2016; Aubert et al., 2017). Here, ‘magnetostrophic’ will only refer to the zeroth-order MS balance to avoid possible confusion between the two types of force balances. Likewise, some authors refer to dynamos as being in the strong-field regime only in the presence of an $\Lambda \sim \mathcal{O}(1)$ magnetic field, i.e. dynamos controlled by a zeroth-order MS balance (e.g., Roberts, 1978; Dormy, 2016; Dormy et al., 2018). Many other authors consider strong field simply as the magnetic energy being much larger than the kinetic energy (e.g., Schaeffer et al., 2017; Aubert et al., 2017). This is the definition that we will retain here.

Section 5.2 presents the numerical models and methods. The results are presented in Section 5.3, followed by a discussion in Section 5.4.

5.2 Numerical model

We consider a spherical shell of thickness $L = r_o - r_i$ and radius ratio $r_i/r_o = 0.35$, where r_i and r_o are the inner and outer radii. The shell rotates with angular frequency Ω about the axis \mathbf{e}_z . The inclosed fluid of density ρ and (kinematic) viscosity ν is electrically conducting and incompressible. Convection is driven by a fixed superadiabatic temperature difference ΔT between the inner and the outer boundary. Gravity \mathbf{g} increases linearly with radius.

We solve the geodynamo equations in non-dimensional form using the Boussinesq approximation to obtain the velocity field \mathbf{u} , magnetic induction \mathbf{B} and temperature perturbation T . We adopt L as reference length scale, the viscous diffusion time L^2/ν serves as time unit, temperature is scaled by ΔT and magnetic induction by $\sqrt{\rho\mu\lambda\Omega}$, where μ is the magnetic permeability and λ the magnetic diffusivity of the fluid. This results in the following set of equations:

$$\frac{\partial \mathbf{u}}{\partial t} + \mathbf{u} \cdot \nabla \mathbf{u} + \frac{2}{E} \mathbf{e}_z \times \mathbf{u} = -\nabla p + \frac{Ra}{Pr r_o} T + \frac{1}{EPm} (\nabla \times \mathbf{B}) \times \mathbf{B} + \nabla^2 \mathbf{u}, \quad (5.2.1)$$

$$\frac{\partial T}{\partial t} + \mathbf{u} \cdot \nabla T = \frac{1}{Pr} \nabla^2 T, \quad (5.2.2)$$

$$\frac{\partial \mathbf{B}}{\partial t} = \nabla \times (\mathbf{u} \times \mathbf{B}) + \frac{1}{Pm} \nabla^2 \mathbf{B}, \quad (5.2.3)$$

$$\nabla \cdot \mathbf{u} = 0, \quad (5.2.4)$$

$$\nabla \cdot \mathbf{B} = 0, \quad (5.2.5)$$

where p is the pressure. The non-dimensional control parameters of the system are the Ekman number

$$E = \frac{\nu}{\Omega L^2}, \quad (5.2.6)$$

the hydrodynamic Prandtl number

$$Pr = \frac{\nu}{\kappa}, \quad (5.2.7)$$

the magnetic Prandtl number

$$Pm = \frac{\nu}{\lambda}, \quad (5.2.8)$$

and the Rayleigh number

$$Ra = \frac{\alpha g_o L^3 \Delta T}{\nu \kappa}, \quad (5.2.9)$$

where κ is the thermal diffusivity, α the thermal expansion coefficient and g_o the gravity at the outer boundary.

Both boundaries are assumed to be electrically insulating with vanishing velocity field (no-slip) and fixed temperature. All models are simulated with the open-source numerical code MagIC (Wicht, 2002; Gastine et al., 2016, <https://github.com/magic-sph/magic>), which uses Chebychev polynomials in the radial direction and a spherical harmonic decomposition in the angular directions. MagIC relies on the library SHTns (Schaeffer, 2013, <https://bitbucket.org/nschaeff/shtns>) for efficient calculation of the spherical harmonic transforms. Diffusion terms are integrated implicitly in time using a Crank-Nicolson scheme, while a second-order Adams-Bashforth scheme is employed for the explicit treatment of the remaining terms. For the explicit time stepping, numerical stability requires the maximum allowable time step to satisfy a Courant criterion, which is constrained by the spacing of the radial grid points (Christensen et al., 1999). To alleviate the time step restrictions due to the Alfvén waves propagating close to the boundaries, we adopt a mapping of the Gauss-Lobatto collocation grid points (Kosloff and Tal-Ezer, 1993). This leads to an increase of the maximum allowable time step by up to a factor two and therefore results in a significant reduction of the computational costs (e.g., Boyd, 2001, Section 16.9).

To systematically study the force balance that drives the convection in geodynamo models, we perform a series of 95 numerical simulations spanning the parameter range $10^{-6} \leq E \leq 10^{-4}$, $0.07 \leq Pm \leq 15$ and $1.5 \times 10^6 \leq Ra \leq 2.66 \times 10^{10}$ with $Pr = 1$. The control parameters and relevant output parameters of the analysed models are given in Table B.1. Fig. 5.1 shows the regime diagrams for the three different Ekman numbers considered here following Christensen and Aubert (2006). The shaded regions represent areas of the parameter space where no self-sustained dynamos could be found. Depending on the geometry of the generated magnetic field we distinguish between dipolar and multipolar dynamos. The transition between these two regimes appears to shift towards higher supercriticalities (Ra/Ra_c) as the Ekman number decreases, while the onset of dynamo action seems to remain approximately at constant Ra/Ra_c . Decreasing the Ekman number also extends the region of dynamo action (region of self-sustained dynamos) towards lower Pm (Christensen et al., 1999; Christensen and Aubert, 2006). None of the investigated dynamo models in the dipolar regime exhibited reversals of the magnetic field polarity. However, for our models with strong magnetic turbulence we expect that reversals could occur, provided the simulations would cover long enough timescales (e.g., Heimpel and Evans, 2013). For the explored control parameters, verifying this would be extremely demanding in terms of computational resources. Therefore, this is currently not feasible within the scope of a systematic parameter space survey. To reduce the duration of transients after the start of the simulations, the dynamo models were initiated with an equilibrated solution with similar input parameters whenever possible. Note that close to the transition of the dipolar to the multipolar regime, bistable dynamos can be found (Petitdemange, 2018). This can be attributed to the strength of the seed magnetic field. Similarly, some models close to the onset of dynamo action do require a strong magnetic field at the outset for convection to be able to sustain it. Such bistabilities that depend on the initial conditions have been studied in detail by Petitdemange (2018) for the same physical setup. In our study, however, we only consider the dipole-dominated dynamos in all of these cases. To obtain an extensive

Table 5.1: Control parameters of four representative dynamo models with coloured symbols to locate them in the regime diagrams (Fig. 5.1).

Model	E	Ra	Ra/Ra_c	Pm
● A	10^{-6}	2.66×10^{10}	148.5	0.456
● B	10^{-4}	2.2×10^6	3.2	12
● C	10^{-6}	2×10^9	11.2	0.25
◆ D	10^{-5}	4×10^8	37.8	0.1

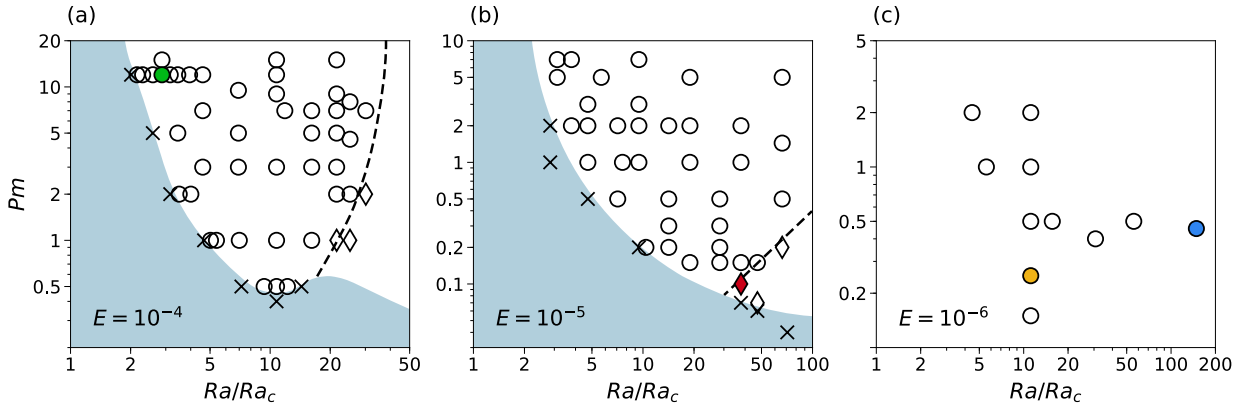


Figure 5.1: Regime diagrams for $E = 10^{-4}$, $E = 10^{-5}$ and $E = 10^{-6}$. Shaded regions represent areas of the parameter space where no self-sustained dynamos exist (computationally too expensive to determine for $E = 10^{-6}$). All dynamo models have been computed with $Pr = 1$. Circles represent dipolar, diamonds multipolar and crosses failed dynamos. The dashed lines tentatively delineate the transition between dipolar and multipolar dynamos. The control parameters of the dynamo models highlighted by coloured symbols are given in Table 5.1.

picture of the evolution of the force balance when changing the control parameters, we reproduced several recently published dynamo models (Yadav et al., 2016; Aubert et al., 2017; Dormy et al., 2018), as well as models covering the parameter space that has been classically explored (e.g., Kutzner and Christensen, 2002; Christensen and Aubert, 2006).

For our following analysis we will mainly focus on four cases which we consider to be representative for the investigated parameter space. Table 5.1 summarises the control parameters of these models, along with the coloured symbols used to locate them in the regime diagrams presented in Fig. 5.1.

5.3 Results

5.3.1 Force balance spectra

For our systematic study of the force balance, we follow the method introduced by [Aubert et al. \(2017\)](#) and decompose each force into spherical harmonic contributions:

$$F_{rms}^2 = \frac{1}{V} \int_{r_i+b}^{r_o-b} \sum_{\ell=0}^{\ell_{\max}} \sum_{m=0}^{\ell} F_{\ell m}^2 r^2 dr = \sum_{\ell=0}^{\ell_{\max}} F_{\ell}^2, \quad (5.3.1)$$

where b represents the thickness of the viscous boundary layers. Viscous boundary layers are excluded from the calculations since we are primarily interested in the force balance in the bulk of the fluid. The resulting force balance spectra of the four cases given in [Table 5.1](#) are illustrated in [Fig. 5.2](#). Most force balance spectra of the dynamo models in the dipolar regime are structurally very similar. The model **A** (see [Fig. 5.2a](#)), which is among the “path”-dynamos analysed by [Aubert et al. \(2017\)](#), can be considered as a typical example. At zeroth order, it is characterised by a quasi-geostrophic balance between pressure and the Coriolis force. The ageostrophic part of the Coriolis force is then balanced by buoyancy at small spherical harmonic degrees and by the Lorentz force at large ℓ . This QG-MAC balance has been identified in several recent studies (e.g., [Yadav et al., 2016](#); [Schaeffer et al., 2017](#); [Aubert et al., 2017](#)). This balance is, however, quite significantly disturbed by inertia and viscous forces since they are only one to two orders of magnitude smaller than the leading-order forces.

[Dormy \(2016\)](#) recently suggested that dynamo models governed by a magnetostrophic balance at zeroth order can be attained even in a computationally moderate regime by adopting a setup close to the onset of convection to minimise inertial effects and with large Pm to maintain a strong influence of the Lorentz force. Our study confirms that in these dynamo models the Lorentz force is of approximately the same magnitude as the total Coriolis force. Therefore, these models do indeed approach magnetostrophy when considering volume-integrated forces. However, the length scale dependent analysis of model **B** (which corresponds to one of the configurations considered by [Dormy et al., 2018](#)) using the force balance spectra (see [Fig. 5.2b](#)) reveals the same basic structure as for the QG-MAC cases, i.e. like for model **A** we observe a geostrophic balance at zeroth order, followed by a first-order balance between the ageostrophic Coriolis, buoyancy and Lorentz forces. This indicates that these models do not represent a force balance regime that is different from the one of most dipole-dominated dynamo models. Yet, due to the role of inertia getting minimised, the separation between the Lorentz force and second-order forces increases compared to QG-MAC cases at larger supercriticalities. Therefore, one may refer to such dynamo models as strong-field cases.

The only occurrences of dipole-dominated dynamo models that cannot be attributed to the QG-MAC regime can be found in regions of the parameter space close to the onset of dynamo action. Model **C** (see [Fig. 5.2c](#)) can be considered as an example for such dynamo models at low Pm , which are characterised by a significantly weaker Lorentz force compared to

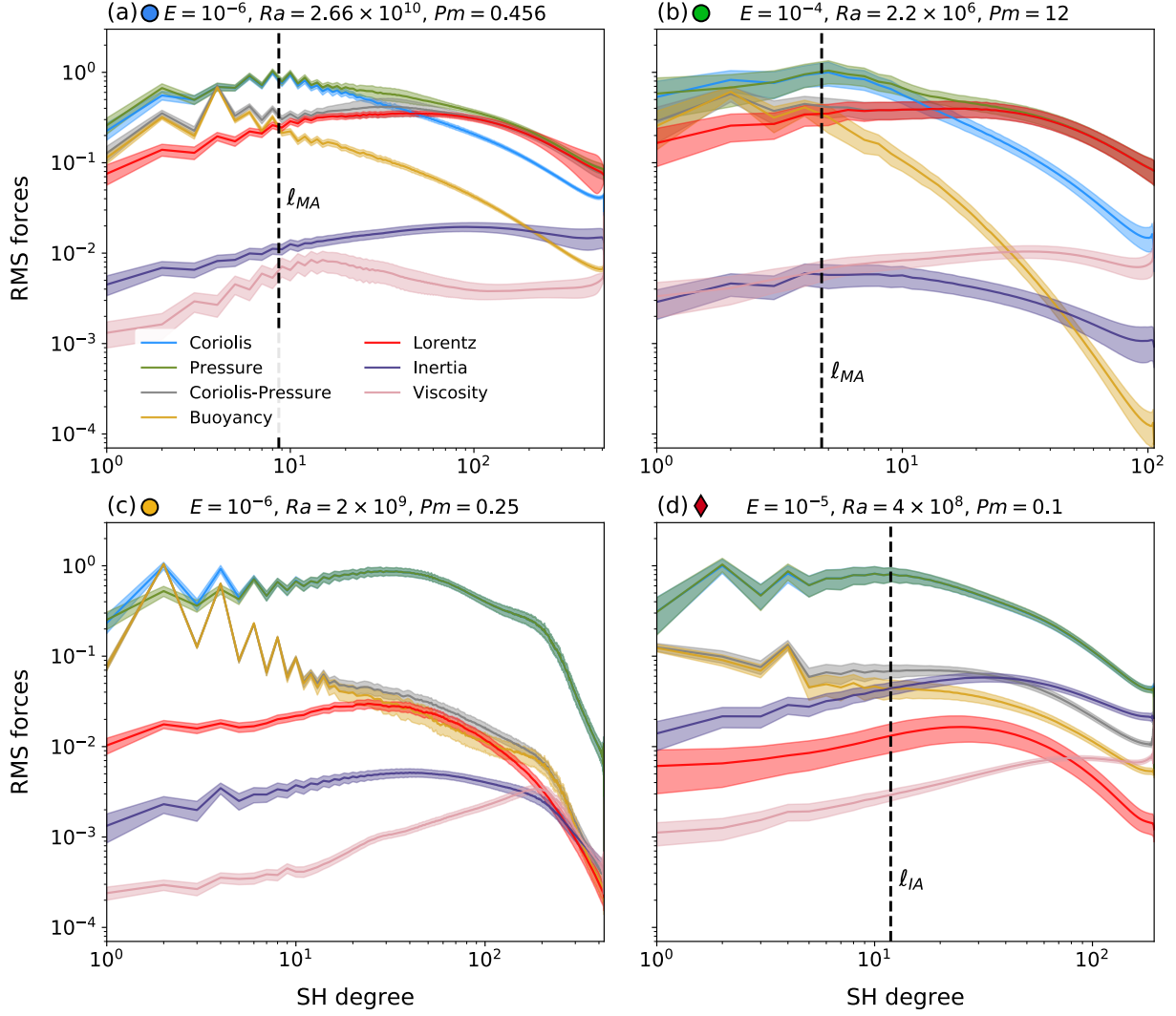


Figure 5.2: Force balance spectra for examples of different types of force balances excluding the viscous boundary layers. The spherical harmonic contributions of the r.m.s. forces are normalised with respect to the peak of the Coriolis force. The solid lines represent the time averages of the forces. The corresponding shaded regions represent one standard deviation. a-b: Examples of QG-MAC balances of dipole-dominated dynamos at $E = 10^{-6}$ and $E = 10^{-4}$. c: Example of a special case with control parameters close to the onset of dynamo action at $E = 10^{-6}$. d: Example of QG-CIA balance of a multipolar dynamo at $E = 10^{-5}$. The four coloured symbols refer to the location of the dynamos in the parameter space (see Fig. 5.1). The vertical dashed lines correspond to the cross-over length scales defined in section 5.3.1.2.

typical QG-MAC cases. While the Lorentz force is still larger than inertia and viscous forces at large scales, it becomes very weak towards smaller scales and as a result does not balance the geostrophic Coriolis force at any point.

By increasing the vigour of convection one eventually reaches the transition from the dipolar to the multipolar regime (e.g., [Kutzner and Christensen, 2002](#); [Christensen and Aubert, 2006](#)). Model **D** (see Fig. 5.2d) is an example of a multipolar dynamo close to this transition. Its force balance spectrum features a significantly weaker Lorentz force than the QG-MAC cases. This decrease of the Lorentz force might be related to the increasing role of inertia ([Christensen and Aubert, 2006](#)) or the breaking of the equatorial symmetry of the flow ([Garcia et al., 2017](#)). For multipolar cases inertia becomes a first-order contribution to the force balance, such that they are controlled by a first-order CIA (Coriolis-Inertia-Archimedean) balance ([Gillet and Jones, 2006](#)). At zeroth order these dynamos exhibit a quasi-geostrophic balance again. Therefore, analogously to QG-MAC, we refer to this type of force balance as QG-CIA balance.

5.3.1.1 “Strong-fieldness”

To evaluate, based on the force balance spectra, which of the dynamos can be attributed to the strong-field regime, we introduce the “strong-fieldness” δ . This parameter quantifies the separation between the Lorentz force and the second-order forces (inertia and viscous forces) and is defined as:

$$\delta = \sqrt{\frac{\sum_{\ell=1}^{\ell_{\max}} F_{\text{Lorentz},\ell}^2}{\sum_{\ell=1}^{\ell_{\max}} \max(F_{\text{inertia},\ell}^2, F_{\text{viscous},\ell}^2)}}. \quad (5.3.2)$$

Fig. 5.3a-b show extrapolated contour levels of δ for the investigated parameter space at $E = 10^{-4}$ and $E = 10^{-5}$. For $E = 10^{-6}$, the limited number of simulations does not allow a meaningful linear interpolation required to draw the contour lines. As a consequence, only the data points are displayed as a scatterplot in Fig. 5.3c. We observe that δ reaches its maximum for dynamos at low Ra/Ra_c and high Pm for all three Ekman numbers. This confirms the results by [Dormy \(2016\)](#) and [Dormy et al. \(2018\)](#) who suggested that strong-field dynamos can be attained for this parameter range. The smallest values of δ are found close to the onset of dynamo action and in the multipolar regime where the Lorentz force falls below the level of inertia. Decreasing the Ekman number from $E = 10^{-4}$ to $E = 10^{-6}$ leads to an overall increase of δ . In parallel, the parameter region of dynamos with $\delta \gg 1$, which corresponds to QG-MAC dynamos, gradually extends towards lower values of Pm .

The influence of viscous forces on δ decreases strongly with decreasing Ekman number. As a consequence, δ can be approximated by the ratio between the magnetic and kinetic energies \mathcal{M} :

$$\mathcal{M} = \frac{E_{\text{mag}}}{E_{\text{kin}}} = \frac{B^2}{\rho\mu U^2}, \quad (5.3.3)$$

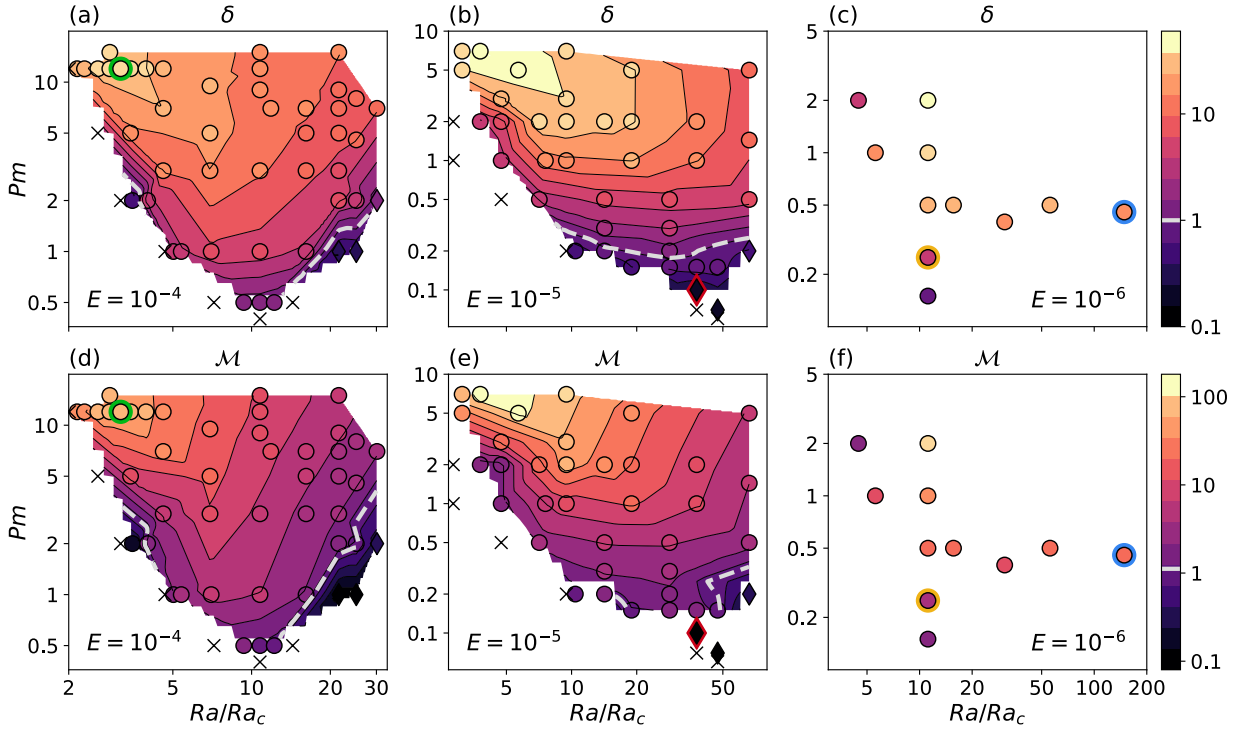


Figure 5.3: Regime diagrams for Ekman numbers $E = 10^{-4}$, $E = 10^{-5}$ and $E = 10^{-6}$ with linear interpolations of the “strong-fieldness” δ (Eq. 5.3.2, panels a-c) and the ratio of the magnetic and kinetic energies \mathcal{M} (Eq. 5.3.3, panels e-f). The light grey dashed lines correspond to a value of 1. The symbols are filled with the values computed from the simulation output. The meaning of the symbols is the same as in Fig. 5.1. The symbols of the models given in Table 5.1 are highlighted by coloured edges.

which represents a proxy for the relative magnitudes of the Lorentz force and inertia. The linear interpolations of \mathcal{M} for the explored parameter space are shown in Fig. 5.3d-f. Comparison of the integral diagnostic \mathcal{M} to δ shows a broad agreement. The discrepancy in the amplitude between the two parameters can be explained by the independence of \mathcal{M} on length scales, while they are inherently included in the definition of δ due to the explicit calculation of the forces. Additionally, viscosity still represents a sizeable contribution at large Ekman numbers.

5.3.1.2 Cross-over length scale

Following Aubert et al. (2017), we use the spectral representations of the forces to introduce the cross-over length scales d_{\perp} . These are defined as the length scales where two forces are of equal amplitude. This implies that these forces are in balance under the constraint of some remainder of the Coriolis force. Hence, this scale corresponds in fact to a three-terms balance. To obtain the cross-over length scale which corresponds to the first-order force balance, we therefore determine the spherical harmonic degree, ℓ_{MA} , where buoyancy and the Lorentz force are of equal magnitude in the case of QG-MAC dynamos. Analogously, we also identify the cross-overs between buoyancy and inertia, ℓ_{IA} , and buoyancy and viscous forces, ℓ_{VA} , for QG-CIA and QG-VAC (Quasi-Geostrophic Viscous-Archimedean-Coriolis) dynamos, respectively. Hence, we determine the three following spherical harmonic degrees:

$$\ell_{\text{MA}} = \underset{\ell}{\operatorname{argmin}} (|F_{\text{Lorentz},\ell} - F_{\text{buoyancy},\ell}|), \quad (5.3.4)$$

$$\ell_{\text{IA}} = \underset{\ell}{\operatorname{argmin}} (|F_{\text{inertia},\ell} - F_{\text{buoyancy},\ell}|), \quad (5.3.5)$$

$$\ell_{\text{VA}} = \underset{\ell}{\operatorname{argmin}} (|F_{\text{viscous},\ell} - F_{\text{buoyancy},\ell}|). \quad (5.3.6)$$

For our example cases (see Table 5.1), the cross-overs are highlighted by vertical dashed lines in Fig. 5.2. The associated length scales are defined as $d_{\perp} = \pi/\ell_{\perp}$. Note that none of the investigated models exhibits a first-order QG-VAC balance since we exclude viscous boundary layers from the integration of the forces and the bulk viscosity is too small to enter the first-order force balance. Several dynamos close to the onset of dynamo action feature force balances where the Lorentz force, inertia and buoyancy are of the same order of magnitude. Due to the lack of separation between the three forces, it does not make sense to define a cross-over length scale based on one individual force in such cases. Dynamos featuring a force balance with ill-posed cross-overs, e.g. model **C** (see Fig. 5.2c), also do not allow the determination of a unique relevant cross-over length scale.

5.3.2 Convective pattern

To qualitatively analyse the effect of the governing force balance on the dominant length scale of the convective flow, we turn to the equatorial planes of the radial velocity of the dynamos, which are presented in Fig. 5.4.

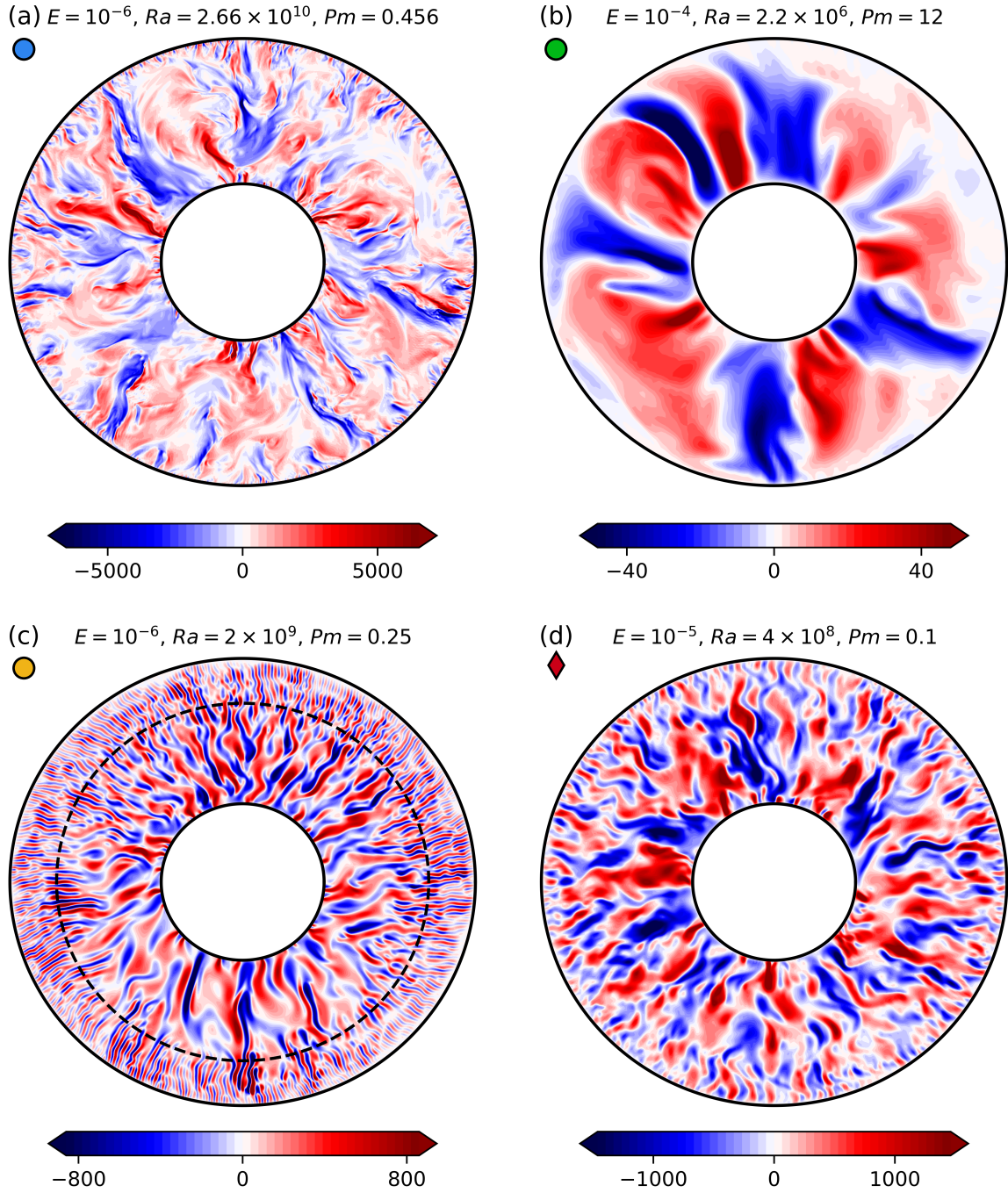


Figure 5.4: Radial velocity in the equatorial plane for the four simulations highlighted in Fig. 5.1. The abrupt change of the convective length scale towards the outer boundary in the equatorial plane of model **C** (panel c) is highlighted by a dashed circle at radius $r \sim 0.8 r_o$.

In the equatorial planes of both QG-MAC dynamos (models **A** and **B**) one can observe elongated structures of the scale of the system size despite the large difference in the input parameters (see Fig. 5.4a-b). Since model **A** is far more supercritical than model **B**, it also shows a greater range of length scales with small-scale features developing close to the outer boundary (e.g., Sakuraba and Roberts, 2009). The equatorial plane of model **C** (see Fig. 5.4c) features a rather abrupt change in the size of the convective cells as it transitions from large elongated structures in the interior of the shell to very small scales towards the outer boundary. Yadav et al. (2016) also observed such layers of small-scale convection in their simulations at $E = 10^{-6}$, which they attributed to a weak Lorentz force in these regions. The equatorial plane of the multipolar dynamo (model **D**, see Fig. 5.4d) shows mostly small convective scales, which resemble that of non-magnetic convection due to inertia being much stronger compared to the Lorentz force (see Fig. 5.2d) (e.g., Gillet and Jones, 2006; Gastine et al., 2016). A gradual decrease of the convective scale with radius can also be observed in the equatorial plane of the multipolar dynamo.

The dominant length scales of these models can be characterised by the peaks of the poloidal kinetic energy spectra:

$$\ell_{\text{pol}} = \underset{\ell}{\operatorname{argmax}} (\mathcal{E}_{\text{pol}}). \quad (5.3.7)$$

Comparison of the cross-over length scales to the observed number of up- and downwellings, as well as to ℓ_{pol} , shows a satisfactory agreement for the QG-MAC cases (models **A** and **B**). This becomes, however, more challenging for models **C** and **D** due to the overall smaller convective cells and the additional strong radial dependence of the length scales. This suggests that analysing the radial dependence of the force balances will help to fully understand how the cross-over length scales relate to the observed convective scales.

5.3.3 2D force spectra

Changes of the convective length scale in the radial direction, like in the equatorial plane of case **C** (see Fig. 5.4c), suggest an underlying change in the dominant force balance with radius. To quantify this effect, we introduce a measure of the local forces defined as:

$$F_{\ell}^2(r) = \sum_{m=0}^{\ell} F_{\ell m}^2. \quad (5.3.8)$$

The resulting 2D force spectra of the dynamo models discussed above are illustrated in Fig. 5.5. We exclude pressure and Coriolis forces from this representation since all investigated models are, on global scales, quasi-geostrophic at zeroth order, and restrict our focus on the contributions of first- and second-order forces.

The 2D spectra of the QG-MAC dynamos (models **A** and **B**, see Fig. 5.5a-b) show a balance between the ageostrophic Coriolis force and buoyancy on large scales (small spherical harmonic degrees) and by the Lorentz force on small scales (large ℓ) for all radii (excluding viscous boundary layers). In model **A** the Lorentz force is very strong

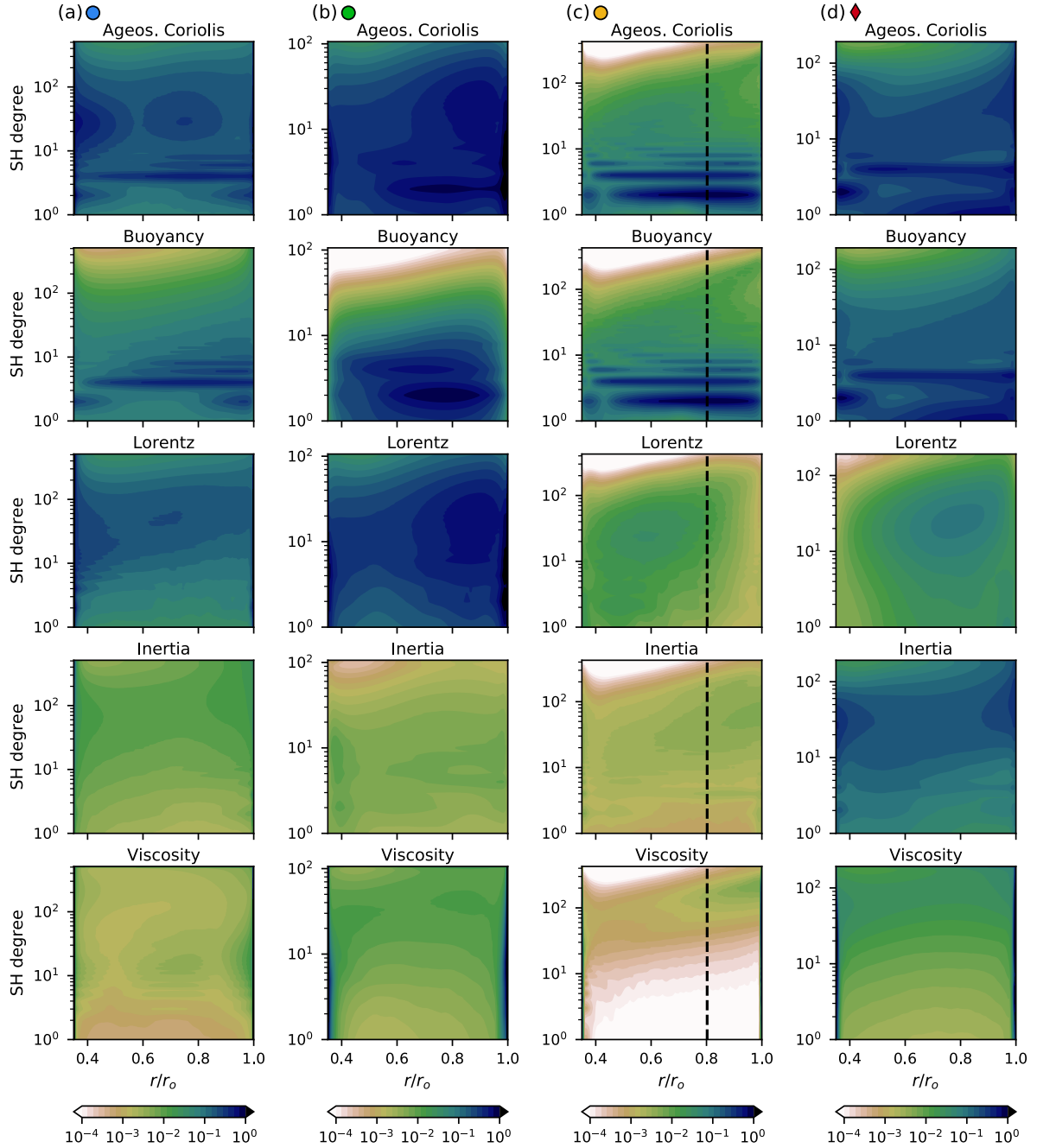


Figure 5.5: 2D force balance spectra of the dynamo models highlighted in Fig. 5.1. The geostrophic balance formed by pressure and Coriolis force is omitted since it is on a global scale present in all of the investigated dynamo models. The 2D force spectra of each model are normalised by the maximum of the forces excluding the viscous boundary layers. The vertical dashed lines at $r \sim 0.8 r_o$ in panel (c) correspond to the change of the convective length scale that can be observed in the equatorial plane of model C (see Fig. 5.4c).

throughout the entire volume. Yet, one can observe a maximum close to the inner boundary from which it tends to decrease with increasing radius. Model **B** also displays a strong Lorentz force throughout the entire shell, however, with a localised maximum towards the outer boundary at intermediate length scales. Note that buoyancy only slightly depends on radius in model **A**, while in model **B** it is significantly larger in the inner part of the volume compared to the boundaries. This is expected as the lower vigour of convection in models with Rayleigh numbers close to the onset of convection leads to a overall less efficient heat transport, and therefore to the formation of thick thermal boundary layers.

In the 2D force spectra of model **C** (see Fig. 5.5c), the ageostrophic Coriolis force is balanced by buoyancy and Lorentz force for radii $r \lesssim 0.8 r_o$, therefore exhibiting a first-order QG-MAC balance which explains the elongated flow structures in this portion of the volume. However, the Lorentz force is overall considerably weaker on small length scales compared to most QG-MAC dynamos. For larger radii, we observe a significant decrease of the Lorentz force. Additionally, inertia and viscosity increase towards the outer boundary. As a consequence, the ageostrophic Coriolis force is in the outer part of the shell almost entirely balanced by buoyancy and to a smaller extent by inertia and viscous forces. Since inertia and viscous forces are slightly larger than the Lorentz force in this region, the force balance of the dynamo is close to a QG-CIA/QG-VAC regime which appears to be the reason for the layer of small-scale convection that is visible in Fig. 5.4c. This change in the governing force balance depending on the radius also explains why the cross-over length scale in the fully integrated force balance spectrum is ill-posed for model **C** (see Fig. 5.2c).

In the multipolar dynamo (model **D**, see Fig. 5.5d), the ageostrophic Coriolis force is largely balanced by buoyancy and inertia at all radii. The Lorentz force remains smaller than inertia throughout the entire shell, and therefore does never contribute to the first-order force balance. As a consequence, the dynamo is controlled by a QG-CIA balance throughout the entire shell.

The 2D force spectra of all four models show that the viscosity is predominantly confined to the inner and outer boundaries, which justifies our decision to exclude the viscous boundary layers when calculating the integrated forces (see Eq. 5.3.1). While at $E = 10^{-4}$ the viscous boundary layers still extend into the shell, they become very thin at lower Ekman numbers like $E = 10^{-6}$. At $E = 10^{-4}$, both the bulk viscosity and inertia are only about one order of magnitude smaller than the leading order forces. Hence, they may still significantly influence the overall force balance. Decreasing the Ekman number to $E = 10^{-6}$ leads to the bulk viscosity and inertia being two to three orders of magnitude lower than the first-order forces.

5.3.3.1 Cross-over length scales of 2D force spectra

The 2D force spectra further allow us to determine the cross-over length scales at each radial level. To obtain an idea on how well these match the convective scale in the equatorial plane, we compare them to $\ell_{\text{pol}}(r)$. Fig. 5.6 illustrates the 2D spectra of the poloidal kinetic energy for the four example cases, along with the cross-over length scales linked to the different types of force balances for each radial level. While it is generally possible to

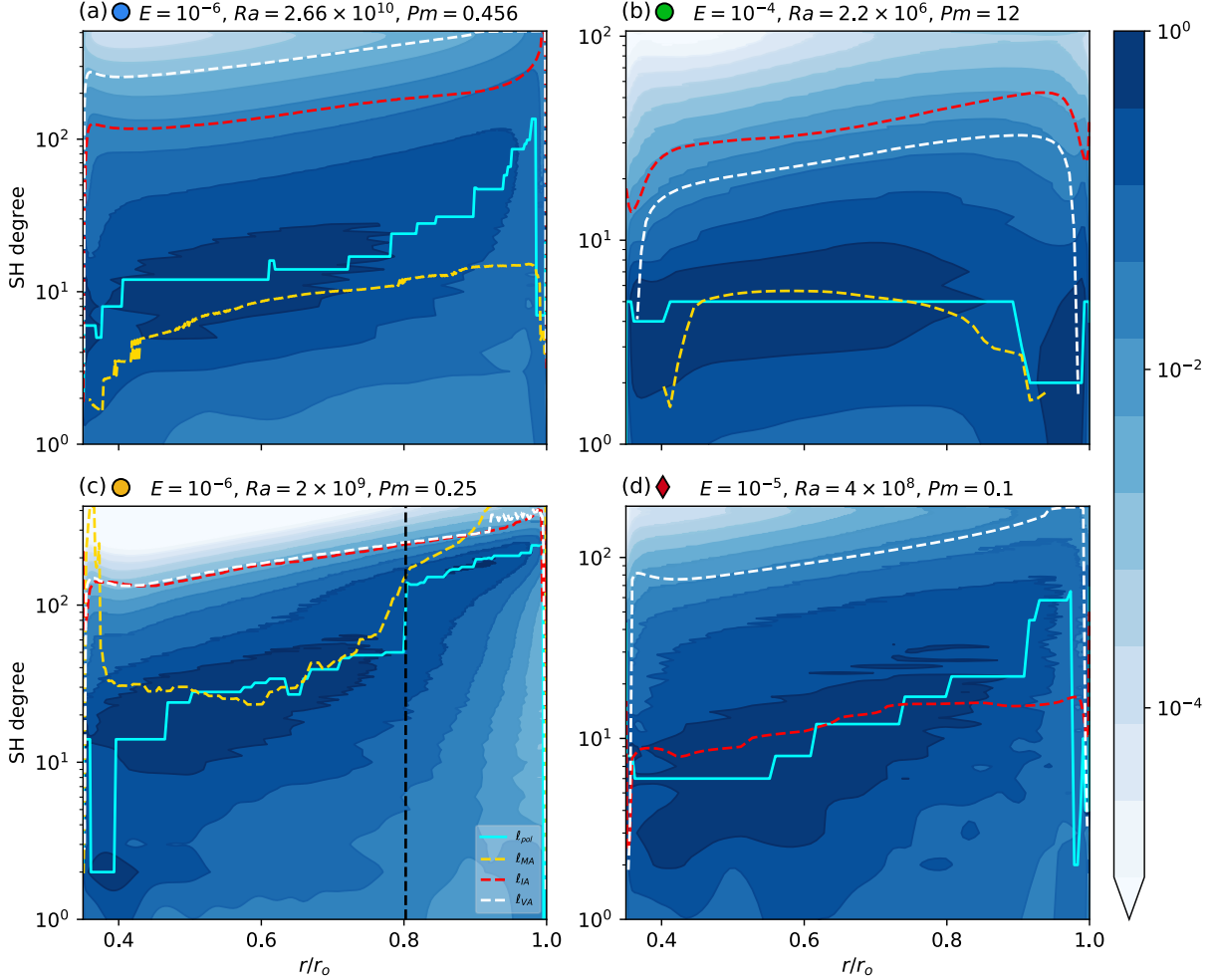


Figure 5.6: 2D-spectra of the poloidal kinetic energy of the dynamo models highlighted in Fig. 5.1. Each 2D-spectrum is normalised by its maximum value. The solid blue line connects the peaks of the poloidal kinetic energy spectra (ℓ_{pol}) for each each radial level. The dashed lines are the harmonic degrees of the crossings in the corresponding force balance spectra; yellow: ℓ_{MA} , scale at which buoyancy and Lorentz force are equal; red: ℓ_{IA} , scale at which buoyancy and inertia are equal; grey: ℓ_{VA} , scale at which buoyancy and viscous forces are equal. The vertical dashed line at $r \sim 0.8 r_o$ in panel (c) corresponds to the change of the convective length scale that can be observed in the equatorial plane of model **C** (see Fig. 5.4c).

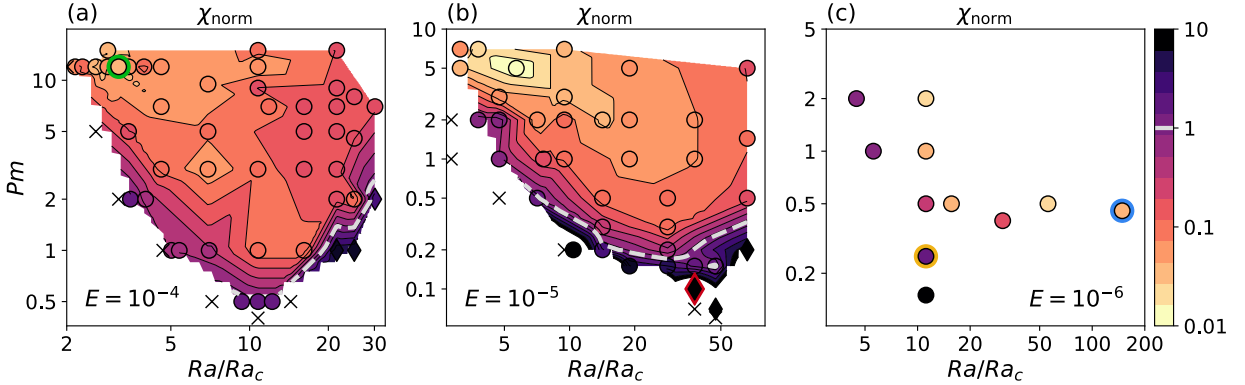


Figure 5.7: Regime diagrams for Ekman numbers $E = 10^{-4}$, $E = 10^{-5}$ and $E = 10^{-6}$ with linear interpolations of χ_{norm} (Eq. 5.3.10), with small values of χ_{norm} corresponding to QG-MAC dynamos and large values to non-QG-MAC dynamos. The symbols are filled with the values computed from the simulation outputs. The meaning of the symbols is the same as in Fig. 5.1. The symbols of the models given in Table 5.1 are highlighted by coloured edges.

determine the scales at which the buoyancy-inertia and buoyancy-viscous pairs are of equal magnitude for nearly all radii, the crossing between buoyancy and Lorentz force becomes ill-posed in the thermal boundary layers, where buoyancy is weak. This is especially the case for the strong-field dynamos that are run at low supercritical Rayleigh numbers and are therefore only weakly driven, which leads to the formation of thick thermal boundary layers. In several multipolar dynamos and dynamos close to the onset of convection it is also not possible to determine ℓ_{MA} in some parts of the volume, or in a few cases even the entire shell, because of the Lorentz force being too weak relative to buoyancy.

Fig. 5.6a-b show that for both QG-MAC dynamos (models **A** and **B**) ℓ_{MA} is in good agreement with ℓ_{pol} in the bulk of the volume. In addition, ℓ_{IA} and ℓ_{VA} do not match ℓ_{pol} with the exception of the viscous boundary layers, where viscosity and therefore ℓ_{VA} becomes relevant. The separation between the length scales corresponding to the different force balances is larger in model **A** compared to model **B** since it operates at a lower Ekman number.

For model **C** (see Fig. 5.6c), ℓ_{MA} is close to ℓ_{pol} for most of the interior of the volume. Although close to the inner boundary it is not possible to determine a relevant crossing as the spectral contributions of the Lorentz force and buoyancy overlap. This corresponds, however, only to a small portion of the total volume. For the outer region ℓ_{MA} starts to deviate from ℓ_{pol} at $r \gtrsim 0.9r_o$. Beyond this radius, ℓ_{IA} and ℓ_{VA} corresponding to a CIA and VAC balance, respectively, start to match the peaks of the poloidal energy better. This confirms what we observe in the 2D force spectra (see Fig. 5.5c), which revealed a QG-MAC balance in the interior of the shell and a QG-CIA/QG-VAC regime towards the outer boundary. Hence, the agreement of the different cross-over length scales with ℓ_{pol} , i.e. the convective length scales, indeed appears to reflect the force balance at the given radius.

For the multipolar dynamo (model **D**, see Fig. 5.6d), ℓ_{IA} fits ℓ_{pol} best. This is expected

since the first-order force balance corresponds to a CIA balance. Due to the weak Lorentz force it is not possible to determine ℓ_{MA} for this dynamo.

These results suggest that by quantifying the agreement between the peak of the poloidal kinetic energy spectra and the harmonic degrees of the different types of crossings, we can obtain a measure for the type of force balance that controls the dynamo. Therefore, we calculate the volumetric relative misfit between ℓ_{pol} and the crossings ℓ_{\perp} (ℓ_{MA} , ℓ_{IA} and ℓ_{VA}) using the following formula:

$$\chi_i = \sqrt{\frac{4\pi}{V} \int_r \left(\frac{\ell_{\text{pol}}(r) - \ell_{\perp}(r)}{\ell_{\text{pol}}(r)} \right)^2 r^2 dr}, \quad (5.3.9)$$

where $i = [\text{MAC}, \text{CIA}, \text{VAC}]$. We again exclude viscous boundary layers. Additionally, we restrict the computation of the misfits of all three types of crossings to the part of the volume where ℓ_{MA} is defined. Since the focus of our study is on finding dynamo models with a force balance relevant to the Earth's core conditions, a simple classification in QG-MAC and non-QG-MAC dynamos is sufficient at first. Therefore, we normalise the misfit that we obtain for the QG-MAC balance by the one for the next best fitting force balance (either QG-CIA or QG-VAC), i.e.

$$\chi_{\text{norm}} = \frac{\chi_{\text{MAC}}}{\min(\chi_{\text{CIA}}, \chi_{\text{VAC}})}. \quad (5.3.10)$$

This allows us to quantify the discrepancy between the misfit of the cross-over length scales corresponding to a QG-MAC balance and the other types of force balances and therefore essentially whether the dynamo is controlled by a QG-MAC balance or not. Linear interpolations of χ_{norm} for the investigated parameter space are shown in Fig. 5.7. Comparison of Fig. 5.7 to the same type of representation for δ and \mathcal{M} (see Fig. 5.3) shows that in the region of the parameter space at low Ra/Ra_c and high Pm , where one can find the strong-field dynamos, we also observe the smallest values for χ_{norm} , i.e. the best agreement between ℓ_{pol} and ℓ_{MA} . One notable difference is that δ and \mathcal{M} transition generally quite smoothly throughout the parameter space from large to small values as indicated by the equidistant spacing of the contour lines. For χ_{norm} , however, the smaller values found in the region of strong-field dynamos extend to lower values of Pm , before decaying rather steeply near the onset of dynamo action and close to the transition from the dipolar to the multipolar regime. Therefore, χ_{norm} seems to allow for a better distinction between the different force balance regimes. Decreasing the Ekman number gradually extends the boundaries of the QG-MAC regime towards lower Pm and higher Ra/Ra_c .

5.4 Discussion

Dynamo action in the Earth's outer core is expected to be controlled by a balance between pressure, Coriolis, buoyancy and Lorentz forces, with marginal contributions from inertia and viscous forces (e.g., Roberts and King, 2013). Current numerical simulations of the

geodynamo, however, operate at much larger inertia and viscosity because of computational limitations. This has led to conflicting interpretations of the classical data set, casting some doubt on the physical relevance of these models.

By performing a systematic survey of the numerically accessible parameter space, we attempted to provide a better understanding of the force balances controlling the flow dynamics in dynamo models. To this end, we resorted to the length scale based approach introduced by [Aubert et al. \(2017\)](#) and decomposed the amplitudes of the forces into spherical harmonic contributions. We extended this method by additionally looking at the radial dependence of a local force balance measure to analyse possible transitions within the fluid volume. Based on the agreement of the thereby obtained cross-over scales, i.e. scales where three forces are in balance, and the convective scales, we introduced a measure that allows to categorise the force balances into three end-member cases. In agreement with recent studies (e.g., [Yadav et al., 2016](#); [Aubert et al., 2017](#); [Schaeffer et al., 2017](#)), we find that the majority of the dipole-dominated dynamos are at leading order controlled by a quasi-geostrophic balance between pressure and the Coriolis force. The ageostrophic part of the Coriolis force is then balanced by buoyancy on large scales and the Lorentz force on small scales. This QG-MAC balance seems to be very stable throughout the parameter space, with the exception of boundary regimes. Beyond the transition from the dipolar to the multipolar regime inertial effects become more significant so that inertia now balances the ageostrophic Coriolis force at small scales, while the Lorentz force becomes secondary. The resulting dynamos are therefore governed by a QG-CIA balance at leading order. Close to the onset of dynamo action the Lorentz force also falls onto or below the level of inertia and viscous forces. As a result the QG-MAC balance is lost in these regions for at least parts of the fluid volume. Therefore, one may refer to these dynamos as QG-Hybrid cases. These three different force balance regimes are summarised in a sketch in [Fig. 5.8](#). Decreasing the Ekman number extends the region of dynamos controlled by a QG-MAC balance towards lower values of Pm , while the transition to the QG-CIA regime (the multipolar regime) moves towards higher supercriticalities.

Analysis of the “strong-fieldness” and the ratio of magnetic and kinetic energies of the dynamos confirms that the strongest-field dynamos can be found in the parts of the parameter space with high Pm and low Ra/Ra_c as suggested by [Dormy \(2016\)](#). This is mainly a result of the role of inertia being minimised at low supercriticalities. When decreasing the Ekman number, this region of strong-field dynamos will therefore by construction expand to larger supercriticalities due to the increase of rotational effects on the fluid. These strong-field dynamos do indeed approach magnetostrophy when considering volume-integrated forces. However, the introduction of a finer length scale dependent force balance analysis revealed that these cases are actually controlled by a QG-MAC balance comparable to most dynamo models published to date.

Most dynamo models feature a nearly radially independent force balance. However, in several QG-MAC dynamos a gradual decrease of the convective scale can be observed towards the outer boundary. This can be attributed to a smaller Lorentz force in this region (e.g., [Yadav et al., 2016](#)). Yet, it does not involve a change of the leading-order

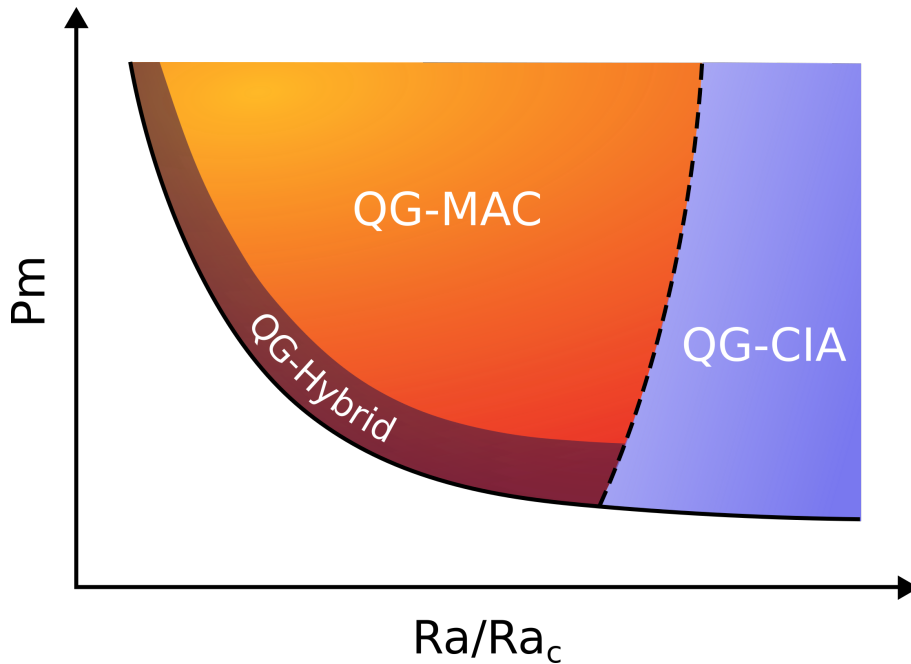


Figure 5.8: Sketch of the three different force balance regimes attained in our study independent of the Ekman number. The dashed line marks the transition between the dipolar and multipolar regime.

force balance. However, by lowering Pm dynamos can be found for which the convective length scale changes very abruptly from elongated structures in the interior of the shell to small-scale convection in the outer part. The 2D analysis of the force balance spectra showed that for these cases the force balance changed from a QG-MAC balance in the interior to a mixed QG-CIA/QG-VAC balance towards the outer boundary. By further decreasing Pm the QG-MAC balance is gradually lost in larger parts of the volume. This stands in contrast to a common strategy in dynamo modelling, which is to decrease Pm as much as possible to approach Earth’s core conditions (e.g., [Sheyko et al., 2016](#)). Our results, however, show that following this approach may lead to a significant decrease of the Lorentz force and therefore to the loss of the physically relevant force balance when getting too close to the onset of dynamo action. Strategies such as employed by [Dormy \(2016\)](#) and [Aubert et al. \(2017\)](#), which aim at preserving the governing force balance when decreasing the Ekman number (by keeping a constant relation between the control parameters), are immune to this.

Future work should focus on asserting the Ekman number dependence of the boundaries of the different force balance regimes. It would also be of interest to perform a more in depth analysis of length scales.

Acknowledgements

We would like to thank two anonymous reviewers for their constructive comments and Rakesh Yadav for kindly providing the restart files of the dynamo models at $E = 10^{-6}$ that were studied by [Yadav et al. \(2016\)](#). We acknowledge support from the Fondation Del Duca of Institut de France (JA, 2017 Research Grant). Numerical computations were performed at S-CAPAD, IPGP and using HPC resources from GENCI-CINES (Grants 2016-A0020402122 and 2018-A0020402122). This project has received funding from the European Union's Horizon 2020 research and innovation programme under the Marie Skłodowska-Curie grant agreement No 665850.

Chapter 6

Relating force balances and flow length scales in geodynamo simulations

This chapter together with Chapter 3 is a reproduction of the Geophysical Journal International (GJI) article [Schwaiger et al. \(2020\)](#). In the published version, Chapter 3 is located in between Sections 6.1 and 6.2. In this study, we show how to relate force balances to convective flow length scales. Thereby, we confirm the dynamical influence of the Lorentz force in dynamo models controlled by a geophysically-relevant force equilibrium. By extrapolating scaling laws to the conditions of the Earth, we propose that the dominant scale of convection in the outer core is about 200 km.

Abstract

In fluid dynamics, the scaling behaviour of flow length scales is commonly used to infer the governing force balance of a system. The key to a successful approach is to measure length scales that are simultaneously representative of the energy contained in the solution (energetically relevant) and also indicative of the established force balance (dynamically relevant). In the case of numerical simulations of rotating convection and magneto-hydrodynamic dynamos in spherical shells, it has remained difficult to measure length scales that are both energetically and dynamically relevant, a situation that has led to conflicting interpretations, and sometimes misrepresentations of the underlying force balance. By analysing an extensive set of magnetic and non-magnetic models, we focus on two length scales that achieve both energetic and dynamical relevance. The first one is the peak of the poloidal kinetic energy spectrum, which we successfully compare to crossover points on spectral representations of the force balance. In most dynamo models, this result confirms that the dominant length scale of the system is controlled by a previously proposed quasi-geostrophic (QG-) MAC (Magneto-Archimedean-Coriolis) balance. In non-magnetic convection models, the analysis generally favours a QG-CIA (Coriolis-Inertia-Archimedean)

balance. Viscosity, which is typically a minor contributor to the force balance, does not control the dominant length scale at high convective supercriticalities in the non-magnetic case, and in the dynamo case, once the generated magnetic energy largely exceeds the kinetic energy. In dynamo models, we introduce a second energetically relevant length scale associated with the loss of axial invariance in the flow. We again relate this length scale to another crossover point in scale-dependent force balance diagrams, which marks the transition between large-scale geostrophy (the equilibrium of Coriolis and pressure forces) and small-scale magnetostrophy, where the Lorentz force overtakes the Coriolis force. Scaling analysis of these two energetically and dynamically relevant length scales suggests that the Earth's dynamo is controlled by a QG-MAC balance at a dominant scale of about 200 km, while magnetostrophic effects are deferred to scales smaller than 50 km.

6.1 Introduction

Turbulent convective motions of liquid metal in the Earth's outer core initiate dynamo action that maintains the geomagnetic field. Based on the magneto-hydrodynamic theory of convection-driven dynamos, it is known that the fluid flow in the Earth's core is influenced by six different forces, namely Coriolis, pressure, buoyancy, Lorentz, inertial and viscous forces. Our main tool to study their relative importance and thus to know which dynamical regime the Earth's core is in, are dimensionless numbers, which can be computed from the core's physical properties (see Table 6.1). These can be interpreted as order of magnitude estimates of the ratio between two forces. Since the Earth is a rapidly-rotating system, the relative strengths of the individual forces with respect to the Coriolis force are considered. In the following, we adopt the thickness of the outer core L as a characteristic flow length scale. The dimensionless numbers therefore only provide an estimate of the global-scale force balance. It can be expected that the force balance differs at smaller scales.

The ratio between viscous and Coriolis forces can be estimated with the help of the Ekman number

$$E = \frac{\nu}{\Omega L^2} \sim \mathcal{O}(10^{-15}), \quad (6.1.1)$$

while the relative amplitude of inertia compared to Coriolis forces is given by the Rossby number

$$Ro = \frac{U}{\Omega L} \sim \mathcal{O}(10^{-6}). \quad (6.1.2)$$

In the above two definitions, Ω denotes the Earth's rotation rate, U a characteristic flow velocity and ν the kinematic viscosity. The smallness of E and Ro allows us to conclude that in the Earth's core inertial and in particular viscous contributions are insignificant compared to rotational effects at large scales. The strength of buoyancy relative to Coriolis forces can be estimated by defining the following buoyancy number

$$Bu = \frac{\alpha T' g_o}{\Omega U} \sim \mathcal{O}(10^{-1}), \quad (6.1.3)$$

where α represents the thermal expansion coefficient, T' a superadiabatic temperature perturbation and g_o the gravity at the core-mantle boundary. The ratio between Lorentz and Coriolis forces in planetary dynamos is often assessed by evaluating the traditional form of the Elsasser number, which is defined by

$$\Lambda_t = \frac{B^2}{\rho\mu\lambda\Omega} \sim \mathcal{O}(10), \quad (6.1.4)$$

where B is the magnetic field strength, ρ the fluid density, μ the magnetic permeability and λ the magnetic diffusivity. This definition suggests a dominant role of the Lorentz force in governing the flow dynamics. However, it has been argued that the traditional Elsasser number is an unreliable measure of the force ratio due to some of the underlying assumptions possibly not being fully satisfied in turbulent dynamos (see e.g. [Soderlund et al., 2012, 2015](#); [Dormy, 2016](#)). A more exact estimate can be obtained using the so-called dynamic Elsasser number (e.g. [Christensen et al., 1999](#); [Cardin et al., 2002](#); [Soderlund et al., 2012, 2015](#))

$$\Lambda_d = \frac{B^2}{\rho\mu\Omega UL} \sim \mathcal{O}(10^{-2}). \quad (6.1.5)$$

In contrast to Λ_t , the dynamic Elsasser number indicates that the Lorentz force is two orders of magnitude smaller than the Coriolis force, suggesting that convection dynamics are rotationally-dominated. The final force that has not been considered so far is the one due to pressure. In the case of negligible inertia and viscosity, the pressure force compensates the part of the Coriolis force that is not balanced by buoyancy and Lorentz forces. The hierarchy of the forces indicated by dimensionless numbers is different depending on which Elsasser number is used to estimate the Lorentz force. It is clear, however, that in either case viscosity and inertia represent the least important contributions, since they are far smaller than the other four forces. When considering the dynamic Elsasser number, buoyancy and Lorentz forces come about one or two orders of magnitude below the prevailing force equilibrium between pressure and Coriolis forces. The leading-order force balance in this case is therefore geostrophic (e.g. [Busse, 1970](#)). The traditional Elsasser number, on the other hand, suggests a much stronger Lorentz force, so that the dominant force balance would be between pressure, Coriolis and Lorentz forces, which is termed magnetostrophic (MS) balance (e.g. [Roberts, 1978](#)). As already pointed out above, the non-dimensional numbers only provide information about the force balance on the system scale. The true force balance in the Earth's core is likely more complicated due to the length-scale dependence of the forces (e.g. [Aurnou and King, 2017](#); [Aubert et al., 2017](#)). Based on scaling analysis of Λ_d (Eq. 6.1.5), which is described in detail in Section 3.2, [Aurnou and King \(2017\)](#) for instance argued that only the large-scale flow is predominantly geostrophic, while magnetostrophy occurs on smaller scales.

The nature of the leading-order force balance has a significant effect on the convective pattern. A dominant geostrophic balance would result in convection being primarily organised into columnar eddies that are aligned with the rotation axis as a result of the so-called

Table 6.1: Typical estimates of physical properties of the Earth’s outer core. References: 1 = [Dziewonski and Anderson \(1981\)](#), 2 = [Pozzo et al. \(2013\)](#), 3 = [Gomi et al. \(2013\)](#), 4 = [Jones \(2015\)](#), 5 = [Stacey \(1993\)](#), 6 = [Pozzo et al. \(2012\)](#), 7 = [Finlay and Amit \(2011\)](#), 8 = [Gillet et al. \(2010\)](#).

Symbol	Definition	Estimate	Reference
Ω	Rotation rate	$7.29 \times 10^{-5} \text{ s}^{-1}$	
L	Thickness of outer core	$2.26 \times 10^6 \text{ m}$	1
ρ	Mean core density	$1.1 \times 10^4 \text{ kg m}^{-3}$	1
g_o	Gravity at core-mantle boundary	10.68 m s^{-2}	1
μ	Magnetic permeability	$4\pi \times 10^{-7} \text{ H m}^{-1}$	
ν	Kinematic viscosity	$10^{-6} \text{ m}^2 \text{ s}^{-1}$	2
α	Thermal expansion coefficient	10^{-5} K^{-1}	3
T'	Typical superadiabatic temperature perturbation	10^{-4} K	4
c_p	Specific heat capacity at constant pressure	$850 \text{ J kg}^{-1} \text{ K}^{-1}$	5
k	Thermal conductivity	$100 \text{ W m}^{-1} \text{ K}^{-1}$	6
κ	Thermal diffusivity	$10^{-5} \text{ m}^2 \text{ s}^{-1}$	$\kappa = k/\rho c_p$
λ	Magnetic diffusivity	$0.7 \text{ m}^2 \text{ s}^{-1}$	6
U	Typical flow velocity	$4 \times 10^{-4} \text{ m s}^{-1}$	7
B	Typical magnetic field strength	$4 \times 10^{-3} \text{ T}$	8

Proudman-Taylor theorem. In the case of magnetostrophy, on the other hand, the Lorentz force would be able to relax this rotational constraint, and thus break up the columnarity of the flow, resulting in larger scale flow. Core flow inversions based on observations of the secular variation of the Earth's magnetic field show consistency with leading-order geostrophy (e.g. Pais and Jault, 2008; Gillet et al., 2012; Aubert, 2020). However, solutions to the core flow problem are non-unique, and the unknown contribution from unresolved length scales in the magnetic field and secular variation limits the spatial resolution of the inverted flows to spherical harmonic degrees well below $\ell = 14$ (e.g. Hulot et al., 2015). Therefore, smaller unresolvable scales could still be in a magnetostrophic state.

In addition to observations and theoretical considerations, numerical simulations are an important tool for our understanding of the geodynamo mechanism. Computational constraints make it currently impossible to simulate the extreme range of spatial and temporal scales present in the Earth's core (e.g. Schaeffer et al., 2017). Nonetheless, dynamo models can provide valuable insights into our planet's core dynamics if they operate in a relevant force balance regime, since this would allow a meaningful extrapolation of the numerical results to realistic parameters. Two different approaches have been used to assess the dynamical regime such simulations operate in. First, the comparison of the scaling behaviour of measured flow length scales to scaling laws, which allows one to infer the underlying force balance. Second, the explicit calculation of the magnitude of the individual forces.

The analysis of the scaling behaviour of convective length scales in geodynamo simulations has not resulted in an agreement with a scaling law based on a geophysically-relevant force balance (see Chapter 3 for details about the scaling laws). Instead, it has been shown that typical flow length scale measures roughly follow the viscous scaling (e.g. King and Buffett, 2013; Oruba and Dormy, 2014). This has led to the suggestion that convection in numerical dynamos is viscously-controlled and therefore not applicable to the Earth's core.

Explicit calculations of the root-mean-square (r.m.s.) strength of the forces in the dynamo models (e.g. Wicht and Christensen, 2010; Soderlund et al., 2012; Yadav et al., 2016; Aubert et al., 2017; Aubert, 2019; Schwaiger et al., 2019) did not confirm a dominant role of viscosity. Instead, these studies showed that the force equilibrium in geodynamo simulations is typically composed of a zeroth-order balance between Coriolis and pressure forces, followed by a balance between buoyancy, Lorentz and ageostrophic Coriolis forces. This type of force balance has been referred to as quasi-geostrophic Magneto-Archimedean-Coriolis (QG-MAC) balance (Aubert, 2019; Schwaiger et al., 2019). Inertia and viscosity were found to be second-order contributions, although the difference between them and the first-order forces proved to be rather small in models computed at moderate control parameters, in particular if viscous boundary layers are not excluded (Soderlund et al., 2012). Recent high-resolution simulations (e.g. Yadav et al., 2016; Aubert et al., 2017; Schaeffer et al., 2017; Aubert, 2019) in advanced parameter regimes showed that the relative importance of viscosity and inertia decreases in more realistic setups. The leading-order structure of the force balance, however, remains essentially unchanged. While these studies brought more insight to the discussion about the underlying physics in numerical dynamos, it has still remained an outstanding task to successfully relate force balances to convective

flow length scales.

The contradiction between the results obtained by applying theoretical scalings to a flow length scale and the explicit force balance calculation is likely the result of two often overlooked questions: *(i)* How do we estimate length scales that are sufficiently representative of the energy contained in the solution? *(ii)* Is the length scale measure representative of the underlying force equilibria?

The recent introduction of a spectral analysis of the forces by [Aubert et al. \(2017\)](#) has provided access to the length scale dependence of the force balance. This approach revealed that the zeroth-order force balance in geophysically-relevant numerical models is either geostrophic at all scales, or subdivided into large-scale geostrophy and small-scale magnetostrophy. Similarly, in the first-order MAC equilibrium the ageostrophic Coriolis force is predominantly balanced by buoyancy at large scales, and by the Lorentz force towards smaller scales. The respective transitions between large- and small-scale balances define triple points, at which three forces are of comparable magnitude. The associated length scales are referred to as cross-over length scales, which are by construction characteristic of the underlying physics. The goal of this paper is to relate them to energetically relevant flow length scales, as well as to theoretical scaling laws. To this end, we will analyse a series of dynamo models as well as non-magnetic rotating convection models for comparison. The study presented here is a follow-up to [Schwaiger et al. \(2019\)](#), where the force balance in the considered dynamo models was systematically analysed, and to [Aubert et al. \(2017\)](#) and [Aubert \(2019\)](#), in which the force balance tools and the concept of cross-over length scales were introduced.

We describe the numerical models and methods in Section 6.2. The results of our study are presented and discussed in Sections 6.3 and 6.4. Our conclusions are summarised in Section 6.5. Note that throughout the manuscript, when we use the terms ‘dominant’ or ‘leading-order’ force balance, we refer to the zeroth-order force equilibrium.

6.2 Methods

6.2.1 Numerical models

For the present study, we extend the set of numerical dynamo models analysed by [Schwaiger et al. \(2019\)](#) with non-magnetic rotating convection models. In both sets of simulations, we consider a spherical shell rotating about the axis \mathbf{e}_z with constant angular frequency Ω , with a ratio between the inner and outer radii of $r_i/r_o = 0.35$. The shell is filled with an incompressible fluid of density ρ and kinematic viscosity ν , which is electrically conducting in the dynamo models and electrically insulating in the rotating convection models. An imposed temperature difference $\Delta T = T_o - T_i$ between the two bounding spheres drives convection of the fluid. In addition to being held at constant temperatures, both boundaries are mechanically rigid and electrically insulating.

We solve the dimensionless magneto-hydrodynamic equations under the Boussinesq approximation for the velocity field \mathbf{u} , magnetic field \mathbf{B} and temperature T . The shell

depth $L = r_o - r_i$ serves as the reference length scale and the viscous diffusion time L^2/ν is the time unit. The temperature is scaled by ΔT , and the magnetic field by $\sqrt{\rho\mu\lambda\Omega}$, where μ is the magnetic permeability and λ the magnetic diffusivity. The dimensionless gravity profile is assumed to be linear and follows $g(r) = r/r_o$. Hence, we end up with the following system of equations:

$$\frac{\partial \mathbf{u}}{\partial t} + \mathbf{u} \cdot \nabla \mathbf{u} + \frac{2}{E} \mathbf{e}_z \times \mathbf{u} = -\nabla p + \frac{Ra}{Pr} \frac{\mathbf{r}}{r_o} T + \frac{1}{EPm} (\nabla \times \mathbf{B}) \times \mathbf{B} + \nabla^2 \mathbf{u}, \quad (6.2.1)$$

$$\frac{\partial T}{\partial t} + \mathbf{u} \cdot \nabla T = \frac{1}{Pr} \nabla^2 T, \quad (6.2.2)$$

$$\frac{\partial \mathbf{B}}{\partial t} = \nabla \times (\mathbf{u} \times \mathbf{B}) + \frac{1}{Pm} \nabla^2 \mathbf{B}, \quad (6.2.3)$$

$$\nabla \cdot \mathbf{u} = 0, \quad (6.2.4)$$

$$\nabla \cdot \mathbf{B} = 0, \quad (6.2.5)$$

where p corresponds to the dimensionless pressure. The control parameters governing this set of equations are the Ekman number

$$E = \frac{\nu}{\Omega L^2}, \quad (6.2.6)$$

the hydrodynamic Prandtl number

$$Pr = \frac{\nu}{\kappa}, \quad (6.2.7)$$

the magnetic Prandtl number

$$Pm = \frac{\nu}{\lambda} \quad (6.2.8)$$

and the Rayleigh number

$$Ra = \frac{\alpha g_o L^3 \Delta T}{\nu \kappa}, \quad (6.2.9)$$

where κ is the thermal diffusivity, α the thermal expansion coefficient and g_o the gravity at the outer boundary.

All simulations considered in this study were computed using the open-source code MagIC (Wicht, 2002; Gastine et al., 2016, freely available at <https://github.com/magic-sph/magic>). To numerically solve Eqs. (6.2.1-6.2.5) in the spherical coordinate system (r, θ, φ) , the solenoidal vector fields \mathbf{u} and \mathbf{B} are decomposed into poloidal and toroidal potentials

$$\mathbf{u} = \nabla \times \nabla \times (W \mathbf{e}_r) + \nabla \times (Z \mathbf{e}_r), \quad (6.2.10)$$

$$\mathbf{B} = \nabla \times \nabla \times (G \mathbf{e}_r) + \nabla \times (H \mathbf{e}_r), \quad (6.2.11)$$

where \mathbf{e}_r is the radial unit vector. The spatial discretisation of the unknown scalar fields W , Z , G , H , T and p involves a spherical harmonic expansion up to degree and order ℓ_{\max} in the angular directions, and a Chebyshev decomposition with N_r collocation points in the radial direction. MagIC employs the open-source library SHTns (Schaeffer, 2013, freely available at <https://bitbucket.org/nschaeff/shtns>) for efficient computation of the spherical harmonic transforms. The equations are integrated in time using a semi-implicit adaptive time stepping algorithm. The Coriolis force and the non-linear terms are treated explicitly using a second-order Adams-Bashforth scheme, while the remaining terms are advanced implicitly with a Crank-Nicolson scheme.

To investigate the link between force balances and observable flow length scales, we analyse 95 dynamo models and 24 non-magnetic rotating convection models. The set of dynamo models is nearly identical to the one studied by Schwaiger et al. (2019, Table A1), with the only difference being that the run time of some of the simulations has been increased to improve the statistics of the output parameters. The control parameters and relevant results of the non-magnetic cases can be found in Table B.2.

6.2.2 Energetically relevant length scales

In numerical dynamo and rotating convection models, characteristic length scales of the convective flow are typically obtained from the kinetic energy spectra. In our study, we consider the time-averaged spectrum of the poloidal kinetic energy, which is defined by (see Glatzmaier, 2013, p. 159)

$$\mathcal{E}_{\text{pol}} = \sum_{\ell=0}^{\ell_{\max}} \mathcal{E}_{\text{pol},\ell}, \quad (6.2.12)$$

where

$$\mathcal{E}_{\text{pol},\ell} = \int_{r_i}^{r_o} \sum'_{m=0}^{\ell} \ell(\ell+1) \left[\frac{\ell(\ell+1)}{r^2} |W_{\ell}^m|^2 + \left| \frac{\partial W_{\ell}^m}{\partial r} \right|^2 \right] dr. \quad (6.2.13)$$

In the above expression W_{ℓ}^m is the poloidal flow potential of degree ℓ and order m . The prime on the summation indicates that the $m=0$ contribution entering the sum is multiplied by one half. We choose the peak of the spectrum of \mathcal{E}_{pol} to characterise the convective pattern of the flow in our simulations, i.e.

$$\ell_{\text{pol}} = \underset{\ell}{\operatorname{argmax}} (\mathcal{E}_{\text{pol},\ell}). \quad (6.2.14)$$

The degree ℓ_{pol} can be associated to a length scale \mathcal{L}_{pol} through the definition of the characteristic half-wavelength (see e.g. Backus et al., 1996, p. 101)

$$\mathcal{L}_{\text{pol}} = \frac{\pi r_m}{\sqrt{\ell_{\text{pol}}(\ell_{\text{pol}}+1)}} \approx \frac{\pi r_m}{\ell_{\text{pol}}}, \quad (6.2.15)$$

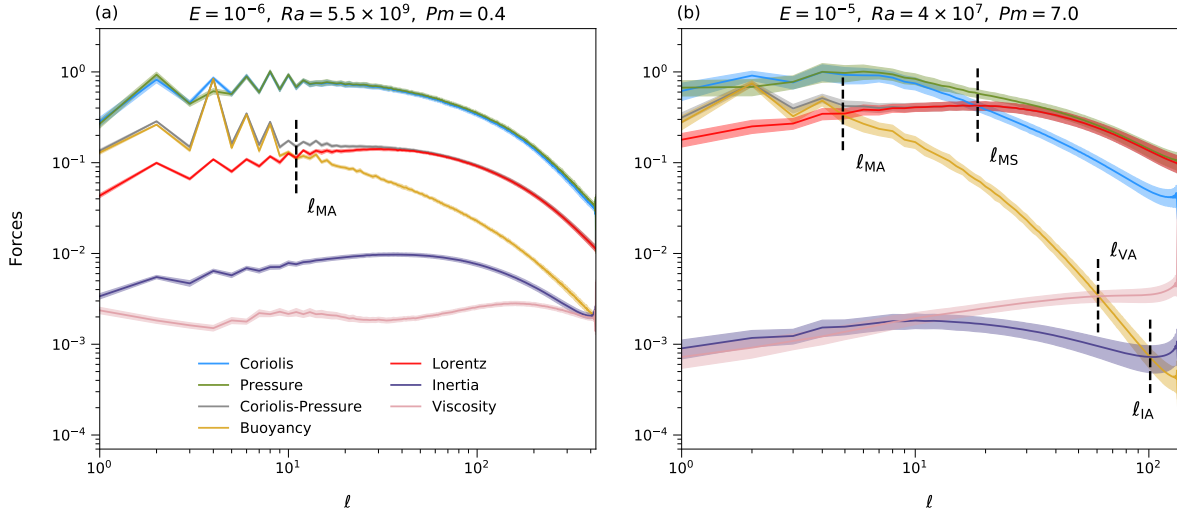


Figure 6.1: Examples of time-averaged force balance spectra for two strong-field QG-MAC dynamos. The amplitudes of the spherical harmonic contributions of the forces are normalised relative to the peak of the Coriolis force. The shaded regions correspond to one standard deviation in time. (a) Force balance of a dynamo ($M = E_{\text{mag}}/E_{\text{kin}} \approx 10$) governed by a prevailing geostrophic balance at all length scales, followed by a first-order MAC balance. (b) Force balance of a dynamo ($M \approx 200$) with a subdivided zeroth-order force balance that is controlled by a geostrophic balance at large scales (small ℓ) that transitions into a magnetostrophic balance towards smaller scales (large ℓ).

where the mid-shell radius $r_m = (r_i + r_o)/2$ is approximated by 1 when $r_i/r_o = 0.35$. As we shall see in Fig. 6.2a, \mathcal{L}_{pol} enables the recovery of results previously obtained with the more commonly used energy-weighted length scale (Christensen and Aubert, 2006), while being more representative of the dominant scale of convection and arguably less sensitive to second-order force balances that would control the tail of the spectrum (e.g. Aubert et al., 2017; Dormy et al., 2018).

6.2.3 Dynamically relevant length scales

To examine whether the energetically relevant flow length scales can be related to the governing force balances, we define dynamically relevant length scales, i.e. length scales that are representative of the underlying force equilibria. To this end, we rely on the spectral representation of the force balance introduced by Aubert et al. (2017). This requires an expression of each force vector \mathbf{f} in terms of scalar potentials, i.e.

$$\mathbf{f} = \mathcal{R}\mathbf{e}_r + r\nabla\mathcal{S} + \mathbf{r} \times \nabla\mathcal{T}, \quad (6.2.16)$$

where $\mathbf{r} = r\mathbf{e}_r$ is the radius vector. \mathcal{R} , \mathcal{S} and \mathcal{T} represent the radial, spheroidal and toroidal scalar fields, respectively. The latter three quantities can then be expanded in spherical

harmonics, such that

$$\mathbf{f} = \sum_{\ell=0}^{\ell_{\max}} \sum_{m=-\ell}^{\ell} \mathcal{R}_{\ell}^m Y_{\ell}^m \mathbf{e}_r + \mathcal{S}_{\ell}^m r \nabla Y_{\ell}^m + \mathcal{T}_{\ell}^m \mathbf{r} \times \nabla Y_{\ell}^m, \quad (6.2.17)$$

where Y_{ℓ}^m are the spherical harmonic functions of degree ℓ and order m . The energy of the force vector (excluding viscous boundary layers) can then be obtained by computing

$$\begin{aligned} F^2 &= \int_V \mathbf{f}^2 dV \\ &= 2 \int_{r_i+b}^{r_o-b} \sum_{\ell=0}^{\ell_{\max}} \sum_{m=0}^{\ell}{}' |\mathcal{R}_{\ell}^m|^2 + \ell(\ell+1) (|\mathcal{S}_{\ell}^m|^2 + |\mathcal{T}_{\ell}^m|^2) r^2 dr, \end{aligned} \quad (6.2.18)$$

where b is the thickness of the viscous boundary layers. The prime on the summation again indicates that the first term of the sum is multiplied by one half. The above expression can be rewritten as

$$F^2 = \sum_{\ell=0}^{\ell_{\max}} \mathcal{F}_{\ell}^2, \quad (6.2.19)$$

where

$$\mathcal{F}_{\ell}^2 = 2 \int_{r_i+b}^{r_o-b} \sum_{m=0}^{\ell}{}' |\mathcal{R}_{\ell}^m|^2 + \ell(\ell+1) (|\mathcal{S}_{\ell}^m|^2 + |\mathcal{T}_{\ell}^m|^2) r^2 dr. \quad (6.2.20)$$

The above formalism can be used not only to compute spectra of individual forces, but also to measure the degree of cancellation between forces, such as between the pressure gradient and the Coriolis force, which yields the ageostrophic Coriolis force.

Figure 6.1 illustrates the force spectra \mathcal{F}_{ℓ} (time-averaged and normalised by the peak of the spectrum of the Coriolis force) of two dynamos controlled by a QG-MAC balance. This type of force equilibrium has been shown to be the governing force balance of most dipole-dominated dynamos in a systematic parameter space survey by [Schwaiger et al. \(2019\)](#). At zeroth order these dynamos are controlled by a balance between pressure and Coriolis forces, the so-called geostrophic balance. However, depending on the strength of the magnetic field, the geostrophic balance is either present at all length scales (see Fig. 6.1a) or restricted to large scales, that is small spherical harmonic degrees (see Fig. 6.1b). In the latter case, the zeroth-order balance morphs into a balance between pressure and Lorentz forces towards smaller scales, forming a magnetostrophic balance. The Lorentz force contributes to this balance predominantly in the form of magnetic pressure. At the following order, the cancellation between pressure and Coriolis forces, the ageostrophic Coriolis force, is balanced by buoyancy at large scales (small ℓ) and the Lorentz force at small scales (large ℓ). This first-order balance is typically referred to as MAC balance.

Finally, inertia and viscous forces contribute at second order. To indicate the “strong-fieldness” of the dynamo, i.e. the dynamical influence of the Lorentz force relative to the second-order forces, we will use the ratio between the magnetic and kinetic energies $M = E_{\text{mag}}/E_{\text{kin}}$ (e.g. [Schwaiger et al., 2019](#)). In the following, we will refer to cases with $M \geq 10$ as strong-field dynamos.

In dynamo models, there are up to four possible cross-overs of forces (see Fig. 6.1), which can be linked to different types of force balances: MAC, CIA, VAC and MS (magnetostrophic). The types of crossings which can be observed in a given dynamo model directly depends on the relative strength of the individual forces. The spherical harmonic degrees ℓ_{MA} , ℓ_{IA} and ℓ_{VA} , corresponding to first- or higher-order MAC, CIA and VAC force balances, represent the scales at which the Lorentz force, inertia and viscous forces are of the same amplitude as buoyancy, respectively. Thus, we define

$$\ell_{\text{MA}} = \underset{\ell}{\operatorname{argmin}} (|\mathcal{F}_{\text{Lorentz},\ell} - \mathcal{F}_{\text{buoyancy},\ell}|), \quad (6.2.21)$$

$$\ell_{\text{IA}} = \underset{\ell}{\operatorname{argmin}} (|\mathcal{F}_{\text{inertia},\ell} - \mathcal{F}_{\text{buoyancy},\ell}|), \quad (6.2.22)$$

$$\ell_{\text{VA}} = \underset{\ell}{\operatorname{argmin}} (|\mathcal{F}_{\text{viscous},\ell} - \mathcal{F}_{\text{buoyancy},\ell}|). \quad (6.2.23)$$

The magnetostrophic crossing ℓ_{MS} occurring at zeroth order, represents the scale at which Lorentz and Coriolis forces are in balance. It is therefore given by

$$\ell_{\text{MS}} = \underset{\ell}{\operatorname{argmin}} (|\mathcal{F}_{\text{Coriolis},\ell} - \mathcal{F}_{\text{Lorentz},\ell}|). \quad (6.2.24)$$

The length scales associated to these crossings (the so-called cross-over length scales) are again given by the characteristic half-wavelength associated to each degree (see Eq. 6.2.15)

$$\mathcal{L} = \frac{\pi r_m}{\ell}. \quad (6.2.25)$$

6.3 Results

6.3.1 Convective length scales in dynamo simulations

In planetary dynamos, the flow length scale is expected to be controlled by the Lorentz force. Therefore, we will examine in the following sections whether it is possible to relate the QG-MAC length scale $\mathcal{L}_{\text{MA}}/L = \pi/\ell_{\text{MA}}$ and the magnetostrophic cross-over length scale $\mathcal{L}_{\text{MS}}/L = \pi/\ell_{\text{MS}}$ to observable (energetically relevant) flow length scales. In addition, we will also examine their scaling behaviour to assess the validity of the aforementioned theoretical scalings in our numerical models.

6.3.1.1 QG-MAC length scale

One of the most frequently invoked results in favour of a QG-VAC balance in numerical dynamos is the apparent compatibility of a spectrally weighted kinetic energy length scale

6. RELATING FORCE BALANCES AND FLOW LENGTH SCALES IN GEODYNAMO SIMULATIONS

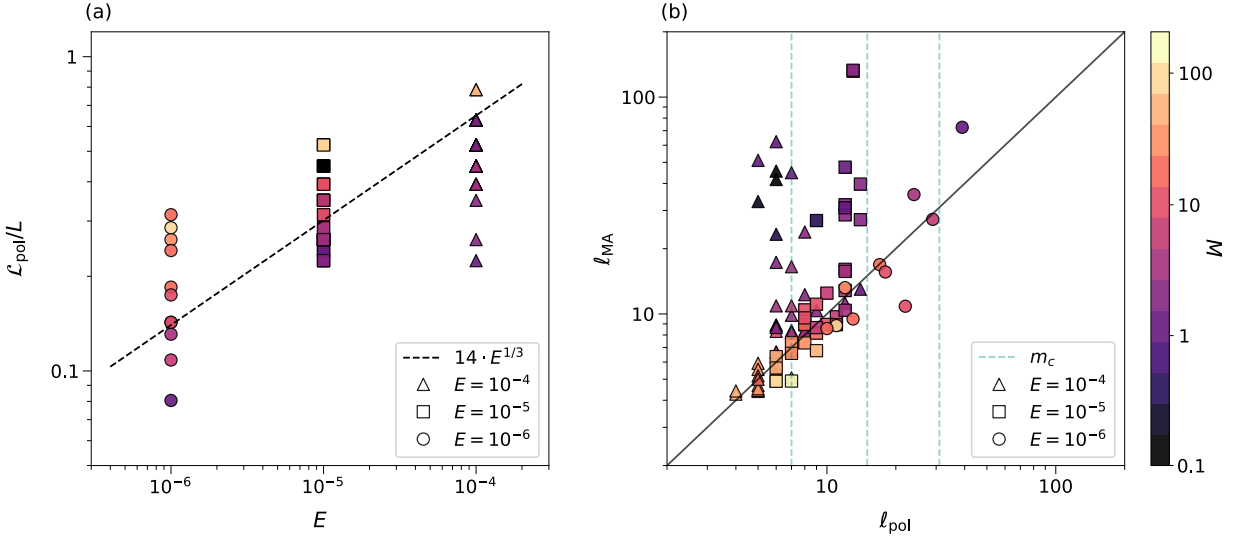


Figure 6.2: (a) $\mathcal{L}_{\text{pol}}/L$ (Eq. 6.2.15) as a function of the Ekman number E . The black dashed line corresponds to the viscous scaling $\mathcal{L}_{\perp}/L \sim E^{1/3}$. (b) Comparison of the spherical harmonic degree at which buoyancy and Lorentz forces are of equal magnitude in the force balance spectra, l_{MA} , (see Fig. 6.1 for examples) to the peak of the poloidal kinetic energy spectrum l_{pol} . The spherical harmonic degrees can be converted to length scales using Eq.(6.2.25). The green vertical dashed lines correspond to the respective azimuthal wavenumber of convection onset m_c for $E \in \{10^{-4}, 10^{-5}, 10^{-6}\}$ from left to right. The symbols in both panels are coloured with M .

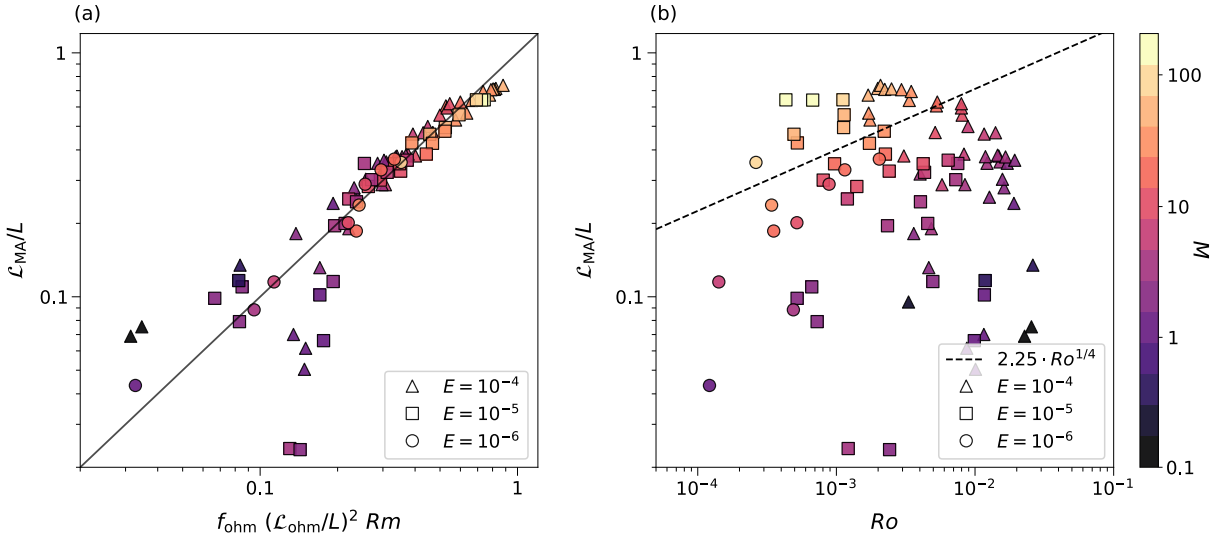


Figure 6.3: (a) Comparison of the QG-MAC length scale $\mathcal{L}_{\text{MA}}/L = \pi/l_{\text{MA}}$ to the theoretical scaling given by Eq. (3.1.17). (b) $\mathcal{L}_{\text{MA}}/L$ as a function of Ro . The black dashed line corresponds to the theoretical scaling $\mathcal{L}_{\perp}/L \sim Ro^{1/4}$. The prefactor 2.4 was obtained by considering only dynamos with $M = E_{\text{mag}}/E_{\text{kin}} \geq 10$. The symbols in both panels are coloured with M .

(Christensen and Aubert, 2006) with the viscous $E^{1/3}$ -scaling (e.g. King and Buffett, 2013; Oruba and Dormy, 2014). Figure 6.2a shows the spectral peak length scale \mathcal{L}_{pol} as a function of the Ekman number. We observe that \mathcal{L}_{pol} also appears to follow a similar trend. This is however misleading, as the scatter of \mathcal{L}_{pol} at each given Ekman number is almost as large as the change in length scale predicted by the viscous scaling. This indicates that in this case simply considering the Ekman number as a diagnostic, without a more detailed analysis, has little to no predictive power for the underlying force balance.

The comparison of the dynamically relevant cross-over ℓ_{MA} and the peak of the poloidal kinetic energy ℓ_{pol} shown in Fig. 6.2b offers a more meaningful approach to link the dominant convective length scale to the governing physics. All models where ℓ_{MA} is well defined are included independent of the type of the first-order force balance. To include information about the force balance of the dynamos, the symbols of the models are coloured with the ratio between the magnetic and kinetic energies M . We observe that ℓ_{MA} is in good agreement with ℓ_{pol} for dynamos with sufficiently large M ($M \geq 10$), which suggests that the convective scale is indeed controlled by a first-order MAC balance in these models. For dynamos with $1 < M < 10$ this correlation becomes less obvious due to the QG-MAC balance being increasingly perturbed by viscous and/or inertial effects. Finally, we observe no correlation between ℓ_{MA} and ℓ_{pol} for dynamos with $M \leq 1$, as expected since these models are no longer controlled by a QG-MAC balance. The influence of second-order forces on the convective scale in dynamos with $M < 10$ is further highlighted by the fact that for each of the considered Ekman numbers, ℓ_{pol} seems to cluster around the respective critical azimuthal wavenumber of convection onset (green vertical dashed lines in Figure 6.2b), which follow the viscous scaling (Eq. 3.1.5). The onset values have been computed using the open-source generalised eigenvalue solver *Singe* (Vidal and Schaeffer, 2015, freely available at <https://bitbucket.org/nschaeff/singe>).

Given that \mathcal{L}_{MA} seems to correspond to an observable flow length scale in QG-MAC dynamos, we will now examine whether it is consistent with the theoretical predictions based on the assumption of a first-order MAC balance as suggested by Davidson (2013) (see Section 3.1.3). The comparison between \mathcal{L}_{MA} and the prediction of the integral length scale \mathcal{L}_{\perp} obtained from the equivalence between large- and small-scale vorticities (Eq. 3.1.17) is shown in Fig. 6.3a. The symbols corresponding to the individual models are again coloured with M . We observe that for numerical dynamos with strong magnetic control ($M \geq 10$), i.e. QG-MAC dynamos, the predicted and measured length scales are overall in good agreement. This suggests that the vorticity equivalence is reasonably well satisfied for these cases. The cross-over length scale \mathcal{L}_{MA} thus appears to correspond to the integral length scale \mathcal{L}_{\perp} as defined by Davidson (2013). This is again much less the case for dynamos with smaller M since those dynamos either feature a significant contribution of inertial/viscous effects or are controlled by a different first-order force balance.

The second scaling of \mathcal{L}_{\perp} (Eq. 3.1.20) by Davidson (2013) which further assumes the rotational independence of the vorticities is shown in Fig. 6.3b, in which $\mathcal{L}_{\text{MA}}/L$ is plotted versus Ro . However, no correlation is found between $\mathcal{L}_{\text{MA}}/L$ and the theoretical $\mathcal{L}_{\perp}/L \sim Ro^{1/4}$ scaling, even in the limit of $M \geq 10$. Including the factor $f_{\text{ohm}}^{1/2}$ in Eq. (3.1.20)

does not improve the correlation between the two quantities, which is why it is omitted in Fig. 6.3b. There are several possible explanations for this. One of them being that our numerical models are not operating in a regime of $Pm \ll 1$, the physical limit in which the scaling (3.1.20) was devised. Therefore, viscous dissipation is still significant (although some of the very high Pm runs do have large f_{ohm}). Additionally, the assumption of $B^2/\rho\mu$ being independent of the rotation rate, which is required for this scaling, is potentially not well satisfied in the models (Schirner, 2013). In Fig. 6.3b, we also observe that the data points show a dependency on M , with larger length scales typically corresponding to larger M . This hints at a feedback between the magnetic field and the velocity field, which suggests that scaling the Lorentz force as $B^2/\mu\mathcal{L}_\perp$ is likely too crude an approximation. While there are a number of reasons that could lead to the scaling law not being applicable to numerical dynamos, it should also be noted that in our models in which $M \geq 10$, Ro only covers slightly more than one order of magnitude, which might not be enough for a fair assessment of its validity.

6.3.1.2 Magnetostrophic cross-over length scale

In many strong-field dynamos the zeroth-order geostrophic balance is only present at large scales, while it turns into a balance between pressure and Lorentz forces towards smaller scales (see Fig. 6.1b). This transition from geostrophy to magnetostrophy occurs at the magnetostrophic cross-over length scale at which Lorentz and Coriolis forces are of equal magnitude (Aurnou and King, 2017). The effect of this dichotomy of the zeroth-order force balance is visualised in Fig. 6.4 for one parameter configuration considered by Dormy et al. (2018). We observe that the flow is organised into large-scale columns (spanning the entire shell) that are aligned with the rotation axis, indicating a dominant geostrophic balance on large scales. On smaller scales the columns are broken up especially in regions with an intense magnetic field.

Unlike the QG-MAC crossing ℓ_{MA} , the magnetostrophic cross-over ℓ_{MS} does not match with ℓ_{pol} in any of our dynamos models. Therefore, it does not appear to control the dominant scale of convection. It is, however, still possible to relate ℓ_{MS} to the fluid flow. To this end, we decompose the cylindrical radial velocity, u_s , into its geostrophic (u_s^g) and ageostrophic (u_s^a) components. 3-D renderings of these three velocities are shown in Fig. 6.5. To construct u_s^g , we average u_s along the rotation axis, which yields a flow component that completely satisfies the Proudman-Taylor theorem (Eq. 3.1.2). For the integration, we consider the regions inside and outside the inner core tangent cylinder (TC) separately, since the fluid volumes inside the TC have to be averaged independently in the northern and southern hemispheres. Therefore, we compute for

• $r_i \leq s \leq r_o$ (i.e. outside TC)

$$\bar{u}_s^g(s, \varphi) = \frac{1}{2h_o} \int_{-h_o}^{h_o} u_s(s, \varphi, z) dz, \quad (6.3.1)$$

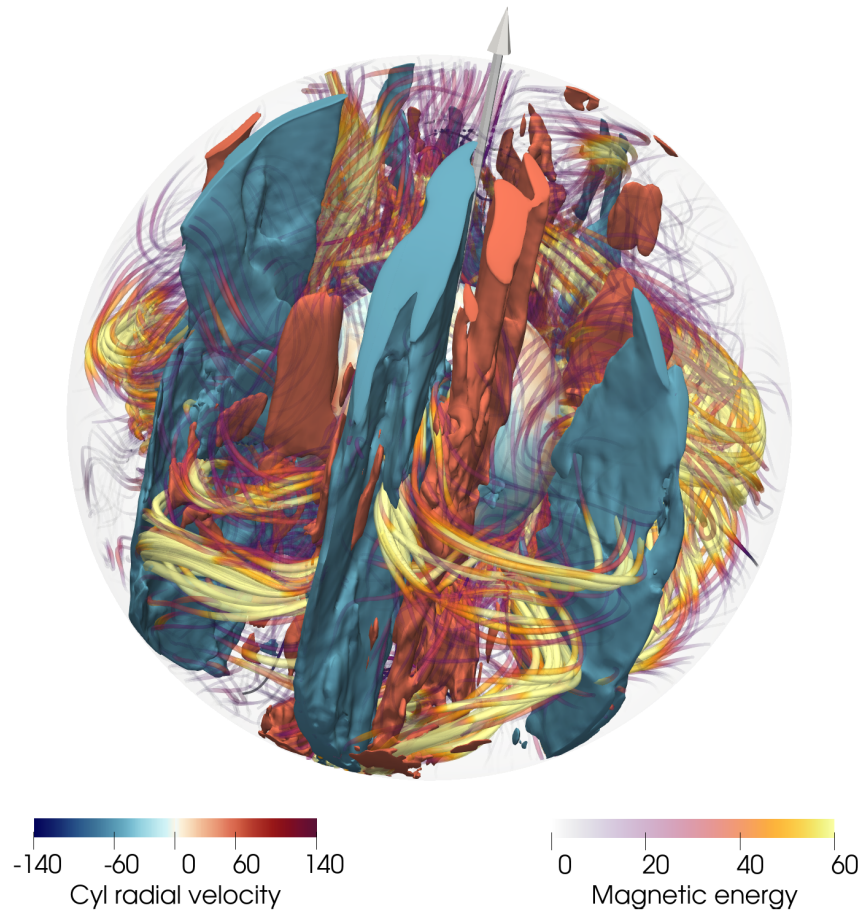


Figure 6.4: 3D-rendering of the columnar convection pattern and the magnetic field lines in a strong-field dynamo at $E = 10^{-5}$, $Ra = 4 \times 10^7$ and $Pm = 7$. The columns aligned with the rotation axis (represented by the arrow) correspond to isosurfaces of the cylindrical radial velocity $u_s \in \{-60, 60\}$. The magnetic field lines are coloured according to the magnetic energy. Additionally, their thickness increases with the magnetic energy. The force balance corresponding to this case is shown in Fig. 6.1b.

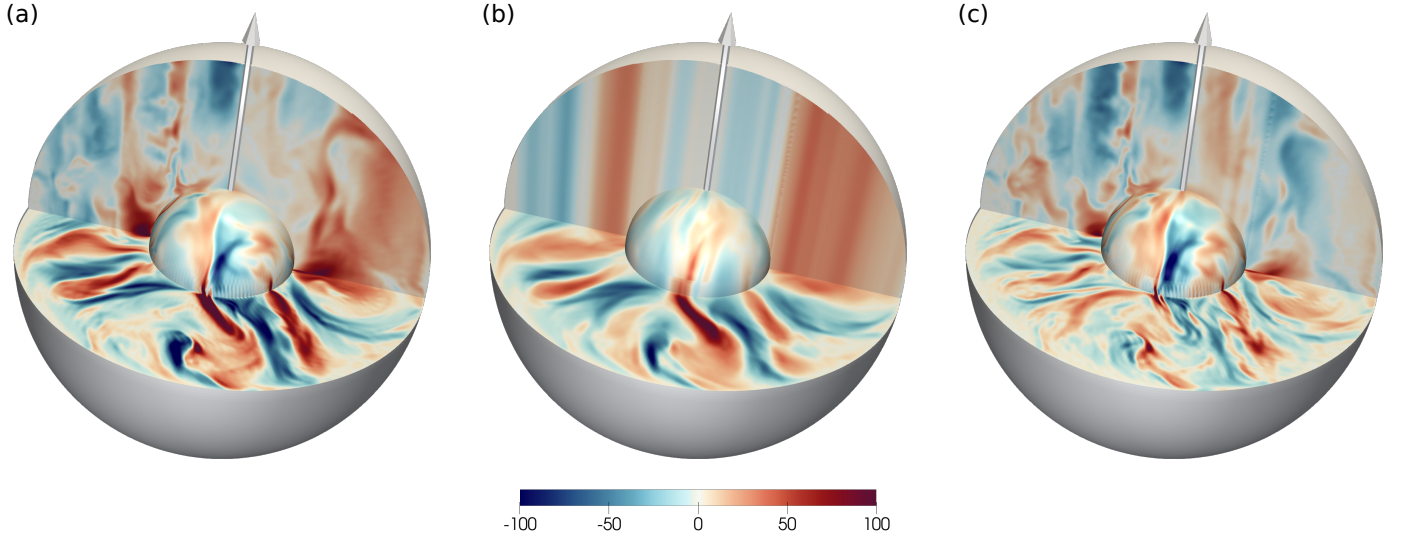


Figure 6.5: 3-D renderings of (a) the total cylindrical radial velocity u_s , (b) the geostrophic component u_s^g of u_s , and (c) the ageostrophic component u_s^a of u_s for the numerical dynamo at $E = 10^{-5}$, $Ra = 4 \times 10^7$ and $Pm = 7$. In each panel, the arrow marks the rotation axis. The force balance corresponding to this case is shown in Fig. 6.1b.

- $0 \leq s < r_i$ and $z > 0$ (i.e. inside TC, northern hemisphere)

$$\bar{u}_s^g(s, \varphi) = \frac{1}{h_o - h_i} \int_{h_i}^{h_o} u_s(s, \varphi, z) dz, \quad (6.3.2)$$

- $0 \leq s < r_i$ and $z < 0$ (i.e. inside TC, southern hemisphere)

$$\bar{u}_s^g(s, \varphi) = \frac{1}{h_o - h_i} \int_{-h_o}^{-h_i} u_s(s, \varphi, z) dz, \quad (6.3.3)$$

where $h_i = \sqrt{r_i^2 - s^2}$, $h_o = \sqrt{r_o^2 - s^2}$, and s is the cylindrical radius. Subsequently, we expand the z -averaged flow $\bar{u}_s^g(s, \varphi)$ along the rotation axis back into the initial spherical geometry, which yields the perfectly axially-aligned flow component $u_s^g(r, \theta, \varphi)$ visible in Fig. 6.5b. The ageostrophic flow component (see Fig. 6.5c) is then given by

$$u_s^a = u_s - u_s^g. \quad (6.3.4)$$

We construct time-averaged spectra of these three velocities as a function of the degree ℓ using spherical harmonic transforms. Figure 6.6a illustrates the resulting spectra for the strong-field dynamo whose force balance is shown in Fig. 6.1b. We observe that the large

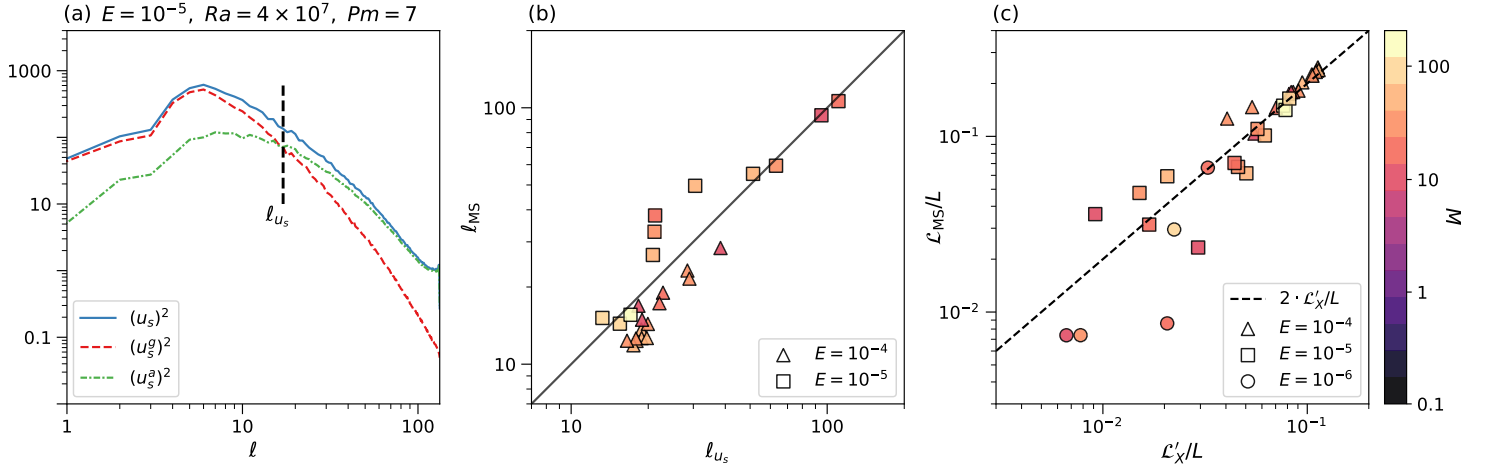


Figure 6.6: (a) Example of spectra of the total cylindrical radial velocity u_s (solid blue line), its geostrophic component u_s^g (dashed red line), and its ageostrophic component u_s^a (dash-dotted green line) for the numerical dynamo at $E = 10^{-5}$, $Ra = 4 \times 10^7$ and $Pm = 7$. The force balance corresponding to this case is illustrated in Fig. 6.1b. ℓ_{u_s} represents the crossing between the spectra of u_s^g and u_s^a . (b) Comparison of the magnetostrophic crossing ℓ_{MS} defined by the force balance spectra (see Fig. 6.1b) to ℓ_{u_s} . (c) Comparison of $\mathcal{L}_{MS}/L = \pi/\ell_{MS}$ with the estimate \mathcal{L}'_X/L provided by the theoretical scaling (6.3.5). The symbols are coloured with M .

scales are almost entirely dominated by the geostrophic flow component, while the small scales are predominantly ageostrophic as expected from the corresponding force balance spectrum. The spherical harmonic degree ℓ_{u_s} beyond which the flow is mostly ageostrophic does appear to coincide with the magnetostrophic cross-over ℓ_{MS} . Repeating this analysis for other cases for which ℓ_{MS} is well-defined, shows that ℓ_{u_s} and ℓ_{MS} generally seem to be in good agreement as shown in Fig. 6.6b. This indicates that $\mathcal{L}_{MS}/L = \pi/\ell_{MS}$ does indeed represent the length scale beyond which the zeroth-order geostrophy is broken up by the Lorentz force. The large spatial resolutions required for our most extreme simulations restricted this type of analysis to dynamo models with $E \geq 10^{-5}$.

For the comparison of the magnetostrophic cross-over length scales obtained from the force balance spectra, \mathcal{L}_{MS} , to the ones predicted by the Elsasser number scaling suggested by Aurnou and King (2017), \mathcal{L}_X (Eq. 3.2.10), we restrict ourselves to numerical dynamos in which ℓ_{MS} is well-defined and $M \geq 10$. This ensures that the leading-order force balance contains a magnetostrophic range and is not significantly disturbed by inertia and/or viscous forces. \mathcal{L}_{MS} however does not show any correlation with \mathcal{L}_X , especially since in our models \mathcal{L}_X varies over a much larger range of magnitudes than \mathcal{L}_{MS} . If we slightly modify the scaling by Aurnou and King (2017) by assuming similar scales for the fluid flow and the magnetic field, i.e. $\mathcal{L}_U \sim \mathcal{L}_B$ (e.g. Aubert et al., 2017), instead of different ones and follow the same lines of reasoning as described in Section 3.2, we end up with the following

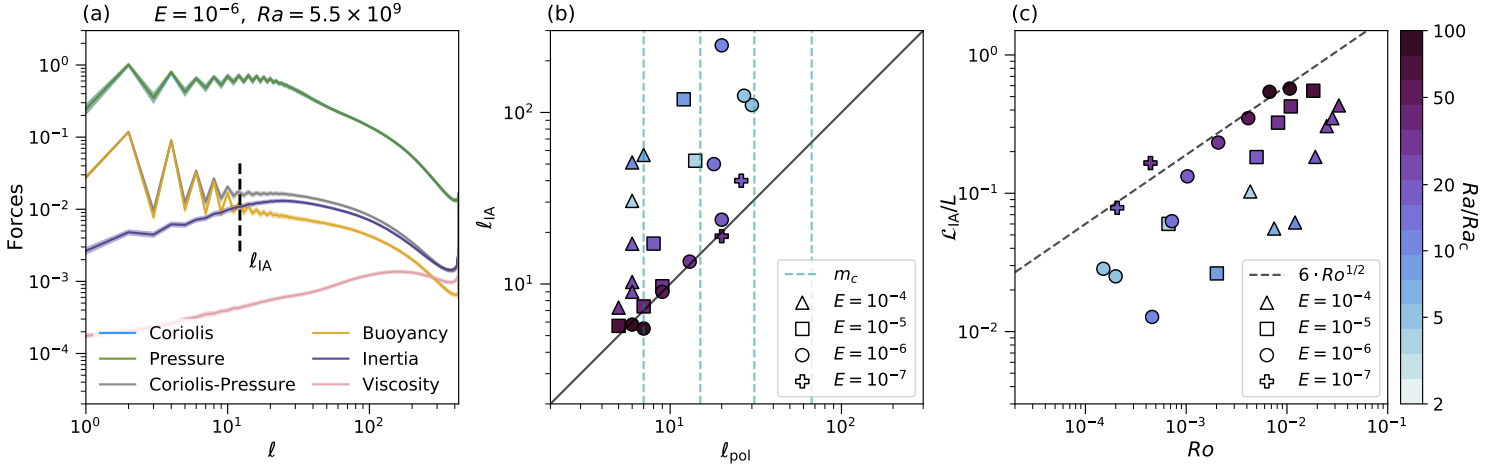


Figure 6.7: (a) Example of a time-averaged force balance spectrum of a non-magnetic numerical model with $E = 10^{-6}$, $Ra = 5.5 \times 10^9$ ($Ra/Ra_c \approx 30$) and $Pr = 1$. The amplitudes of the spherical harmonic contributions of the forces are normalised relative to the peak of the Coriolis force. The shaded regions correspond to one standard deviation in time. ℓ_{IA} is defined as the spherical harmonic degree at which buoyancy and inertia intersect. (b) Comparison of ℓ_{IA} to the peak of the poloidal kinetic energy spectrum ℓ_{pol} , which serves as reference for the dominant flow length scale in the rotating convection models. The green vertical dashed lines correspond to the respective azimuthal wavenumber of convection onset m_c for $E \in \{10^{-4}, 10^{-5}, 10^{-6}, 10^{-7}\}$ from left to right. (c) $\mathcal{L}_{IA}/L = \pi/\ell_{IA}$ as a function of Ro . The black dashed line corresponds to the theoretical scaling $\mathcal{L}_{\perp}/L \sim Ro^{1/2}$. The symbols in panels (b) and (c) are coloured with the supercriticality Ra/Ra_c .

definition for the magnetostrophic cross-over length scale:

$$\frac{\mathcal{L}'_X}{L} = \frac{\Lambda_t}{Rm}. \quad (6.3.5)$$

The comparison between \mathcal{L}'_X/L and \mathcal{L}_{MS}/L is shown in Fig. 6.6c. We observe that although the estimate \mathcal{L}'_X/L does not offer a perfect prediction for \mathcal{L}_{MS}/L , it still gives a reasonable order of magnitude estimate of the magnetostrophic cross-over length scales defined by the force balance spectra.

6.3.2 Convective length scales in rotating convection simulations

In the previous sections, we have shown that the scales at which forces equilibrate in dynamo models correspond to observable convective flow scales. In this section, we will now focus on rotating convection models without the influence of a magnetic field, and investigate whether comparable results can be obtained. Figure 6.7a illustrates the force balance of the non-magnetic counterpart to the dynamo model shown in Fig. 6.1a. Similar to the dynamo model, the zeroth-order force balance is geostrophic at all length scales in the non-magnetic case. At the next order, the ageostrophic Coriolis force is now balanced

by buoyancy at large scales and inertia towards smaller scales. ℓ_{IA} corresponds to the harmonic degree where the latter two forces are of equal amplitude. Analogously to the magnetic case, we refer to this type of combination of zeroth- and first-order force balance as QG-CIA balance. Viscosity contributes at second order, about one order of magnitude smaller than inertia for the given example. We would like to emphasise, that although both the QG-MAC and the QG-CIA model are geostrophic at zeroth order, the separation between zeroth- and first-order force balance is considerably larger for the latter, indicating a larger degree of geostrophy of the convective flow in the non-magnetic case.

Like for the dynamo models, we again examine whether we can relate the crossing ℓ_{IA} defined by the first-order force balance to the dominant convective flow length scale represented by ℓ_{pol} in spectral space. The comparison of the two length scales, expressed by the associated spherical harmonic degree, is shown in Fig. 6.7b. The symbols corresponding to the individual models are coloured with the supercriticality Ra/Ra_c to visualise their proximity to the convection onset. We observe that ℓ_{IA} matches reasonably well with ℓ_{pol} above $Ra/Ra_c \gtrsim 25$. In these cases, which are governed by a QG-CIA balance according to the force balance spectra, inertia hence appears to control the flow length scale. For lower supercriticalities, we again observe to a first approximation a clustering of ℓ_{pol} around the critical azimuthal wavenumbers at convection onset for the respective Ekman numbers. This suggests a viscous control of the convective flow in weakly supercritical models (e.g. [Gastine et al., 2016](#); [Long et al., 2020](#)).

Given that $\mathcal{L}_{\text{IA}}/L = \pi/\ell_{\text{IA}}$ can be associated with the dominant convective length scale in models that are controlled by a QG-CIA balance, we now want to evaluate whether it follows the predicted Rhines scaling given by relation (3.1.8). Figure 6.7c shows $\mathcal{L}_{\text{IA}}/L$ as a function of Ro . We observe that $\mathcal{L}_{\text{IA}}/L$ starts to approach the $\mathcal{L}_{\perp}/L \sim Ro^{1/2}$ scaling towards the lowest Ekman numbers and largest supercriticalities considered in this study similarly to the results obtained by [Gastine et al. \(2016\)](#) and [Guervilly et al. \(2019\)](#). However, the length scales for the different Ekman numbers do not collapse on a single curve. This indicates that the analysed models have not fully reached the inertial regime, although they appear to be trending towards it.

6.4 Discussion

Several recent studies helped to define the different force balance regimes attained in numerical dynamos by explicitly computing the individual forces ([Yadav et al., 2016](#); [Aubert et al., 2017](#); [Aubert, 2019](#); [Schwaiger et al., 2019](#)). It, however, still remained an outstanding task to successfully link the force balances to convective flow length scales. Our study suggests that this can be achieved by using the cross-over length scales defined by the spectral representation of force balances introduced by [Aubert et al. \(2017\)](#). We have found that in dynamos controlled by a QG-MAC balance, the scale at which the Lorentz force and buoyancy balance, \mathcal{L}_{MA} , appears to correspond to the dominant convective scale. This demonstrates the dynamical influence of the Lorentz force in such models. In addition, we have shown that \mathcal{L}_{MA} can be reasonably well estimated using the proportionality between

large- and small-scale vorticities (Eq. 3.1.17) following the theoretical considerations suggested by Davidson (2013). Assuming $f_{\text{ohm}} = 1$, $Rm = 1000$, $\mathcal{L}_{\text{ohm}} = 20$ km (Aubert, 2019) and $L = 2260$ km yields $\mathcal{L}_{\text{MA}} \approx 200$ km ($\ell_{\text{MA}} = \pi L / \mathcal{L}_{\text{MA}} \approx 40$) for the Earth’s outer core.

The $\mathcal{L}_{\perp} \sim Ro^{1/4}L$ scaling by Davidson (2013), which additionally assumes rotational independence of the vorticities is not well satisfied by our numerical dynamos. This indicates that this assumption might not be valid in at least the parameter regime covered by our simulations (Schirmer, 2013). Possible reasons for this could be that most of the analysed models operate at rather moderate magnetic Reynolds number, Rm , and fairly large Pm compared to the Earth’s core, where $Rm \sim \mathcal{O}(10^3)$ and $Pm \sim \mathcal{O}(10^{-6})$. That being said, the exploration of a larger range of Ro might lead to a reassessment of the validity of the scaling law. This would however require far more computational resources. Alternatively, the results could possibly be improved by decreasing Pr which would allow a lower Pm to be reached at a given Ekman number.

The second cross-over length scale of the Lorentz force, that is the magnetostrophic cross-over length scale \mathcal{L}_{MS} , can also be retrieved from the convective flow. Our results indicate that it corresponds to the length scale at which the flow dynamics change from predominantly geostrophic (at large scales) to predominantly ageostrophic towards smaller scales. We have shown that a reasonable order of magnitude estimate of \mathcal{L}_{MS} can be obtained from a modified version of the Elsasser number scaling suggested by Aurnou and King (2017) by assuming similar scales for velocity and magnetic fields (Eq. 6.3.5). Considering $\Lambda_t = 10$ and $Rm = 1000$ (Christensen et al., 2010) yields $\mathcal{L}_{\text{MS}} \approx 50$ km ($\ell_{\text{MS}} = \pi L / \mathcal{L}_{\text{MS}} \approx 140$) for the Earth’s core.

These results highlight the dynamical influence of the Lorentz force in QG-MAC dynamos, and offer supporting evidences that force balance crossings reflect convective flow length scales. We would like to emphasise that our results indicate that it is not necessary for the Lorentz force to reach leading order to be dynamically relevant. The dominant scale of convection in QG-MAC dynamos appears to always be controlled by the scale at which buoyancy and Lorentz forces equilibrate in the first-order balance. This is the case independent of whether the zeroth-order balance is geostrophic at all length scales, or subdivided into large-scale geostrophy and small-scale magnetostrophy.

We have obtained comparable results for non-magnetic rotating convection simulations. In models that are controlled by a QG-CIA balance, which is the case at sufficiently high supercriticalities ($Ra/Ra_c \gtrsim 25$), the cross-over length scale defined by the first-order force balance, \mathcal{L}_{IA} , again seems to be reflected in the dominant scale of convection. The comparison of \mathcal{L}_{IA} to the Rhines scaling $\mathcal{L}_{\perp} \sim Ro^{1/2}L$ suggests that the inviscid regime has not been attained for the Ekman numbers considered in this study. The models at the highest supercriticalities and lowest Ekman numbers, however, appear to approach it. The fact that the Rhines scaling is not fully met could be attributed to the viscous dissipation in the boundary layers still being significant even at the lowest considered Ekman numbers (Gastine et al., 2016). The recent study by Guervilly et al. (2019), in which a quasi-geostrophic approximation of spherical convection is used to reduce the

Table 6.2: Theoretical scaling laws and thereby estimated values for the convective flow length scale in the Earth’s outer core. The predictions are obtained by assuming $E = 10^{-15}$, $Ro = 10^{-6}$, $Rm = 1000$, $\Lambda_t = 10$, $\mathcal{L}_{\text{ohm}} = 20$ km and $L = 2260$ km.

Force balance	Scaling law	Predicted value
QG-VAC	$\mathcal{L}_{\perp} \sim E^{1/3}L$	~ 20 m
QG-CIA	$\mathcal{L}_{\perp} \sim Ro^{1/2}L$	~ 20 km
QG-MAC	$\mathcal{L}_{\perp} \sim Rm \mathcal{L}_{\text{ohm}}^2/L$	~ 200 km
QG-MAC	$\mathcal{L}_{\perp} \sim Ro^{1/4}L$	~ 100 km
QG-MS	$\mathcal{L}'_X \sim \Lambda_t/Rm$	~ 50 km

computational costs, suggests that Ekman numbers as low as $E \sim 10^{-9}$ might be required to fully reach the inertial regime. Such extreme parameters are currently still out of reach in 3-D simulations. Given that for the investigated Ekman numbers \mathcal{L}_{IA} does not fall onto a single curve yet, we assume a prefactor of 10 for the Rhines scaling, which is slightly larger than what our simulations indicate. Using $\mathcal{L}_{\text{IA}} \sim 10 Ro^{1/2}L$ consistent with the results by [Guervilly et al. \(2019\)](#), yields $\mathcal{L}_{\text{IA}} \approx 20$ km ($\ell_{\text{IA}} = \pi L/\mathcal{L}_{\text{IA}} \approx 350$) for the Earth’s outer core in the absence of a magnetic field. For comparison, the viscous scale predicted from Eq. (3.1.5) would be on the order of twenty meters if $E = 10^{-15}$ is considered. A summary of the theoretical scalings and the predicted flow length scales for the Earth’s outer core is given in Table 6.2. Overall, the separation between the different scales is not large, with the exception of the viscous scale, which is about a factor $10^3 - 10^4$ smaller than the other scales.

6.5 Conclusions

Our main findings can be summarised by the following points:

(i) Length-scale-dependent analysis of the forces shows that in QG-MAC dynamos, the scale at which buoyancy and Lorentz forces are of equal magnitude is reflected in the dominant scale of convection. Similar results hold for non-magnetic rotating convection simulations that are controlled by a QG-CIA balance. In these models, the scale at which buoyancy and inertia equilibrate can be associated to the primary convective scale.

(ii) In most QG-MAC dynamos, the dominant force balance is divided into large-scale geostrophy and small-scale magnetostrophy. The analysis of the axial invariance of the flow reveals that the length scale which marks this transition can be retrieved from the convective pattern. In agreement with the prevailing force balance, the flow is close to invariant along the axis of rotation on large scales, while this is much less the case on smaller scales.

(iii) Assuming that the Earth’s dynamo is controlled by a QG-MAC balance, analysing the scaling behaviour of the two characteristic length scales found in geodynamo models

suggests that the dominant flow length scale in the Earth’s core is about 200 km, while magnetostrophic effects are deferred to scales smaller than 50 km.

Future contributions to the discussion on convective flow length scales in numerical dynamo models could involve the analysis of the z -averaged flow due to the prevailing (large-scale) geostrophy, as has been done for the 3-D models of non-magnetic rotating convection in [Guervilly et al. \(2019\)](#). This would allow access to the integral flow length scale \mathcal{L}_\perp perpendicular to the rotation axis. A similar strategy could potentially also be applied to the computation of the force balance, which might provide additional insights on how to relate force balances to convective flow length scales.

Acknowledgements

We would like to thank two anonymous reviewers for their constructive comments. We acknowledge support from the Fondation Del Duca of Institut de France (JA, 2017 Research Grant). Numerical computations were performed at S-CAPAD, IPGP and using HPC resources from GENCI-CINES and GENCI-TGCC (Grants A0040402122 and A0060402122). This project has received funding from the European Union’s Horizon 2020 research and innovation programme under the Marie Skłodowska-Curie grant agreement No 665850. All figures have been generated using either `matplotlib` ([Hunter, 2007](#)) or `paraview`.

Chapter 7

Conclusions and perspectives

Convection of liquid metal in the Earth's outer core is responsible for driving the geodynamo and thus for maintaining the geomagnetic field. Physical arguments about the force balance governing the flow dynamics are provided by core properties derived from seismological and geomagnetic observations, in combination with mineral-physical considerations and experiments. These offer the possibility to estimate the order of magnitude of force ratios. Due to the low viscosity of liquid iron under core conditions and the rapid rotation of the Earth, inertial and viscous forces are expected to be negligible. However, the hierarchy of the remaining forces, namely buoyancy, pressure, Coriolis and Lorentz forces, has been the subject of a long-standing controversy. It has been suggested that the prevailing force equilibrium could be either geostrophic (e.g. [Busse, 1970](#)) or magnetostrophic (e.g. [Roberts, 1978](#)). In the former case, the dominant force balance is only between Coriolis and pressure forces, whereas in the latter case it additionally includes the Lorentz force. Alternatively, a length-scale dependent combination of the two with geostrophy dominating the large scales was suggested ([Aurnou and King, 2017](#)). If geostrophy is prevailing, the Lorentz force enters the force balance at the next order, where it is compensated by buoyancy and non-geostrophic Coriolis forces. To incorporate the ageostrophic dynamics required to drive the geodynamo, we refer to this type of force equilibrium as quasi-geostrophic Magneto-Archimedean-Coriolis (QG-MAC) balance ([Davidson, 2013](#)).

In addition to observations and theoretical considerations, numerical simulations are an important tool for our understanding of the Earth's dynamo mechanism. Since the first geodynamo models were calculated 25 years ago by [Glatzmaier and Roberts \(1995\)](#), steadily increasing computational resources have led to more and more realistic solutions capable of reproducing numerous features of the geomagnetic field (e.g. [Christensen et al., 2010](#)). Because of these similarities between models and observations, numerical dynamos are increasingly used in data assimilation frameworks with the aim of drawing conclusions about the state of the core. But despite such successes, it remains uncertain whether these results are obtained for the right physical reasons, since current numerical simulations still work with parameters that are far from the expected conditions of the Earth's core. Studies that attempted to determine the numerically-achieved physical regime led to contradictory interpretations. Some argued for geophysically-relevant force balances, i.e. QG-MAC (e.g.

Yadav et al., 2016; Aubert et al., 2017; Schaeffer et al., 2017) or magnetostrophic balances (e.g. Dormy, 2016; Dormy et al., 2018), while others have suggested that the dynamics could be viscously controlled (e.g. King and Buffett, 2013; Oruba and Dormy, 2014) and thus not applicable to the Earth’s core. Since the different studies typically include different control parameters for the simulations considered, the diverging results could be due either to misinterpretations or to the fact that the respective models operate in different dynamical regimes. Therefore, the first goal of this work was to systematically investigate the force balance in the numerically accessible parameter space to see which different dynamical regimes can be found and whether the transitions between them are sharp or not. The second goal was to relate the computed force equilibria to measures of the convective flow length scales, a task that has proven to be challenging in the past and has consequently led to some confusion about the force balance in dynamo models in the first place.

7.1 Summary of the results

7.1.1 Force balance regimes

Our systematic study of the force balance revealed three different regimes. We found that the majority of dipole-dominated dynamos are governed by a QG-MAC balance. The use of the spectral representation of the forces introduced by Aubert et al. (2017), for which two examples are shown in Fig. 7.1, allowed us to access their length-scale dependence. This revealed that in QG-MAC dynamos the zeroth-order balance can either be geostrophic on all length scales (see Fig. 7.1a) or split into large-scale geostrophy and small-scale magnetostrophy (see Fig. 7.1b). The degree of magnetostrophy, i.e. up to which maximum length scale the flow dynamics are in a magnetostrophic equilibrium, depends on the relative strength of the Lorentz force and thus on the combination of supercriticality and magnetic Prandtl number. At the order below the prevailing force balance, the ageostrophic part of the Coriolis force is mainly compensated by buoyancy on large scales and by the Lorentz force towards smaller scales. Inertia and viscous forces represent second-order contributions. This QG-MAC balance seems to be structurally very robust throughout the investigated parameter space, with the exception of “boundary regimes”. Beyond the boundary between the dipolar and multipolar regimes, inertial effects gain importance. As a result, inertia compensates the ageostrophic Coriolis force on small scales instead of the Lorentz force, which becomes secondary in these cases. Such dynamos are therefore governed by a quasi-geostrophic Coriolis-Inertia-Archimedean (QG-CIA) balance (e.g. Cardin and Olson, 1994; Aubert et al., 2001; Guervilly et al., 2019). Close to the onset of dynamo action, the magnitude of the Lorentz force also decreases to or below the strength of inertial and viscous forces. As a result, the QG-MAC balance is lost in these regions, at least for parts of the fluid volume. Thus, we termed such dynamos QG-Hybrid cases. The three different force balance regimes are summarised in Fig. 7.2. Decreasing the Ekman number extends the domain of dynamos controlled by a QG-MAC equilibrium towards lower magnetic Prandtl numbers and higher supercriticalities.

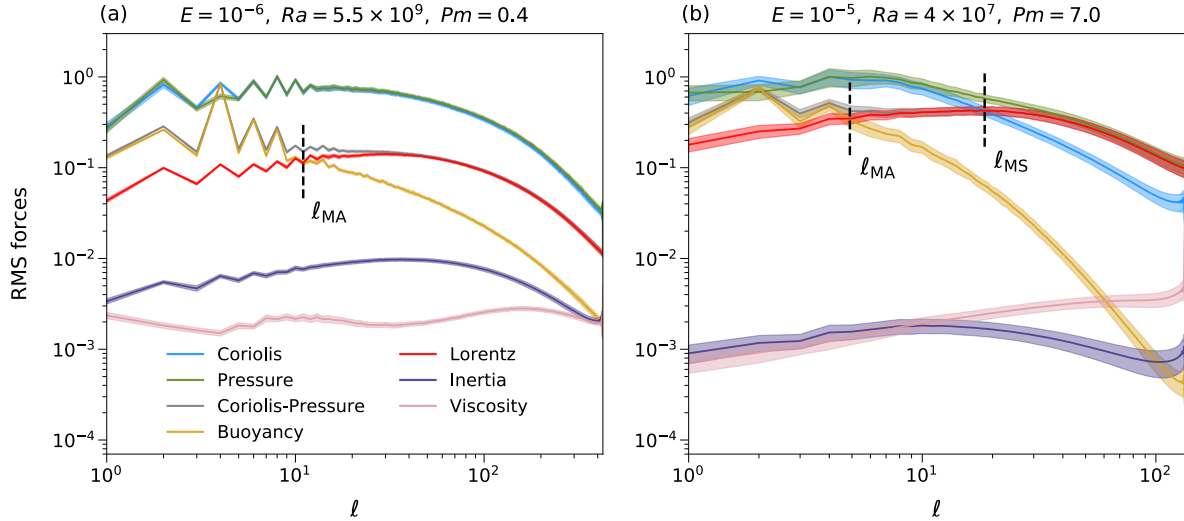


Figure 7.1: Examples of time-averaged force balance spectra for two QG-MAC dynamos. The r.m.s. amplitudes of the spherical harmonic contributions of the forces are normalised relative to the peak of the Coriolis force. The shaded regions correspond to one standard deviation in time. (a) Force balance of a dynamo governed by a prevailing geostrophic balance on all length scales, followed by a first-order MAC balance. (b) Force balance of a dynamo with a split zeroth-order force balance that is controlled by a geostrophic balance on large scales (small ℓ) that transitions into a magnetostrophic balance towards smaller scales (large ℓ).

Within the analysed parameter space, we were not able to find dynamos that exhibit system-scale magnetostrophy. Dormy (2016) and Dormy et al. (2018) proposed that such models could be found close to the onset of convection (Ra close to critical) and in conditions of reduced magnetic diffusivity (high Pm). Our simulations at the same parameters showed that dynamos in this region do indeed appear to approach the magnetostrophic regime when volume-integrated forces are considered. However, the length-scale dependent force balance analysis revealed that these cases are also controlled by a QG-MAC balance similar to most numerical simulations published to date. In these models, only the flow length scales about a factor three or four smaller than the integral flow length scale are in a magnetostrophic equilibrium, which is a common feature of QG-MAC dynamos towards larger Pm and/or high Ra/Ra_c . It is worth noting, though, that these cases correspond to the strongest-field dynamos observed in our study. The greater strength of the Lorentz force relative to the second-order forces in these models in comparison to QG-MAC dynamos at different parameters is mainly due to the fact that inertial effects are minimized at low supercriticality levels. When lowering the Ekman number, this region of strong-field dynamos will thus by construction expand towards larger supercriticalities owing to the increase of rotational effects on the fluid.

In geodynamo modeling it is a common strategy to decrease Pm as much as possible to approach the conditions expected in the Earth’s core. We found, however, that lowering Pm to a value too close to the onset of dynamo action can lead to the loss of the QG-MAC

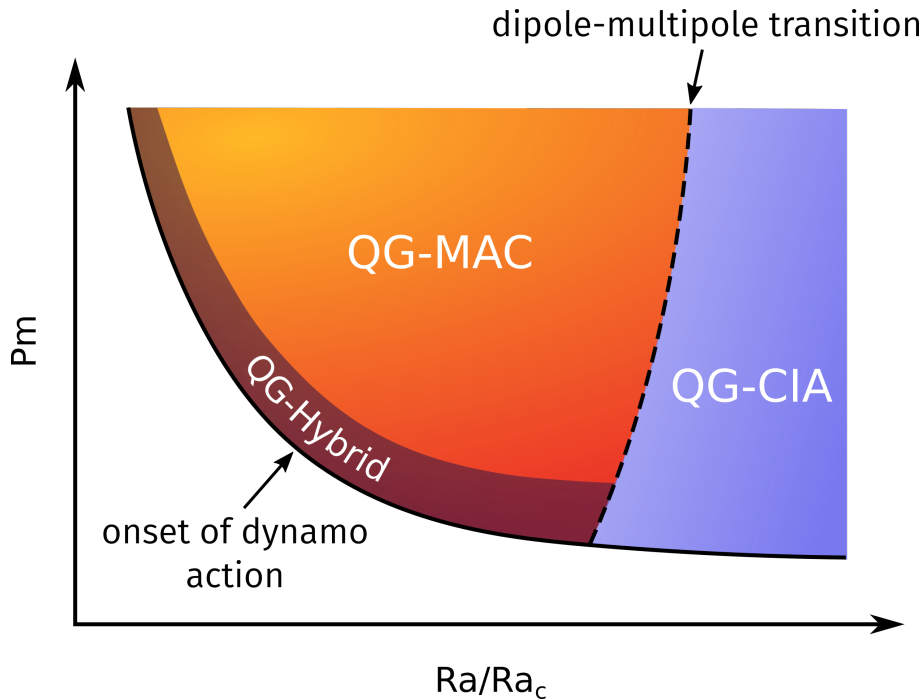


Figure 7.2: Sketch of the three different force balance regimes attained in our study independent of the Ekman number. The dashed line marks the transition between the dipolar and multipolar regime. The solid black line denotes the onset of dynamo action.

balance in large parts of the (or even in the entire) volume which may result in viscosity and inertia being dynamically more important overall than the Lorentz force, and thus to a force balance that is not geophysically relevant. For example, oscillatory low- Pm dynamos, as described by [Sheyko et al. \(2016\)](#), are found just beyond the transition from the QG-Hybrid to the QG-CIA regime. Therefore, care must be taken when choosing the input parameters. Strategies such as those employed by [Dormy \(2016\)](#) and [Aubert et al. \(2017\)](#) are immune to this, since they aim at preserving the governing force balance when decreasing the Ekman number by keeping a constant relation between the control parameters.

Overall, our systematic investigation of the dynamical regime in numerical geodynamo models allows us to conclude that the majority of numerical dynamos are controlled by a QG-MAC balance, and thus by a force equilibrium that could prevail in the Earth's core, while cases where viscosity and inertia play a dominant role are the exception rather than the norm. These results are published in the *Geophysical Journal International* (GJI) article [Schwaiger et al. \(2019\)](#).

7.1.2 Relating force balances to flow length scales

One of the main reasons that led to questions about the geophysical relevance of numerical geodynamo simulations was the fact that the analysis of the scaling behavior of typical

flow length scale measures indicated that the flow dynamics might be controlled viscously (King and Buffett, 2013; Oruba and Dormy, 2014). By explicitly calculating the forces, subsequent studies (e.g. Yadav et al., 2016; Aubert et al., 2017), including the results presented here, have shown that this is typically not the case and that the force balance in most models could indeed be relevant to the Earth’s core. Nevertheless, it is still an outstanding task to successfully relate force balances to convective flow length scales. Our study suggests that this can be achieved by using the length scales associated with cross-over points in the spectral diagrams of the force balances. We showed that in most numerical dynamos the peak of the poloidal kinetic energy, which we chose as a measure for the dominant scale of convection, can be related to the scale at which buoyancy and the Lorentz force are in equilibrium. Thus, the QG-MAC balance prevailing in these models is indeed reflected in the convective pattern. In non-magnetic rotating convection simulations, which generally favour a QG-CIA balance at high supercriticalities, we found analogous results. In these cases the scale at which buoyancy and inertia are in balance seems to control the dominant flow length scale. Our results therefore show that viscosity, which generally only makes a small contribution to the force equilibrium, does not control the dominant length scale of convection in the majority of models.

Furthermore, in dynamo simulations with a strong magnetic field, we were able to relate a second crossing point in the scale-dependent force balance diagrams to the convective flow. We found that the scale at which the Lorentz force balances the Coriolis force, the so-called magnetostrophic cross-over length scale, corresponds to the scale beyond which the axial invariance of the flow (which prevails on large scales) is lost. This result is not surprising since this cross-over point marks the transition in the zeroth-order force balance between large-scale geostrophy and small-scale magnetostrophy. The fact that we can correlate both the dominant flow length scale and the scale beyond which the flow loses its columnarity with different crossings of the Lorentz force in the spectral representations of the force balance underlines the dynamical influence of the magnetic field in QG-MAC dynamos. It is worth emphasising that our results indicate that it is not necessary for the Lorentz force to reach leading order to be dynamically relevant. The dominant scale of convection in QG-MAC dynamos always seems to be controlled by the scale at which buoyancy and Lorentz forces balance in the first-order equilibrium. This is the case regardless of whether the zeroth-order balance is geostrophic on all length scales or whether it is divided into large-scale geostrophy and small-scale magnetostrophy.

Finally, we showed that the length scale associated with the crossing between buoyancy and Lorentz forces in QG-MAC dynamos is compatible with predictions based on scaling laws derived by assuming a QG-MAC balance. In addition, we found that the theoretical scaling for the magnetostrophic cross-over length scale provides a reasonable order of magnitude estimate for the corresponding length scale obtained in our models.

7.2 Some preliminary findings and open questions

This work offers the possibility for several future studies. One could be to analyse in more detail the transition between the dipolar and multipolar regime and its effects on the force equilibrium. So far, we have found that the change of the field geometry is accompanied by a rather sharp transition of the prevailing force balance. The state of this analysis presented in the previous chapters was based on only a small number of multipolar cases at relatively low magnetic Prandtl numbers. These models are controlled by a QG-CIA balance, with the Lorentz force being only a secondary contribution. Since then we have computed a few additional multipolar cases at higher Pm at the Ekman number $E = 10^{-5}$. The corresponding updated regime diagram is illustrated in Fig. 7.3 along with some examples of force balances in different parts of the parameter space. We find that within the multipolar regime the Lorentz force becomes stronger with increasing Pm , similar to what we observe in dipole-dominated dynamos, with the difference that inertia remains a first-order contribution on the largest scales. An example of a force balance of such a multipolar model is shown in Fig. 7.3d. We observe that the Lorentz force not only enters the first-order equilibrium at large scales, where it is of comparable magnitude as inertia, but that it even rises to zeroth order on the smallest scales. These are therefore in a magnetostrophic state analogous to what we see in strong-field dynamos in the dipolar regime. The occurrence of magnetostrophy at small scales is thus independent of the field geometry. It should be noted, however, that the magnetostrophic cross-over length scale in multipolar dynamos shifts somewhat towards smaller scales across the regime boundary. All dynamos featuring a magnetostrophic range at small scales are highlighted by filled symbols in Fig. 7.3a. In general, the transition between the dipolar and multipolar regimes seems to be much less drastic in terms of the force balance towards higher values of Pm , the main difference being a jump in the magnitude of inertia across the transition, while the Lorentz force seems to be largely unaffected. In contrast, at lower Pm values in addition to the increase of inertia, a significant drop in the Lorentz force is observed. Overall, the dipole-dominated regime extends towards higher supercriticalities as Pm is increased, which seems to be a result of the associated increase of the Lorentz force in such dynamo models (Menu et al., 2020).

Using these results, it is possible to tentatively update the sketch of the observed force balance regimes shown in Fig. 7.2. To this end, we will slightly modify the names of the different regimes. As before QG stands for quasi-geostrophic, M for magneto, A for Archimedean, C for Coriolis, I for inertia and V for viscous. To account for small-scale magnetostrophy, we additionally add the acronym MS. What we previously referred to as QG-Hybrid balance will now be called QG-VIMAC balance to specify that at the order below the geostrophic balance, viscous, inertial and Lorentz forces contribute approximately equally to balancing buoyancy and ageostrophic Coriolis forces, even though the former three forces are rather small in this equilibrium. Furthermore, we can split the QG-MAC regime into a region where the zeroth-order balance is geostrophic on all length scales (at smaller Pm and lower supercriticality Ra/Ra_c), and a part where the zeroth-order balance is split into large-scale geostrophy and small-scale magnetostrophy (at larger Pm and

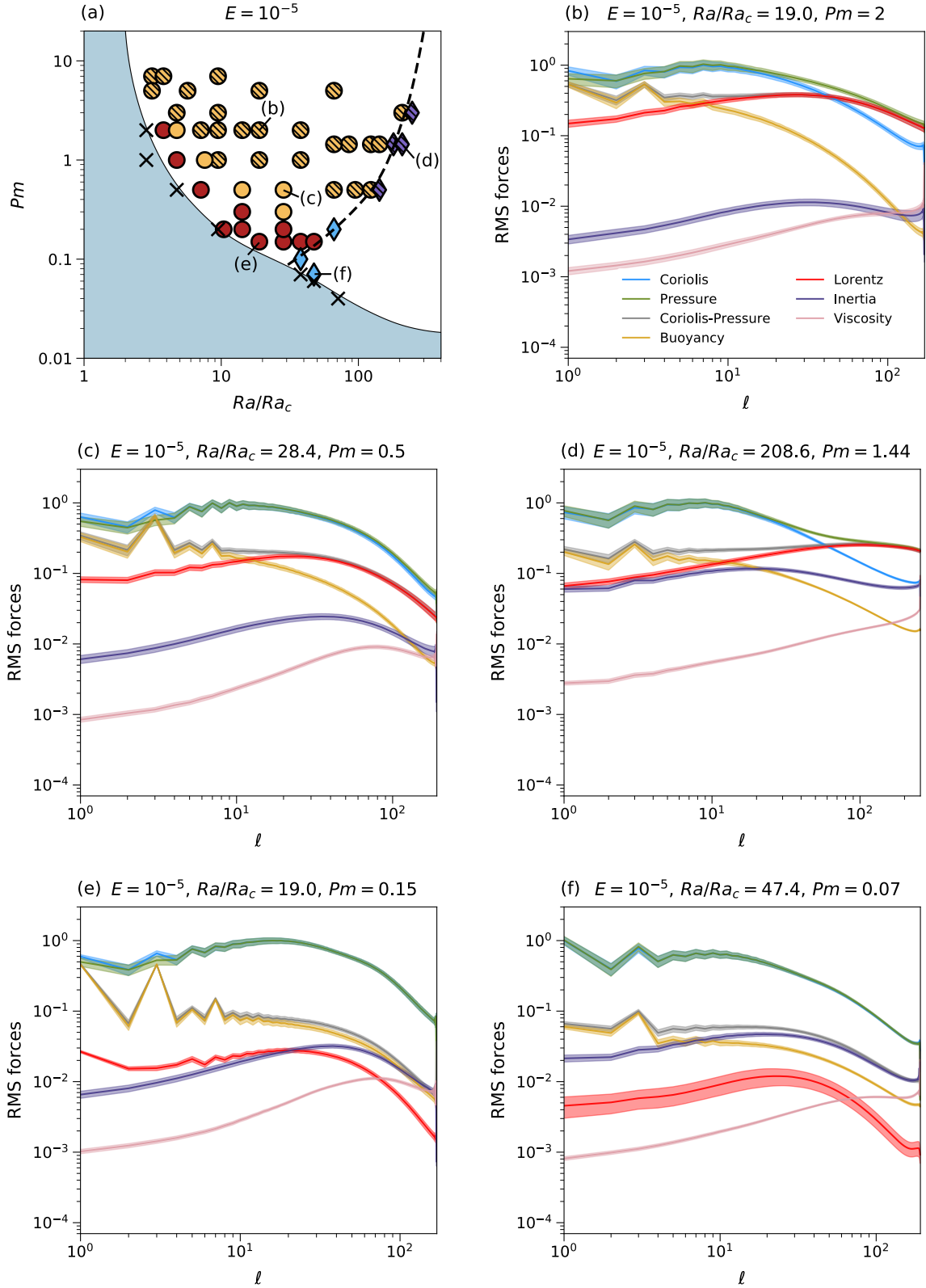


Figure 7.3: (a) Regime diagram at $E = 10^{-5}$ with circles and diamonds denoting dipole- and multipole-dominated dynamos, respectively. The symbols are coloured according to their force balance: QG-MAC (orange), QG-VIMAC (red), QG-CIA (blue), QG-MCIA (purple). Hatched symbols denote models with a magnetostrophic (MS) balance towards small scales. (b-f) Examples of spectral force balance diagrams of models found in the different regimes in (a).

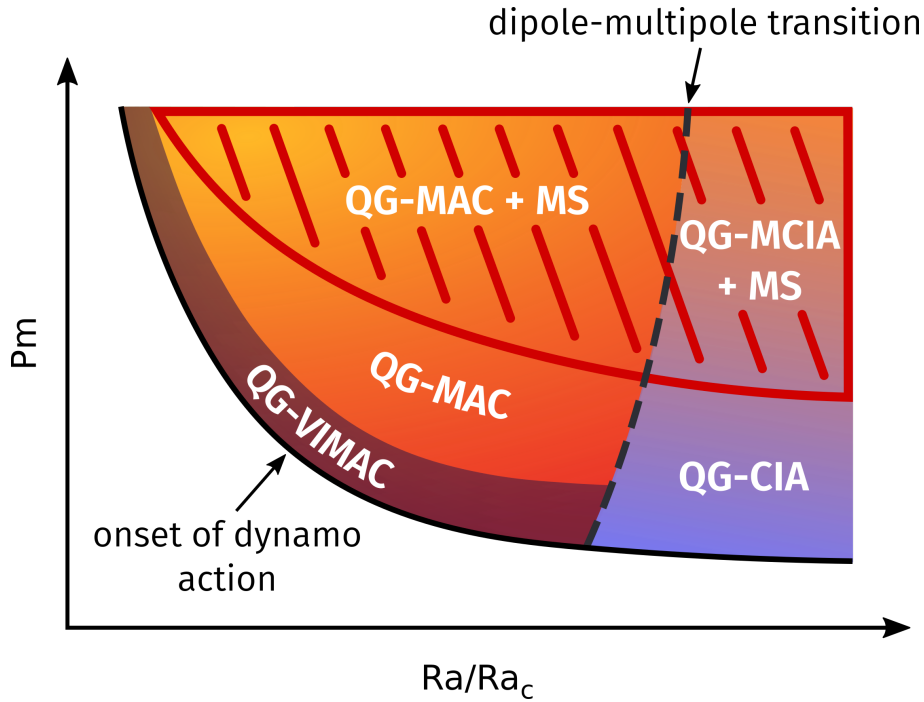


Figure 7.4: Sketch of the different force balance regimes attained in our study independent of the Ekman number. The red hatched area indicates the part of the parameter space where the dominant force equilibrium is divided into large-scale geostrophy and small-scale magnetostrophy. The dashed line marks the transition between the dipolar and multipolar regime. The solid black line denotes the onset of dynamo action.

higher supercriticality Ra/Ra_c). We will therefore refer to the force balance in the latter case as QG-MAC+MS. The transition between the QG-MAC and QG-MAC+MS regime is very gradual, and as mentioned above, the QG-MAC balance controls the dominant flow length scale in both cases. Thanks to the additional simulations, we are now able to divide the dynamos in the multipolar regime into different groups as well. Our results indicate that at low Pm values, they are controlled by a QG-CIA balance, which progressively morphs into a QG-MCIA+MS balance as Pm is increased due to the associated rise of the Lorentz force, which enters the large-scale first-order balance as well as the small-scale zeroth-order equilibrium. The updated sketch containing all these different force balance regimes is shown in Fig. 7.4.

To further investigate the behaviour of the dipole-multipole transition, additional simulations should be computed at different Ekman numbers. Since the multipolar dynamos considered in our study are restricted to the regime boundary, it would also be interesting to see how the equilibrium of forces changes towards higher supercriticalities. There are also a number of open questions about how the positions of the different force balance boundaries within the regime diagram vary as a function of the control parameters. It would in particular be useful to determine the Ekman number dependence of the minimum Pm values necessary to reach the QG-MAC or the QG-MAC+MS regimes, which

would then allow us to extrapolate these boundaries to the conditions of the Earth’s core and could potentially be used to better constrain the force balance governing the geodynamo. In addition, it would also be insightful to explore how the regime diagram changes when different values for the hydrodynamic Prandtl number are taken into account, since Pr in the Earth’s core is expected to be in the range of $0.1 - 100$ (the larger value corresponding to 100% chemical forcing), whereas our simulations were computed with $Pr = 1$. At lower Pr values, for example, we expect an increase of inertial effects (e.g. [Aubert et al., 2001](#)), which would probably shift the transition between the dipolar and multipolar regimes to less supercritical Rayleigh numbers, thus reducing the extent of QG-MAC dynamos along the Ra/Ra_c -axis. On the other hand, reducing Pr would allow us to reach smaller magnetic Prandtl numbers at a given Ekman number.

7.3 Implications for the geodynamo

To conclude this thesis, we would like to discuss what the implications of our results are regarding the force equilibrium that governs the flow dynamics in the Earth’s core. By combining the fact that by far the majority of dipole-dominated geodynamo models analysed in our study are dominated by a QG-MAC balance and that simulations calculated at more extreme parameters ([Aubert et al., 2017](#); [Schaeffer et al., 2017](#); [Aubert, 2019](#)) also show the same kind of leading-order force balance, we suggest that the Earth’s core probably operates in the QG-MAC regime as well. Our results do not provide any evidence for the alternative possibility of system-scale magnetostrophy, however, they do indicate that magnetostrophic effects are most likely to be present towards smaller scales as suggested by [Aurnou and King \(2017\)](#). To be more specific, the proposed dynamic regime of the Earth’s core can therefore be called QG-MAC+MS. Using theoretical scaling laws to extrapolate the associated flow length scales found in dynamo simulations to the conditions of the Earth’s core hints that the dominant flow length scale of the geodynamo is about 200 km, while magnetostrophy occurs on scales below 50 km. These values hence suggest that the separation between these two length scales is not very large. Scrutinising the ratio of the integral flow length scale and the magnetostrophic cross-over length scale in our set of numerical dynamos, as well as assessing which models produce an Earth-like magnetic field by computing the quantitative criteria introduced by [Christensen et al. \(2010\)](#), could help to better constrain the location of the geodynamo in [Fig. 7.4](#).

Appendix A

Derivation of terms for the evolution equations of the scalar potentials

The viscous term (4.2.9) for the evolution equation of the poloidal flow potential W (in the Boussinesq approximation) can be derived as follows:

$$\begin{aligned}
 \mathbf{e}_r \cdot \nabla^2 \mathbf{u} &= \nabla^2 u_r - \frac{2u_r}{r^2} - \frac{2}{r^2 \sin \theta} \frac{\partial}{\partial \theta} (u_\theta \sin \theta) - \frac{2}{r^2 \sin \theta} \frac{\partial u_\varphi}{\partial \varphi} \\
 &= \nabla^2 u_r - \frac{2u_r}{r^2} - \frac{2}{r} \nabla_H \cdot \mathbf{u} \\
 &= \nabla^2 u_r - \frac{2u_r}{r^2} - \frac{2}{r} \left[\underbrace{\nabla \cdot \mathbf{u}}_{=0} - \frac{1}{r^2} \frac{\partial}{\partial r} (r^2 u_r) \right] \\
 &= \nabla^2 u_r - \frac{2u_r}{r^2} + \frac{2}{r^3} \frac{\partial}{\partial r} (r^2 u_r).
 \end{aligned} \tag{A.0.1}$$

We will see that it is convenient to express the Laplacian term as

$$\nabla^2 u_r = \frac{1}{r^2} \left[\nabla^2 (r^2 u_r) - \frac{4}{r} \frac{\partial u_r}{\partial r} - 6u_r \right]. \tag{A.0.2}$$

Inserting this into (A.0.1) results in

$$\mathbf{e}_r \cdot \nabla^2 \mathbf{u} = \frac{1}{r^2} \left[\nabla^2 (r^2 u_r) - 4r \frac{\partial u_r}{\partial r} - 8u_r + \frac{2}{r} \frac{\partial}{\partial r} (r^2 u_r) \right]. \tag{A.0.3}$$

The radial derivative $\partial u_r / \partial r$ can be rewritten as

$$\frac{\partial u_r}{\partial r} = \frac{1}{r^2} \left[\frac{\partial}{\partial r} (r^2 u_r) - 2r u_r \right]. \tag{A.0.4}$$

Substituting this into (A.0.3) then leads to

$$\mathbf{e}_r \cdot \nabla^2 \mathbf{u} = \frac{1}{r^2} \left[\nabla^2 (r^2 u_r) - \frac{2}{r} \frac{\partial}{\partial r} (r^2 u_r) \right]. \tag{A.0.5}$$

Inserting

$$u_r = -\nabla_H^2 W. \quad (\text{A.0.6})$$

into relation (A.0.5) results in

$$\mathbf{e}_r \cdot \nabla^2 \mathbf{u} = -\nabla_H^2 \left[\nabla^2 W - \frac{2}{r} \frac{\partial W}{\partial r} \right]. \quad (\text{A.0.7})$$

Decomposing the Laplacian into its radial and horizontal parts, i.e.

$$\nabla^2 W = \frac{1}{r^2} \frac{\partial}{\partial r} \left(r^2 \frac{\partial W}{\partial r} \right) + \nabla_H^2 W, \quad (\text{A.0.8})$$

finally yields

$$\mathbf{e}_r \cdot \nabla^2 \mathbf{u} = -\nabla_H^2 \left[\frac{\partial^2 W}{\partial r^2} + \nabla_H^2 W \right]. \quad (\text{A.0.9})$$

For the viscous term (4.2.13) in the evolution equation of the toroidal flow potential Z , it follows analogously

$$\mathbf{e}_r \cdot \nabla \times (\nabla^2 \mathbf{u}) = -\nabla_H^2 \left[\frac{\partial^2 Z}{\partial r^2} + \nabla_H^2 Z \right], \quad (\text{A.0.10})$$

since

$$\nabla \times (\nabla^2 \mathbf{u}) = \nabla^2 (\nabla \times \mathbf{u}), \quad (\text{A.0.11})$$

and

$$(\nabla \times \mathbf{u})_r = -\nabla_H^2 Z. \quad (\text{A.0.12})$$

The viscous term (4.2.28) for the evolution equation of the pressure can be derived as follows:

$$\begin{aligned} \nabla_H \cdot (\nabla^2 \mathbf{u}) &= \nabla \cdot (\nabla^2 \mathbf{u}) - \frac{1}{r^2} \frac{\partial}{\partial r} [r^2 (\nabla^2 \mathbf{u})] \\ &= \nabla^2 (\underbrace{\nabla \cdot \mathbf{u}}_{=0}) - \frac{1}{r^2} \frac{\partial}{\partial r} [r^2 (\nabla^2 \mathbf{u})_r] \\ &= -\frac{1}{r^2} \frac{\partial}{\partial r} [r^2 (\nabla^2 \mathbf{u})_r]. \end{aligned} \quad (\text{A.0.13})$$

Using relation (A.0.9) results in the following expression

$$\begin{aligned} \nabla_H \cdot (\nabla^2 \mathbf{u}) &= \nabla_H^2 \frac{\partial}{\partial r} \left(\frac{\partial^2 W}{\partial r^2} + \nabla_H^2 W \right) \\ &= \nabla_H^2 \left(\frac{\partial^3 W}{\partial r^3} + \nabla_H^2 \frac{\partial W}{\partial r} - \frac{2}{r} \nabla_H^2 W \right). \end{aligned} \quad (\text{A.0.14})$$

In the double curl formulation, the viscous term (4.2.35) is derived from the following:

$$\begin{aligned}
 \mathbf{e}_r \cdot \nabla \times \nabla \times \nabla^2 \mathbf{u} &= \frac{\partial}{\partial r} (\nabla \cdot \nabla^2 \mathbf{u}) - (\mathbf{e}_r \cdot \nabla^2) \nabla^2 \mathbf{u} \\
 &= \frac{\partial}{\partial r} \left[\nabla^2 (\underbrace{\nabla \cdot \mathbf{u}}_{=0}) \right] - (\mathbf{e}_r \cdot \nabla^2) \nabla^2 \mathbf{u} \\
 &= - (\mathbf{e}_r \cdot \nabla^2) \nabla^2 \mathbf{u}.
 \end{aligned} \tag{A.0.15}$$

By replacing \mathbf{u} with $\nabla^2 \mathbf{u}$ in relation (A.0.5) this can be rewritten as

$$- (\mathbf{e}_r \cdot \nabla^2) \nabla^2 \mathbf{u} = -\frac{1}{r^2} \left[\nabla^2 (r^2 (\nabla^2 \mathbf{u})_r) - \frac{2}{r} \frac{\partial}{\partial r} [r^2 (\nabla^2 \mathbf{u})_r] \right] \tag{A.0.16}$$

Decomposing the Laplacian into its radial and horizontal parts yields

$$- (\mathbf{e}_r \cdot \nabla^2) \nabla^2 \mathbf{u} = -\frac{1}{r^2} \left[\frac{1}{r^2} \frac{\partial}{\partial r} \left(r^2 \frac{\partial}{\partial r} (r^2 (\nabla^2 \mathbf{u})_r) \right) + \nabla_H^2 (r^2 (\nabla^2 \mathbf{u})_r) - \frac{2}{r} \frac{\partial}{\partial r} (r^2 (\nabla^2 \mathbf{u})_r) \right]. \tag{A.0.17}$$

After inserting expression (A.0.9) one finally obtains

$$\mathbf{e}_r \cdot \nabla \times \nabla \times \nabla^2 \mathbf{u} = \nabla_H^2 \left[\frac{\partial^4 W}{\partial r^4} + 2 \nabla_H^2 \frac{\partial^2 W}{\partial r^2} - \frac{4}{r} \nabla_H^2 \frac{\partial W}{\partial r} + \nabla_H^2 \left(\nabla_H^2 + \frac{6}{r^2} \right) W \right]. \tag{A.0.18}$$

Appendix B

Results of simulations

B.1 Dynamo models

Table B.1: Summary of the relevant parameters of the numerical models that were analysed for this study. All dynamo models have been computed with $Pr = 1$ and $r_i/r_o = 0.35$. Nu is the Nusselt number, Rm the magnetic Reynolds number, f_{ohm} the ohmic dissipation fraction and f_{dip} the relative dipole strength as defined in [Christensen and Aubert \(2006\)](#). ℓ_{\perp} corresponds to the spherical harmonic degree at which buoyancy and Lorentz forces are of equal magnitude. For cases where this crossing is ill-posed, or the Lorentz force is of the same magnitude or weaker than inertia and/or viscous forces no value is provided.

	Ra	Pm	Nu	Rm	Λ	\mathcal{M}	δ	χ_{norm}	f_{ohm}	f_{dip}	ℓ_{pol}	ℓ_{\perp}	(N_r, ℓ_{max})
	$E = 10^{-4}$												
1	1.500×10^6	12.000	1.40	209.6	8.50	23.9	20.02	0.07	0.60	0.82	5	5.93	(49, 96)
2	1.600×10^6	12.000	1.42	205.2	11.02	32.5	22.07	0.09	0.66	0.84	5	5.57	(49, 96)
3	1.800×10^6	12.000	1.48	203.5	19.24	57.5	28.92	0.03	0.73	0.82	5	4.73	(49, 96)
4	2.000×10^6	12.000	1.60	238.5	25.10	54.3	30.08	0.05	0.73	0.77	5	4.46	(61, 106)
5	2.000×10^6	15.000	1.64	312.1	35.16	55.6	29.32	0.04	0.71	0.72	4	3.46	(65, 128)
6	2.200×10^6	12.000	1.71	267.9	29.87	51.0	29.20	0.03	0.72	0.76	5	4.51	(61, 106)
7	2.400×10^6	5.000	1.63	153.3	3.67	8.1	13.76	0.12	0.52	0.86	6	8.35	(49, 96)
8	2.400×10^6	12.000	1.83	299.8	34.08	46.4	26.44	0.06	0.71	0.74	4	4.51	(61, 106)
9	2.440×10^6	2.000	1.37	66.3	0.03	0.2	0.41	1.03	0.04	0.97	5	—	(41, 85)
10	2.750×10^6	12.000	1.99	353.7	38.94	38.0	24.12	0.08	0.70	0.72	5	4.53	(61, 106)
11	2.790×10^6	2.000	1.55	72.3	0.42	1.6	3.47	0.41	0.28	0.93	6	17.32	(41, 85)
12	3.200×10^6	3.000	1.78	120.5	2.12	4.4	10.20	0.1	0.48	0.88	7	9.87	(41, 96)
13	3.200×10^6	7.000	2.07	234.8	21.26	27.5	23.86	0.05	0.71	0.78	6	4.94	(61, 106)

Continued on next page

B. RESULTS OF SIMULATIONS

	Ra	Pm	Nu	Rm	Λ	\mathcal{M}	δ	χ_{norm}	f_{ohm}	f_{dip}	ℓ_{pol}	ℓ_{\perp}	(N_r, ℓ_{max})
14	3.200×10^6	12.000	2.18	416.0	44.11	31.2	22.06	0.05	0.67	0.69	5	4.61	(61, 106)
15	3.500×10^6	1.000	1.86	46.4	0.45	2.1	2.64	0.48	0.36	0.97	8	23.87	(41, 85)
16	3.750×10^6	1.000	1.97	48.4	0.69	3.0	3.72	0.5	0.44	0.96	7	16.54	(41, 85)
17	4.830×10^6	3.000	2.46	154.8	8.54	10.9	15.17	0.05	0.67	0.86	6	6.70	(41, 96)
18	4.830×10^6	5.000	2.65	263.1	18.52	13.6	17.97	0.08	0.66	0.76	7	5.20	(61, 106)
19	4.830×10^6	9.500	2.80	507.7	43.33	16.2	16.74	0.06	0.63	0.67	5	5.00	(49, 106)
20	4.880×10^6	1.000	2.35	57.8	1.55	4.7	5.57	0.34	0.55	0.96	7	10.92	(41, 85)
21	6.500×10^6	0.500	2.84	43.6	0.49	1.3	1.23	1.29	0.31	0.97	5	—	(41, 85)
22	7.500×10^6	0.500	3.25	50.4	0.60	1.2	1.22	1.01	0.31	0.96	6	—	(41, 64)
23	7.500×10^6	1.000	3.16	84.6	2.70	3.8	5.01	0.08	0.54	0.95	6	10.91	(41, 85)
24	7.500×10^6	3.000	3.44	249.7	11.87	5.8	10.31	0.1	0.59	0.78	7	8.19	(49, 106)
25	7.500×10^6	9.000	3.64	726.6	53.23	9.2	12.92	0.12	0.56	0.63	6	5.67	(49, 106)
26	7.500×10^6	12.000	3.67	957.0	77.88	10.3	14.16	0.05	0.55	0.60	6	5.30	(65, 128)
27	7.500×10^6	15.000	3.68	1195.4	99.66	10.6	13.38	0.08	0.53	0.58	7	5.08	(65, 133)
28	8.250×10^6	7.000	3.83	622.6	39.97	7.3	11.94	0.09	0.56	0.64	6	6.32	(49, 106)
29	8.500×10^6	0.500	3.64	57.9	0.64	1.0	1.08	1.01	0.29	0.95	7	—	(41, 85)
30	1.125×10^7	1.000	4.28	127.0	3.41	2.1	3.58	0.08	0.48	0.91	8	12.29	(41, 85)
31	1.125×10^7	3.000	4.51	366.1	14.37	3.2	6.95	0.15	0.53	0.73	6	8.92	(49, 106)
32	1.125×10^7	5.000	4.59	594.4	29.30	4.2	8.89	0.18	0.53	0.66	7	8.40	(49, 106)
33	1.125×10^7	7.000	4.61	814.6	46.53	5.0	10.36	0.15	0.53	0.62	7	6.78	(61, 128)
34	1.500×10^7	1.000	5.90	227.7	0.49	0.1	0.36	5.48	0.11	0.31	6	—	(41, 85)
35	1.500×10^7	2.000	5.41	324.0	9.27	1.8	4.12	0.16	0.47	0.77	12	11.23	(41, 85)
36	1.500×10^7	3.000	5.46	473.0	16.21	2.2	5.45	0.15	0.48	0.71	9	10.38	(49, 106)
37	1.500×10^7	5.000	5.46	757.2	33.83	3.0	6.87	0.19	0.48	0.64	6	8.82	(49, 106)
38	1.500×10^7	7.000	5.47	1038.1	53.11	3.5	7.77	0.16	0.48	0.59	8	8.35	(61, 128)
39	1.500×10^7	9.000	5.45	1309.4	74.79	4.0	8.80	0.14	0.47	0.57	7	8.28	(65, 133)
40	1.500×10^7	15.000	5.38	2108.2	147.91	5.1	9.75	0.12	0.42	0.52	6	6.71	(65, 133)
41	1.750×10^7	1.000	6.53	255.2	0.66	0.1	0.38	6.08	0.12	0.31	6	—	(61, 106)
42	1.750×10^7	2.000	6.09	381.5	8.83	1.2	3.28	0.11	0.43	0.75	14	13.01	(61, 106)
43	1.750×10^7	4.560	5.98	785.2	32.62	2.4	6.14	0.19	0.47	0.65	11	8.91	(61, 106)
44	1.750×10^7	8.000	5.96	1327.8	69.66	3.2	7.85	0.15	0.45	0.57	8	8.43	(61, 128)
45	2.100×10^7	2.000	7.21	522.6	4.05	0.3	1.21	1.61	0.26	0.28	6	—	(61, 128)
46	2.100×10^7	7.000	6.61	1353.1	63.08	2.4	6.50	0.17	0.45	0.58	6	8.69	(81, 133)

$$E = 10^{-5}$$

Continued on next page

B. RESULTS OF SIMULATIONS

	Ra	Pm	Nu	Rm	Λ	\mathcal{M}	δ	χ_{norm}	f_{ohm}	f_{dip}	ℓ_{pol}	ℓ_{\perp}	(N_r, ℓ_{max})
47	3.300×10^7	5.000	1.83	271.5	3.74	27.4	36.83	0.03	0.75	0.27	8	7.70	(81, 133)
48	3.300×10^7	7.000	1.87	346.2	7.15	42.5	37.42	0.05	0.78	0.75	9	6.79	(97, 133)
49	4.000×10^7	2.000	1.33	104.1	0.09	1.7	3.54	0.67	0.26	0.97	12	31.88	(81, 133)
50	4.000×10^7	7.000	2.12	303.1	23.01	180.8	61.43	0.02	0.88	0.84	6	4.92	(97, 133)
51	5.000×10^7	1.000	1.52	72.6	0.09	1.8	3.03	0.58	0.33	0.96	14	39.73	(81, 133)
52	5.000×10^7	2.000	1.43	132.9	0.16	1.8	5.10	0.68	0.30	0.87	12	28.63	(81, 133)
53	5.000×10^7	3.000	2.05	240.9	2.21	12.1	23.33	0.06	0.69	0.76	8	10.46	(81, 133)
54	6.000×10^7	5.000	2.81	337.2	26.37	117.5	57.82	0.01	0.87	0.80	7	4.93	(97, 170)
55	7.500×10^7	0.500	2.22	60.8	0.20	2.8	2.96	0.98	0.44	0.90	13	—	(81, 133)
56	7.500×10^7	2.000	2.49	194.1	3.27	17.6	33.57	0.05	0.77	0.91	8	8.96	(81, 133)
57	8.000×10^7	1.000	2.46	120.0	0.93	6.5	12.55	0.13	0.63	0.84	10	12.50	(81, 133)
58	1.000×10^8	1.000	3.06	140.5	1.76	9.1	14.19	0.11	0.69	0.91	9	11.10	(81, 133)
59	1.000×10^8	2.000	3.67	225.5	11.35	45.3	36.12	0.09	0.86	0.91	6	6.39	(81, 133)
60	1.000×10^8	3.000	3.90	341.1	21.15	55.4	37.40	0.04	0.85	0.83	6	5.65	(97, 170)
61	1.000×10^8	7.000	4.07	779.9	63.63	74.9	31.72	0.04	0.80	0.75	6	4.96	(97, 170)
62	1.100×10^8	0.200	3.01	39.6	0.07	0.9	0.45	—	0.23	0.99	12	—	(97, 170)
63	1.500×10^8	0.200	4.10	51.0	0.19	1.4	0.86	1.41	0.33	0.96	14	—	(97, 170)
64	1.500×10^8	0.300	4.28	72.6	0.42	2.4	2.11	0.31	0.44	0.91	13	—	(81, 133)
65	1.500×10^8	0.500	4.45	116.9	1.03	3.8	4.54	0.09	0.56	0.90	12	16.08	(81, 133)
66	1.500×10^8	2.000	5.13	346.3	15.87	26.8	29.72	0.04	0.82	0.87	7	7.39	(97, 170)
67	2.000×10^8	0.150	6.31	55.8	0.24	1.2	0.62	3.78	0.34	0.98	12	—	(97, 170)
68	2.000×10^8	1.000	6.02	240.4	7.03	12.3	15.42	0.06	0.77	0.94	8	9.60	(97, 170)
69	2.000×10^8	2.000	6.31	451.4	19.88	19.7	24.82	0.05	0.80	0.84	9	8.18	(97, 170)
70	2.000×10^8	5.000	6.57	1107.2	63.20	26.1	24.92	0.05	0.74	0.74	7	6.60	(97, 170)
71	3.000×10^8	0.150	9.90	78.8	0.55	1.3	0.69	2.32	0.43	0.96	13	—	(97, 170)
72	3.000×10^8	0.200	9.89	99.3	0.99	2.0	1.33	0.35	0.51	0.96	14	—	(97, 170)
73	3.000×10^8	0.300	9.34	136.8	1.70	2.8	2.48	0.1	0.58	0.94	12	15.72	(97, 170)
74	3.000×10^8	0.500	8.43	202.0	3.16	3.9	5.11	0.08	0.65	0.95	12	12.83	(97, 192)
75	4.000×10^8	0.100	12.38	89.3	0.10	0.1	0.22	—	0.19	0.25	7	—	(97, 192)
76	4.000×10^8	0.150	12.52	98.8	0.89	1.4	0.84	1.27	0.48	0.97	12	—	(97, 192)
77	4.000×10^8	1.000	10.33	432.5	13.02	7.0	9.80	0.07	0.74	0.90	11	9.71	(121, 256)
78	4.000×10^8	2.000	10.55	845.0	30.59	8.6	13.97	0.07	0.73	0.81	10	8.96	(121, 256)
79	5.000×10^8	0.070	14.70	77.9	0.07	0.1	0.16	—	0.17	0.24	7	—	(97, 192)
80	5.000×10^8	0.150	14.28	116.8	1.07	1.2	0.87	0.91	0.49	0.97	12	—	(97, 192)

Continued on next page

B. RESULTS OF SIMULATIONS

	Ra	Pm	Nu	Rm	Λ	\mathcal{M}	δ	χ_{norm}	f_{ohm}	f_{dip}	ℓ_{pol}	ℓ_{\perp}	(N_r, ℓ_{max})
81	7.000×10^8	0.200	18.93	236.2	0.86	0.3	0.59	9.28	0.36	0.30	9	—	(121, 256)
82	7.000×10^8	0.500	15.35	375.5	8.28	2.9	4.70	0.15	0.68	0.94	11	8.95	(121, 256)
83	7.000×10^8	1.440	15.64	1018.0	27.55	3.8	6.94	0.11	0.68	0.85	12	10.42	(121, 256)
84	7.000×10^8	5.000	15.18	3286.8	131.81	6.2	7.86	0.12	0.56	0.70	9	8.87	(121, 256)
85	9.000×10^8	1.440	18.22	1219.6	35.06	3.4	6.37	0.11	0.67	0.84	8	10.11	(121, 256)
86	1.000×10^9	0.500	19.76	517.6	10.18	1.9	4.42	0.12	0.66	0.92	11	10.29	(161, 256)
87	1.300×10^9	0.500	23.59	651.8	11.34	1.3	3.79	0.14	0.64	0.89	10	10.68	(161, 256)
88	1.300×10^9	1.440	22.90	1656.2	43.80	2.3	5.29	0.14	0.63	0.81	10	10.52	(161, 256)
89	1.500×10^9	0.500	27.40	858.0	7.15	0.5	1.83	1.09	0.51	0.25	6	15.81	(240, 256)
90	1.500×10^9	1.440	24.86	1865.1	46.76	2.0	5.11	0.14	0.61	0.80	8	10.78	(240, 256)
91	1.900×10^9	1.440	29.82	2597.1	32.97	0.7	3.02	0.54	0.52	0.23	7	13.41	(240, 256)
92	2.200×10^9	1.440	31.83	2837.2	38.66	0.7	2.92	0.60	0.51	0.16	6	13.02	(240, 256)
93	2.200×10^9	3.000	29.59	5015.1	135.77	1.6	4.10	0.18	0.46	0.67	8	10.59	(240, 256)
94	2.600×10^9	3.000	33.15	6113.2	109.70	0.9	3.94	0.49	0.45	0.26	6	12.15	(280, 341)
$E = 10^{-6}$													
95	8.000×10^8	2.000	1.37	243.0	0.04	1.5	3.27	0.68	0.23	0.91	39	72.58	(161, 341)
96	1.000×10^9	1.000	1.67	141.9	0.15	7.6	15.12	0.76	0.63	0.81	29	25.77	(161, 426)
97	2.000×10^9	0.150	2.84	57.1	0.04	1.8	0.82	—	0.32	0.93	22	—	(161, 341)
98	2.000×10^9	0.250	3.42	97.9	0.14	3.5	3.70	1.33	0.49	0.77	24	—	(193, 426)
99	2.000×10^9	0.500	4.93	176.5	1.22	19.8	19.65	0.21	0.82	0.90	17	16.90	(161, 426)
100	2.000×10^9	1.000	4.98	340.9	2.65	22.9	37.09	0.03	0.84	0.92	12	13.22	(193, 426)
101	2.000×10^9	2.000	5.69	525.9	11.74	85.3	83.90	0.02	0.91	0.93	11	8.86	(193, 426)
102	2.800×10^9	0.500	6.98	259.5	1.72	12.8	16.58	0.03	0.78	0.88	18	15.63	(193, 426)
103	5.500×10^9	0.100	12.27	128.7	0.16	1.0	0.75	-	0.41	0.81	26	—	(289, 426)
104	5.500×10^9	0.400	12.78	358.0	3.61	11.3	12.36	0.12	0.80	0.88	22	11.07	(289, 426)
105	1.000×10^{10}	0.080	26.00	176.8	0.54	1.4	1.07	-	0.54	0.92	16	—	(321, 512)
106	1.000×10^{10}	0.250	22.17	365.2	4.10	7.7	9.07	-	0.80	0.87	12	13.48	(321, 597)
107	1.000×10^{10}	0.500	20.05	580.9	11.53	17.2	17.52	0.02	0.87	0.94	13	9.64	(321, 512)
108	2.660×10^{10}	0.030	49.63	162.6	0.27	0.3	0.42	-	0.46	0.39	10	—	(768, 597)
109	2.660×10^{10}	0.080	45.71	281.1	2.87	2.9	2.80	-	0.74	0.94	18	10.35	(720, 597)
110	2.660×10^{10}	0.150	44.20	466.2	6.36	4.4	5.52	-	0.80	0.93	13	8.93	(720, 597)
111	2.660×10^{10}	0.456	41.22	1085.6	30.10	11.8	11.11	0.04	0.90	0.94	11	8.76	(361, 512)

B.2 Rotating convection models

B. RESULTS OF SIMULATIONS

Table B.2: Summary of the relevant parameters of the non-magnetic rotating convection simulations considered in the present study. All models have been computed with $Pr = 1$ and $r_i/r_o = 0.35$. Nu represents the Nusselt number.

	Ra	Nu	Ro	Re	ℓ_{pol}	ℓ_{IA}	(N_r, ℓ_{max})
$E = 10^{-4}$							
1	3.000×10^6	1.51	4.31×10^{-3}	43.15	6	31.18	(41, 85)
2	4.830×10^6	2.13	7.46×10^{-3}	74.56	7	55.57	(41, 85)
3	7.500×10^6	3.02	1.20×10^{-2}	120.12	6	52.66	(41, 85)
4	1.125×10^7	4.67	1.89×10^{-2}	189.28	6	23.43	(41, 85)
5	1.500×10^7	5.87	2.48×10^{-2}	247.81	6	9.58	(41, 85)
6	1.750×10^7	6.51	2.82×10^{-2}	282.45	6	8.26	(65, 128)
7	2.100×10^7	7.27	3.27×10^{-2}	327.17	5	6.37	(65, 133)
$E = 10^{-5}$							
8	4.000×10^7	1.39	6.66×10^{-4}	66.63	14	51.31	(97, 170)
9	1.000×10^8	2.44	2.01×10^{-3}	201.38	12	120.4	(97, 213)
10	2.000×10^8	5.41	4.99×10^{-3}	499.27	8	14.99	(97, 256)
11	3.000×10^8	9.01	8.15×10^{-3}	815.16	9	8.66	(121, 288)
12	4.000×10^8	11.95	1.09×10^{-2}	1092.02	7	6.33	(121, 288)
13	7.000×10^8	18.13	1.82×10^{-2}	1824.76	5	4.69	(161, 426)
$E = 10^{-6}$							
14	8.000×10^8	1.42	1.51×10^{-4}	150.56	30	110.64	(129, 256)
15	1.000×10^9	1.55	2.00×10^{-4}	199.62	27	125.53	(129, 256)
16	2.000×10^9	2.38	4.59×10^{-4}	458.87	20	244.43	(129, 341)
17	2.800×10^9	3.42	7.21×10^{-4}	721.33	18	43.13	(161, 426)
18	3.500×10^9	4.74	1.03×10^{-3}	1028.67	20	22.49	(181, 426)
19	5.500×10^9	9.42	2.05×10^{-3}	2045.89	12	12.25	(201, 426)
20	1.000×10^{10}	19.68	4.13×10^{-3}	4125.75	9	6.50	(321, 512)
21	1.600×10^{10}	30.78	6.71×10^{-3}	6714.67	6	4.78	(385, 597)
22	2.660×10^{10}	46.46	1.06×10^{-2}	10613.04	5	4.46	(513, 853)
$E = 10^{-7}$							
23	6.500×10^{10}	4.15	2.07×10^{-4}	2074.51	26	34.83	(433, 682)
24	1.000×10^{11}	7.92	4.42×10^{-4}	4420.00	20	19.00	(513, 682)

Bibliography

- R. Abarca del Rio, D. Gambis, and D. A. Salstein. Interannual signals in length of day and atmospheric angular momentum. *Annales Geophysicae*, 18(3):347–364, 2000. doi: 10.1007/s00585-000-0347-9. URL <https://doi.org/10.1007/s00585-000-0347-9>.
- M. Abramowitz and I. A. Stegun. *Handbook of Mathematical Functions with Formulas, Graphs, and Mathematical Tables*. Dover Publications, 1970.
- D. Alfè, M. J. Gillan, and G. D. Price. Ab initio chemical potentials of solid and liquid solutions and the chemistry of the Earth’s core. *The Journal of Chemical Physics*, 116(16):7127–7136, 2002a. doi: 10.1063/1.1464121. URL <https://doi.org/10.1063/1.1464121>.
- D. Alfè, G. D. Price, and M. J. Gillan. Iron under Earth’s core conditions: Liquid-state thermodynamics and high-pressure melting curve from ab initio calculations. *Physical Review B*, 65:165118, Apr 2002b. doi: 10.1103/PhysRevB.65.165118. URL <https://link.aps.org/doi/10.1103/PhysRevB.65.165118>.
- P. Alken, E. Thébaud, C. D. Beggan, H. Amit, J. Aubert, J. Baerenzung, T. N. Bondar, W. Brown, S. Califf, A. Chambout, A. Chulliat, G. Cox, C. C. Finlay, A. Fournier, N. Gillet, A. Grayver, M. D. Hammer, M. Holschneider, L. Huder, G. Hulot, T. Jager, C. Kloss, M. Korte, W. Kuang, A. Kuvshinov, B. Langlais, J.-M. L  ger, V. Lesur, P. W. Livermore, F. J. Lowes, S. Macmillan, W. Magnes, M. Manda, S. Marsal, J. Matzka, M. C. Metman, T. Minami, A. Morschhauser, J. E. Mound, M. Nair, S. Nakano, N. Olsen, F. J. Pav  n-Carrasco, V. G. Petrov, G. Ropp, M. Rother, T. J. Sabaka, S. Sanchez, D. Saturnino, N. R. Schnepf, X. Shen, C. Stolle, A. Tangborn, L. T  ffner-Clausen, H. Toh, J. M. Torta, J. Varner, F. Vervelidou, P. Vigneron, I. Wardinski, J. Wicht, A. Woods, Y. Yang, Z. Zeren, and B. Zhou. International Geomagnetic Reference Field: the thirteenth generation. *Earth, Planets and Space*, July 2020. URL <http://eprints.whiterose.ac.uk/165378/>.
- A. P. Anufriev, C. A. Jones, and A. M. Soward. The Boussinesq and anelastic liquid approximations for convection in the Earth’s core. *Physics of the Earth and Planetary Interiors*, 152(3):163–190, 2005. ISSN 0031-9201. doi: <https://doi.org/10.1016/j.pepi.2005.06.004>. URL <http://www.sciencedirect.com/science/article/pii/S0031920105001068>.

- U. M. Ascher, S. J. Ruuth, and B. T. R. Wetton. Implicit-Explicit Methods for Time-Dependent Partial Differential Equations. *SIAM Journal on Numerical Analysis*, 32(3): 797–823, 1995. URL <http://www.jstor.org/stable/2158449>.
- U. M. Ascher, S. J. Ruuth, and R. J. Spiteri. Implicit-explicit Runge-Kutta methods for time-dependent partial differential equations. *Applied Numerical Mathematics*, 25(2):151–167, 1997. ISSN 0168-9274. doi: [https://doi.org/10.1016/S0168-9274\(97\)00056-1](https://doi.org/10.1016/S0168-9274(97)00056-1). URL <http://www.sciencedirect.com/science/article/pii/S0168927497000561>. Special Issue on Time Integration.
- J. Aubert. Flow throughout the Earth’s core inverted from geomagnetic observations and numerical dynamo models. *Geophysical Journal International*, 192(2):537–556, 2013. ISSN 0956-540X. doi: 10.1093/gji/ggs051. URL <https://doi.org/10.1093/gji/ggs051>.
- J. Aubert. Earth’s core internal dynamics 1840-2010 imaged by inverse geodynamo modelling. *Geophysical Journal International*, 197(3):1321–1334, 2014. ISSN 0956-540X. doi: 10.1093/gji/ggu064. URL <https://doi.org/10.1093/gji/ggu064>.
- J. Aubert. Geomagnetic forecasts driven by thermal wind dynamics in the Earth’s core. *Geophysical Journal International*, 203(3):1738–1751, 2015. ISSN 0956-540X. doi: 10.1093/gji/ggv394. URL <https://doi.org/10.1093/gji/ggv394>.
- J. Aubert. Approaching Earth’s core conditions in high-resolution geodynamo simulations. *Geophysical Journal International*, 219(Supplement 1):S137–S151, 05 2019. ISSN 0956-540X. doi: 10.1093/gji/ggz232. URL <https://doi.org/10.1093/gji/ggz232>.
- J. Aubert. Recent geomagnetic variations and the force balance in Earth’s core. *Geophysical Journal International*, 221(1):378–393, 01 2020. ISSN 0956-540X. doi: 10.1093/gji/ggaa007. URL <https://doi.org/10.1093/gji/ggaa007>.
- J. Aubert, D. Brito, H.-C. Nataf, P. Cardin, and J.-P. Masson. A systematic experimental study of rapidly rotating spherical convection in water and liquid gallium. *Physics of the Earth and Planetary Interiors*, 128(1):51–74, 2001. ISSN 0031-9201. doi: [https://doi.org/10.1016/S0031-9201\(01\)00277-1](https://doi.org/10.1016/S0031-9201(01)00277-1). URL <http://www.sciencedirect.com/science/article/pii/S0031920101002771>. Dynamics and Magnetic Fields of the Earth’s and Planetary Interiors.
- J. Aubert, S. Labrosse, and C. Poitou. Modelling the palaeo-evolution of the geodynamo. *Geophysical Journal International*, 179(3):1414–1428, 2009. doi: 10.1111/j.1365-246X.2009.04361.x. URL <https://onlinelibrary.wiley.com/doi/abs/10.1111/j.1365-246X.2009.04361.x>.
- J. Aubert, T. Gastine, and A. Fournier. Spherical convective dynamos in the rapidly rotating asymptotic regime. *Journal of Fluid Mechanics*, 813:558–593, 2017. doi: 10.1017/jfm.2016.789.

- J. M. Aurnou and E. M. King. The cross-over to magnetostrophic convection in planetary dynamo systems. *Proceedings of the Royal Society A: Mathematical, Physical and Engineering Sciences*, 473(2199):20160731, 2017. doi: 10.1098/rspa.2016.0731. URL <https://royalsocietypublishing.org/doi/abs/10.1098/rspa.2016.0731>.
- G. Backus, R. Parker, and C. Constable. *Foundations of Geomagnetism*. Cambridge University Press, 1996.
- O. Barrois, N. Gillet, and J. Aubert. Contributions to the geomagnetic secular variation from a reanalysis of core surface dynamics. *Geophysical Journal International*, 211(1): 50–68, 07 2017. ISSN 0956-540X. doi: 10.1093/gji/ggx280. URL <https://doi.org/10.1093/gji/ggx280>.
- G. K. Batchelor. *An Introduction to Fluid Dynamics*. Cambridge University Press, 2000.
- F. Birch. Elasticity and constitution of the Earth's interior. *Journal of Geophysical Research (1896-1977)*, 57(2):227–286, 1952. doi: 10.1029/JZ057i002p00227. URL <https://agupubs.onlinelibrary.wiley.com/doi/abs/10.1029/JZ057i002p00227>.
- F. Birch. Density and composition of mantle and core. *Journal of Geophysical Research (1896-1977)*, 69(20):4377–4388, 1964. doi: 10.1029/JZ069i020p04377. URL <https://agupubs.onlinelibrary.wiley.com/doi/abs/10.1029/JZ069i020p04377>.
- J. Bloxham and A. Jackson. Time-dependent mapping of the magnetic field at the core-mantle boundary. *Journal of Geophysical Research: Solid Earth*, 97(B13):19537–19563, 1992. doi: 10.1029/92JB01591. URL <https://agupubs.onlinelibrary.wiley.com/doi/abs/10.1029/92JB01591>.
- J. P. Boyd. *Chebyshev and Fourier spectral methods*. Courier Corporation, 2001.
- S. I. Braginsky. Torsional Magnetohydrodynamic Vibrations in the Earth's Core and Variations in Day Length. *Geomagnetism and Aeronomy*, 10:1, 1970.
- S. I. Braginsky and P. H. Roberts. Equations governing convection in earth's core and the geodynamo. *Geophysical & Astrophysical Fluid Dynamics*, 79(1-4):1–97, 1995. doi: 10.1080/03091929508228992. URL <https://doi.org/10.1080/03091929508228992>.
- B. A. Buffett. Tidal dissipation and the strength of the Earth's internal magnetic field. *Nature*, 468(7326):952–954, 2010. doi: 10.1038/nature09643. URL <https://doi.org/10.1038/nature09643>.
- E. C. Bullard. The magnetic field within the Earth. *Proceedings of the Royal Society of London. Series A. Mathematical and Physical Sciences*, 197(1051):433–453, 1949. doi: 10.1098/rspa.1949.0074. URL <https://royalsocietypublishing.org/doi/abs/10.1098/rspa.1949.0074>.

- F. H. Busse. Thermal instabilities in rapidly rotating systems. *Journal of Fluid Mechanics*, 44(3):441–460, 1970. doi: 10.1017/S0022112070001921.
- S. Cabanes, J. Aurnou, B. Favier, and M. Le Bars. A laboratory model for deep-seated jets on the gas giants. *Nature Physics*, 13(4):387–390, 2017. doi: 10.1038/nphys4001. URL <https://doi.org/10.1038/nphys4001>.
- M. A. Calkins. Quasi-geostrophic dynamo theory. *Physics of the Earth and Planetary Interiors*, 276:182–189, Mar. 2018. doi: 10.1016/j.pepi.2017.05.001.
- P. Cardin and P. Olson. Chaotic thermal convection in a rapidly rotating spherical shell: consequences for flow in the outer core. *Physics of the Earth and Planetary Interiors*, 82(3):235–259, 1994. ISSN 0031-9201. doi: [https://doi.org/10.1016/0031-9201\(94\)90075-2](https://doi.org/10.1016/0031-9201(94)90075-2). URL <http://www.sciencedirect.com/science/article/pii/0031920194900752>.
- P. Cardin, D. Brito, D. Jault, H.-C. Nataf, and J.-P. Masson. Towards a rapidly rotating liquid sodium dynamo experiment. *Magnetohydrodynamics c/c of Magnitnaia Hidrodinamika*, 38:177–189, 2002. URL <https://hal.archives-ouvertes.fr/hal-00000875>.
- S. Chandrasekhar. *Hydrodynamic and hydromagnetic stability*. Clarendon Press: Oxford University Press, 1961.
- U. Christensen, P. Olson, and G. A. Glatzmaier. Numerical modelling of the geodynamo: a systematic parameter study. *Geophysical Journal International*, 138(2):393–409, 08 1999. ISSN 0956-540X. doi: 10.1046/j.1365-246X.1999.00886.x. URL <https://doi.org/10.1046/j.1365-246X.1999.00886.x>.
- U. R. Christensen. Geodynamo models: Tools for understanding properties of Earth’s magnetic field. *Physics of the Earth and Planetary Interiors*, 187(3):157–169, 2011. ISSN 0031-9201. doi: <https://doi.org/10.1016/j.pepi.2011.03.012>. URL <http://www.sciencedirect.com/science/article/pii/S0031920111000720>. Special Issue: Planetary Magnetism, Dynamo and Dynamics.
- U. R. Christensen and J. Aubert. Scaling properties of convection-driven dynamos in rotating spherical shells and application to planetary magnetic fields. *Geophysical Journal International*, 166(1):97–114, 07 2006. ISSN 0956-540X. doi: 10.1111/j.1365-246X.2006.03009.x. URL <https://doi.org/10.1111/j.1365-246X.2006.03009.x>.
- U. R. Christensen and J. Wicht. 8.10 - Numerical Dynamo Simulations. In G. Schubert, editor, *Treatise on Geophysics (Second Edition)*, pages 245–277. Elsevier, Oxford, second edition edition, 2015. ISBN 978-0-444-53803-1. doi: <https://doi.org/10.1016/B978-0-444-53802-4.00145-7>. URL <http://www.sciencedirect.com/science/article/pii/B9780444538024001457>.

- U. R. Christensen, J. Aubert, P. Cardin, E. Dormy, S. Gibbons, G. A. Glatzmaier, E. Grote, Y. Honkura, C. Jones, M. Kono, M. Matsushima, A. Sakuraba, F. Takahashi, A. Tilgner, J. Wicht, and K. Zhang. A numerical dynamo benchmark. *Physics of the Earth and Planetary Interiors*, 128(1):25–34, 2001. ISSN 0031-9201. doi: [https://doi.org/10.1016/S0031-9201\(01\)00275-8](https://doi.org/10.1016/S0031-9201(01)00275-8). Dynamics and Magnetic Fields of the Earth’s and Planetary Interiors.
- U. R. Christensen, J. Aubert, and G. Hulot. Conditions for Earth-like geodynamo models. *Earth and Planetary Science Letters*, 296(3):487–496, 2010. ISSN 0012-821X. doi: <https://doi.org/10.1016/j.epsl.2010.06.009>. URL <http://www.sciencedirect.com/science/article/pii/S0012821X10003833>.
- C. Constable and M. Korte. Is Earth’s magnetic field reversing? *Earth and Planetary Science Letters*, 246(1):1–16, 2006. ISSN 0012-821X. doi: <https://doi.org/10.1016/j.epsl.2006.03.038>. URL <http://www.sciencedirect.com/science/article/pii/S0012821X0600269X>.
- C. G. Constable and S. C. Constable. *Satellite Magnetic Field Measurements: Applications in Studying the Deep Earth*, pages 147–159. American Geophysical Union (AGU), 2013. ISBN 9781118666012. doi: 10.1029/150GM13. URL <https://agupubs.onlinelibrary.wiley.com/doi/abs/10.1029/150GM13>.
- J. Crank and P. Nicolson. A practical method for numerical evaluation of solutions of partial differential equations of the heat-conduction type. *Mathematical Proceedings of the Cambridge Philosophical Society*, 43(1):50–67, 1947. doi: 10.1017/S0305004100023197.
- P. Davidson. *Turbulence*. Oxford University Press, 2004. URL <https://books.google.fr/books?id=Vb1DCQAAQBAJ>.
- P. A. Davidson. *An Introduction to Magnetohydrodynamics*. Cambridge Texts in Applied Mathematics. Cambridge University Press, 2001. doi: 10.1017/CBO9780511626333.
- P. A. Davidson. Scaling laws for planetary dynamos. *Geophysical Journal International*, 195(1):67–74, 06 2013. ISSN 0956-540X. doi: 10.1093/gji/ggt167. URL <https://doi.org/10.1093/gji/ggt167>.
- P. A. Davidson, P. J. Staplehurst, and S. B. Dalziel. On the evolution of eddies in a rapidly rotating system. *Journal of Fluid Mechanics*, 557:135–144, 2006. doi: 10.1017/S0022112006009827.
- C. Davies, M. Pozzo, D. Gubbins, and D. Alfè. Constraints from material properties on the dynamics and evolution of Earth’s core. *Nature Geoscience*, 8(9):678–685, 2015. doi: 10.1038/ngeo2492. URL <https://doi.org/10.1038/ngeo2492>.

- N. de Koker, G. Steinle-Neumann, and V. Vlček. Electrical resistivity and thermal conductivity of liquid Fe alloys at high P and T, and heat flux in Earth's core. *Proceedings of the National Academy of Sciences*, 109(11):4070–4073, 2012. ISSN 0027-8424. doi: 10.1073/pnas.1111841109. URL <https://www.pnas.org/content/109/11/4070>.
- S. Dolginov, L. N. Zhuzgov, N. V. Pushkov, L. O. Tyurmina, and I. V. Fryazinov. Some results of measurements of the constant geomagnetic field above the USSR from the third artificial Earth satellite. *Geomagnetism and Aeronomy*, 2:877–889, 1962.
- E. Dormy. *Modélisation numérique de la dynamo terrestre*. PhD thesis, Institut de physique du globe (Paris), 1997.
- E. Dormy. Strong-field spherical dynamos. *Journal of Fluid Mechanics*, 789:500–513, 2016. doi: 10.1017/jfm.2015.747.
- E. Dormy and A. M. Soward. *Mathematical aspects of natural dynamos*. CRC Press, 2007.
- E. Dormy, L. Oruba, and L. Petitdemange. Three branches of dynamo action. *Fluid Dynamics Research*, 50(1):011415, jan 2018. doi: 10.1088/1873-7005/aa769c. URL <https://doi.org/10.1088/1873-7005/aa769c>.
- A. M. Dziewonski and D. L. Anderson. Preliminary reference Earth model. *Physics of the Earth and Planetary Interiors*, 25(4):297–356, 1981. ISSN 0031-9201. doi: [https://doi.org/10.1016/0031-9201\(81\)90046-7](https://doi.org/10.1016/0031-9201(81)90046-7). URL <http://www.sciencedirect.com/science/article/pii/0031920181900467>.
- W. M. Elsasser. Induction Effects in Terrestrial Magnetism Part I. Theory. *Physical Review*, 69:106–116, Feb 1946. doi: 10.1103/PhysRev.69.106. URL <https://link.aps.org/doi/10.1103/PhysRev.69.106>.
- C. C. Finlay and H. Amit. On flow magnitude and field-flow alignment at Earth's core surface. *Geophysical Journal International*, 186(1):175–192, 07 2011. ISSN 0956-540X. doi: 10.1111/j.1365-246X.2011.05032.x. URL <https://doi.org/10.1111/j.1365-246X.2011.05032.x>.
- C. C. Finlay, M. Dumberry, A. Chulliat, and M. A. Pais. Short Timescale Core Dynamics: Theory and Observations. *Space Science Reviews*, 155(1):177–218, 2010. doi: 10.1007/s11214-010-9691-6. URL <https://doi.org/10.1007/s11214-010-9691-6>.
- C. C. Finlay, N. Olsen, S. Kotsiaros, N. Gillet, and L. Tøffner-Clausen. Recent geomagnetic secular variation from Swarm and ground observatories as estimated in the CHAOS-6 geomagnetic field model. *Earth, Planets and Space*, 68(1):112, 2016. doi: 10.1186/s40623-016-0486-1. URL <https://doi.org/10.1186/s40623-016-0486-1>.
- H. W. Fisk. Isopors and isoporic movement. *Bull. Int. Geod. Geophys. Union*, 8:280–292, 1931.

- A. Fournier, J. Aubert, and E. Thébault. Inference on core surface flow from observations and 3-D dynamo modelling. *Geophysical Journal International*, 186(1):118–136, 07 2011. ISSN 0956-540X. doi: 10.1111/j.1365-246X.2011.05037.x. URL <https://doi.org/10.1111/j.1365-246X.2011.05037.x>.
- E. Friis-Christensen, H. Lühr, and G. Hulot. Swarm: A constellation to study the Earth’s magnetic field. *Earth, Planets and Space*, 58(4):351–358, 2006. doi: 10.1186/BF03351933. URL <https://doi.org/10.1186/BF03351933>.
- F. Garcia, L. Oruba, and E. Dormy. Equatorial symmetry breaking and the loss of dipolarity in rapidly rotating dynamos. *Geophysical & Astrophysical Fluid Dynamics*, 111(5):380–393, 2017. doi: 10.1080/03091929.2017.1347785. URL <https://doi.org/10.1080/03091929.2017.1347785>.
- T. Gastine. pizza: an open-source pseudo-spectral code for spherical quasi-geostrophic convection. *Geophysical Journal International*, 217(3):1558–1576, 02 2019. ISSN 0956-540X. doi: 10.1093/gji/ggz103. URL <https://doi.org/10.1093/gji/ggz103>.
- T. Gastine, J. Wicht, and J. Aubert. Scaling regimes in spherical shell rotating convection. *Journal of Fluid Mechanics*, 808:690–732, 2016. doi: 10.1017/jfm.2016.659.
- T. Gastine, J. Aubert, and A. Fournier. Dynamo-based limit to the extent of a stable layer atop Earth’s core. *Geophysical Journal International*, 222(2):1433–1448, 05 2020. ISSN 0956-540X. doi: 10.1093/gji/ggaa250. URL <https://doi.org/10.1093/gji/ggaa250>.
- N. Gillet and C. A. Jones. The quasi-geostrophic model for rapidly rotating spherical convection outside the tangent cylinder. *Journal of Fluid Mechanics*, 554:343–369, 2006. doi: 10.1017/S0022112006009219.
- N. Gillet, M. A. Pais, and D. Jault. Ensemble inversion of time-dependent core flow models. *Geochemistry, Geophysics, Geosystems*, 10(6), 2009. doi: 10.1029/2008GC002290. URL <https://agupubs.onlinelibrary.wiley.com/doi/abs/10.1029/2008GC002290>.
- N. Gillet, D. Jault, E. Canet, and A. Fournier. Fast torsional waves and strong magnetic field within the Earth’s core. *Nature*, 465(7294):74–77, 2010. doi: 10.1038/nature09010. URL <https://doi.org/10.1038/nature09010>.
- N. Gillet, N. Schaeffer, and D. Jault. Rationale and geophysical evidence for quasi-geostrophic rapid dynamics within the Earth’s outer core. *Physics of the Earth and Planetary Interiors*, 202-203:78–88, 2012. ISSN 0031-9201. doi: <https://doi.org/10.1016/j.pepi.2012.03.006>. URL <http://www.sciencedirect.com/science/article/pii/S0031920112000520>.
- N. Gillet, D. Jault, and C. C. Finlay. Planetary gyre, time-dependent eddies, torsional waves, and equatorial jets at the Earth’s core surface. *Journal of Geophysical Research: Solid Earth*, 120(6):3991–4013, 2015. doi: 10.1002/2014JB011786. URL <https://agupubs.onlinelibrary.wiley.com/doi/abs/10.1002/2014JB011786>.

- N. Gillet, L. Huder, and J. Aubert. A reduced stochastic model of core surface dynamics based on geodynamo simulations. *Geophysical Journal International*, 219(1):522–539, 07 2019. ISSN 0956-540X. doi: 10.1093/gji/ggz313. URL <https://doi.org/10.1093/gji/ggz313>.
- K.-H. Glassmeier and B. T. Tsurutani. Carl Friedrich Gauss - General Theory of Terrestrial Magnetism - a revised translation of the German text. *History of Geo- and Space Sciences*, 5(1):11–62, 2014. doi: 10.5194/hgss-5-11-2014. URL <https://hgss.copernicus.org/articles/5/11/2014/>.
- G. A. Glatzmaier. Numerical simulations of stellar convective dynamos. I. the model and method. *Journal of Computational Physics*, 55(3):461–484, 1984. ISSN 0021-9991. doi: [https://doi.org/10.1016/0021-9991\(84\)90033-0](https://doi.org/10.1016/0021-9991(84)90033-0). URL <http://www.sciencedirect.com/science/article/pii/0021999184900330>.
- G. A. Glatzmaier. *Introduction to modeling convection in planets and stars: Magnetic field, density stratification, rotation*. Princeton University Press, 2013.
- G. A. Glatzmaier and P. H. Roberts. A three-dimensional self-consistent computer simulation of a geomagnetic field reversal. *Nature*, 377(6546):203–209, 1995. doi: 10.1038/377203a0. URL <https://doi.org/10.1038/377203a0>.
- H. Gomi, K. Ohta, K. Hirose, S. Labrosse, R. Caracas, M. J. Verstraete, and J. W. Hernlund. The high conductivity of iron and thermal evolution of the Earth’s core. *Physics of the Earth and Planetary Interiors*, 224:88–103, 2013. ISSN 0031-9201. doi: <https://doi.org/10.1016/j.pepi.2013.07.010>. URL <http://www.sciencedirect.com/science/article/pii/S0031920113001052>.
- D. Gubbins. Finding core motions from magnetic observations. *Philosophical Transactions of the Royal Society of London. Series A, Mathematical and Physical Sciences*, 306(1492): 247–254, 1982. doi: 10.1098/rsta.1982.0084. URL <https://royalsocietypublishing.org/doi/abs/10.1098/rsta.1982.0084>.
- C. Guervilly, P. Cardin, and N. Schaeffer. Turbulent convective length scale in planetary cores. *Nature*, 570(7761):368–371, 2019. doi: 10.1038/s41586-019-1301-5. URL <https://doi.org/10.1038/s41586-019-1301-5>.
- B. Gutenberg. Über Erdbebenwellen. *Göttingen Nachr.*, pages 125–176, 1912.
- E. Halley. A theory of the variation of the Magnetical Compass. *Philosophical Transactions of the Royal Society of London*, 13(148):208–221, 1683. doi: 10.1098/rstl.1683.0031. URL <https://royalsocietypublishing.org/doi/abs/10.1098/rstl.1683.0031>.
- E. Halley. On the cause of the change in the variation of the magnetic needle, with a hypothesis of the structure of the internal parts of the Earth. *Philosophical Transactions of the Royal Society of London*, 17:470–478, 1692.

- M. H. Heimpel and M. E. Evans. Testing the geomagnetic dipole and reversing dynamo models over Earth's cooling history. *Physics of the Earth and Planetary Interiors*, 224: 124–131, 2013. ISSN 0031-9201. doi: <https://doi.org/10.1016/j.pepi.2013.07.007>. URL <http://www.sciencedirect.com/science/article/pii/S0031920113001027>.
- R. G. Hills. *Convection in the Earth's mantle due to viscous shear at the core-mantle interface and due to large scale buoyancy*. PhD thesis, New Mexico State Univ., University Park, Jan. 1979.
- K. Hirose, S. Labrosse, and J. Hernlund. Composition and State of the Core. *Annual Review of Earth and Planetary Sciences*, 41(1):657–691, 2013. doi: 10.1146/annurev-earth-050212-124007. URL <https://doi.org/10.1146/annurev-earth-050212-124007>.
- R. Hollerbach. On the theory of the geodynamo. *Physics of the Earth and Planetary Interiors*, 98(3):163–185, 1996. ISSN 0031-9201. doi: [https://doi.org/10.1016/S0031-9201\(96\)03185-8](https://doi.org/10.1016/S0031-9201(96)03185-8). URL <http://www.sciencedirect.com/science/article/pii/S0031920196031858>.
- R. Holme. 8.04 - Large-Scale Flow in the Core. In G. Schubert, editor, *Treatise on Geophysics (Second Edition)*, pages 91–113. Elsevier, Oxford, second edition edition, 2015. ISBN 978-0-444-53803-1. doi: <https://doi.org/10.1016/B978-0-444-53802-4.00138-X>. URL <http://www.sciencedirect.com/science/article/pii/B978044453802400138X>.
- G. Hulot, C. Eymin, B. Langlais, M. Mandea, and N. Olsen. Small-scale structure of the geodynamo inferred from Oersted and Magsat satellite data. *Nature*, 416(6881):620–623, 2002. doi: 10.1038/416620a. URL <https://doi.org/10.1038/416620a>.
- G. Hulot, T. J. Sabaka, N. Olsen, and A. Fournier. 5.02 - The Present and Future Geomagnetic Field. In G. Schubert, editor, *Treatise on Geophysics (Second Edition)*, pages 33–78. Elsevier, Oxford, second edition edition, 2015. ISBN 978-0-444-53803-1. doi: <https://doi.org/10.1016/B978-0-444-53802-4.00096-8>. URL <http://www.sciencedirect.com/science/article/pii/B9780444538024000968>.
- J. D. Hunter. Matplotlib: A 2D Graphics Environment. *Computing in Science Engineering*, 9(3):90–95, 2007.
- A. Jackson. Time-dependency of tangentially geostrophic core surface motions. *Physics of the Earth and Planetary Interiors*, 103(3):293–311, 1997. ISSN 0031-9201. doi: [https://doi.org/10.1016/S0031-9201\(97\)00039-3](https://doi.org/10.1016/S0031-9201(97)00039-3). URL <http://www.sciencedirect.com/science/article/pii/S0031920197000393>. The Jackfest special issue: A collection of papers to honor Jack Jacobs.

- A. Jackson and C. Finlay. 5.05 - Geomagnetic Secular Variation and Its Applications to the Core. In G. Schubert, editor, *Treatise on Geophysics (Second Edition)*, pages 137–184. Elsevier, Oxford, second edition edition, 2015. ISBN 978-0-444-53803-1. doi: <https://doi.org/10.1016/B978-0-444-53802-4.00099-3>. URL <http://www.sciencedirect.com/science/article/pii/B9780444538024000993>.
- A. Jackson, A. R. T. Jonkers, and M. R. Walker. Four centuries of geomagnetic secular variation from historical records. *Philosophical Transactions of the Royal Society of London. Series A: Mathematical, Physical and Engineering Sciences*, 358(1768):957–990, 2000. doi: 10.1098/rsta.2000.0569. URL <https://royalsocietypublishing.org/doi/abs/10.1098/rsta.2000.0569>.
- J. A. Jacobs. The Earth’s Inner Core. *Nature*, 172(4372):297–298, 1953.
- D. Jault, C. Gire, and J. L. Le Mouel. Westward drift, core motions and exchanges of angular momentum between core and mantle. *Nature*, 333(6171):353–356, 1988. doi: 10.1038/333353a0. URL <https://doi.org/10.1038/333353a0>.
- H. Jeffreys. The Rigidity of the Earth’s Central Core. *Geophysical Supplements to the Monthly Notices of the Royal Astronomical Society*, 1(7):371–383, 06 1926. ISSN 2051-1965. doi: 10.1111/j.1365-246X.1926.tb05385.x. URL <https://doi.org/10.1111/j.1365-246X.1926.tb05385.x>.
- A. Jephcoat and P. Olson. Is the inner core of the Earth pure iron? *Nature*, 325(6102):332–335, 1987. doi: 10.1038/325332a0. URL <https://doi.org/10.1038/325332a0>.
- C. A. Jones. 8.05 - Thermal and Compositional Convection in the Outer Core. In G. Schubert, editor, *Treatise on Geophysics (Second Edition)*, pages 115–159. Elsevier, Oxford, second edition edition, 2015. ISBN 978-0-444-53803-1. doi: <https://doi.org/10.1016/B978-0-444-53802-4.00141-X>. URL <http://www.sciencedirect.com/science/article/pii/B978044453802400141X>.
- A. R. T. Jonkers, A. Jackson, and A. Murray. Four centuries of geomagnetic data from historical records. *Reviews of Geophysics*, 41(2), 2003. doi: 10.1029/2002RG000115. URL <https://agupubs.onlinelibrary.wiley.com/doi/abs/10.1029/2002RG000115>.
- A. Kageyama and T. Sato. Computer simulation of a magnetohydrodynamic dynamo. II. *Physics of Plasmas*, 2(5):1421–1431, 1995. doi: 10.1063/1.871485. URL <https://doi.org/10.1063/1.871485>.
- J. M. Kay and R. M. Nedderman. *Fluid mechanics and transfer processes*. Cambridge University Press, 1985.
- E. M. King and B. A. Buffett. Flow speeds and length scales in geodynamo models: The role of viscosity. *Earth and Planetary Science Letters*, 371-372:156–162, 2013. ISSN 0012-821X. doi: <https://doi.org/10.1016/j.epsl.2013.04.001>. URL <http://www.sciencedirect.com/science/article/pii/S0012821X13001829>.

- C. Kloss and C. C. Finlay. Time-dependent low-latitude core flow and geomagnetic field acceleration pulses. *Geophysical Journal International*, 217(1):140–168, 01 2019. ISSN 0956-540X. doi: 10.1093/gji/ggy545. URL <https://doi.org/10.1093/gji/ggy545>.
- M. Kono. 5.01 - Geomagnetism: An Introduction and Overview. In G. Schubert, editor, *Treatise on Geophysics (Second Edition)*, pages 1–31. Elsevier, Oxford, second edition edition, 2015. ISBN 978-0-444-53803-1. doi: <https://doi.org/10.1016/B978-0-444-53802-4.00095-6>. URL <http://www.sciencedirect.com/science/article/pii/B9780444538024000956>.
- D. Kosloff and H. Tal-Ezer. A Modified Chebyshev Pseudospectral Method with an $O(N-1)$ Time Step Restriction. *Journal of Computational Physics*, 104(2):457–469, 1993. ISSN 0021-9991. doi: <https://doi.org/10.1006/jcph.1993.1044>. URL <http://www.sciencedirect.com/science/article/pii/S0021999183710442>.
- C. Kutzner and U. R. Christensen. From stable dipolar towards reversing numerical dynamos. *Physics of the Earth and Planetary Interiors*, 131(1):29 – 45, 2002. ISSN 0031-9201. doi: [https://doi.org/10.1016/S0031-9201\(02\)00016-X](https://doi.org/10.1016/S0031-9201(02)00016-X). URL <http://www.sciencedirect.com/science/article/pii/S003192010200016X>.
- R. A. Langel, R. H. Estes, G. D. Mead, E. B. Fabiano, and E. R. Lancaster. Initial geomagnetic field model from Magsat vector data. *Geophysical Research Letters*, 7(10):793–796, 1980. doi: 10.1029/GL007i010p00793. URL <https://agupubs.onlinelibrary.wiley.com/doi/abs/10.1029/GL007i010p00793>.
- J. Larmor. How could a rotating body such as the sun become a magnet? *British Association for the Advancement of Science*, 87:159–160, 1919.
- J. L. Le Mouél. Outer-core geostrophic flow and secular variation of Earth’s geomagnetic field. *Nature*, 311(5988):734–735, 1984. doi: 10.1038/311734a0. URL <https://doi.org/10.1038/311734a0>.
- I. Lehmann. P’. *Bureau Central Séismologique International Strasbourg: Publications du Bureau Central Scientifiques*, 14:87–115, 1936.
- R. S. Long, J. E. Mound, C. J. Davies, and S. M. Tobias. Scaling behaviour in spherical shell rotating convection with fixed-flux thermal boundary conditions. *Journal of Fluid Mechanics*, 889:A7, 2020. doi: 10.1017/jfm.2020.67.
- D. E. Loper and P. H. Roberts. A study of conditions at the inner core boundary of the earth. *Physics of the Earth and Planetary Interiors*, 24(4):302–307, 1981. ISSN 0031-9201. doi: [https://doi.org/10.1016/0031-9201\(81\)90117-5](https://doi.org/10.1016/0031-9201(81)90117-5). URL <http://www.sciencedirect.com/science/article/pii/0031920181901175>.

- F. J. Lowes. Spatial Power Spectrum of the Main Geomagnetic Field, and Extrapolation to the Core. *Geophysical Journal International*, 36(3):717–730, 03 1974. ISSN 0956-540X. doi: 10.1111/j.1365-246X.1974.tb00622.x. URL <https://doi.org/10.1111/j.1365-246X.1974.tb00622.x>.
- W. Lowrie and W. Alvarez. One hundred million years of geomagnetic polarity history. *Geology*, 9(9):392–397, 09 1981. ISSN 0091-7613. doi: 10.1130/0091-7613(1981)9<392:OHMYOG>2.0.CO;2. URL [https://doi.org/10.1130/0091-7613\(1981\)9<392:OHMYOG>2.0.CO;2](https://doi.org/10.1130/0091-7613(1981)9<392:OHMYOG>2.0.CO;2).
- W. V. R. Malkus. Magnetoconvection in a Viscous Fluid of Infinite Electrical Conductivity. *Astrophysical Journal*, 130:259, 1959. doi: 10.1086/146714.
- P. Marti, M. A. Calkins, and K. Julien. A computationally efficient spectral method for modeling core dynamics. *Geochemistry, Geophysics, Geosystems*, 17(8):3031–3053, 2016. doi: 10.1002/2016GC006438. URL <https://agupubs.onlinelibrary.wiley.com/doi/abs/10.1002/2016GC006438>.
- B. Martorell, J. Brodholt, I. G. Wood, and L. Vočadlo. The effect of nickel on the properties of iron at the conditions of Earth’s inner core: Ab initio calculations of seismic wave velocities of Fe–Ni alloys. *Earth and Planetary Science Letters*, 365:143–151, 2013. ISSN 0012-821X. doi: <https://doi.org/10.1016/j.epsl.2013.01.007>. URL <http://www.sciencedirect.com/science/article/pii/S0012821X13000150>.
- P. M. Mathews, T. A. Herring, and B. A. Buffett. Modeling of nutation and precession: New nutation series for nonrigid Earth and insights into the Earth’s interior. *Journal of Geophysical Research: Solid Earth*, 107(B4), 2002. doi: 10.1029/2001JB000390. URL <https://agupubs.onlinelibrary.wiley.com/doi/abs/10.1029/2001JB000390>.
- P. Mauersberger. Das Mittel der Energiedichte des geomagnetischen Hauptfeldes an der Erdoberfläche und seine säkulare Änderung. *Gerlands Beiträge zur Geophysik*, 65:207–215, 1956.
- M. D. Menu, L. Petitdemange, and S. Galtier. Magnetic effects on fields morphologies and reversals in geodynamo simulations. *Physics of the Earth and Planetary Interiors*, 307:106542, 2020. ISSN 0031-9201. doi: <https://doi.org/10.1016/j.pepi.2020.106542>. URL <http://www.sciencedirect.com/science/article/pii/S0031920119302997>.
- F. Nimmo. 8.02 - Energetics of the Core. In G. Schubert, editor, *Treatise on Geophysics (Second Edition)*, pages 27–55. Elsevier, Oxford, second edition edition, 2015a. ISBN 978-0-444-53803-1. doi: <https://doi.org/10.1016/B978-0-444-53802-4.00139-1>. URL <http://www.sciencedirect.com/science/article/pii/B9780444538024001391>.

- F. Nimmo. 9.08 - Thermal and Compositional Evolution of the Core. In G. Schubert, editor, *Treatise on Geophysics (Second Edition)*, pages 201–219. Elsevier, Oxford, second edition edition, 2015b. ISBN 978-0-444-53803-1. doi: <https://doi.org/10.1016/B978-0-444-53802-4.00160-3>. URL <http://www.sciencedirect.com/science/article/pii/B9780444538024001603>.
- R. D. Oldham. The Constitution of the Interior of the Earth, as Revealed by Earthquakes. *Quarterly Journal of the Geological Society*, 62(1-4):456–475, 1906. ISSN 0370-291X. doi: 10.1144/GSL.JGS.1906.062.01-04.21. URL <https://jgs.lyellcollection.org/content/62/1-4/456>.
- N. Olsen, G. Hulot, V. Lesur, C. C. Finlay, C. Beggan, A. Chulliat, T. J. Sabaka, R. Floberghagen, E. Friis-Christensen, R. Haagmans, S. Kotsiaros, H. Lühr, L. Tøffner-Clausen, and P. Vigneron. The Swarm Initial Field Model for the 2014 geomagnetic field. *Geophysical Research Letters*, 42(4):1092–1098, 2015. doi: 10.1002/2014GL062659. URL <https://agupubs.onlinelibrary.wiley.com/doi/abs/10.1002/2014GL062659>.
- P. Olson and H. Amit. Changes in earth’s dipole. *Naturwissenschaften*, 93(11): 519–542, 2006. doi: 10.1007/s00114-006-0138-6. URL <https://doi.org/10.1007/s00114-006-0138-6>.
- L. Oruba and E. Dormy. Predictive scaling laws for spherical rotating dynamos. *Geophysical Journal International*, 198(2):828–847, 06 2014. ISSN 0956-540X. doi: 10.1093/gji/ggu159. URL <https://doi.org/10.1093/gji/ggu159>.
- M. A. Pais and D. Jault. Quasi-geostrophic flows responsible for the secular variation of the Earth’s magnetic field. *Geophysical Journal International*, 173(2):421–443, 2008. doi: 10.1111/j.1365-246X.2008.03741.x. URL <https://onlinelibrary.wiley.com/doi/abs/10.1111/j.1365-246X.2008.03741.x>.
- M. A. Pais, O. Oliveira, and F. Nogueira. Nonuniqueness of inverted core-mantle boundary flows and deviations from tangential geostrophy. *Journal of Geophysical Research: Solid Earth*, 109(B8), 2004. doi: 10.1029/2004JB003012. URL <https://agupubs.onlinelibrary.wiley.com/doi/abs/10.1029/2004JB003012>.
- E. N. Parker. Hydromagnetic dynamo models. *The Astrophysical Journal*, 122:293, 1955.
- L. Petitdemange. Systematic parameter study of dynamo bifurcations in geodynamo simulations. *Physics of the Earth and Planetary Interiors*, 277:113–132, 2018. ISSN 0031-9201. doi: <https://doi.org/10.1016/j.pepi.2018.02.001>. URL <http://www.sciencedirect.com/science/article/pii/S0031920117301875>.
- J.-P. Poirier. Light elements in the Earth’s outer core: A critical review. *Physics of the Earth and Planetary Interiors*, 85(3):319 – 337, 1994. ISSN 0031-9201. doi: [https://doi.org/10.1016/0031-9201\(94\)90120-1](https://doi.org/10.1016/0031-9201(94)90120-1). URL <http://www.sciencedirect.com/science/article/pii/0031920194901201>.

- M. Pozzo, C. Davies, D. Gubbins, and D. Alfè. Thermal and electrical conductivity of iron at Earth's core conditions. *Nature*, 485(7398):355–358, 2012. doi: 10.1038/nature11031. URL <https://doi.org/10.1038/nature11031>.
- M. Pozzo, C. Davies, D. Gubbins, and D. Alfè. Transport properties for liquid silicon-oxygen-iron mixtures at Earth's core conditions. *Physical Review B*, 87:014110, Jan 2013. doi: 10.1103/PhysRevB.87.014110. URL <https://link.aps.org/doi/10.1103/PhysRevB.87.014110>.
- W. H. Press, B. P. Flannery, S. A. Teukolsky, and W. T. Vetterling. *Numerical Recipes in FORTRAN 77: Volume 1, Volume 1 of Fortran Numerical Recipes: The Art of Scientific Computing*. Cambridge University Press, 1992. ISBN 9780521430647. URL <https://books.google.fr/books?id=cHxGAAAAAYAAJ>.
- R. Raynaud, J. Guilet, H.-T. Janka, and T. Gastine. Magnetar formation through a convective dynamo in protoneutron stars. *Science Advances*, 6(11), 2020. doi: 10.1126/sciadv.aay2732. URL <https://advances.sciencemag.org/content/6/11/eaay2732>.
- P. B. Rhines. Waves and turbulence on a beta-plane. *Journal of Fluid Mechanics*, 69(3): 417–443, 1975. doi: 10.1017/S0022112075001504.
- P. H. Roberts. Magneto-convection in a rapidly rotating fluid. *Rotating Fluids in Geophysics (ed. PH Roberts & AM Soward)*, pages 421–435, 1978.
- P. H. Roberts and E. M. King. On the genesis of the Earth's magnetism. *Reports on Progress in Physics*, 76(9):096801, sep 2013. doi: 10.1088/0034-4885/76/9/096801. URL <https://doi.org/10.1088%2F0034-4885%2F76%2F9%2F096801>.
- P. H. Roberts and S. Scott. On Analysis of the Secular Variation. *Journal of geomagnetism and geoelectricity*, 17(2):137–151, 1965. doi: 10.5636/jgg.17.137.
- P. H. Roberts, Z. J. Yu, and C. T. Russell. On the 60-year signal from the core. *Geophysical & Astrophysical Fluid Dynamics*, 101(1):11–35, 2007. doi: 10.1080/03091920601083820. URL <https://doi.org/10.1080/03091920601083820>.
- A. Sakuraba and P. H. Roberts. Generation of a strong magnetic field using uniform heat flux at the surface of the core. *Nature Geoscience*, 2(11):802–805, 2009. doi: 10.1038/ngeo643. URL <https://doi.org/10.1038/ngeo643>.
- N. Schaeffer. Efficient spherical harmonic transforms aimed at pseudospectral numerical simulations. *Geochemistry, Geophysics, Geosystems*, 14(3):751–758, 2013. doi: 10.1002/ggge.20071. URL <https://agupubs.onlinelibrary.wiley.com/doi/abs/10.1002/ggge.20071>.
- N. Schaeffer, D. Jault, H.-C. Nataf, and A. Fournier. Turbulent geodynamo simulations: a leap towards Earth's core. *Geophysical Journal International*, 211(1):1–29, 06 2017. ISSN 0956-540X. doi: 10.1093/gji/ggx265. URL <https://doi.org/10.1093/gji/ggx265>.

- M. Schinner. Rotational threshold in global numerical dynamo simulations. *Monthly Notices of the Royal Astronomical Society: Letters*, 431(1):L78–L82, 02 2013. ISSN 1745-3925. doi: 10.1093/mnrasl/slt012. URL <https://doi.org/10.1093/mnrasl/slt012>.
- G. Schubert, D. L. Turcotte, and P. Olson. *Mantle convection in the Earth and planets*. Cambridge University Press, 2001.
- T. Schwaiger, T. Gastine, and J. Aubert. Force balance in numerical geodynamo simulations: a systematic study. *Geophysical Journal International*, 219(Supplement 1): S101–S114, 04 2019. ISSN 0956-540X. doi: 10.1093/gji/ggz192. URL <https://doi.org/10.1093/gji/ggz192>.
- T. Schwaiger, T. Gastine, and J. Aubert. Relating force balances and flow length scales in geodynamo simulations. *Geophysical Journal International*, 224(3):1890–1904, 11 2020. ISSN 0956-540X. doi: 10.1093/gji/ggaa545. URL <https://doi.org/10.1093/gji/ggaa545>.
- A. Sheyko, C. C. Finlay, and A. Jackson. Magnetic reversals from planetary dynamo waves. *Nature*, 539(7630):551–554, 2016. doi: 10.1038/nature19842. URL <https://doi.org/10.1038/nature19842>.
- A. Sheyko, C. Finlay, J. Favre, and A. Jackson. Scale separated low viscosity dynamos and dissipation within the Earth’s core. *Scientific Reports*, 8(1):12566, 2018. doi: 10.1038/s41598-018-30864-1. URL <https://doi.org/10.1038/s41598-018-30864-1>.
- L. Silva, L. Jackson, and J. Mound. Assessing the importance and expression of the 6 year geomagnetic oscillation. *Journal of Geophysical Research: Solid Earth*, 117(B10), 2012. doi: 10.1029/2012JB009405. URL <https://agupubs.onlinelibrary.wiley.com/doi/abs/10.1029/2012JB009405>.
- K. M. Soderlund, E. M. King, and J. M. Aurnou. The influence of magnetic fields in planetary dynamo models. *Earth and Planetary Science Letters*, 333-334:9–20, 2012. ISSN 0012-821X. doi: <https://doi.org/10.1016/j.epsl.2012.03.038>. URL <http://www.sciencedirect.com/science/article/pii/S0012821X12001689>.
- K. M. Soderlund, A. Sheyko, E. M. King, and J. M. Aurnou. The competition between Lorentz and Coriolis forces in planetary dynamos. *Progress in Earth and Planetary Science*, 2(1):24, 2015. doi: 10.1186/s40645-015-0054-5. URL <https://doi.org/10.1186/s40645-015-0054-5>.
- F. D. Stacey. Thermodynamic relationships and the properties of iron at Earth’s core conditions. In *Proceedings of the Conference for the Association for the International Advancement of High Pressure*. Colorado Springs, Colorado, 1993.

- S. V. Starchenko and C. A. Jones. Typical Velocities and Magnetic Field Strengths in Planetary Interiors. *Icarus*, 157(2):426–435, 2002. ISSN 0019-1035. doi: <https://doi.org/10.1006/icar.2002.6842>. URL <http://www.sciencedirect.com/science/article/pii/S0019103502968429>.
- J. A. Tarduno, R. D. Cottrell, M. K. Watkeys, A. Hofmann, P. V. Doubrovine, E. E. Mamajek, D. Liu, D. G. Sibeck, L. P. Neukirch, and Y. Usui. Geodynamo, Solar Wind, and Magnetopause 3.4 to 3.45 Billion Years Ago. *Science*, 327(5970):1238–1240, 2010. ISSN 0036-8075. doi: 10.1126/science.1183445. URL <https://science.sciencemag.org/content/327/5970/1238>.
- J. A. Tarduno, R. D. Cottrell, W. J. Davis, F. Nimmo, and R. K. Bono. A Hadean to Paleoproterozoic geodynamo recorded by single zircon crystals. *Science*, 349(6247):521–524, 2015. ISSN 0036-8075. doi: 10.1126/science.aaa9114. URL <https://science.sciencemag.org/content/349/6247/521>.
- J.-P. Valet and A. Fournier. Deciphering records of geomagnetic reversals. *Reviews of Geophysics*, 54(2):410–446, 2016. doi: 10.1002/2015RG000506. URL <https://agupubs.onlinelibrary.wiley.com/doi/abs/10.1002/2015RG000506>.
- J. Vidal and N. Schaeffer. Quasi-geostrophic modes in the Earth’s fluid core with an outer stably stratified layer. *Geophysical Journal International*, 202(3):2182–2193, 07 2015. ISSN 0956-540X. doi: 10.1093/gji/ggv282. URL <https://doi.org/10.1093/gji/ggv282>.
- L. Vočadlo. 2.06 - Earth’s Core: Iron and Iron Alloys. In G. Schubert, editor, *Treatise on Geophysics (Second Edition)*, pages 117–147. Elsevier, Oxford, second edition edition, 2015. ISBN 978-0-444-53803-1. doi: <https://doi.org/10.1016/B978-0-444-53802-4.00032-4>. URL <http://www.sciencedirect.com/science/article/pii/B9780444538024000324>.
- L. Vočadlo, D. Alfè, M. J. Gillan, and G. D. Price. The properties of iron under core conditions from first principles calculations. *Physics of the Earth and Planetary Interiors*, 140(1):101–125, 2003. ISSN 0031-9201. doi: <https://doi.org/10.1016/j.pepi.2003.08.001>. URL <http://www.sciencedirect.com/science/article/pii/S0031920103001675>. Geophysical and Geochemical Evolution of the Deep Earth.
- K. A. Whaler. Geomagnetic evidence for fluid upwelling at the core-mantle boundary. *Geophysical Journal International*, 86(2):563–588, 08 1986. ISSN 0956-540X. doi: 10.1111/j.1365-246X.1986.tb03844.x. URL <https://doi.org/10.1111/j.1365-246X.1986.tb03844.x>.
- J. Wicht. Inner-core conductivity in numerical dynamo simulations. *Physics of the Earth and Planetary Interiors*, 132(4):281–302, 2002. ISSN 0031-9201. doi: [https://doi.org/10.1016/S0031-9201\(02\)00078-X](https://doi.org/10.1016/S0031-9201(02)00078-X). URL <http://www.sciencedirect.com/science/article/pii/S003192010200078X>.

- J. Wicht and U. R. Christensen. Torsional oscillations in dynamo simulations. *Geophysical Journal International*, 181(3):1367–1380, 06 2010. ISSN 0956-540X. doi: 10.1111/j.1365-246X.2010.04581.x. URL <https://doi.org/10.1111/j.1365-246X.2010.04581.x>.
- J. Wicht and S. Sanchez. Advances in geodynamo modelling. *Geophysical & Astrophysical Fluid Dynamics*, 113(1-2):2–50, 2019. doi: 10.1080/03091929.2019.1597074. URL <https://doi.org/10.1080/03091929.2019.1597074>.
- C.-C. Wu and P. H. Roberts. On a dynamo driven topographically by longitudinal libration. *Geophysical and Astrophysical Fluid Dynamics*, 107(1-2):20–44, 2013. doi: 10.1080/03091929.2012.682990.
- R. K. Yadav, T. Gastine, U. R. Christensen, S. J. Wolk, and K. Poppenhaeger. Approaching a realistic force balance in geodynamo simulations. *Proceedings of the National Academy of Sciences*, 113(43):12065–12070, 2016. ISSN 0027-8424. doi: 10.1073/pnas.1608998113. URL <https://www.pnas.org/content/113/43/12065>.
- S. Zatman and J. Bloxham. Torsional oscillations and the magnetic field within the Earth’s core. *Nature*, 388(6644):760–763, Aug. 1997.

Acknowledgements

First and foremost, I would like to sincerely thank my supervisors Julien Aubert and Thomas Gastine for their guidance and support throughout my PhD thesis. This work has benefitted greatly from their scientific experience and in-depth knowledge of planetary dynamos. Many thanks to both of them for always being available and for their advice whenever I had scientific questions or administrative difficulties. I am deeply indebted to them for their assistance in my application to come to Paris.

I would like to extend my gratitude to Henri-Claude Nataf and Johannes Wicht for reviewing my manuscript, and for their feedback and constructive comments during my defence. My thanks also go to Krista Soderlund, Céline Guervilly and Alexandre Fournier for their helpful discussions and participation in my thesis committee.

I would also like to express my heartfelt thanks to Florian Lhuillier and Stuart Gilder, who mentored me during my Bachelor's and Master's in Munich. It was their lectures and the discussions with them that sparked my interest in geomagnetism and the dynamics of the Earth's core. Florian Lhuillier in particular spent a lot of time introducing me to scientific working techniques. Ultimately, it was his commitment to research that inspired me to pursue a PhD.

Next, I would like to thank the members of the laboratory "Dynamique des Fluides Géologiques". It was a pleasure to come to work every day and be part of a team made up of so many kind people. A warm thanks goes to Geneviève Brandeis for sharing her office with me and for being good company over the past three years. A special thank you also goes to Jenny Wong for her conviviality and for proof-reading my manuscript. I also wish to thank my fellow PhD students and everyone at the Institut de Physique du Globe de Paris whom I met during the course of my dissertation.

I gratefully acknowledge the funding that I received for my PhD project through an INSPIRE (INterdiSciPlinarity and excellence for doctoral training of International REsearchers in Paris) fellowship, which was co-financed by the European Commission (European Union's Horizon 2020 research and innovation programme under the Marie Skłodowska-Curie grant agreement No 665850) and the Université Sorbonne Paris Cité.

Finally, I would like to warmly thank my friends and family. Without their encouragement and support, this work would not have been possible.

Geodynamo simulations in the Earth's core dynamical regime: a systematic study

Abstract

The geomagnetic field is generated by dynamo action in the Earth's liquid outer core. In this thesis, the force balance controlling the convective flow dynamics which drive this dynamo mechanism is studied using numerical simulations. To this end, we compute and analyse a large series of models. We find that most numerical dynamos are governed by a so-called quasi-geostrophic Magneto-Archimedean-Coriolis (QG-MAC) balance. This type of force equilibrium refers to a physical setup in which the dominant force balance is between Coriolis and pressure forces (geostrophic balance), while Lorentz, buoyancy and ageostrophic Coriolis forces, i.e. the part of the Coriolis force not compensated by pressure, equilibrate at the next order. Inertia and viscous forces represent secondary contributions. In QG-MAC dynamos with a strong magnetic field, the Lorentz force becomes dominant towards the smallest flow length scales such that these are in a magnetostrophic (Coriolis-Pressure-Lorentz) balance. Spectral analysis of the force balance shows that in QG-MAC models, the length scale at which buoyancy and Lorentz forces are of equal magnitude controls the dominant scale of convection. In addition, we show that the scale at which the prevailing force balance changes from large-scale geostrophy to small-scale magnetostrophy, can be related to the loss of the axial invariance of the flow. Our results suggest that the Earth's core is most likely controlled by a QG-MAC balance, in which the dominant force equilibrium transitions into a magnetostrophic balance towards small scales. Extrapolation of theoretical scalings which assume this type of force balance to the conditions of the Earth's core suggests that the dominant flow length scale of the geodynamo is about 200 km, while magnetostrophic effects are deferred to scales below 50 km.

Key words: Core, Geodynamo, Numerical modelling

Simulations de la géodynamo dans le régime dynamique du noyau de la Terre : une étude systématique

Résumé

Le champ géomagnétique est généré par l'action de la dynamo dans le noyau externe liquide de la Terre. Dans cette thèse, l'équilibre des forces qui contrôle la dynamique de l'écoulement convectif à l'origine de ce mécanisme de dynamo est étudié à l'aide de simulations numériques. À cette fin, nous calculons et analysons une grande série de modèles. Nous constatons que la plupart des dynamos numériques sont régies par une balance dite quasi-géostrophique Magnéto-Archimédienne-Coriolis (QG-MAC). Ce type d'équilibre des forces fait référence aux cas dans lesquels l'équilibre des forces dominantes est celui entre les forces de Coriolis et les forces de pression (équilibre géostrophique), tandis que les forces de Lorentz, de flottabilité et de Coriolis agéostrophique, c'est-à-dire la partie de la force de Coriolis non compensée par la pression, s'équilibrent à l'ordre suivant. L'inertie et les forces visqueuses représentent des contributions secondaires. Dans les dynamos QG-MAC à fort champ magnétique, la force de Lorentz devient dominante vers les plus petites échelles de longueur d'écoulement, de sorte que celles-ci sont en équilibre magnétostrophique (Coriolis-Pressure-Lorentz). L'analyse spectrale de la balance des forces montre que dans les modèles QG-MAC, l'échelle de longueur à laquelle la flottabilité et les forces de Lorentz sont en équilibre contrôle l'échelle dominante de convection. De plus, nous montrons que l'échelle à laquelle la balance des forces dominante passe de la géostrophie à grande échelle à la magnétostrophie à petite échelle, peut être liée à la perte de l'invariance axiale de l'écoulement. Nos résultats suggèrent que le noyau de la Terre est probablement contrôlé par une balance QG-MAC, dans laquelle l'équilibre de force dominant passe d'une balance géostrophique à une balance magnétostrophique à petite échelle. L'extrapolation des échelles théoriques qui supposent ce type d'équilibre des forces aux conditions du noyau terrestre suggère que l'échelle dominante de longueur de flux de la géodynamo est d'environ 200 km, tandis que les effets magnétostrophiques sont décalés vers des échelles inférieures à 50 km.

Mots clés : Noyau, Géodynamo, Modélisation numérique